Nonlinear nanophotonics in plasmonic and graphene structures

Daria Smirnova

A thesis submitted for the degree of
Doctor of Philosophy
The Australian National University

March, 2016

Declaration

This thesis is an account of research undertaken in the Nonlinear Physics Centre within the Research School of Physics and Engineering at the Australian National University between March 2013 and November 2015 while I was enrolled for the Doctor of Philosophy degree.

This research was carried out under the supervision of Prof. Yuri S. Kivshar, Dr. Ilya V. Shadrivov and Dr. Elena A. Ostrovskaya. Except where acknowledged in the customary manner, the material presented in this thesis is, to the best of my knowledge, original and has not been submitted in whole or part for a degree in any university.

Daria Smirnova
March, 2016

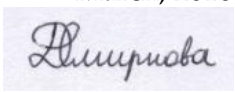

Publications

Refereed journal articles

Articles containing results included in this thesis are in bold.

1. D. A. Smirnova, A. I. Smirnov, and A. A. Zharov, "Two-dimensional plasmonic eigenmode nanolocalization in an inhomogeneous metal-dielectric-metal slot waveguide," JETP Lett. 96, 245-250 (2012).

2. A. A. Zharov, D.A. Smirnova, and A. I. Smirnov, "Nonlinear resonant control of cross-cut photonic flows," J. Opt. Soc. Am. B 29, 443-449 (2012).

3. A. A. Zharov, N. A. Zharova, D. A. Smirnova, and A. A. Zharov Jr., "Three-dimensional nanofocusing of light through surface plasmon scattering by a lump-like defect in metal/dielectric/metal slot waveguides," J. Opt. Soc. Am. B 30, 626-630 (2013).

4. A. A. Zharov Jr., D. A. Smirnova, and A. A. Zharov, "Verification of effective refraction index approach to the surface plasmon propagation in ultrathin tapered metal-dielectric-metal slot waveguides," J. Opt. Soc. Am. B 30, 1601-1605 (2013).

5. **R. E. Noskov, D. A. Smirnova, and Yu. S. Kivshar, "Subwavelength solitons and Faraday waves in two-dimensional lattices of metal nanoparticles," Opt. Lett. 38, 2554-2556 (2013).**

6. **D. A. Smirnova, A. V. Gorbach, I. V. Iorsh, I. V. Shadrivov, and Yu. S. Kivshar, "Nonlinear switching with a graphene coupler," Phys. Rev. B 88, 045443-4 (2013).**

7. Yu. V. Bludov, D. A. Smirnova, Yu. S. Kivshar, N. M. R. Peres, and M. I. Vasilevskiy, "Nonlinear TE-polarized surface polaritons on graphene," Phys. Rev. B 89, 035406-6 (2014).

8. **D. A. Smirnova, I. V. Shadrivov, A. I. Smirnov, and Yu. S. Kivshar, "Dissipative plasmon-solitons in multilayer graphene," Laser & Photonics Rev. 8, 291-296 (2014).**

9. **D. A. Smirnova, I. V. Iorsh, I. V. Shadrivov, and Yu. S. Kivshar, "Multilayer graphene waveguides," JETP Lett. 99, 456-460 (2014).**

10. **D. Smirnova, P. Buslaev, I. Iorsh, I. V. Shadrivov, P. A. Belov, and Yu. S. Kivshar, "Deeply subwavelength electromagnetic Tamm states in graphene metamaterials," Phys. Rev. B 89, 245414-4 (2014).**

11. L. A. Smirnov, D. A. Smirnova, E. A. Ostrovskaya, and Yu. S. Kivshar, "Dynamics and stability of dark solitons in exciton-polariton condensates," Phys. Rev. B 89, 235310-11 (2014).

12. **D. A. Smirnova, I. V. Shadrivov, A. E. Miroshnichenko, A. I. Smirnov, and Yu. S. Kivshar, "Second-harmonic generation by a graphene nanoparticle," Phys. Rev. B 90, 035412-7 (2014).**

13. **R. E. Noskov, D. A. Smirnova, and Yu. S. Kivshar, "Plasmonic kinks and walking solitons in nonlinear lattices of metal nanoparticles," Philos. Trans. R. Soc. Lond. A 372, 20140010 (2014).**

14. **D. Smirnova and Yu. S. Kivshar, "Second-harmonic generation in subwavelength graphene waveguides," Phys. Rev. B 90, 165433-5 (2014).**

15. **Yu. V. Bludov, D. A. Smirnova, Yu. S. Kivshar, N. M. R. Peres, and M. V. Vasilevskiy, "Discrete solitons in graphene metamaterials,"Phys. Rev. B 91, 045424-8 (2015).**

16. **D. A. Smirnova, R. E. Noskov, L. A. Smirnov, and Yu. S. Kivshar, "Dissipative plasmon solitons in graphene nanodisk arrays," Phys. Rev. B 91, 075409-6 (2015).**

17. K. Yu. Bliokh, D. Smirnova, and F. Nori, "Quantum spin Hall effect of light," Science **348**, 1448-1451 (2015).

18. **D. A. Smirnova and A. S. Solntsev, "Cascaded third harmonic generation in hybrid graphene-semiconductor waveguides," Phys. Rev. B 92, 155410-5 (2015).**

19. A. P. Slobozhanyuk, A. B. Khanikaev, D. S. Filonov, D. A. Smirnova, A. E. Miroshnichenko, and Yu. S. Kivshar, "Experimental demonstration of topological effects in bianisotropic metamaterials," Sci. Rep. **6**, 22270 (2016).

20. **D. A. Smirnova, A. E. Miroshnichenko, Yu. S. Kivshar, and A. B. Khanikaev, "Tunable nonlinear graphene metasurfaces," Phys. Rev. B 92, 161406-6(R) (2015).**

21. D. Smirnova, S. H. Mousavi, Z. Wang, Yu. S. Kivshar, and A. B. Khanikaev, "Trapping and guiding surface plasmons in graphene landscapes," submitted.

Other publications

1. I. Iorsh, P. Belov, D. Smirnova, I. Shadrivov, and Yu. Kivshar, "Terahertz hyperbolic metamaterials and nonlinear couplers in graphene," SPIE Newsroom, DOI:10.1117/2.1201406.005445 (2014).

2. D. A. Smirnova, I. V. Shadrivov, and Yu. S. Kivshar, "Graphene Plasmonics: Exploring Surface Nonlinearities," Australian Optical Society News 28 (4), 31 (2014).

Full-text international conference proceedings

1. R. E. Noskov, D. A. Smirnova, and Yu. S. Kivshar, "Subwavelength solitons and pattern formation in two-dimensional lattices of nonlinear metal nanoparticles," 7th International Congress on Advanced Electromagnetic Materials in Microwaves and Optics, Metamaterials 2013.

2. A. I. Smirnov, N. V. Ilin, and D. A. Smirnova, "Self-action effects for the laser radiation scattered by metal nanoparticles," 15th International Conference on Transparent Optical Networks, ICTON 2013.

Acknowledgments

I would like to express my deepest gratitude to my principal supervisor Prof. Yuri Kivshar for his patient guidance, insight, continuous encouragement and believing in me over the years of my candidature.

I sincerely thank Dr. Elena Ostrovskaya for wise and always timely advising, and benevolent help in all the troubles.

I am very grateful to all my collaborators, colleagues and co-authors with whom I have interacted over these years, and particularly, to the representatives of my alma mater – Dr. Roman Noskov and Dr. Ilya Shadrivov. Special great thanks to Prof. Alexander Khanikaev, Dr. Andrey Miroshnichenko and Dr. Konstantin Bliokh for sharing their outstanding professional experience with me and many captivating discussions.

I am also much indebted to my family and friends for their unconditional support.

Abstract

Going beyond the diffraction limit of light, nanophotonics studies nontrivial physical phenomena involving the interaction of photons with nanostructured media. Within decades of fruitful developments, the field of nanophotonics has become a prominent area of research with applications ranging from integrated optical circuits and ultrafast photonic devices to super-imaging, nanolasing and biosensing. Nonlinear intensity-dependent optical effects, facilitated by strong light-matter interaction, are indispensable in modern photonics, enriching the beauty of physics comprised and providing novel opportunities for subwavelength light control.

To date, the possibilities of photon nanoscale confinement and operations with photonic flows are primarily associated with surface plasmons that are localized in the vicinity of metal-dielectric interfaces infrared or visible-frequency electromagnetic eigenmodes originating from coupling of the electromagnetic field to the electron oscillations in a metal plasma. Physics of light interaction with metal structures that are much smaller than the free space wavelength of light constitutes one of the most significant branches of contemporary nanophotonics – nanoplasmonics. Combining strong surface plasmon resonances and high intrinsic nonlinearities in the deep subwavelength scales, plasmonic structures offer a unique playground to develop novel concepts for light manipulation at the nanoscale. Tight field confinement in plasmonic systems can boost the efficiency of various nonlinear optical effects, the study of which can help delineate a roadmap in designing novel subwavelength nonlinear optical elements.

Recently, graphene, a single atomic layer of graphite, has emerged as a promising alternative to noble metals for applications in plasmonics. The study of plasmonic effects in doped graphene structures has attracted special interest from the nanoplasmonics research community due to novel functionalities suggested by such systems, including an extraordinary field confinement by a graphene layer, tunability of graphene properties through doping or electrostatic gating and longer lifetimes in the infrared and terahertz frequency ranges, which is extremely important for biomedical and security applications. In addition, graphene demonstrates strong and tunable optical nonlinearity and it can be incorporated into various components of nanoscale optics. However, the potential of the nonlinear response of graphene is not yet fully realized and almost not studied, especially in the resonant plasmonic geometries. It is therefore of significant interest to construct analytical models for the underlying principles and explore the viability of nonlinear optical effects in graphene-based photonic devices.

This thesis focuses on the nonlinear photonics of plasmonic and graphene-based nanostructures. Exploiting nonlinear optical response, it develops theoretical ideas for the all-optical light control at subwavelength scales and studies the advantageous possibilities of manipulating electromagnetic waves by utilizing the unique properties of graphene.

Chapter 2 presents a comprehensive study of nonlinear dynamics in arrays of optically driven plasmonic nanoparticles with a Kerr-like nonlinear response. We perform detailed modulation instability analysis and demonstrate the pattern formation and the existence of plasmonic kinks and nonlinear localized modes in the form of trapped and walking solitons in such systems under control guidance of the external driving field.

Chapters 3 and 4 include a theoretical prediction and analytical description of manifold nonlinear effects that can be actualized due to the graphene nonlinear response. Utilizing conventional concepts of photonics and metal plasmonics combined with unique electronic and optical properties of graphene, we establish a theoretical framework for designing various graphene-enhanced components of nanoscale optics and nanodevices, such as waveguides, couplers, nano-antennas and metasurfaces. These studies outline substantial features of graphene as a promising material for surface physics and plasmonics, and envision their potential applications in optical nanocircuits, optoelectronics, metamaterials, and THz technology.

Specifically, in Chapter 3 we investigate the nonlinear self-action of surface plasmons and the generation of subwavelength solitons in graphene waveguides and multilayers. Our studies elucidate the nonlinear switching of light in two coupled layers of graphene, the formation of nonlinear modes in graphene metamaterials, and the excitation of dissipative plasmon solitons coupled to the external driving source via an evanescent field.

Chapter 4 examines the harmonic generation in different geometries with graphene. We develop theoretical models for the resonant (enhanced) second-harmonic generation from a graphene-wrapped dielectric spherical nanoparticle and frequency conversion in graphene-based waveguides through the phase-matched nonlinear interaction of the plasmonic modes. We describe the second-harmonic generation from a double-layer graphene structure with modulated conductivity and nonlinear plasmon-to-plasmon conversion in hybrid graphene-semiconductor waveguides, predicting the cascading effect in the third-harmonic generation. Finally, we propose the concept of tunable nonlinear graphene metasurfaces composed of a graphene layer and a planar gold metamaterial. We demonstrate that such hybrid graphene metasurfaces provide strong tunability and dramatic field enhancement, giving rise to the enhanced nonlinear response and high efficiency of the second-harmonic generation.

Chapter 5 summarizes the results and concludes this thesis.

Contents

Chapter 1

Motivation and outline

Nanophotonics and plasmonics

The recent decade has been marked by the rapid development of a relatively new research direction in science – nanophotonics – that combines studies of the interaction of electromagnetic radiation (primarily in the visible and IR ranges) with particles and material inhomogeneities of characteristic size from one to hundreds of nanometers [1–4]. An interest in this research has been stimulated, in many respects, by the attempt to increase the rate of data processing up to terahertz frequencies and higher, which is beyond the capabilities of present-day electronics because of RC delays. However, there are no fundamental restrictions for nanophotonics [5, 6]. A photon is regarded to be an ideal elementary information carrier as it possesses zero mass, moreover, a signal transmitted by photons has maximum possible speed (speed of light). In computer technologies, the main challenge in implementing optical data transfer is transformation of electronic signals to optical and back, as well as the creation of new devices that would allow the light control at nanoscale. Still another important impulse for nanophotonics advancement is the development of novel methods for diagnosing and imaging objects with subwavelength resolutions [7–9]. These methods are in high demand for physical, medical and biological studies, as well as for controlling various nanotechnological processes. For solution of these problems, it is necessary to create the conditions under which electromagnetic fields will be localized on nanoscale.

To date, nanolocalization of light is associated primarily with surface plasmon-polaritons, which are the collective excitations of bound electrons and photons that are spatially confined to regions much smaller than the wavelength of the photon with the same energy, providing means for extreme concentration of electromagnetic energy [2, 10–14]. For instance, in metal-dielectric-metal slot waveguides, transverse localization of plasmonic modes in the near infrared and visible ranges may amount up to 30 - 40 nm, which can be up to 50 times smaller than the wavelength of light in free space. However, their propagation length is limited to a few micrometers only due to the rather strong ohmic loss in metal. Such propagation length may be insufficient for many nanophotonic applications. Hence, special means are needed to increase the propagation length using, e.g., amplifying media [15] and nanofocusing effects in tapering plasmonic waveguides [16, 17]. In the infrared and terahertz ranges, nanolocalized surface plasmon-polariton modes with weaker attenuation may be supported by doped graphene films and various multilayer graphene structures. The use of purely dielectric structures, which however usually have worse characteristics from the viewpoint of field localization, may significantly reduce ohmic loss in nanophotonic devices [18].

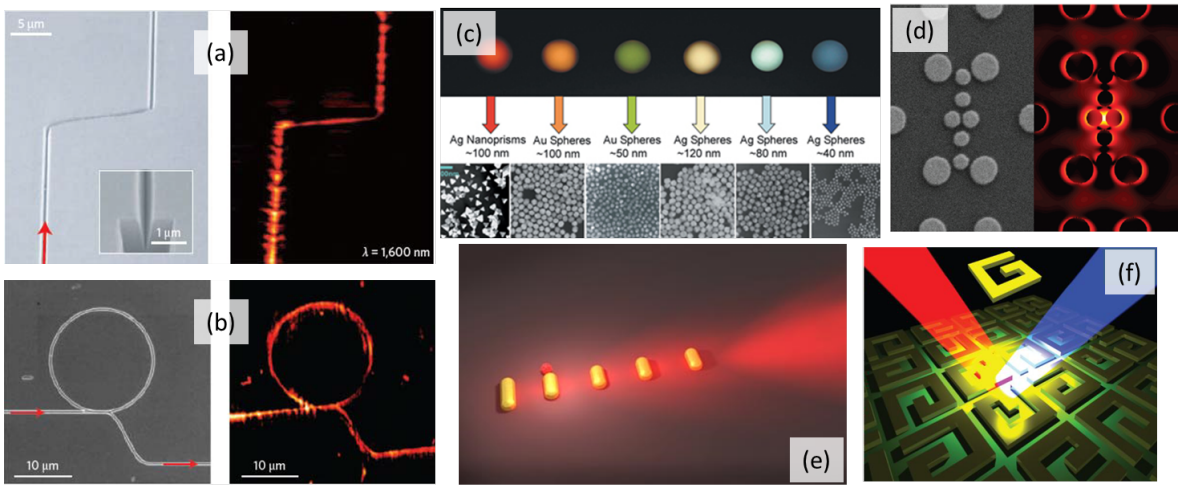

Figure 1.1: Facets of plasmonics: (a) bent plasmonic waveguide and (b) plasmonic ring resonator [39–41]; (c) size-dependent optical properties of gold nanoparticles [42], (d) array of metallic nanoparticles with large electric near-field enhancement [43], (e) optical antenna for directional light emission [44], (f) illustration of the second-harmonic generation (SHG) from G-shaped nanostructures, arranged in a chiral unit cell [45].

The present-day nanophotonics has greatly advanced in the manufacturing and study of open nanosize optical resonators that are actually resonant *nanoantennas* [19, 20]. For example, metal [13] and graphene-coated [21–23] nanoparticles sustaining high-Q surface plasmon-polariton modes as well as dielectric nanoparticles with high enough index of refraction [24, 25] may be used as such resonators. Surface and bulk clusters of nanoparticles resonantly responding to IR radiation and visible light may be treated as optical *metamaterials* (artificial media with pre-designed properties) by analogy with microwave systems [26–28].

At sufficiently strong applied electromagnetic fields, nanophotonics reaches the regimes when not only linear properties but also nonlinear characteristics, dependent on the intensity of illumination, of the materials used should be taken into consideration [29–37]. Historically, the rapid development of nonlinear optics began with the demonstration of powerful coherent light sources, i.e. lasers, in the middle of the 20th century. It led to the discovery of a rich diversity of fascinating and eminently useful *nonlinear-optical effects*, including wavelength conversion, stimulated Raman scattering, self-focusing, four-wave mixing, and many others, in both classical and quantum regimes of light-matter interaction. The nonlinear interaction of light waves, exchanging momentum and energy, allows for the generation of optical fields at new frequencies that are practically important, including the harmonics of the incident radiation or sum- or difference-frequency signals. One of the other remarkable general properties of nonlinear systems is their ability to support nonlinear localized modes – self-trapped localized states or *solitons* which can propagate over long distances without changing their shape, due to, for example, a balance between nonlinearity and dispersion (or diffraction). A special kind of solitons, the so-called *discrete soliton*, appears as an intrinsic localized mode in periodic systems [38].

Given the fact that considerable amounts of electromagnetic energy can be confined to small volumes, nonlinear optical phenomena are of particular interest in nanostructures, opening up exclusive prospects for engineering fast and strong optical nonlinearity and controlling light by light. By virtue of the subwavelength localization of eigenmodes and the resonant character of their excitation, nonlinear effects may be quite pronounced, even

at relatively weak external fields. So it is reasonable to find practical applications for them in specific devices [33, 35, 46]. Particularly, *nonlinear plasmonic structures* enable the down scaling of the size and required optical powers for nonlinear components. This is because of a boost of the intrinsic material nonlinearity through the resonant plasmon field enhancement along with a nanoscale confinement of surface plasmons [33, 47–50], which is important for a fully functional nanocircuitry (some examples of plasmonic functional elements are shown in Fig. 1.1). Such nonlinear aspects of nanophotonics are considered in the present thesis.

Doped graphene as a tunable plasmonic material

For many decades, plasmons have primarily been associated with conventional metals such as gold and silver. However, these noble metals suffer large ohmic losses, and the excited surface plasmons have a very low tunability in fixed structures. These limitations substantially restrict further development and applications of plasmonics and call for the exploration of novel plasmonic materials [51]. Recently, graphene, an atomically thin representative of a specific class of materials, two-dimensional crystals, has been suggested as an alternative to conventional metal-based structures to confine light and guide surface plasmon polaritons [52]. Its unique properties have generated significant research interest since it was first exfoliated in 2004 (Nobel Prize 2010) [53]. Electromagnetic properties of the structures containing graphene attracted special attention in the past years, leading to the rapid development of a new branch of plasmonics, which is now widely called graphene nanoplasmonics [52, 54–62].

Graphene, a two-dimensional array of carbon atoms arranged in a honeycomb lattice, exhibits remarkable physical characteristics [53, 63–66]. In particular, specifics of the low-energy spectrum of the charge carriers in graphene leads to a number of fascinating effects, including half-integer quantum Hall effect, minimal electrical conductivity, and Klein tunneling [67–69]. To a large extent, the optical response of graphene is captured by the surface optical conductivity related to the chemical potential of graphene, assuming that the induced current in graphene is strictly in-plane (surface current) [70]. The conductivity consists of two parts, namely, intraband and interband contributions. The transition between these two regimes occurs when photon energies are around twice the Fermi energy, where the real part of the conductivity shows a step, meaning that at the higher frequencies, the optical loss in graphene is dominated by interband transitions and, thus, at visible frequencies, graphene is a broadband absorber. In the low temperature limit, intraband conductivity recovers the Drude form and is therefore similar to metals. Being less lossy than noble metals at the terahertz and infrared frequencies, doped graphene can guide transverse magnetic (TM) electromagnetic waves propagating along its surface due to the coupling of the electromagnetic field to the electron excitations. Plasmonic solutions look similar to those at the metal/dielectric interface [57]. The difference enters in specifying the boundary conditions where graphene is treated as a conductive surface characterized by a frequency-dependent surface conductivity. TM-polarized surface plasmon polaritons supported by a graphene monolayer have an extremely short wavelength and a deep subwavelength localization in the direction perpendicular to the surface, and their excitation is rather challenging. Nevertheless, recent experiments demonstrated that it is possible to excite and observe such plasmons using scattering near-field scanning optical microscopy [71–73]; see Fig. 1.2(g).

Contrary to an ordinary metal, it has been shown that graphene also supports TE-type electromagnetic surface waves [81] in a narrow well-defined frequency window. This

type of surface waves exists in graphene as a consequence that the imaginary part of its interband optical conductivity may become negative. Moreover, we have shown that graphene stabilizes nonlinear TE surface waves at the interface between linear and nonlinear dielelctrics since graphene effectively modifies the boundary conditions for the fields [82].

Graphene as a one-atom-thin tunable plasmonic material has attracted special attention from the nanoplasmonics research community. Impelled by many theoretical proposals and experimental results, graphene-based photonics paves a way towards the development of optical metadevices; see Fig. 1.2. In contrast to metal-dielectric structures, the properties of their graphene-based counterparts are more flexible. As an example, graphene can be doped to high values of the electron or hole densities by applying external gate voltage, and this has a dramatic effect on graphene's optical properties [70, 75, 76, 83–86].

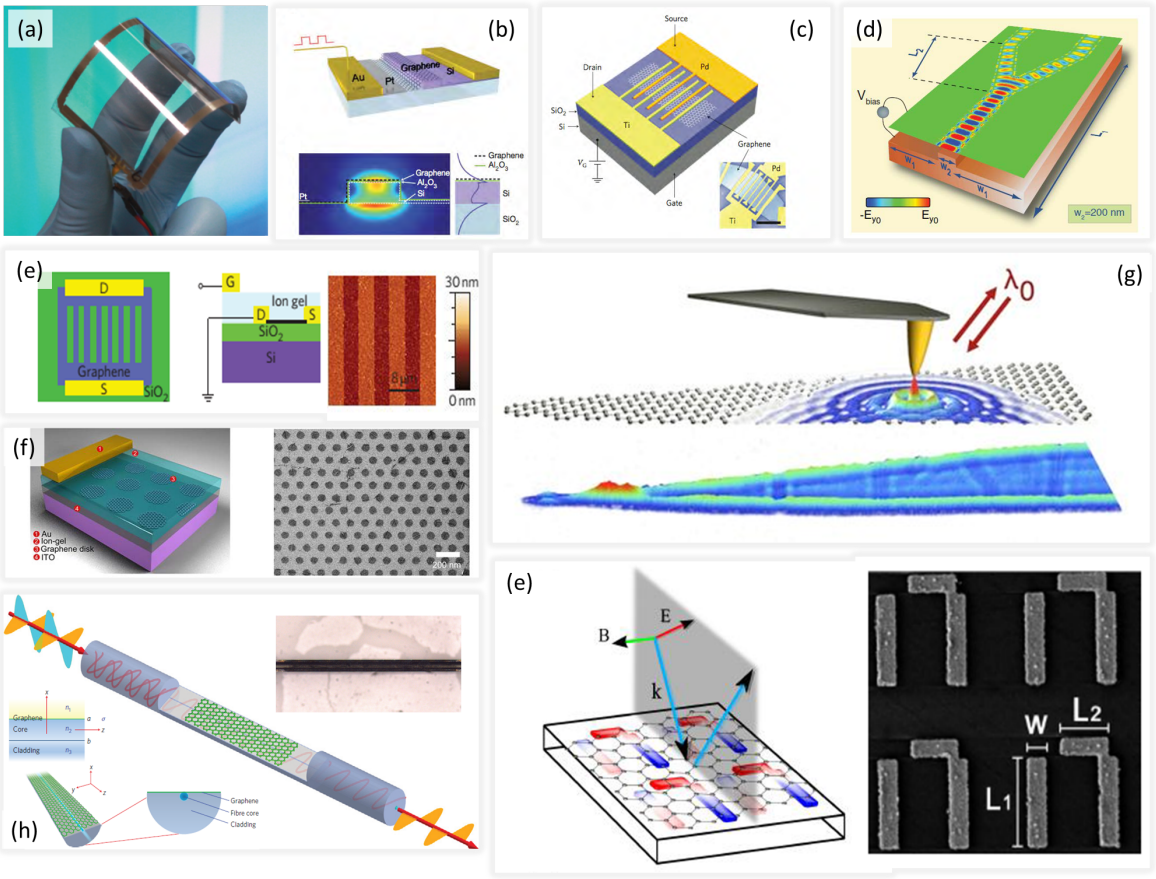

Figure 1.2: Optical applications of graphene: (a) Assembled graphene/polyethylene-terephthalate touch panel showing outstanding flexibility [66]. Broadband and fast (b) graphene photodetector [74] and (c) graphene modulator [75]. (d) Plasmonic waveguide splitter built through inhomogeneous gating of graphene [76]. Patterning of the graphene allows engineering of tunable plasmonic resonances in arrays of (e) nanoribbons [77] and (f) nanodisks [78]. (g) Optical nanoimaging of graphene plasmons [71]. (Upper panel: Sketch of the imaging method. A laser illuminated scanning tip launches plasmons on graphene. Detection is by recording the light backscattered from the tip. Lower panel: Optical image of graphene, where the fringes visualize the interference of the graphene plasmons.) (h) Broadband graphene polarizer based on a side-polished optical fibre [79]. (e) Hybrid graphene/metamaterials structure: Fano-resonant metasurface enhancing infrared response of a monolayer graphene [80].

Furthermore, considering possible integrations, graphene can be incorporated into various photonic setups, including many waveguiding components. It can be placed on top of a variety of substrates, both dielectrics and metals, or it can even be suspended. This creates a plethora of structures where graphene can be useful in the context of optical and plasmonic applications.

Importantly, a tight confinement of graphene plasmons results in the field enhancement indispensable for the observation of strong nonlinear effects. In this respect, the nonlinear response of graphene structures and the plasmonic phenomena with graphene still remain largely unexplored. Graphene posseses a *tunable nonlinearity* that is strongly dependent on the operating frequency, the chemical potential and the relation between them, as well as the external magnetic field applied (theory [87–112], experiments [87, 113–124]). Initially, a strong nonlinear response in graphene was anticipated because of the linear dispersion of carriers, once again featuring the particular role of the energy spectrum nonparabolicity. To describe the nonlinear properties of doped graphene, we employ a quasi-classical description based on the solution of the Boltzmann equation [23, 87–90, 92, 93, 110, 125, 126], which is applicable at low frequencies encompassing the plasmonic regime (see Appendix A.) The second-order effects are forbidden in uniform graphene under normal incidence of radiation because of the symmetry constraints. However, there are different ways to break this restriction and enable the second-order nonlinear processes [87, 105, 106, 126, 127]. Among different mechanisms, we focus on the mechanism dependent on the field inhomogeneity at the graphene surface [23, 88, 91, 125, 126, 128]. For surface plasmons, the corresponding effects are proportional to the in-plane momentum that can be large for guiding modes, manifesting the nonlocality and field enhancement by plasmon confinement.

Our studies aim at the exploration of the specific *surface nonlinearity of graphene* in the resonant geometries, and suggesting novel schemes for light manipulation at the subwavelength scale.

Methods

In this thesis, we develop mathematical models and numerical algorithms for analysis of nonlinear optical phenomena in plasmonic and graphene-based photonic setups. Most of the work is done analytically by using different asymptotic methods of nonlinear physics. In addition to using conventional analytical approaches such as the methods of diffraction and scattering theory, for solving some of the nonlinear problems with graphene guiding structures in Chapters 3 and 4, we apply the recently developed method based on asymptotic expansion of the Maxwell equations where graphene, as a two-dimensional material, can be either incorporated into the nonlinear boundary conditions for fields [129, 130], or utilizing the formalism of the Dirac delta-functions, it can be included as a source in the wave equations (as a delta-function of the surface current) [125, 131, 132]. For simplicity, we employ the latter approach when graphene sheets are supposed to be fully embedded into one dielectric. Assuming that the nonlinear sources and some other factors, such as dissipation, diffraction, etc. (depending on what we are interested in) are small, we then introduce smallness parameters, and use the theory of perturbations to derive the equation for a slowly varying plasmon amplitude, the asymptotic description frequently used in the paraxial and nonlinear optics [38]. One more powerful analytical tool in such problems is the so-called energetic approach [133], basically implicating the use of the Lorentz reciprocity theorem [134, 135]. (See Appendix B). We support our findings by means of direct numerical modeling. In Chapter 4, for the analysis of hybrid graphene metasurfaces [128], we also rely on the first principle numerical simulations performed in the commercial full-

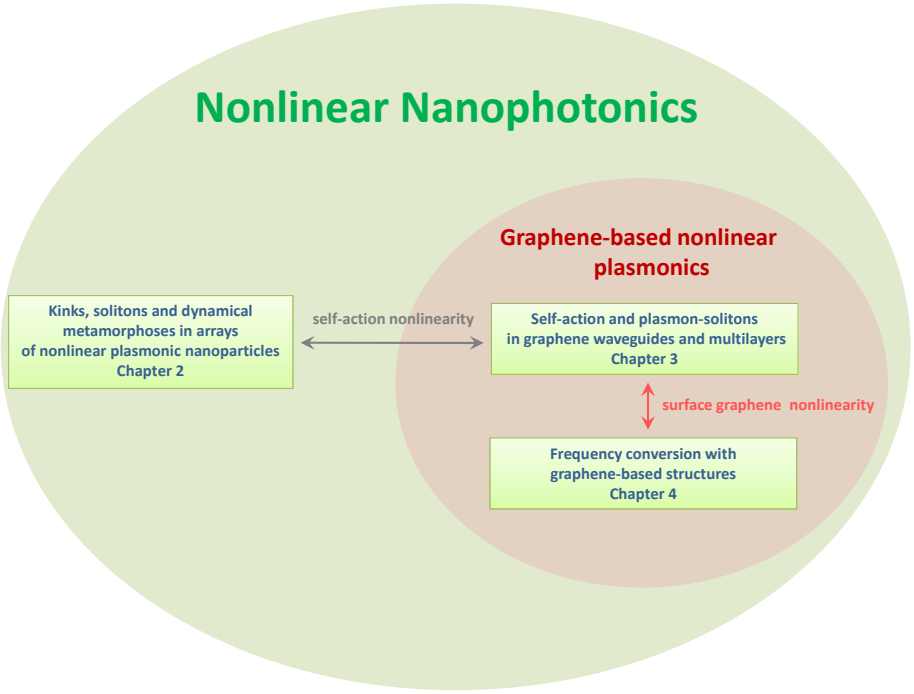

Figure 1.3: Schematic diagram illustrating the scope of the thesis and the connections between the chapters.

vector finite-element-method solver COMSOL Multiphysics.

Thesis organization

This thesis is divided into five chapters, all of which discuss nonlinear effects in plasmonic structures. In Chapter 1, we have given the motivation behind this research. Graphene is the primary focus of the material in Chapters 3 and 4. The layout is as follows.

- Chapter 2 studies nonlinear modes in arrays of resonant plasmonic, both metal and graphene, nanoparticles with Kerr-type nonlinear response in the presence of an external field. We derive the nonlinear evolution equations describing the dynamics of the particles polarization and then analyze the extended and localized solutions of these equations, and their stability and mobility.

- Chapter 3 examines the linear and nonlinear propagation characteristics of light in graphene waveguides and multilayer structures, particularly accentuating self-trapped optical modes in the form of plasmon-solitons due to the self-action nonlinearity of graphene.

- Chapter 4 develops the models of the resonant harmonic generation in different configurations and setups with graphene, specifically utilizing the second-order nonlocal graphene nonlinearity.

- Chapter 5 provides a summary of our results and emphasizes their significance.

The structure of the thesis showing the links between the chapters is depicted schematically in Fig. 1.3.

Chapter 2

Kinks, solitons and dynamical metamorphoses in arrays of nonlinear plasmonic nanoparticles

In this Chapter, we consider both one-dimensional (1D) arrays and two-dimensional (2D) lattices composed of nanosized metal and graphene plasmonic particles with Kerr-type nonlinear response in the presence of an external driving field, and study theoretically a number of novel nonlinear effects in these subwavelength plasmonic systems. First, we explore *modulation instability* and *bistability* in 1D and 2D arrays of nonlinear metal nanoparticles and demonstrate the generation of stationary, drifting, and breathing *kinks* (or switching waves connecting different polarization states). We then demonstrate that optically driven two-dimensional lattices of nonlinear metal nanoparticles can support a variety of dissipative localized modes including *trapped* and *walking solitons*, and plasmonic counterparts of the *Faraday waves*. Next, we reveal that arrays of doped graphene nanodisks can sustain discrete dissipative *scalar solitons* of both longitudinal and transverse polarizations, as well as *vector solitons* composed of two mutually coupled polarization components. We also show the formation of stable resting and moving localized modes in this discrete model under control guidance of the external electric field.

2.1 Modulational instability and plasmonic kinks in nonlinear arrays of metal nanoparticles

Model and governing equations

Figures 2.1(a-d) show the geometries of our problems: identical spherical silver nanoparticles are arranged in 1D chain and 2D square lattice. We assume that these arrays are embedded into a SiO_2 host medium with a permittivity $\varepsilon_h = 2.1$ being driven by an arbitrary electric field at a frequency close to the frequency of the surface plasmon resonance of an individual particle, ω_0. We also assume that the nanoparticle size is much less than the wavelength; and the particle radius, a, and the lattice constant, d, satisfy the condition $d = 3a$, so that we can employ the point-dipole approximation [136]. Taking into account intrinsic metallic nonlinearity, we write a particle's dielectric permittivity as follows

$$\varepsilon_{\mathrm{Ag}} = \varepsilon_\infty - \frac{\omega_p^2}{\omega(\omega - i\nu)} + \chi^{(3)}|\mathbf{E}^{(in)}|^2, \tag{2.1}$$

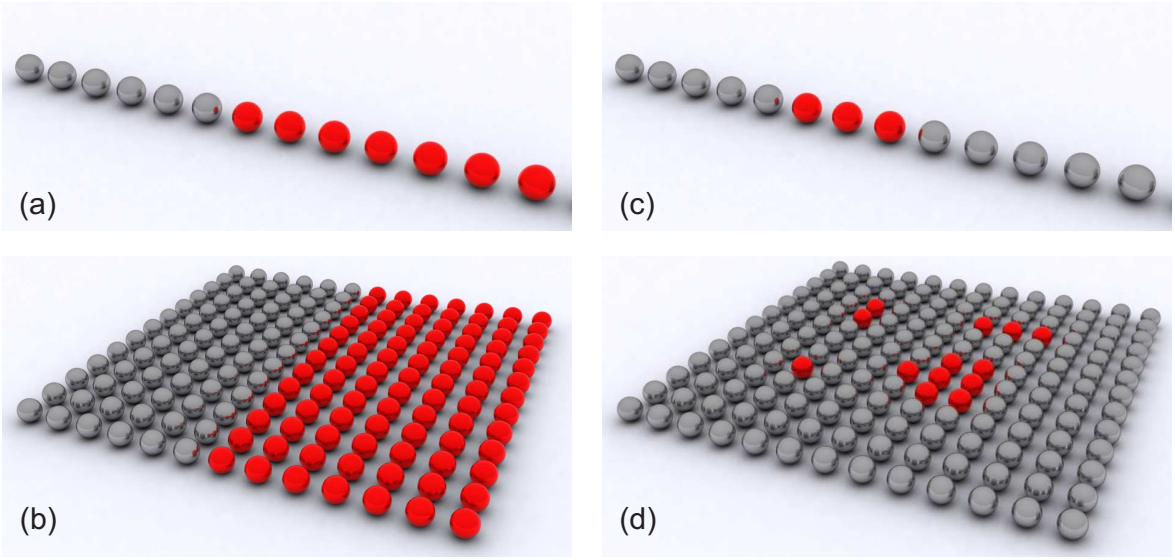

Figure 2.1: Typical profiles of (a,b) kinks and (c,d) solitons in a chain and a square lattice of metallic nanoparticles. Gray and red particles depict low and high values of the local electric field.

where $\varepsilon_\infty = 4.96$, $\hbar\omega_p = 9.54$ eV, $\hbar\nu = 0.055$ eV [137], $\chi^{(3)}$ is the cubic susceptibility, and $\mathbf{E}^{(in)}$ is the local field inside a particle [in this Chapter we accept $\exp(i\omega t)$ time dependence].

In general, several different mechanisms contribute to $\chi^{(3)}$, including pondermotive forces [138], electron confinement [139–141], and interband thermal modulation [142, 143]. This leads to a strong dependency of both real and imaginary parts of $\chi^{(3)}$ on the type of metal, particle size as well as external pulse duration and frequency [144]. However, when a silver nanoparticle with $a \geq 5$ nm is driven at $\omega \sim \omega_0$ by a laser pulse whose energy is significantly less than the silver ablation threshold, electron confinement nonlinearity associated with intra-band electron transitions dominates, resulting in a purely real cubic susceptibility $\chi^{(3)} \simeq 3 \times 10^{-9}$ esu [140, 141].

To study nonlinear dynamics of the nanoparticle arrays, we employ the slow varying amplitude approximation which is fully applicable because each particle acts as a resonantly excited oscillator with slow (in comparison with the light period) inertial response. In the case of a chain of metal nonlinear nanoparticles, the governing equations for the dimensionless envelopes of transversal (with respect to the chain axis) polarization components of the particles can be written as [145–147],

$$-i\frac{dP_n^\perp}{d\tau} + \left(-i\gamma + \Omega + |P_n^\perp|^2\right) P_n^\perp + \sum_{n' \neq n} G_{n-n'} P_{n'}^\perp = E_n^\perp, \tag{2.2}$$

where

$$G_{n-n'}^\perp = \frac{\eta}{2}\left((k_0 d)^2 - \frac{ik_0 d}{|n-n'|} - \frac{1}{|n-n'|^2}\right)\frac{e^{-ik_0 d|n-n'|}}{|n-n'|},$$

$P_n^\perp$ and $E_n^\perp$ are the dimensionless slowly varying amplitudes of the particle's dipole moments and external electric field, respectively, $\eta = \dfrac{3\varepsilon_h}{\varepsilon_\infty + 2\varepsilon_h}\left(\dfrac{a}{d}\right)^3$, $\gamma = \nu/(2\omega_0) + (k_0 a)^3 \varepsilon_h/(\varepsilon_\infty + 2\varepsilon_h)$ describes thermal and radiation losses of particles [note the last term can be neglected as long as $k_0 a << 1$], $k_0 = \omega_0/c\sqrt{\varepsilon_h}$, $\Omega = (\omega - \omega_0)/\omega_0$ and $\tau = \omega_0 t$. Here, we use the same normalization for particle polarization envelopes and external electric field as in Refs. [145–147].

To obtain the governing equations for a 2D lattice, one should make the following replacements in Eq. (2.2): $n \to (n,m)$ in indexes and $|n-n'| \to \sqrt{|n-n'|^2+|m-m'|^2}$ in $G^{\perp}_{n-n',m-m'}$ [148], leading to

$$-i\frac{dP^{\perp}_{n,m}}{d\tau} + \left(\Omega - i\gamma + |P^{\perp}_{n,m}|^2\right) P^{\perp}_{n,m} + \sum_{\substack{n'\neq n \\ m'\neq m}} G^{\perp}_{n-n',m-m'} P^{\perp}_{n',m'} = E^{\perp}_{n,m}, \tag{2.3}$$

where

$$G^{\perp}_{n-n',m-m'} = \frac{\eta}{2}\left[(k_0 d)^2 - \frac{ik_0 d}{\Delta r} - \frac{1}{\Delta r^2}\right]\frac{\exp(-ik_0 d\Delta r)}{\Delta r}.$$

Importantly, in contrast to several other models employed for the study of nonlinear effects in arrays of split-ring resonators [149, 150], our model involves long-range interactions of all nanodisks through the full dipole fields, and it can be applied to both finite and infinite arrays. It also differs from the discrete model reported in Ref. [151] for dipolar Bose-Einstein condensates, which does not contain an external source and accounts only for quasistatic fields in the dipolar reponse of the elements.

Stability analysis

An essential prerequisite for the existence of plasmonic kinks and solitons is a stable continuous external field background featuring a bistability area. Thus, we first investigate stability of the homogeneous stationary solution of Eq. (2.2), when $d/d\tau = 0$, $P^{\perp}_n = P^{\perp}_0$, and $E^{\perp}_n = E^{\perp}_0$. To this end, we assume a periodically modulated perturbation of the form $\delta P^{\perp}_n = A_{\perp}\exp(-iKdn + \lambda_{\perp}\tau) + A^{*}_{\perp}\exp(iKdn + \lambda^{*}_{\perp}\tau)$, where '$*$' means complex conjugation, K is the modulation wavenumber, $A_{\perp}$ is an amplitude of perturbation. Having substituted $P^{\perp}_n = P^{\perp}_0 + \delta P^{\perp}_n$ into Eq. (2.2), we derive the expression for the instability growth rate:

$$\lambda_{\perp} = \mathrm{Im}\sum_{j=1}^{\infty} B^{\perp}_j - \gamma + \left\{|P^{\perp}_0|^4 - \left(2|P^{\perp}_0|^2 + \Omega + \mathrm{Re}\sum_{j=1}^{\infty} B^{\perp}_j\right)^2\right\}^{1/2},$$

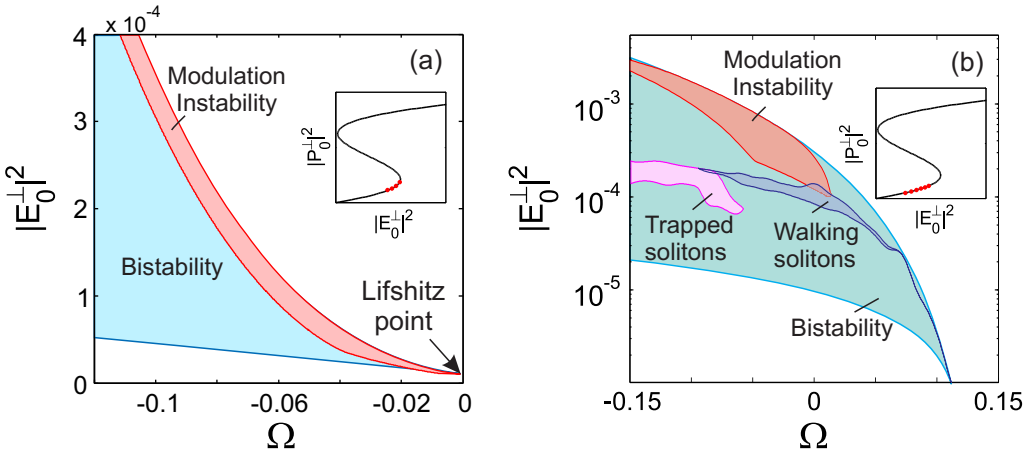

Figure 2.2: Bifurcation diagrams on the parameter plane of $\Omega = (\omega - \omega_0)/\omega_0$ and $|E^{\perp}_0|^2$ when nanoparticle in (a) 1D chains and (b) 2D lattices are driven by the homogeneous electric field oriented transversally with respect to the chain axis and lattice plane, respectively. Insets show the particle stationary polarizations $|P^{\perp}_0|^2$ as a function of $|E^{\perp}_0|^2$, when Ω is taken inside the bistability region, with zones of modulational instability marked by red dots.

where $B_j^{\perp} = \eta\left[(k_0 d)^2 j^{-1} - ik_0 d j^{-2} - j^{-3}\right]\exp\left(-ik_0 dj\right)\cos(Kdj)$. A transition from $G_{n,m}^{\perp}$ to $B_j^{\perp}$ has been made via the replacement $|n-n'| = j$ and taking into account symmetry structure of the series. In the case of a 2D lattice, one should change $j \to \sqrt{j^2+l^2}$ and $\cos(Kdj) \to \cos(K_x dj)\cos(K_y dl)$.

Obviously, the conditions $\mathrm{Re}\,\lambda_{\perp} \geq 0$ at $K = 0$ and $\mathrm{Re}\,\lambda_{\perp} \geq 0$ at $K \neq 0$ define the areas of bistability and modulational instability (MI) of the homogeneous stationary solution of Eq. (2.2) on the plane $(\Omega, |E_0^{\perp}|^2)$, as shown in Fig. 2.2. MI occupies only a small region of intensities close to the upper threshold of the bistability area, making possible kink and soliton generation.

It should be noted that a perfect homogeneous transversal excitation of a chain corresponds to just a normal light incidence, while in the case of a 2D lattice it is beyond practical realization owing to wave nature of light. Nevertheless, the significant recent progress in generation of longitudinally polarized light beams [152] manifests the feasibility of a *quasi-homogeneous* 2D transversal excitation.

Interestingly, MI and bistability zones emerge from the same point for a nanoparticle chain, as shown in Fig. 2.2(a). This bicritical bifurcation point, also known as Lifshitz point, is characterized by co-existence of the first- and second-order phase transitions, and its appearance in a nonlinear plasmonic system shows a universal character of nonlinear dynamics for systems of different nature [153–155].

Kinks

To study kink's dynamics, we perform numerical simulations of Eq. (2.2) for a finite array at initial conditions corresponding to different stable branches of the homogeneous stationary solution over different parts of the array. To suppress the impact of edge effects on kink's dynamics, we consider an array of 200 nanoparticles for a chain and 301x301 nanoparticles for a lattice. Light intensity is taken to be a step-like function of time. Constant $E_0^{\perp}$ results in the constant kink velocity, v. That is why a step-like time dependence of $E_0^{\perp}$ allows us to control v. The velocity sign is defined as positive if the motion of the switching wave leads to the expansion of the region occupied by the upper branch of bistability; otherwise, the velocity is marked as negative. Hereinafter we treat kink's and soliton's velocities as time-averaged values because discrete nature of nanoparticle arrays leads to small-amplitude harmonic oscillations in the instantaneous value of v [156].

The result for a chain is presented in Figs. 2.3(a-c) where the kink velocity is switched from negative to positive values, passing through zero. A rigorous analysis manifests that there is no smooth transition between kinks with negative, positive, and zero velocities, as shown in Fig. 2.3 (c). Moreover, these states possess different structures: kinks with positive and zero velocities are characterized by the one-particle width; while the width of kinks with negative velocity extends for 12 particles. We also notice that negative-velocity kinks exist for the same intensities as stationary (zero-velocity) kinks do. Therefore, to provoke a domain wall to move into the opposite direction, one should force the dipole next to the domain wall switch it into the lower branch of the bistability curve until the domain wall starts moving. An opposite transition can be realized through only variation in the intensity. We attribute this sharp difference between negative- and positive velocity kinks to a long-range dipole-dipole interaction inherited in our model. Importantly, the dependency shown in Fig. 2.3 (c) is typical for any frequency fixed inside a bistability area.

Contrary to their 1D counterparts, 2D kinks with negative and positive velocities are characterized by the same widths of 9 nanoparticles. Moreover, they could have vanishing velocity at one value of the intensity only, which is also referred to as Maxwell point [157].

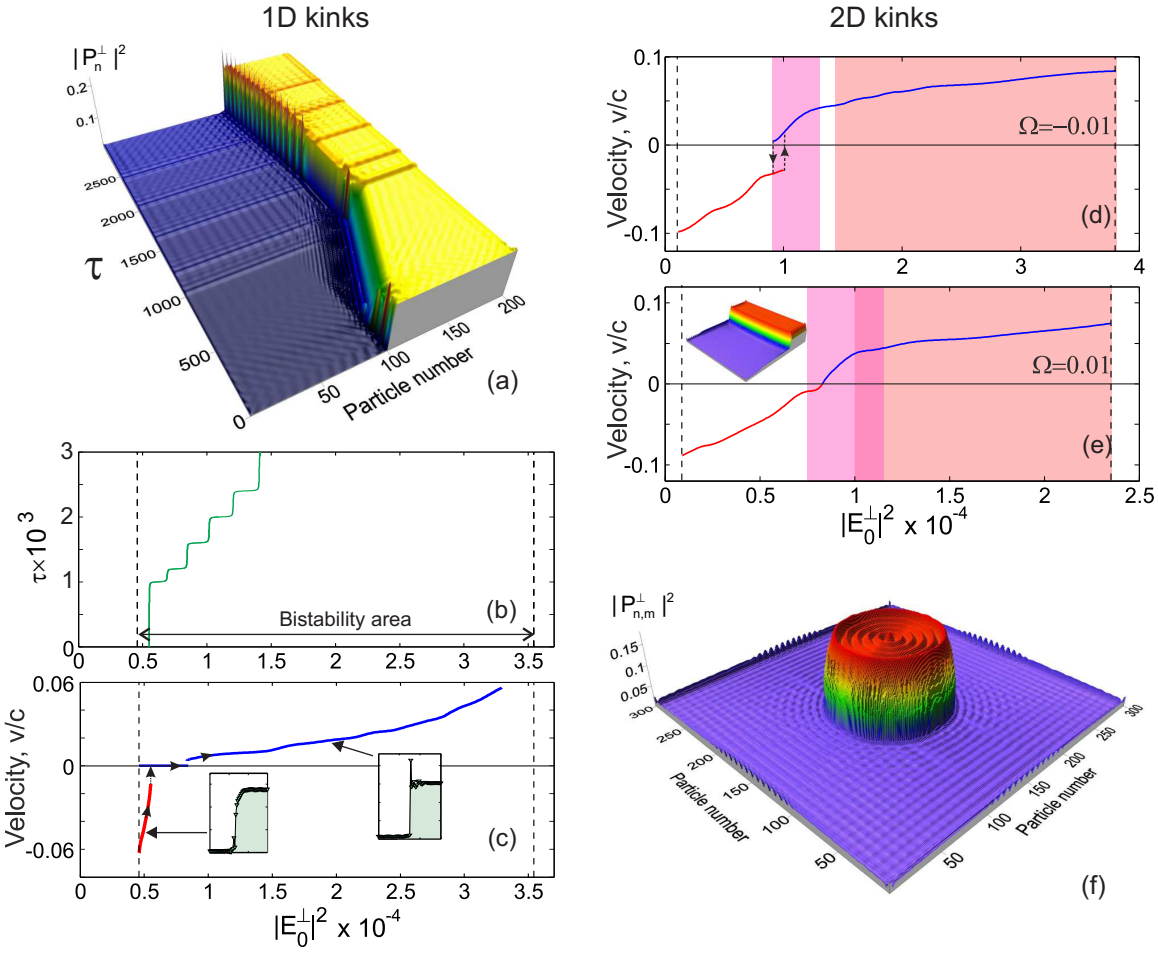

Figure 2.3: General properties of 1D and 2D plasmonic kinks. Panel (a) demonstrates spatiotemporal dynamics of an 1D plasmonic kink when the nanoparticle chain is driven by a homogeneous electric field with a step-like temporal envelope at $\Omega = -0.1$, as shown in (b). Normalized kink's velocity as a function of $|E_0^\perp|^2$ is indicated in (c). Insets depict kink's structures with positive and negative velocities. Panels (d) and (e) show 2D kink's velocity versus $|E_0^\perp|^2$ for $\Omega = -0.01$ and $\Omega = 0.01$, respectively. Red and blue curves correspond to positive-(or zero-) and negative-velocity branches. Shaded areas depict existence domains of solitons (purple) and MI (red). Inset marks 2D kink's profile at a homogeneous excitation. Panel (f) shows a snapshot of a breathing 2D plasmonic kink obtained at $\Omega = -0.01$ and a gaussian profile of the external field: $E_{n,m}^\perp = E_0^\perp \exp(-([n-n_0]^2 + [m-m_0]^2)/\Delta)$, where $n_0 = m_0 = 150$, $\Delta = 250$, and $E_0^\perp = 1.095 \times 10^{-2}$.

When $\Omega \geq 0$ kink's velocity is a monotonically increasing function of the intensity; while at $\Omega < 0$ kinks with negative and positive velocities form a hysteresis loop, as shown in Figs. 2.3 (d) and (e). This feature gives a straightforward recipe to generate plasmonic kinks with a self-pulsing profile: if one excites a lattice by, for instance, a longitudinally-polarized (with respect to a wave vector) gaussian beam with properly chosen a maximal value and a waist [152], then the kink velocity will oscillate between positive and negative branches inside a bistability loop. The period and the radii of such self-oscillations are defined by parameters of the gaussian beam. For the breathing kink, shown in Fig. 2.3(f), they are $\Delta\tau \approx 2400$ (which is equal to 0.5 ps) and $r_{max} - r_{min} = \Delta n \approx 30$ nanoparticles. Thus, this principle can be used to create an ultrafast all-optical plasmonic modulator whose spatiotemporal action will be encoded by spatial gradient of the external field.

2.2 Subwavelength solitons and Faraday waves in lattices of metal nanoparticles

Trapped and walking solitons

Next, we analyze 2D solitons in the lattices. Numerical simulations show that 2D solitons can be divided into the classes of trapped and walking localized modes, as shown in Fig. 2.4. We also identify numerically the existence domains on the parameter plane 'intensity vs frequency' corresponding to trapped and walking solutions and show them in Fig. 2.2(b). A family of trapped solitons includes both symmetric and asymmetric solutions with deeply subwavelength extension of just a few nanoparticles. Importantly, this sort of solitons always remain at rest regardless of the inhomogeneity of the applied field.

Walking solitons are characterized by a wider localization with approximately 150 nanoparticles which does not depend on Ω, $|E_0^{\perp}|^2$, and the width of the step defined by the initial conditions. We find that walking solitons bifurcate at $\Omega = 0$ similar to 2D kinks. When $\Omega \geq 0$, these solitons possess a stable stationary profile, drifting with a comparatively small velocity $\sim 10^{-4}c$, where c is the speed of light, under impact of the edge effects and colliding elastically with the lattice boundaries and between each other. However, at $\Omega < 0$ the walking solitons transform into oscillons [146] which move much faster with the velocity $\sim 10^{-2}c$, merging into one oscillon and radiating through the lattice boundaries. Finally, we notice that a powerful tool for steering of the soliton motion is the phase or amplitude inhomogeneity in the applied field because the drifting direction is defined by an inhomogeneity gradient.

Faraday waves

When the values of frequency and intensity are taken from the MI domain, we observe the generation of nonlinear localized patterns known as Faraday waves [158], as shown in Fig. 2.5 (a). Symmetry of such patterns is driven by the spectrum of eigenmodes excited due to MI. Figure 2.5(b) presents the spectrum of eigenmodes for the pattern in Fig. 2.5(a) which is formed by two zones in the vicinity of $Kd \sim 1.9$ and $Kd \sim 0.8$. Therefore, the Faraday waves are gradually modified in time, being completely different from the modulations induced by the edge effect which repeat the square symmetry of the lattice. Remarkably, the areas of MI and walking solitons can overlap, thus solitons are not destroyed by MI but instead they may exist on the background of Faraday waves.

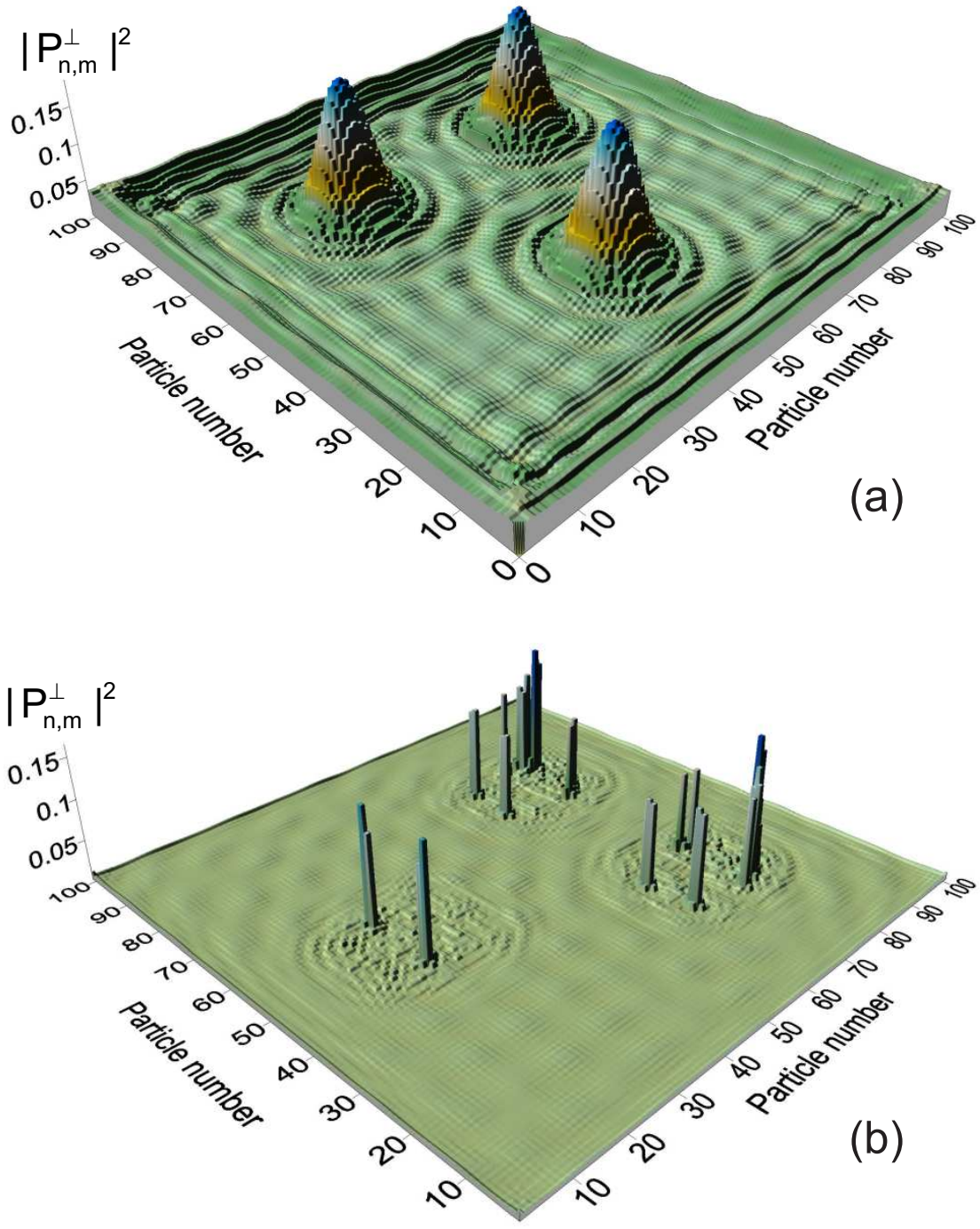

Figure 2.4: Snapshots of particles' polarizations corresponding to (a) walking ($\Omega = 0.01$, $|E_0^{\perp}|^2 = 10^{-4}$) and (b) trapped ($\Omega = -0.1$, $|E_0^{\perp}|^2 = 1.7 \times 10^{-4}$) two-dimensional solitons.

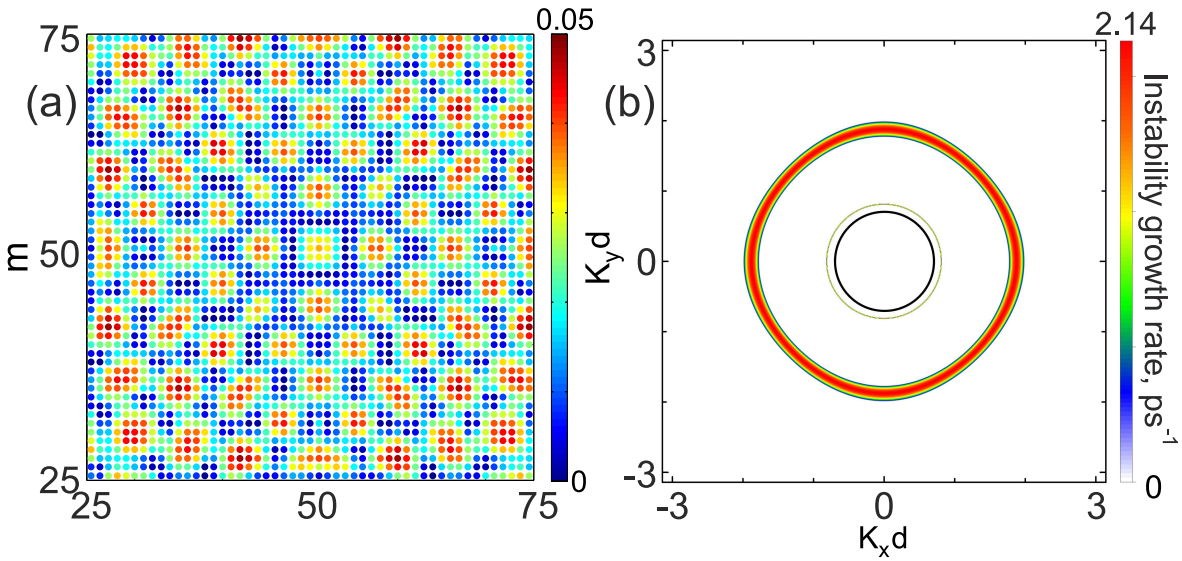

Figure 2.5: (a) Snapshot of the particles' polarizations $|P^{\perp}_{n,m}|^2$ corresponding to Faraday ripples ($\Omega = -0.01$, $|E^{\perp}_0|^2 = 1.5 \times 10^{-4}$). The panel (b) shows the contour map of the instability growth rate in the plane of wave vectors corresponding to (a), and the black circle denotes the light cone, $K = k_0$. The simulations were carried out for a 101 x 101 nanoparticle array.

Parameters

In our calculations summarized above, we deal with dimensionless variables without specifying the exact geometrical parameters of the system and the applied external field. However, for the discussions of experimental realizations of the presented ideas, we have to convert the parameters into dimensional values. The use of the dipole approximation for modeling silver nanoparticles within classical electrodynamics implies that the particle radii should be in the range between 5 nm and 20 nm, and the surface plasmon resonance frequency $\hbar\omega_0 = 3.14$ eV, so that the soliton localization in nanoparticle arrays may reach 0.05λ.

It is also insightful to estimate the maximal pulse duration, because the saturation intensity of the external field $|E^{\perp}_0|^2 \sim 10^{-4} - 10^{-5}$, corresponding to the intensity of $\sim 1 - 10$ MW/cm^2, can lead to thermal damage. Using the value of the ablation threshold of 3.96 J/cm^2 obtained for silver particles in a SiO_2 host matrix in the picosecond regime of illumination [159] and taking into account the amplification of the electric field inside the Ag nanoparticle due to surface plasmon resonance, we evaluate the maximal pulse duration as 5 ns for the peak intensity of 0.75 MW/cm^2 ($|E^{\perp}_0|^2 = 10^{-5}$). Since this value is much greater than the time needed for the generation of nonlinear dissipative modes, being limited by several picosecond, we expect that all predicted nonlinear phenomena can be readily observed in experiment.

Summary

We have studied the transversal nonlinear modes in one-dimensional arrays and two-dimensional lattices of nonlinear metal nanoparticles driven by an external laser beam. We have demonstrated the generation of stationary, drifting, and breathing kinks with a self-oscillating profile, as well as trapped and walking plasmon solitons and Faraday waves.

2.3 Dissipative plasmon solitons in graphene nanodisk arrays

As was mentioned in Chapter 1, being guided by a graphene monolayer, p-polarized plasmons are known to be extremely short-wavelength, and their excitation is rather challenging. In order to decrease the plasmon wavenumbers, as we show in Chapter 3, multilayer graphene structures can be employed [132, 160]. Alternatively, to realize coupling of graphene plasmons with light, the in-plane momentum matching can be attained in the graphene structures with a broken translational invariance, such as graphene patterned periodically in arrays of nanoribbons [77, 161–163] or nanodisks [78, 164, 165]. Being regarded as direct analogs to metal nanoparticles, finite-extent nanoscaled flakes are created by nanostructuring of graphene in the form of disks, rings, and triangles, and they can sustain localized surface plasmons.

Here, we study nonlinear effects in periodic arrays of single-layer graphene nanodisks excited by an external field. We assume that the nanodisks possess a nonlinear response due to the graphene nonlinearity, and demonstrate that this system can support different classes of localized modes comprising several coupled nanodisks characterized by the local field enhancement, the so-called *discrete dissipative plasmon solitons*, as shown schematically in Fig. 2.6. We derive the nonlinear equations describing the evolution of the disks' polarization components, taking into account graphene nonlinear response, intrinsic graphene losses, and a full dipole-dipole coupling between the graphene nanodisks. We reveal that this nonlinear system can support both scalar and vector discrete dissipative solitons and, depending on the inclination of the incident wave, these nonlinear modes can move gradually along the chain.

Model

We consider a one-dimensional chain of identical graphene circular nanodisks driven by an external plane wave, as shown in Fig. 2.6. We assume that the radius of a single disk, a, varies from 15 nm to 100 nm, the array period d satisfies the condition $d \geq 3a$, and the wavelength of the driving field is much larger than a single disk, so that we can neglect boundary, nonlocal, and quantum finite-size effects [57, 166], and treat disks as point dipoles [54, 78, 164, 167]. We also employ the linear surface conductivity as that of a homogeneous graphene sheet, which, at the relatively low photon energies, $\hbar\omega \leq \mathcal{E}_F$, can be written in terms of the Drude model as follows [70, 89, 168],

$$\sigma^{\mathrm{L}}(\omega) = -\frac{ie^2}{\pi\hbar^2}\frac{\mathcal{E}_F}{\left(\omega - i\tau_{\mathrm{intra}}^{-1}\right)}, \tag{2.4}$$

where e is the elementary charge, $\mathcal{E}_F = \hbar v_F\sqrt{\pi n}$ is the Fermi energy, n is the doping electron density, $v_F \approx c/300$ is the Fermi velocity, and τ_{intra} is a relaxation time (we assume $\exp(i\omega t)$ time dependence). Here, for doped graphene we account for intraband transitions only and disregard both interband transitions and temperature effects, implying $k_B T \ll \mathcal{E}_F$, where k_B is the Boltzmann constant and T is the absolute temperature. (See Appendix A and Chapters 3, 4 for more details on graphene surface conductivity.)

Under accepted approximations, the linear response of graphene nanodisks can be characterized via the disk polarizability, written as follows [78],

$$\alpha^{\mathrm{L}}(\omega) = D^3 A\left(\frac{L}{\varepsilon_h} + \frac{i\omega D}{\sigma^{\mathrm{L}}(\omega)}\right)^{-1}, \tag{2.5}$$

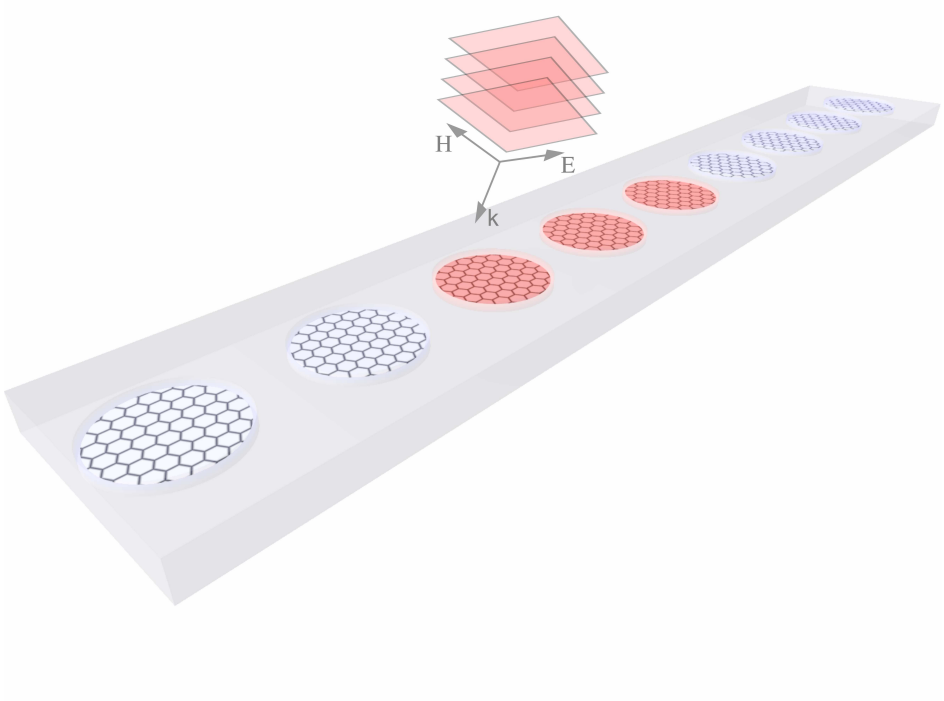

Figure 2.6: Schematic view of a discrete plasmon soliton excited by an external plane wave in a chain of graphene nanodisks. Red and white colors depict high and low values of the local electric field.

where $A = 0.65$, $L = 12.5$, $D = 2a$, $\varepsilon_h = (\varepsilon_1 + \varepsilon_2)/2$, ε_1 and ε_2 are the dielectric permittivities of the substrate and superstrate located below and upper a graphene nanodisk. Being size- and material-independent, the coefficients A and L are extracted from numerical simulations of Maxwell's equations by the boundary element method [164, 169, 170], where graphene is modeled as a thin layer of the thickness $h = 0.5$ nm being described by volume dielectric permittivity,

$$\varepsilon_{\rm gr}^{\rm L}(\omega) = 1 - \frac{i4\pi\sigma^{\rm L}(\omega)}{\omega h}\,. \tag{2.6}$$

Equation (2.5) results in the following expression for the eigenfrequency of the dipole plasmon [54,78]

$$\hbar\omega_0 \approx e\left(\frac{2L}{\varepsilon_1+\varepsilon_2}\frac{\mathcal{E}_F}{\pi D}\right)^{1/2}\,. \tag{2.7}$$

We notice that ω_0 can be tuned by doping ($\mathcal{E}_F$-shift) or shape-cut, which may assist matching waves of different polarizations in circuits based on patterned graphene.

Within the dipole approximation, the local electric field in disks is considered to be homogeneous. To identify it, we model disks as spheroids of the permittivity (2.6). By comparison of Eq. (2.5) and the polarizability of an oblate spheroid [171], one can conclude that the ratio between semi-minor axis $\bar{c}$ of an equivalent ellipsoid and the thickness h should be about $\bar{c}/h \approx 0.627$. To account for the influence of graphene nonlinearity on the disks' polarizations, we define the nonlinear dielectric permittivity as $\varepsilon_{\rm gr}^{\rm NL}(\omega) = \varepsilon_{\rm gr}^{\rm L}(\omega) + \chi_{\rm gr}^{(3)}(\omega)|\mathbf{E}_n^{\rm in}|^2$, where $\mathbf{E}_n^{\rm in}$ is the local field in n-th disk, and cubic volume susceptibility,

$$\chi_{\rm gr}^{(3)}(\omega) = -i\frac{4\pi\sigma^{\rm NL}(\omega)}{\omega h}\,, \tag{2.8}$$

is expressed through the nonlinear self-action correction to the graphene conductivity (see Appendix A), in the local quasi-classical approximation given by [87,89,90,110]

$$\sigma^{\mathrm{NL}}(\omega) = i\frac{9}{8}\frac{e^4}{\pi\hbar^2}\left(\frac{v_F^2}{\mathcal{E}_F\omega^3}\right). \tag{2.9}$$

Next, we study the chain of graphene nanodisks driven by an optical field with the frequency close to he frequency ω_0, and analyze the dynamical response of the disks' polarizations, $p_n^{\perp,||}$. By employing the dispersion relation method [145–148] in close similarity to Section 2.1, we derive the following system of coupled nonlinear equations for the slowly varying amplitudes of the disk dipole moments,

$$\begin{aligned} -i\frac{dP_n^{\perp}}{d\tau} + \left(-i\gamma + \Omega + |\mathbf{P}_n|^2\right)P_n^{\perp} + \sum_{m\neq n} G_{n,m}^{\perp}P_m^{\perp} = E_n^{\perp}, \\ -i\frac{dP_n^{\parallel}}{d\tau} + \left(-i\gamma + \Omega + |\mathbf{P}_n|^2\right)P_n^{\parallel} + \sum_{m\neq n} G_{n,m}^{\parallel}P_m^{\parallel} = E_n^{\parallel}, \end{aligned} \tag{2.10}$$

where

$$\begin{aligned} G_{n,m}^{\perp} &= \frac{\eta}{2}\left((k_0 d)^2 - \frac{ik_0 d}{|n-m|} - \frac{1}{|n-m|^2}\right)\frac{e^{-ik_0 d|n-m|}}{|n-m|}, \\ G_{n,m}^{\parallel} &= \eta\left(\frac{ik_0 d}{|n-m|} + \frac{1}{|n-m|^2}\right)\frac{e^{-ik_0 d|n-m|}}{|n-m|}, \end{aligned}$$

while

$$P_n^{\perp,\parallel} = p_n^{\perp,\parallel}\frac{3\sqrt{\chi_{\mathrm{gr}}^{(3)}(\omega_0)}n_x}{\sqrt{2\left(1-\varepsilon_h+\varepsilon_h/n_x\right)}\varepsilon_h a^2\bar{c}},$$

and

$$E_n^{\perp,\parallel} = -\frac{\varepsilon_h\sqrt{\chi_{\mathrm{gr}}^{(3)}(\omega_0)}E_n^{(ex)\perp,\parallel}}{n_x\sqrt{8\left(1-\varepsilon_h+\varepsilon_h/n_x\right)^3}}$$

are the normalized slowly varying envelopes of the disk dipole moments and the external field, indexes '$\perp$' and '$||$' stand for transversal and longitudinal components with respect to the chain axis, $|\mathbf{P}_n|^2 = |P_n^{\perp}|^2 + |P_n^{\parallel}|^2$, $E_n^{(ex)\perp,\parallel}$ are components of the (not normalized) external electric field acting on n-th disk, $\tau = \omega_0 t$, $\Omega = (\omega-\omega_0)/\omega_0$, $k_0 = \omega_0\sqrt{\varepsilon_h}/c$, c is the speed of light, $n_x = \pi\bar{c}/4a$ is the depolarization factor of the ellipsoid,

$$\gamma = \frac{\nu}{2\omega_0} + \frac{\varepsilon_h}{1-\varepsilon_h+\varepsilon_h/n_x}\left(\frac{k_0^3 a^2\bar{c}}{9{n_x}^2}\right)$$

describes both thermal and radiation energy losses,

$$\eta = \frac{\varepsilon_h}{1-\varepsilon_h+\varepsilon_h/n_x}\left(\frac{a^2\bar{c}}{3{n_x}^2 d^3}\right).$$

It should be noted that the disk polarizability across the flake plane is assumed to vanish owing to atomic-scale thickness of graphene.

In Sections 2.1 and 2.2, we have shown that a similar model describing arrays of metal nanoparticles exhibits interesting nonlinear dynamics for one- and two-dimensional arrays, including the generation of kinks, oscillons, and dissipative solitons [145–148]. Here, we

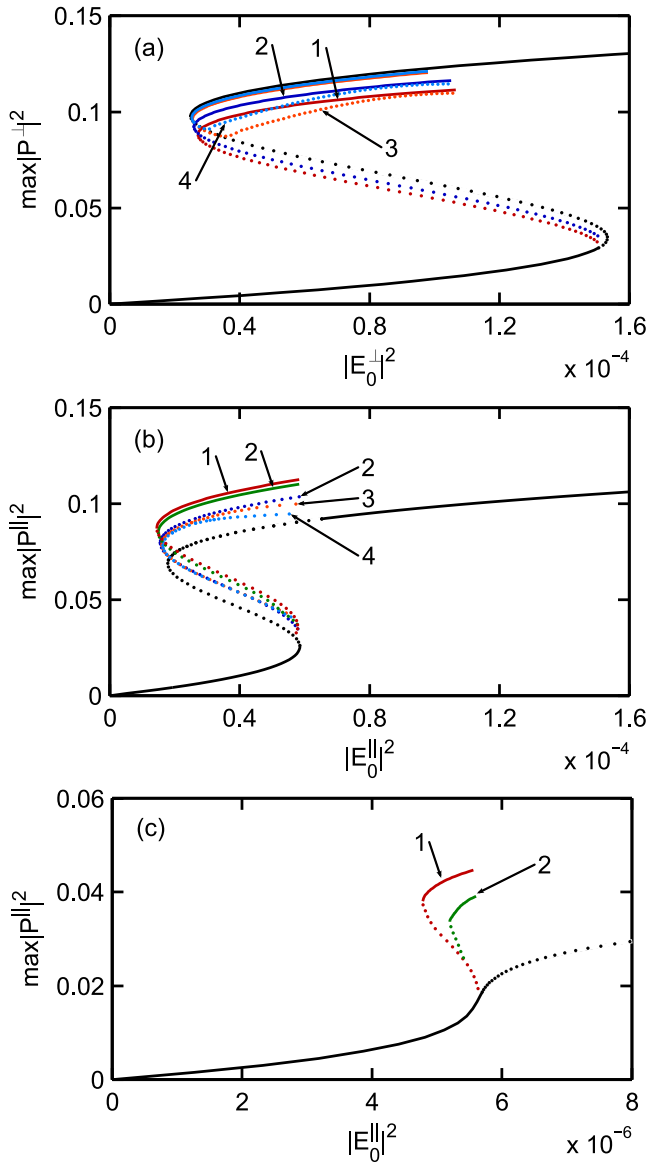

Figure 2.7: Homogeneous stationary solution (black line) and soliton families. Black dotted indicates modulationally unstable part of the dependence. Solid and dotted color curves correspond to stable and unstable branches of solitons with different number of peaks marked by digits: (a) transversely polarized, $\Omega = -0.09$; longitudinally polarized solitons, (b) $\Omega = -0.09$, (c) $\Omega = -0.045$ (green line corresponds to the bound state).

focus on one-dimensional *bright* localized soliton solutions similar of those are known for various discrete dissipative systems with local interactions [157, 172, 173].

Families of discrete solitons

By varying the pump configuration, we can decouple the nonlinear equations (2.10) and analyze *scalar solitons* in each of the polarization components separately. However, in a general case, the polarization components remain coupled, and we should study the case of two-component, or *vector solitons*.

In our calculations here, we employ the following set of parameters: $a = 30$ nm, $\varepsilon_h = 2.1$, $\mathcal{E}_F = 0.6$ eV, $\tau_{\text{intra}} = 0.127$ ps, $d = 3.8a$, and $\hbar\omega_0 \approx 0.165$ eV (which corresponds

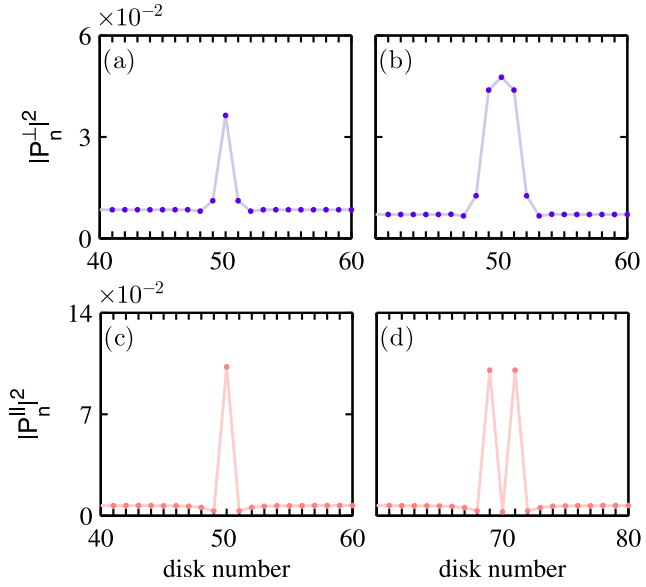

Figure 2.8: Soliton profiles in the case of homogeneous excitation: (a) one-peak transverse soliton at $\Omega = -0.04$, $|E_0^{\perp}|^2 = 1.58 \times 10^{-5}$, (b) three-peak transverse soliton at $\Omega = -0.04$, $|E_0^{\perp}|^2 = 1.4 \times 10^{-5}$, (c) one-hump longitudinal soliton coexisting with a bound state (d) containing two peaks at $\Omega = -0.09$, $|E_0^{\parallel}|^2 = 3 \times 10^{-5}$, sitting on the background of a homogeneous steady state solution.

to the wavelength ≈ 7.5 μm). However, we notice that, within our model, the results remain valid for a broad range of parameters, which can be adjusted for controlling the effect. In particular, the resonant frequency can be shifted to the THz range increasing the disks' diameters up to hundreds of nanometers, yet keeping a doping level below 0.8 eV and loss coefficient $\gamma < 0.1$ for high-quality graphene samples with the scattering time $\tau_{\text{intra}} \sim 0.1 \div 0.4$ ps.

Scalar solitons

First, we excite the chain by a homogeneous electric field with two polarizations: (i) $\mathbf{E}_n = (E_n^{\parallel}, 0)$ and (ii) $\mathbf{E}_n = (0, E_n^{\perp})$. Assuming the driving radiation, e.g. normally incident pump plane wave, has the in-plane electric field component either across or along the chain axis, we solve the decoupled equations of the system Eqs. (2.10).

Since dissipative solitons are supposed to nest on a stable background, we begin with the analysis of a steady homogeneous state and inspecting its modulational stability. For an infinite chain, following [146, 147], we find analytically the homogeneous stationary solutions of Eqs. (2.10) which are characterized by bistability at $\Omega < -0.047$ and $\Omega < -0.018$ for the transversal and longitudinal excitations, respectively, as shown in Figs. 2.7(a,b). For finite chains, conclusions drawn from the analytical considerations have to be verified numerically since the edges may produce additional boundary instabilities. However, typically discrete solitons exist inside or nearby a bistability domain. Therefore, we will focus on these regions to identify soliton families.

In practice, dissipative solitons can be formed, for instance, when the chain is subject to additional narrow beam pulses. Another way for formation of solitons is the collision of switching waves (kinks) [145], step-like distributions which connect quasi-homogeneous levels corresponding to the top and low branches of a bistable curve. In this way, discrete solitons are frequently interpreted as two tightly bound kinks with the opposite polarities.

Applying the standard Newton iteration scheme for a finite chain of 101 disks, we find families of bright solitons, characterized by a snaking bifurcation behavior [156, 173–175], and simultaneously determine their stability, as shown in Fig. 2.7. Remarkably, longitudinal solitons also appear outside the bistability area, where a homogeneous steady state solution is a single-valued function of the pump, provided that the character of the bifurcation is subcritical, particularly, in the certain range of frequencies, $-0.047 < \Omega < -0.04$, for the parameters of Fig. 2.7. Examples of the soliton profiles are depicted in Fig. 2.8.

Within the homogeneous excitation, solitons always stand at rest regardless their width because the effective periodic potential created by the chain requires a finite value of the applied external force to start soliton's motion [157, 175]. In order to study soliton mobility, we excite the chain by the tilted light incidence: $\mathbf{E}_n = (E_0^{\parallel}\exp(-iQdn), 0)$ and $\mathbf{E}_n = (0, E_0^{\perp}\exp(-iQdn))$, where Q is the longitudinal wavenumber.

In contrast to cavity solitons in a model with the nearest-neighbor purely real coupling and focusing nonlinearity [175], the longitudinally polarized one-peak solitons remain trapped at any value of Q. This is associated with the imaginary part of the dipole-dipole interaction. However, wide enough transverse solitons are susceptible to a propelling force. An example of multi-peaked moving solitons is presented in Fig. 2.9. At $Qd \neq 0$, the soliton loses its symmetry [see Figs. 2.9(b,d)] and, in the presence of an in-plane momentum exceeding some critical value, the soliton starts moving along the chain towards the edge where it gets trapped as shown in Fig. 2.9(e).

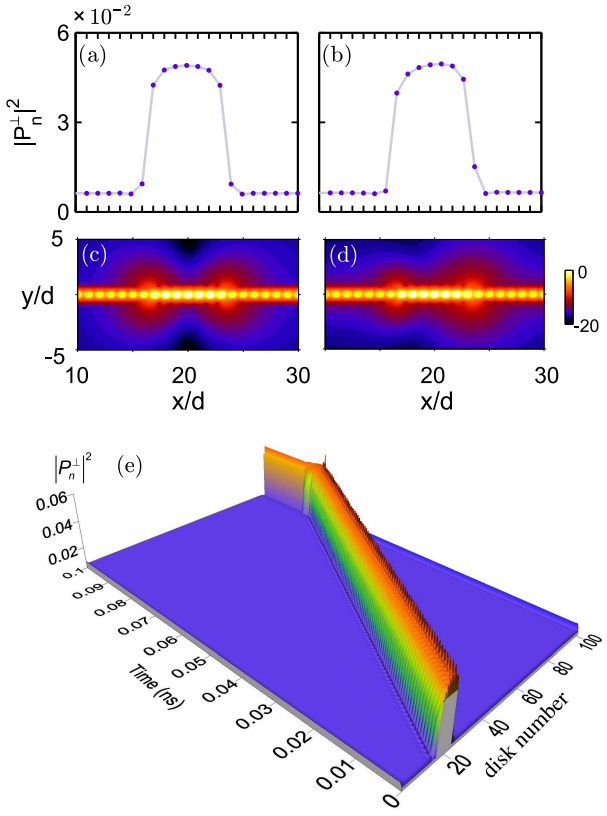

Figure 2.9: Soliton profiles at $|E_0^{\perp}|^2 = 1.28 \times 10^{-5}$, $\Omega = -0.04$, (a) $Qd = 0$ symmetric resting, (b) $Qd = -0.05$ asymmetric resting; (c,d) respective top views of the intensity distribution, $\ln\left(|E|^2/|E|^2_{\max}\right)$, in the plane of the chain; (e) Spatiotemporal dynamics of a drifting soliton at $Qd = -0.2$.

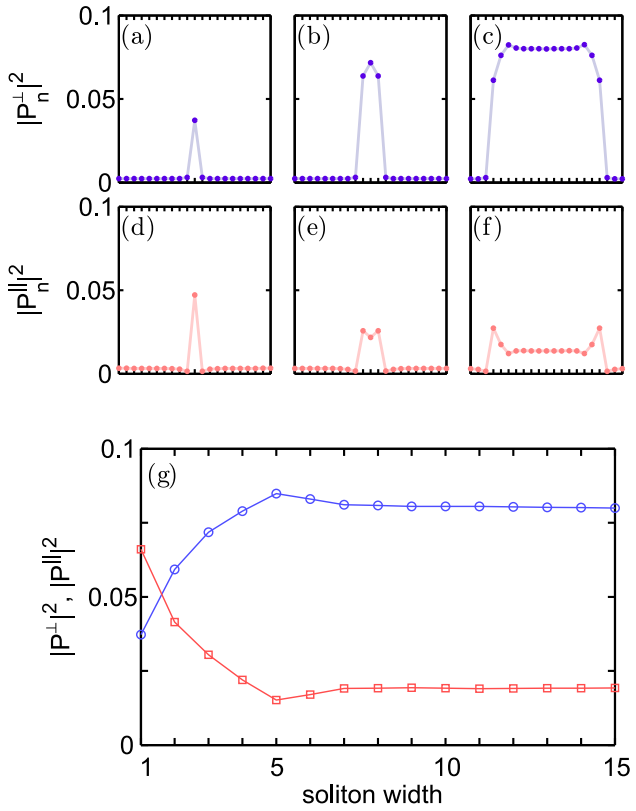

Figure 2.10: Profiles of two-component vector solitons at $|E_0|^2 = 4 \times 10^{-5}$, $\Omega = -0.09$, $\theta = 0.25\pi$ localized on (a,d) one and (b,e) three nanodisks. The case (c,f) shows an example of a broad vector soliton. (g) Dependence of the amplitude in the central excited disk of the vector soliton on the number of excited disks. Circles and squares correspond to the transverse and longitudinal components, respectively.

Vector solitons

Remarkably, coupled equations (2.10) also support two-component vector solitons with a mixed polarization when the excited field contains both nonzero components, $E_0^{\perp,\parallel} \neq 0$, $\mathbf{E}_0 = (E_0^{\perp}, E_0^{\parallel}) = (E_0 \sin\theta, E_0 \cos\theta)$, see examples in Fig. 2.10. In the case of vector solitons, horned longitudinal solitons corresponding to the dotted unstable branches in Fig. 2.7(b), become stabilized. Figure 2.10(g) illustrates a variation of the amplitudes of both components with the growing soliton width.

Parameters

In our analysis presented above, we have operated with dimensionless variables. To estimate the feasibility of the predicted phenomena, we should recover physical values and realistic parameters. In particular, Eqs. (2.8), (2.9) provide the estimate of $\chi_{gr}^{(3)} \sim 10^{-7} - 10^{-6}$ esu for typical parameters, and the dimensionless intensity of the external field, $|E_0^{\perp,\parallel}|^2 \sim 10^{-4}$, corresponds to the physical intensity of ~ 10 kW/cm^2. Even accounting for the local field enhancement inside the graphene nanodisks, the characteristic time scales at which the solitons are formed are estimated to be less than the pulse duration that may cause a graphene damage at the given intensities [176–179]. Thus, there are expectations for the experimental observation of the predicted nonlinear effect that can be used

to construct subwavelength nonlinear elements able to operate in the THz and infrared frequency ranges, while in metal-based structures low-loss discrete nonlinear plasmonic modes appear at infrared and visible frequencies [146, 180–182].

Summary

To conclude, we have studied nonlinear dynamics in nonlinear arrays of graphene nanodisks in the presence of a pumped external field. We have derived nonlinear equations describing the evolution of the nanodisks' polarization, taking into account losses in graphene and a dipole-dipole coupling between the nanodisks. We have demonstrated the existence of families of discrete dissipative solitons and also revealed that such solitons can propagate stably along the chain provided they are excited by the tilted field. We have predicted a new class of discrete vector solitons composed of two mutually coupled polarization components.

Chapter 3

Self-action and plasmon-solitons in graphene waveguides and multilayers

In this Chapter, we explore the guided electromagnetic waves in double-layer and multilayer graphene structures. We first study the formation of *spatial plasmon solitons*, associated with the *self-action nonlinearity* in graphene, and demonstrate nonlinear switching of surface plasmons in two coupled graphene layers. To overcome the effects of plasmon attenuation caused by intrinsic graphene losses, we then propose to employ multilayer graphene excited by an external laser radiation in the Otto configuration. We predict that multilayer stacks of graphene sheets may sustain dissipative plasmon solitons generated and supported by the driving electromagnetic field. Moreover, multilayer graphene waveguides are shown to be capable of increasing the supported TM plasmon wavelength, thus facilitating the excitation of surface waves in graphene and increasing their propagation length. We suggest that both dispersion and localization of the guided modes can be efficiently controlled by changing the number of layers in the stack. We also find that the surface of a terminated multilayer graphene structure supports a special type of surface plasmons which are known as *electromagnetic Tamm states*. The existence of such linear surface modes is linked to the defect of the periodicity at the surface, and their dispersion properties are shown to be tunable by varying the thickness of a dielectric cap layer. We note that the fundamental difference between linear and nonlinear regimes of operation is the possibility to have nonlinear surface states (namely, *surface solitons*) without any structural defects, whereas in the bulk of such nonlinear graphene metamaterial, similar to its metal-dielectric counterparts, localized nonlinear modes can be described by the discrete nonlinear Schrödinger (NLS) equation, and its solutions are associated with stable discrete plasmon solitons.

3.1 Nonlinear graphene coupler

As it has been shown recently, doped graphene is a tunable plasmonic material and it demonstrates a strong nonlinear optical response [87, 89, 90, 107]. This finding, combined with the unprecedented nanoscale field confinement in graphene plasmons [183], has opened a route for the exploration of nonlinear photonic effects in graphene structures, including nonlinear self-action of surface plasmons [129] and generation of subwavelength spatial solitons [184].

In this Section, we study analytically and numerically nonlinear propagation of electromagnetic waves in two closely spaced graphene layers and demonstrate that this double-

layer graphene waveguide can operate as an efficient *nonlinear optical coupler* for both continuous plasmons and for subwavelength spatial optical plasmon-solitons. We analyze the nonlinearity-induced effects of light localization and symmetry breaking in such a graphene coupler, and predict that the inter-layer power-dependent coupling provides a novel physical mechanism for the optical beam control and manipulation at realistic input power levels.

Model

We consider a planar structure created by two parallel layers of graphene, as shown schematically in Fig. 3.1. We assume that the surrounding dielectric material is a homogeneous medium with the dielectric permittivity ε, and study the nonlinear propagation of plasmons in the layers. To describe interaction of plasmons excited in each layer of our structure, we generalize the analytical method developed recently in Ref. [129]. We start with Maxwell's equations describing the propagation of monochromatic electromagnetic waves with the field dependencies $\sim \exp(-i\omega t)$,

$$\begin{aligned} &\nabla \times \mathbf{E} = ik_0 \mathbf{H}\,, \\ &\nabla \times \mathbf{H} = -ik_0 \varepsilon \mathbf{E} + \frac{4\pi}{c}\Big[\delta(x+d/2) + \delta(x-d/2)\Big]\mathbf{J}\,, \end{aligned} \tag{3.1}$$

where $k_0 = \omega/c$ is the wavenumber in free space, ω is the angular frequency, and c is the speed of light. We assume that the graphene layers are placed at $x = \pm d/2$, as indicated by Dirac's delta functions δ with $\mathbf{J}$ being the current density induced in the graphene layers.

In the linear regime, the induced current is proportional to the tangential component of the electric field, $\mathbf{J} = \sigma \mathbf{E}_\tau$, where $\sigma \equiv \sigma^{(R)} + i\sigma^{(I)}$ is a linear frequency-dependent surface conductivity of graphene. Each *isolated* graphene layer supports localized surface plasmons with the TM polarization [129, 183]. When losses are neglected, the magnetic field of these plasmon modes has the form

$$\mathbf{H}_{1,2}^{(0)} = \mathcal{A}_{1,2} h_{1,2}(x) e^{ik_0 \beta z} \mathbf{y_0}, \tag{3.2}$$

with the transverse mode profile given by

$$h_{1,2}(x) = ik_0 \left(\frac{\varepsilon}{\kappa}\right) e^{-\kappa |x \pm d/2|} \begin{cases} 1, & x > \mp d/2\,, \\ -1, & x < \mp d/2\,, \end{cases} \tag{3.3}$$

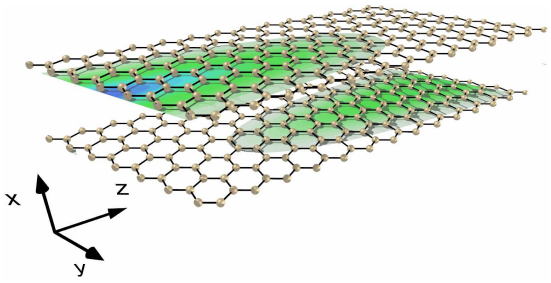

Figure 3.1: Schematic of a nonlinear graphene coupler composed of two layers of graphene. Color pattern demonstrates how a plasmon beam excited in the top layer tunnels to the bottom layer (numerical results not to scale). Bottom layer (which we call layer 1) and top layer (layer 2) are located in the planes $x = -d/2$ and $x = d/2$, respectively.

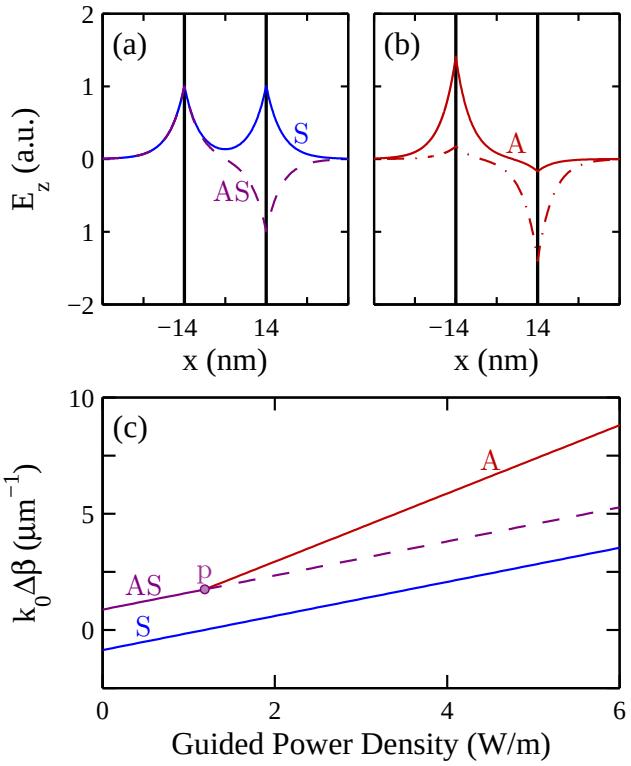

Figure 3.2: (a,b) Examples of the transverse mode profiles for symmetric (S), antisymmetric (AS), and asymmetric (A) modes propagating in the double-layer graphene shown for the E_z component. (c) Shift of the nonlinear propagation constant vs. the mode power density in the guided plasmon mode propagating in the z-direction. Solid/dashed lines correspond to stable/unstable branches.

where upper and lower signs correspond to the subscripts 1 and 2 and associated with the layers located at $x = -d/2$ and $x = d/2$, respectively, cf. Fig. 1, $\kappa = k_0\sqrt{\beta^2 - \varepsilon}$, and the normalized wavenumber β is found from the dispersion relation:

$$\frac{2\varepsilon}{k_0\sqrt{\beta^2-\varepsilon}} = \frac{4\pi}{\omega}\sigma^{(I)}\,. \tag{3.4}$$

To describe the propagation of *nonlinear plasmons* in this double-layer graphene structure, we use the slowly varying envelope approximation usually employed in the physics of optical solitons [38]. To be more specific, for our problem we study weakly dissipative case when $\sigma^{(R)} \ll \sigma^{(I)}$. This dissipation is low when the frequency of the plasmons and Fermi energy of graphene satisfy the relations $\hbar\omega < 1.67\mathcal{E}_F$ ($\sigma^{(I)} > 0$), $k_BT \ll \mathcal{E}_F$ [70], where $\mathcal{E}_F$ is the Fermi energy. We also neglect spatial dispersion, which is valid for $\hbar\omega \leq \mathcal{E}_F$ [70].

To utilize the asymptotic expansion approach, we assume that (i) nonlinear correction to the conductivity σ is small; (ii) waves are localized in y-direction, and their width Λ is such that diffraction remains weak; (iii) evanescent coupling between plasmons excited in different graphene layers is small. Under these assumptions, the induced current can be taken in the form [129]

$$\mathbf{J} = \hat{\sigma}\mathbf{E}_\tau = \left(\sigma + \sigma^{\mathrm{NL}}|E_\tau|^2\right)\mathbf{E}_\tau\,,$$

where σ^{NL} is the self-action nonlinear conductivity of graphene (see Appendix A). To develop the consistent perturbation theory, we further assume that in the resulting equations the terms responsible for the above mentioned effects are of the same order of smallness.

Now we formally introduce a small parameter μ

$$\mu^2 = \max\left\{\left|\frac{\sigma^{(R)}}{\sigma^{(I)}}\right|,\ \left|\frac{\sigma^{NL}|E_\tau|^2}{\sigma^{(I)}}\right|,\ (k_0\beta\Lambda)^2,\ e^{-k_0\sqrt{(\beta^2-\varepsilon)}d}\right\}$$

and derive the equations for slowly varying plasmon amplitudes. We rewrite Maxwell's equations (4.38) as follows

$$\begin{aligned}\nabla\times\mathbf{E}_{1,2} &= ik_0\mathbf{H}_{1,2}\,,\\ \nabla\times\mathbf{H}_{1,2} &= -ik_0\varepsilon\mathbf{E}_{1,2}+\frac{4\pi}{c}\delta(x\pm d/2)\hat{\sigma}(\mathbf{E}_{1,2\tau}+\mathbf{E}_{2,1\tau})\,,\end{aligned} \tag{3.5}$$

so that the superpositions $\mathbf{E}=\mathbf{E}_1+\mathbf{E}_2$ and $\mathbf{H}=\mathbf{H}_1+\mathbf{H}_2$ satisfy the original equations. Then, developing a perturbation theory, the solutions of Eqs. (3.5) are sought in the form of the following asymptotic series

$$\begin{aligned}H_{1,2\,y} &= \left[\mathsf{A}_{1,2}(\mu^2\mathsf{z},\mu\mathsf{y})h_{1,2}(x)+\mu^2\mathsf{H}^{(2)}_{1,2}(\mu^2\mathsf{z},\mu\mathsf{y},x)+\ldots\right]e^{ik_0\beta z}\\ &= \left[\mathcal{A}_{1,2}(z,y)h_{1,2}(x)+H^{(2)}_{1,2}(z,y,x)+\ldots\right]e^{ik_0\beta z}\,,\\ H_{1,2\,z} &= \left[\mu\mathsf{H}^{(1)}_{1,2}(\mu^2\mathsf{z},\mu\mathsf{y},x)+\mu^3\mathsf{H}^{(3)}_{1,2}(\mu^2\mathsf{z},\mu\mathsf{y},x)+\ldots\right]e^{ik_0\beta z}\\ &= \left[H^{(1)}_{1,2}(z,y,x)+H^{(3)}_{1,2}(z,y,x)+\ldots\right]e^{ik_0\beta z}\,.\end{aligned} \tag{3.6}$$

The zero-order term in μ returns the identity for the unperturbed plasmons (3.2)–(4.44). The correction $H^{(1)}_{1,2}$ of the first order in μ is determined from $\nabla\cdot\mathbf{H}_{1,2}=0$ as

$$H^{(1)}_{1,2}=\frac{i}{k_0\beta}\frac{\partial\mathcal{A}_{1,2}}{\partial y}h(x)\,.$$

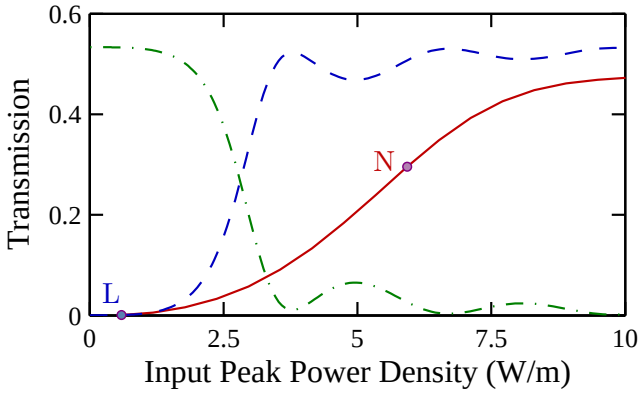

Figure 3.3: Switching characteristics of the nonlinear graphene coupler. Shown is a fraction of the power transmitted in the pumped layer for cw (dashed curve) and soliton input beam (solid curve) in a half-beat-length coupler as a function of the input peak power density. Dashed-dotted curve: calculated relative fractional output power emerging from the other layer in the continuous plasmon regime.

In the order of μ^2 we obtain:

$$\begin{aligned}
&\frac{d^2H_{1,2}^{(2)}}{dx^2}+k_0^2(\varepsilon-\beta^2)H_{1,2}^{(2)}-\frac{4\pi}{c}i\sigma^{(I)}\dot{\delta}(x\pm d/2)E_{1,2z}^{(2)}=F_{1,2}\,,\\
&F_{1,2}=-\left(2ik_0\beta\frac{\partial\mathcal{A}_{1,2}}{\partial z}+\frac{\partial^2\mathcal{A}_{1,2}}{\partial y^2}\right)h_{1,2}(x)+\frac{4\pi}{c}\dot{\delta}(x\pm d/2)\left(\sigma^{(R)}+\sigma^{NL}|\mathcal{A}_{1,2}|^2\right)\mathcal{A}_{1,2}\\
&\qquad+\frac{4\pi}{c}i\sigma^{(I)}\dot{\delta}(x\pm d/2)\mathcal{A}_{2,1}e^{-\kappa d}\,,
\end{aligned}\tag{3.7}$$

where $\dot{\delta}$ denotes the derivative of the delta function, and the corrections

$$E_{1,2z}^{(2)}=\frac{i}{k_0\varepsilon}\frac{\partial H_{1,2}^{(2)}}{\partial x}\tag{3.8}$$

are continuous at $x=\pm d/2$.

Then, applying the Fredholm theorem [185], which states that the solution for the correction $H_{1,2}^{(2)}$ is nondiverging if the eigenmodes of the homogeneous equation for $H_{1,2}^{(2)}$ are orthogonal to the perturbation, we finally derive the nonlinear equations for the slowly varying envelopes $\mathcal{A}_{1,2}$ of the TM-polarized plasmons propagating in each layer,

$$2ik_0\beta\left(\frac{\partial\mathcal{A}_{1,2}}{\partial z}+\gamma\mathcal{A}_{1,2}\right)+\frac{\partial^2\mathcal{A}_{1,2}}{\partial y^2}+g|\mathcal{A}_{1,2}|^2\mathcal{A}_{1,2}=Q\mathcal{A}_{2,1}\,,\tag{3.9}$$

where

$$\begin{aligned}
\gamma&=\frac{2\pi}{c\varepsilon\beta}\sigma^{(R)}(\beta^2-\varepsilon)^{3/2}k_0\,,\\
g&=\frac{4\pi}{c\varepsilon}(\beta^2-\varepsilon)^{3/2}i\sigma^{NL}k_0^2\,,\\
Q&=\frac{4\pi}{c\varepsilon}e^{-\kappa d}\sigma^{(I)}(\beta^2-\varepsilon)^{3/2}k_0^2\,,
\end{aligned}\tag{3.10}$$

are a linear absorption parameter, nonlinear and coupling coefficients, respectively. Remarkably, the equations (3.9), along with the correct analytical expressions for the effective coefficients (3.10), can be obtained in the order $O(\mu^2)$ of the perturbation expansion using the substitution

$$k_0\hat{\beta}=k_0\beta+\left(-i\frac{\partial}{\partial z}-\frac{1}{2k_0\beta}\frac{\partial^2}{\partial y^2}\right)+\dots$$

into the modified dispersion relation (4.44) which in the presence of the second layer takes the form

$$\frac{2\varepsilon}{k_0\sqrt{\hat{\beta}^2-\varepsilon}}=\frac{4\pi}{\omega}\left(\sigma^{(I)}-i\left[\sigma^{(R)}+\sigma^{NL}|\mathcal{A}_1|^2+i\sigma^{(I)}e^{-\kappa d}\frac{\mathcal{A}_2}{\mathcal{A}_1}\right]+\dots\right).\tag{3.11}$$

Nonlinear switching

In the framework of the nonlinear amplitude equations (3.9) disregarding losses and beam diffraction, we can analyze different types of TM-polarized eigenmodes of a nonlinear double-layer graphene waveguide.

The linear frequency-dependent surface conductivity of graphene has been derived in

a number of works [70,186,187], and we employ the following expression

$$\sigma(\omega) = \sigma_{\text{intra}}(\omega) + \sigma_{\text{inter}}(\omega) = \frac{ie^2}{\pi\hbar}\left\{\frac{\mathcal{E}_F}{\hbar\left(\omega + i\tau_{\text{intra}}^{-1}\right)} + \frac{1}{4}\ln\left|\frac{2\mathcal{E}_F - \hbar\omega}{2\mathcal{E}_F + \hbar\omega}\right|\right\}, \tag{3.12}$$

where we assume for doped graphene $\hbar\omega < 2\mathcal{E}_F$ and $k_B T \ll \mathcal{E}_F$ (low temperature limit), where $e = -|e|$ is the electron's charge, k_B is the Boltzmann constant, T is the temperature, $\mathcal{E}_F = \hbar v_F\sqrt{\pi n}$ is the Fermi energy, n is the doping electron density, $v_F \approx c/300$ is the Fermi velocity, and τ_{intra}^{-1} is the relaxation rate. In the semiclassical limit, $\hbar\omega \leq \mathcal{E}_F$ (for relatively low photon energies), the conductivity can be reduced to the Drude form $\sigma(\omega) \approx \sigma_{\text{intra}}(\omega)$,

$$\sigma_{\text{intra}}(\omega) = \frac{ie^2}{\pi\hbar^2}\frac{\mathcal{E}_F}{\left(\omega + i\tau_{\text{intra}}^{-1}\right)}, \tag{3.13}$$

which takes into account only intraband processes [70,89,90] and includes finite relaxation time, usually estimated from the measured impurity-limited DC mobility.

For high enough field intensities, the graphene conductivity becomes nonlinear, and the so-called self-action term (or nonlinear correction to the graphene conductivity) σ^{NL}, can be obtained analytically within the quasi-classical approach based on the solution of the kinetic Boltzmann equation for massless quasiparticles [87,89,90] (see Appendix A).

For further calculations in this Section, we choose the doping level of $\mathcal{E}_F = 0.1$ eV, $\hbar\omega = \mathcal{E}_F$ ($\lambda = 2\pi/k_0 \approx 12.4\ \mu$m), $\tau_{\text{intra}} = 10$ ps [188], $\varepsilon = 4$, and take the separation between the layers as $d = 28$ nm. We take quite large relaxation time and discuss implications of this choice below.

We find that *three types of nonlinear modes* can propagate in this double-layer graphene coupler, namely symmetric (S) with $\mathcal{A}_1 = \mathcal{A}_2$, antisymmetric (AS) with $\mathcal{A}_1 = -\mathcal{A}_2$, and asymmetric (A) mode with $\mathcal{A}_1 \neq \mathcal{A}_2$, similar to the case of a nonlinear dimer [189]. These modes are presented in Fig. 3.2 through their (a,b) transverse profiles and (c) power-dependent shift of the nonlinear propagation constant. In the linear regime, only symmetric (S) and antisymmetric (AS) modes exist. However, above a critical power level, a symmetry breaking [190–194] occurs in this nonlinear system when a novel, asymmetric branch (A) emerges and it describes the nonlinear states where the power is not distributed equally between the lower and upper graphene layers. The asymmetric mode bifurcates at the point "p" from the antisymmetric branch, and it is stable being characterized by a predominant energy concentration in the vicinity of one of the layers. The AS mode becomes unstable above the critical power.

Next, we focus our attention on the power-controlled switching of plasmon beams between the layers and study numerically the propagation of a sech-like input beam launched into the upper layer (as shown in Fig. 3.1). The input beam is selected to be the fundamental solution of a single (uncoupled) nonlinear equation, and it describes a spatial soliton [184]. For the peak power density of 6 W/m, the soliton beam width is about 50 nm. This significant sub-wavelength localization is supported by the high effective Kerr nonlinearity of graphene [129,184].

In Fig. 3.3, we compare the corresponding switching characteristics of the nonlinear graphene coupler for the continuous plasmons (whose amplitude is constant along y) (dashed curve) and for the beams of a finite extent including the soliton switching (solid curves). The coupler length is selected at the half-beat length $L = \pi/(2Q)$, when in the linear regime the input power transfers completely into the second layer [38]. Apart from

an increase of the threshold power density, two regimes of the coupler operation can be clearly distinguished.

For relatively small input powers, in the so-called linear regime, the plasmon beam of the upper layer couples to the lower layer and tunnels almost completely, see Figs. 3.4(a,b). For higher values of the input power, the energy transfer between the layers becomes inhibited, and we observe the nonlinear regime when the plasmon beam remains in the upper layer [see Figs. 3.4(c,d)]. Importantly, the dissipation does not inhibit switching but it modifies the slope of the curves and the asymptotic value of the switching curve not achieving unity, as shown in Fig. 3.3. Therefore, the beam may be effectively routed between the graphene layers by changing its input power.

From the power flow (6 W/m) and knowing the plasmon structure, we estimate the maximum amplitude of the electric field on graphene layer at $7 \cdot 10^6$ V/m, which is below graphene breakdown threshold [177]. In our simulations, however, we assumed low loss graphene, with relaxation time of 10 ps. Such relaxation times were observed in several works with multi-layer structures [188,195], however typical single layer graphene reported so far experimentally, usually exhibits relaxation times of the order of 0.1 ps. Such graphene with higher losses will have shorter plasmon propagation length, and it will require larger, and probably unachievable light intensities. Therefore, we suggest that high quality low loss graphene will potentially be suitable for creating nonlinear couplers.

Further, we discuss the case when two in-phase beams of the identical shape are launched into both the layers being shifted initially by a half of their width with respect to each other. In the linear regime, the power exchange between the layers leads to the effective attraction between the centers of mass of the beams, as can be seen in Figs. 3.5(a,b). However, in the strongly nonlinear regime the energy exchange is suppressed and the mutual interaction of optical solitons generated in the two different layers is accompanied by their repulsion, as shown in Figs. 3.5(c,d).

Summary

We have studied analytically and numerically the propagation of nonlinear electromagnetic waves in a double-layer graphene structure. We have revealed that this structure can operate as an efficient planar nonlinear coupler demonstrating the switching of light between two different layers of graphene. We have studied the nonlinear effects in this

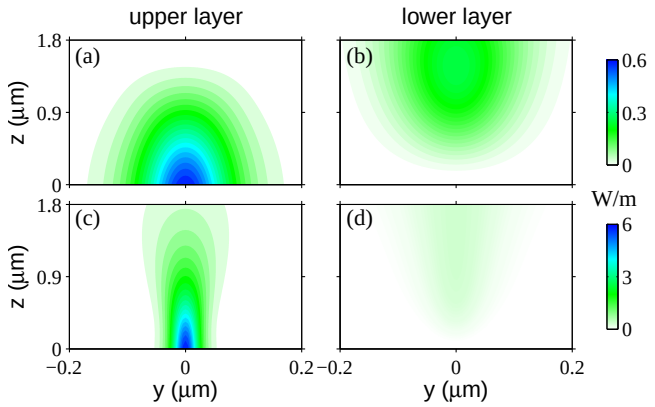

Figure 3.4: Spatial distribution of the power density in the layers of the nonlinear graphene coupler for different input peak power densities: (a,b) linear regime, $P_{\text{in}} = 0.6$ W/m; (c,d) nonlinear regime, $P_{\text{in}} = 6$ W/m; corresponding to the points marked in Fig. 2.3 as L and N, respectively.

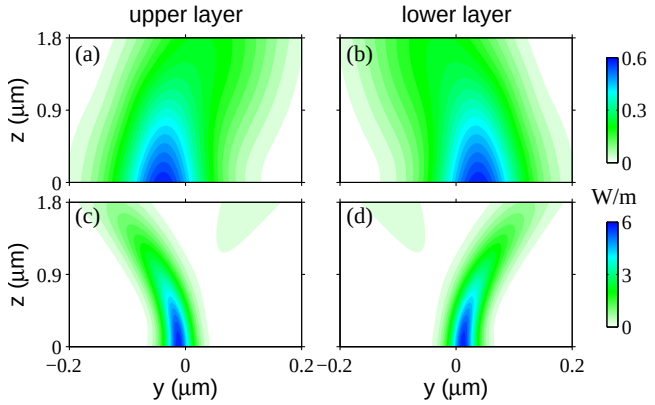

Figure 3.5: Plasmon beam routing in the nonlinear graphene coupler. Spatial distribution of the power density in the layers of the nonlinear graphene coupler for different input peak power densities: (a,b) linear regime, $P_{\text{in}} = 0.6$ W/m; (c,d) nonlinear regime, $P_{\text{in}} = 6$ W/m.

graphene coupler for both constant amplitude waves and subwavelength spatial solitons and described the symmetry breaking and nonlinear switching with novel opportunities for optical beam control and manipulation at the nanoscale.

3.2 Multilayer graphene waveguides

One of the main obstacle impeding the efficient use of graphene in plasmonic devices is the difficulty of excitation of graphene surface plasmon modes, which is due to their deep subwavelength nature [58]. In this Section, we suggest to employ multilayer graphene structures to overcome this difficulty.

Multilayer graphene metamaterials have been studied previously [196, 197], and it has been shown that coupling of the surface plasmons at individual graphene sheets results in the emergence of the hyperbolic isofrequency contours, that can lead to a large density of electromagnetic states in these structures. Here we study the eigenmode dispersion of the multilayer graphene structures with a finite number of layers. We demonstrate that the field localization and modes' wavenumbers can be efficiently controlled by varying the number of layers in the structure, making such stacked graphene structures perspective for real optoelectronic and nanophotonic applications and the observation of strong nonlinear effects [131, 132]. Remarkably, we find that in the long wavelength limit, the dispersion of the fundamental mode of the N-layer graphene structure coincides with the dispersion of a plasmon mode supported by a single graphene layer, but with N times larger conductivity. We also compare our exact dispersion relations with the results provided by the effective media model.

Eigenmode dispersion

Specifically, we consider a structure shown schematically in Fig. 3.6. The graphene waveguide consists of a finite number of layers with deeply subwavelength spacing d filled with dielectric material with permittivity ε. The waveguide is sandwiched between two semi-infinite homogeneous dielectrics, the so-called substrate and superstrate, having dielectric constants of ε_1 and ε_2, respectively. Each of the N graphene layers is placed at $x = md$, where $m \in [0, N-1]$. The capping medium and substrate medium therefore occupy the half-spaces $x < 0$ and $x > (N-1)d$, respectively. We assume harmonic time-dependence

for modes propagating along z axis $\exp(-i\omega t)$ so that the propagation along z-axis is described by the multiplier $\exp(ik_z z)$, where $k_z = \beta k_0$ is the propagation constant, $k_0 = \omega/c$ is the wavenumber in a free space, and β is the normalized wavenumber. Next, we derive the dispersion relation by employing the matrix method [198, 199]. In the regions $md \leq x \leq (m+1)d$, the transverse profile of the magnetic field can be presented in the form,

$$H_y(x) = H_+^m e^{-\kappa x} + H_-^m e^{\kappa x}\,, \tag{3.14}$$

where $\kappa = (k_z^2 - k_0^2\varepsilon)^{1/2}$ is the transverse wavenumber. From the Maxwell equations, we find the z-component of the electric field continuous at the graphene layers, given by $E_z(x) = (i\kappa/k_0\varepsilon)[H_-^m e^{\kappa x} - H_+^m e^{-\kappa x}]$. Since we are looking for localized guided modes vanishing for large $|x|$, we present the field outside the waveguide in the following form

$$H_y(x<0) = H_-^0 e^{\kappa_1 x}, \quad H_y\,(x>(N-1)d) = H_+^{NG} e^{-\kappa_2 x}, \tag{3.15}$$

where $\kappa_{1,2} = (k_z^2 - k_0^2\varepsilon_{1,2})^{1/2}$. To study waves in a multilayer structure, it is convenient to use the transfer matrix method which links the field amplitudes in the adjacent periods, $H_\pm^{m+1}$ and $H_\pm^m$

$$\begin{pmatrix} H_+^{m+1} \\ H_-^{m+1} \end{pmatrix} = \hat{T} \times \begin{pmatrix} H_+^m \\ H_-^m \end{pmatrix}\,, \tag{3.16}$$

where the transfer matrix $\hat{T} = \hat{P}\hat{G}$ is a product of the matrices describing the boundary conditions at the graphene layer

$$\hat{G} = \begin{pmatrix} 1 - 2\pi i\sigma(\omega)\kappa/\omega\varepsilon & 2\pi i\sigma(\omega)\kappa/\omega\varepsilon \\ -2\pi i\sigma(\omega)\kappa/\omega\varepsilon & 1 + 2\pi i\sigma(\omega)\kappa/\omega\varepsilon \end{pmatrix}\,, \tag{3.17}$$

where $\sigma(\omega)$ is the frequency-dependent surface conductivity of a single layer of graphene, and $\hat{P}$ being the propagation matrix of a dielectric layer defined as

$$\hat{P} = \begin{pmatrix} e^{-\kappa d} & 0 \\ 0 & e^{\kappa d} \end{pmatrix}\,. \tag{3.18}$$

In our calculations, we neglect losses and assume $\hbar\omega < 1.67\mathcal{E}_F$ ($\mathrm{Im}\,\sigma > 0$), taking

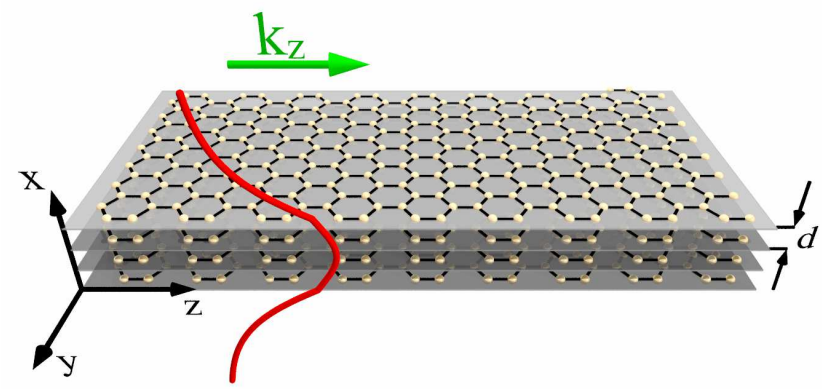

Figure 3.6: Geometry of the multilayer graphene waveguide. The broken curve shows schematically the profile of the continuous z-component of the electric field for the fundamental mode guided by the slab.

conductivity for highly doped or gated graphene ($k_BT \ll \mathcal{E}_F$) in the form [58,70]

$$\sigma(\omega) = \frac{ie^2}{\pi\hbar}\left[\frac{\mathcal{E}_F}{\hbar\omega} + \frac{1}{4}\ln\frac{(2\mathcal{E}_F - \hbar\omega)}{(2\mathcal{E}_F + \hbar\omega)}\right]. \tag{3.19}$$

For an infinite periodic structure, we employ the Bloch theorem, $H_{\pm}^{m+1} = H_{\pm}^{m} e^{iK_B d}$, and obtain the dispersion of Bloch waves in the form

$$\cos(K_B d) = \cosh(\kappa d) - \frac{\kappa}{2\varepsilon}\frac{4\pi\sigma(\omega)}{ick_0}\sinh(\kappa d)\,. \tag{3.20}$$

If d is large enough (or, equivalently, $k_z \to \infty$), the above expression approaches the dispersion relation for surface p-polarized plasmons supported by a single graphene layer surrounded by dielectrics with permittivity ε [183]:

$$\frac{2\varepsilon}{\kappa} = \frac{4\pi\sigma(\omega)}{ick_0}\,. \tag{3.21}$$

The matrices of the boundary conditions for the outermost graphene layers can be written as

$$\hat{G}_1 = \frac{1}{2}\begin{pmatrix} 1+\mathcal{Z}_1 & 1-\mathcal{Z}_1 \\ 1-\mathcal{Z}_1^* & 1+\mathcal{Z}_1^* \end{pmatrix}, \tag{3.22}$$

$$\hat{G}_{NG} = \frac{1}{2}\begin{pmatrix} 1+\mathcal{Z}_{NG} & 1-\mathcal{Z}_{NG} \\ 1-\mathcal{Z}_{NG}^* & 1+\mathcal{Z}_{NG}^* \end{pmatrix}, \tag{3.23}$$

where

$$\mathcal{Z}_1 = \frac{\kappa_1\varepsilon}{\kappa\varepsilon_1} - \frac{4\pi}{c}\frac{i\sigma(\omega)\kappa_1}{k_0\varepsilon_1}, \tag{3.24}$$

$$\mathcal{Z}_{NG} = \frac{\kappa\varepsilon_2}{\kappa_2\varepsilon} - \frac{4\pi}{c}\frac{i\sigma(\omega)\kappa}{k_0\varepsilon}. \tag{3.25}$$

A linear relationship between the field amplitudes on both sides of the multilayer structure can be written in the matrix form

$$\begin{pmatrix} H_+^{NG} \\ 0 \end{pmatrix} = \hat{M} \times \begin{pmatrix} 0 \\ H_-^0 \end{pmatrix}, \tag{3.26}$$

where the matrix $\hat{M}$ is obtained sequentially multiplying the matrices $\hat{G}$ and $\hat{P}$: $\hat{M} = \hat{G}_{NG}(\hat{P}\hat{G})^{N-2}\hat{P}\hat{G}_1$. By setting $m_{22} = 0$, we obtain the dispersion relation for localized modes, from which we can find the wavenumber for a given frequency numerically. Once we found the wavenumber, we then calculate the corresponding wavefunction using the matrix relation for the amplitudes in the adjacent periods. The physical origin of the modes is similar to that in other coupled systems, and N interacting graphene sheets will support N non-degenerate plasmon modes originating from coupling of plasmons of individual graphene layers.

All the possible cases of the dielectric permittivities distributions can be divided by symmetry into symmetric ($\varepsilon_1 = \varepsilon_2$) and asymmetric ($\varepsilon_1 \neq \varepsilon_2$) cases. In the case $\varepsilon_1 = \varepsilon_2 = \varepsilon$, all the modes lie in the allowed band, whereas in all other cases branches can span in the forbidden band where the Bloch number has an imaginary part and, thus, the respective

modes are strongly localized in the vicinity of the waveguide boundary.

In the most general case when all three dielectric constants (ε, ε_1 and ε_2) are different, for large separations (or, equivalently, $k_z \to \infty$) there exist $(N-2)$ degenerate states with an asymptote given by Eq. (3.21) and 2 non-degenerate states with asymptotes

$$\frac{\varepsilon}{\kappa} + \frac{\varepsilon_{1,2}}{\kappa_{1,2}} = \frac{4\pi\sigma(\omega)}{i\omega}\,. \tag{3.27}$$

Being mostly confined near the layers $x = 0$ and $x = (N-1)d$, two latter modes are related to the surface Bloch waves localized near the edges of the multilayer waveguide, and they can be attributed to the so-called Tamm states.

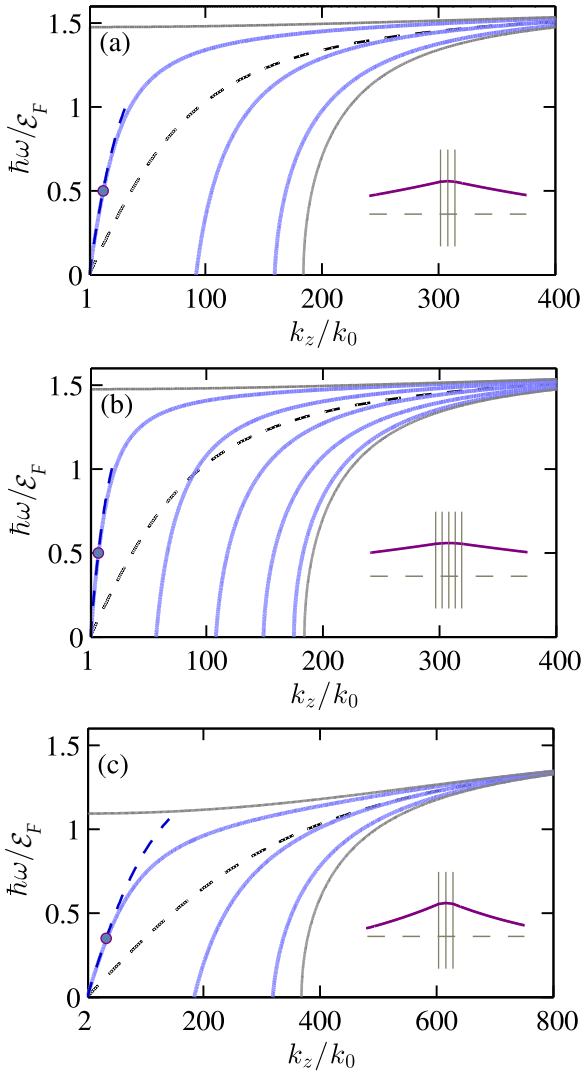

Figure 3.7: Dispersion of the eigenmodes of the multilayer graphene waveguides consisting of 3 (a,c) and 5 (b) layers. The surrounding media and interlayer spacers are made from the same material with dielectric permittivity $\varepsilon = 1$ (a,b) and $\varepsilon = 4$ (c). Period of the structure is $d = 8$ nm in all the cases. Gray solid lines show the boundaries of the allowed band for the localized propagating solutions inside the graphene slab. Black dashed line shows the dispersion of the surface plasmon for a single graphene layer; blue dashed line corresponds to the dispersion of a surface plasmon localized at the two-dimensional conducting layer with permittivity $N\sigma$. Insets show the electric field profile $|E_z|$ for the fundamental mode at frequency $\hbar\omega = 0.5\mathcal{E}_F$ (a,b) and $\hbar\omega = 0.35\mathcal{E}_F$ (c).

Next, we consider a symmetric case $\varepsilon_1 = \varepsilon_2 = \varepsilon$. For $N = 2$ and $\varepsilon = \varepsilon_1 = \varepsilon_2$, we have $\hat{M} = \hat{G}\hat{P}\hat{G}$, and immediately obtain the dispersion relation for the symmetric and antisymmetric modes guided by a graphene double-layer structure, studied earlier in Refs [131,200]:

$$1 + \frac{2\pi i\sigma(\omega)\kappa}{\omega\varepsilon}\left(1 \pm e^{-\kappa d}\right) = 0\,. \tag{3.28}$$

Importantly, for small spacing between the layers ($\kappa d \ll 1$), the *symmetric* mode dispersion [positive sign in Eq. (3.28)] coincides with the dispersion of a single plasmon (3.21), where conductivity is double that of a single graphene layer. It means that for the fundamental symmetric mode, adding two graphene layers effectively doubles the conductivity of graphene.

For $N \geq 3$, transfer matrix is $\hat{M} = \hat{G}(\hat{P}\hat{G})^{N-1}$. Using the Tchebychev identity, the dispersion relation for the N-layer waveguide can be analytically simplified, namely,

$$t_{21}U_{N-2}(a)g_{12} + \left[t_{22}U_{N-2}(a) - U_{N-3}(a)\right]g_{22} = 0\,, \tag{3.29}$$

where t_{ij}, g_{ij} are the elements of the matrices $\hat{T}$ and $\hat{G}$, $U_k(a)$ are the Tchebychev polynomials with the argument $a = (t_{11} + t_{22})/2$. We look for the case of closely spaced layers, and linearize Eq. (3.29) with respect to the small parameter κd to obtain

$$1 + \frac{2\pi i\kappa N\sigma(\omega)}{\omega\varepsilon} + (N-1)\kappa d = 0, \tag{3.30}$$

where the third term can be omitted due to smallness of κd. This leads us to the equation for the surface plasmon dispersion (3.21), where the single graphene conductivity is replaced by N times larger conductivity, $N\sigma(\omega)$. Figure 3.7 shows the dispersion of the eigenmodes of the multilayer graphene waveguide for different parameters. We can see that for the fundamental mode in the low frequency region, where $\kappa d \ll 1$, the dispersion of the mode is well described by the dispersion of the plasmon localized at the graphene layer with permittivity $N\sigma$ (these dispersions are shown with blue dashed lines). The wavenumbers of such plasmons are significantly smaller, than those of the single layer, and therefore they should have longer propagation distances, being easier to excite.

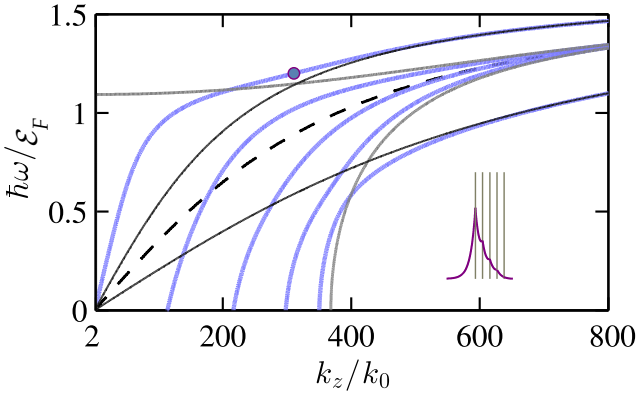

Figure 3.8: Dispersion of the asymmetric multilayer graphene waveguide, $\varepsilon_1 = 1$, $\varepsilon_2 = 10$, $\varepsilon = 4$, $d = 8$ nm. Gray solid lines show the boundaries of the allowed band for the localized propagating solutions inside the graphene slab. The dispersion branches that cross the boundary of the allowed band correspond to the surface Tamm states. Inset shows the profile of the electric field $|E_z|$ for the Tamm state for the parameters depicted with the point at the dispersion branch at $\hbar\omega = 1.2\mathcal{E}_F$.

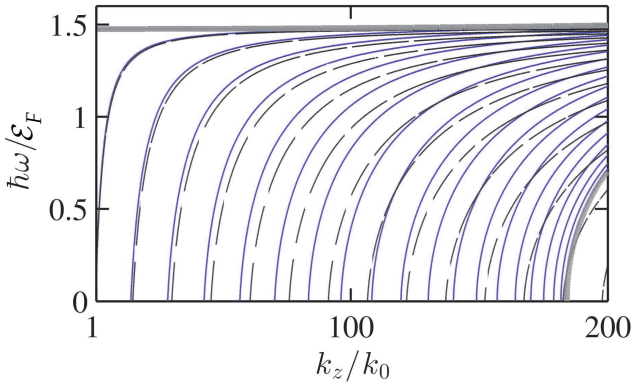

Figure 3.9: Comparison between the dispersion curves of the eigenmodes obtained from the exact solution (solid lines) and by means of the effective model (dashed lines), for $N = 20$, $d = 8$ nm, $\varepsilon_1 = \varepsilon_2 = \varepsilon = 1$.

If we now consider the asymmetric waveguide, $\varepsilon_1 \neq \varepsilon_2$, we observe the emergence of the surface electromagnetic states, with the dispersion lying outside the allowed band region as shown in figure 3.8. As was mentioned above, this leads to a finite imaginary part of the Bloch wavevector and localization of the mode at one of the interfaces of the structure, as shown in the inset of Fig. 3.8.

Comparison with the effective hyperbolic medium model

Now we compare the obtained eigenmode dispersion with the results provided by the effective medium model. Within this model, the multilayer structure is described as an uniform hyperbolic medium with dielectric permittivity tensor components defined as [196]: $\varepsilon_{yy} = \varepsilon_{zz} = \varepsilon + 4i\pi\sigma(\omega)/(ck_0d)$, $\varepsilon_{xx} = \varepsilon$. General dispersion equation for the hyperbolic waveguide can be written in the form:

$$\cos(k_xD)(k_x\kappa_1\varepsilon_2\varepsilon_{zz} + k_x\varepsilon_{zz}\varepsilon_1\kappa_2) + \sin(k_xD)(\varepsilon_{zz}^2\kappa_1\kappa_2 - k_x^2\varepsilon_1\varepsilon_2) = 0, \tag{3.31}$$

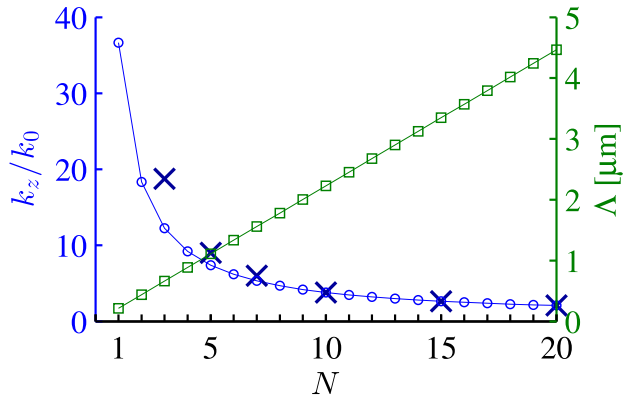

Figure 3.10: Dependence of the normalized wavenumber of the fundamental guided mode k_z/k_0 (circles) and the effective width of the mode Λ (squares) on the number of layers in the structure, solid curves are guides for eye. The parameters are $d = 8$ nm, $\varepsilon_1 = \varepsilon_2 = \varepsilon = 1$, $\hbar\omega/\mathcal{E}_F = 0.5$, $\mathcal{E}_F = 0.1$ eV. Crosses show the result of the effective medium model.

where $k_x = [\varepsilon_{zz}k_0^2 - k_z^2(\varepsilon_{zz}/\varepsilon_{xx})]^{1/2}$ and $D = (N-1)d$. Figure 3.9 shows the comparison between the effective model and the exact solution obtained by the transfer matrix method. We notice a good agreement between the two approaches in the limit $k_x d \ll \pi$.

We would like to emphasize that, by varying the number of layers in the multilayer graphene waveguide, we can effectively control the wavenumber of the fundamental guided mode. When the wavenumber of the mode grows, it becomes harder to excite the mode optically from the vacuum. Moreover, another important property of the waveguide is the effective mode width Λ which is a sum of the actual waveguide thickness and double the localization length of the waveguide mode outside the waveguide, $\Lambda = (N-1)d + 2/\kappa$.

Figure 3.10 shows the dependence of the values k_z/k_0 and Λ on the number of layers. As was mentioned above, at the chosen frequency the normalized wavenumber of the wave decreases as $1/N$, so that we can easier excite the mode by increasing the number of layers. Accordingly, the effective waveguide thickness grows linearly with the number of layers. We can also observe, that as we increase the number of layers, the mode dispersion is better described within the effective media model (shown with the crosses).

Summary

We have studied the dispersion properties of the plasmonic modes guided by multilayer graphene structures. We have revealed that the localization of the fundamental mode can be substantially controlled by varying the number of layers in the graphene structure, which can serve as an additional parameter for optimizing designs in graphene-based nanophotonics. We have demonstrated that by using multilayer graphene structures one can control efficiently the degree of localization of plasmon modes, as well as their group and phase velocities.

3.3 Dissipative plasmon-solitons in multilayer graphene

In the context of potential optical and plasmonic applications, graphene can be incorporated into various photonic structures, including many waveguiding components. It can be placed on top of a variety of substrates, both dielectrics and metals, or it can be even suspended. However, the coupling of electromagnetic energy to graphene in such integrated systems is extremely difficult because of a large wavenumber mismatch. In order to decrease the wavenumber of the waves guided by graphene, one can employ *multilayer graphene*, a structure consisting of a few graphene monolayers with small enough separations between the layers [201], whose effective conductivity increases and the wavenumber of the surface plasmons substantially decreases with the number of layers. The corresponding wavenumber reduction is accompanied by a weaker mode localization, which is important for inter-component coupling.

In this Section we consider the generation of surface plasmons in the presence of a plane wave incident from a high-refractive-index dielectric material at the angle larger than the angle of the total internal reflection, see Fig. 2.1(a). Surface plasmons are supported by a graphene multilayer being coupled to the incident plane wave via an evanescent field. We demonstrate that in such a geometry the plane wave can act as an external driving source for the plasmon excitations, or as a pump that compensates the propagation losses. The plane wave can resonantly excite surface plasmons and, in the nonlinear case, dissipative plasmon-solitons. We extend the previous results for the soliton formation in a lossless monolayer presented in Ref. [184] to the non-conservative case when the self-localized waves are *dissipative solitons*, in which not only nonlinearity has to compensate diffraction,

but also gain has to compensate loss. For such solitons no analytical expression can be found, and the soliton profiles have to be calculated numerically.

As suggested in Refs [201, 202], for the multilayer graphene the conductivity of the N-layer structure is N times larger than that of the monolayer graphene. The validity of this assumption depends on the interlayer hopping and a type of stacking [203]. However, as was established experimentally, epitaxial non-Bernal stacked multilayer graphene exhibits optical properties similar to those of a single layer [204], and these properties are defined by Dirac-like electrons. Furthermore, as was shown in Section 3.2, the dispersion relation for the lowest order electromagnetic mode guided by N closely spaced graphene layers approaches at low frequencies the dispersion of a monolayer graphene, for which one assumes the conductivity N times larger than that of graphene.

The thickness of a stack of graphene layers that we consider here is much smaller than both the plasmon wavelength and transverse confinement of a surface plasmon. This condition is satisfied even for the number of layers up to 20 with the separations between layers of several nanometers. As a result, a stack of layers can be treated as a conductive sheet described by the Dirac δ-function, similar as in the case of graphene monolayer [205]. Thus, the electrodynamic formalism for both mono- and multi-layer structures is the same, and in what follows we derive equations applicable to both types of the structures.

Derivation of the governing equation

We consider a planar geometry shown in Fig. 3.11, with a conductive sheet placed at $x = -d/2$. The sheet is surrounded by a dielectric material with permittivity ε. In the numerical examples below, without loss of generality, we assume that $\varepsilon = 1$. A high-dielectric-index material with dielectric constant ε_h occupies the half-space $x > d/2$. A plane electromagnetic wave is incident on the interface between high and low dielectric index materials. We suppose that the plane wave is incident at the angle greater than the angle of the total internal reflection, and with the tangential component of the wavevector close to the plasmon wavenumber. As a result, the surface plasmon wavenumber β_1 normalized to ω/c, satisfies the condition $\sqrt{\varepsilon_h} > \beta_1 > \sqrt{\varepsilon}$. The distance between the dielectric halfspace and graphene d is large enough so that its coupling to the plane wave is exponentially weak, and we use this assumption in the asymptotic model developed below.

We start our derivation from the Maxwell's equations written in the form

$$\begin{cases} \nabla \times \mathbf{E} = ik_0 \mathbf{H}\,, \\ \nabla \times \mathbf{H} = -ik_0 \varepsilon_2(x)\mathbf{E} + \dfrac{4\pi}{c}\delta(x + d/2)\hat{\sigma}\mathbf{E}_\tau\,. \end{cases} \tag{3.32}$$

Here, $\mathbf{E}\cdot e^{-i\omega t}$ and $\mathbf{H}\cdot e^{-i\omega t}$ are the electric and magnetic fields, respectively, $k_0 = \omega/c$ is the wavenumber in free space, ω is the angular frequency, c is the speed of light, $\hat{\sigma} = N\hat{\sigma_1}$ is an equivalent surface conductivity of the N-layer graphene, with each layer characterized by a surface conductivity $\hat{\sigma_1} = \sigma_{\text{intra}} + \sigma^{\text{NL}}|E_\tau|^2 \equiv i\sigma^{(I)} + \sigma^{(R)} + \sigma^{\text{NL}}|E_\tau|^2$, where σ^{NL} is the nonlinear conductivity (see Appendix A), subscript τ refers to the field component tangential to the interface, and distribution of the dielectric permittivity is described by a step function

$$\varepsilon_2(x) = \begin{cases} \varepsilon\,, & x < d/2, \\ \varepsilon_h\,, & x > d/2. \end{cases} \tag{3.33}$$

We use the so-called split-field method, and represent the electric and magnetic fields as a

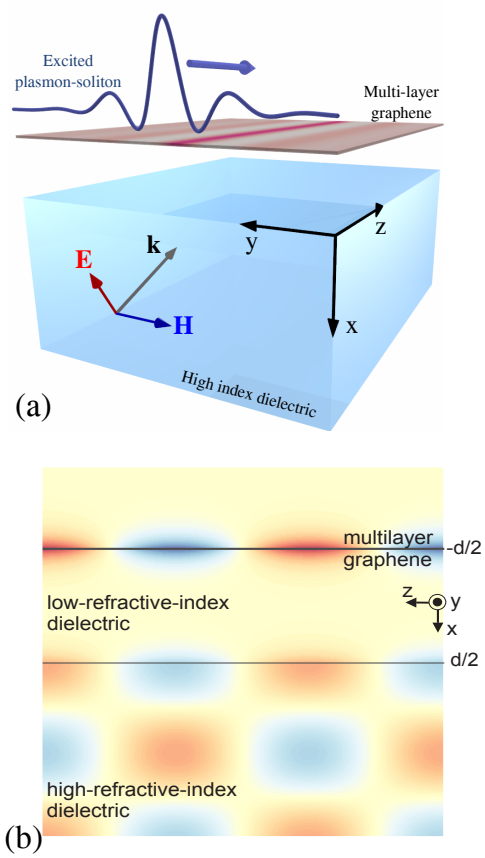

Figure 3.11: (a) Schematic of the problem. (b) Side view of the structure overlapped with profile of the z-component of the electric field. Wave incident from the right bottom corner is reflected from the interface, and forms an interference pattern for $x > d/2$. Due to evanescent coupling it excites surface plasmon wave guided by the graphene structure at $x = -d/2$.

superposition $\mathbf{E} = \mathbf{E}_1 + \mathbf{E}_2$, $\mathbf{H} = \mathbf{H}_1 + \mathbf{H}_2$ satisfying the following set of equations:

$$\begin{aligned}
&\nabla \times \mathbf{E}_{1,2} = ik_0 \mathbf{H}_{1,2}\,, \\
&\nabla \times \mathbf{H}_1 = -ik_0 \varepsilon_1(x)\mathbf{E}_1 + \frac{4\pi}{c}\delta(x + d/2)\hat{\sigma}(\mathbf{E}_{1\tau} + \mathbf{E}_{2\tau})\,, \\
&\nabla \times \mathbf{H}_2 = -ik_0 \varepsilon_2(x)\mathbf{E}_2 - ik_0(\varepsilon_2(x) - \varepsilon_1(x))\mathbf{E}_1\,,
\end{aligned} \tag{3.34}$$

where $\varepsilon_1(x) = \varepsilon$ is constant. For large spacing d the fields with index "1" describe surface plasmon polaritons supported by graphene layer, while the fields with index "2" describe wave scattering by the interface between ε and ε_h.

Following the approach employed earlier in Refs. [129,131], we assume that dissipation is low, the nonlinear part of conductivity is much smaller than the linear part, waves are localized in the y direction, with localization width Λ such that diffraction remains weak ($k_0\beta_1\Lambda \gg 1$). We introduce the small parameter

$$\mu^2 = \max\left\{\left|\frac{\sigma^{(R)}}{\sigma^{(I)}}\right|,\ \left|\frac{\sigma^{NL}|E_\tau|^2}{\sigma^{(I)}}\right|,\ (k_0\beta_1\Lambda)^{-2},\ e^{-2\kappa d}\right\}\,, \tag{3.35}$$

where $\kappa = k_0\sqrt{\beta_1^2 - \varepsilon}$, so that the radiative losses of the plasmon are small and proportional

to $e^{-2\kappa d}$. Equations (3.34) can now be rewritten as

$$\begin{cases} \nabla \times \mathbf{E}_{1,2} = ik_0 \mathbf{H}_{1,2}\,, \\ \nabla \times \mathbf{H}_1 = -ik_0 \varepsilon_1(x)\mathbf{E}_1 + \frac{4\pi}{c}\delta(x+d/2) i\sigma^{(I)}\mathbf{E}_{1\tau} + \mathcal{F}_1\,, \\ \nabla \times \mathbf{H}_2 = -ik_0 \varepsilon_2(x)\mathbf{E}_2 + \mathcal{F}_2\,, \end{cases} \tag{3.36}$$

where the interaction terms

$$\begin{aligned} \mathcal{F}_1 &= \frac{4\pi}{c}\delta(x+d/2)\left\{\left[\sigma^{(R)} + \sigma^{\mathrm{NL}}|E_{1\tau}|^2\right]\mathbf{E}_{1\tau} + i\sigma^{(I)}\mathbf{E}_{2\tau}\right\}, \\ \mathcal{F}_2 &= -ik_0\left[\varepsilon_2(x) - \varepsilon_1(x)\right]\mathbf{E}_1, \end{aligned} \tag{3.37}$$

are small perturbations such that $\mathcal{F}_1 \sim \mu^2$ and $\mathcal{F}_2 \sim \mu$. As discussed above, by setting $\mathcal{F}_1 = 0$ we obtain the equation for the surface plasmons on a graphene layer, whose profile $h_1(x)$ is then written as

$$h_1(x) = ik_0\left(\frac{\varepsilon}{\kappa}\right)e^{-\kappa|x+d/2|}\begin{cases} 1, & x > -d/2\,, \\ -1, & x < -d/2\,, \end{cases} \tag{3.38}$$

and the dispersion relation for the plasmon is found from the boundary conditions,

$$\frac{2\varepsilon}{\kappa} = \frac{4\pi}{\omega}\sigma^{(I)}\,. \tag{3.39}$$

Now we employ the perturbation theory and represent the magnetic field in the form $\mathbf{H}_1 = \{H_{1\,y}, H_{1\,z}\}$

$$\begin{aligned} H_{1\,y} &= \left[\mathcal{A}_1(z,y)h_1(x) + H_1^{(2)}(z,y,x)\right]e^{ik_0\beta_1 z}\,, \\ H_{1\,z} &= H_1^{(1)}(z,y,x)e^{ik_0\beta_1 z}\,, \end{aligned} \tag{3.40}$$

where $H_{1\,y,z}^{(1,2)} \sim \mu^{1,2}$, $\dfrac{\partial \mathcal{A}_1}{\partial y} \sim \mu$. These assumptions lead to $\dfrac{\partial \mathcal{A}_1}{\partial z} \sim \mu^2$, since the complex plasmon amplitude changes along z axis due to dissipation, diffraction and radiative effects, which are considered small. Substituting Eq. (3.40) into Eq. (3.34), in the first order of μ we obtain an equation for the field $\mathbf{H}_2 = H_2^{(1)}\mathbf{y}_0$ in the form

$$\begin{aligned} &\frac{d^2 H_2^{(1)}}{dx^2} + k_0^2(\varepsilon_2(x) - \beta_1^2)H_2^{(1)} + ik_0(\varepsilon_h - \varepsilon)\delta(x-d/2)E_{2z}^{(1)} = F_2\,, \\ &F_2 = k_0^2\left[\varepsilon_2(x) - \varepsilon_1(x)\right]\mathcal{A}_1 h_1(x) + ik_0(\varepsilon - \varepsilon_h)\delta(x-d/2)\mathcal{A}_1 e^{-\kappa d}\,. \end{aligned} \tag{3.41}$$

The plane wave incident from the semi-space $x > d/2$ is written as $H_0 e^{-ik_2(x-d/2)+ik_0\beta_2 z}$, where we assume $k_2 \equiv k_0\sqrt{\varepsilon_h - \beta_2^2} \approx k_h \equiv k_0\sqrt{\varepsilon_h - \beta_1^2}$ (i.e. $|\beta_1 - \beta_2|/\beta_{1,2} \sim \mu^2$), and $H_0 \sim \mu$. The wave experiences the total internal reflection from the interface $x = d/2$. Taking into account the boundary conditions of continuity of the tangential components of the magnetic and electric fields, $\mathbf{H} = \mathbf{H}_1 + \mathbf{H}_2$, $E_z = E_{1\,z} + E_{2\,z}$ at $x = d/2$, we find the amplitude of the electric field at the interface in the following form

$$E_{2z}^{(1)}(d/2) = \frac{\varepsilon k_h - i\varepsilon_h\kappa}{\varepsilon k_h + i\varepsilon_h\kappa}\mathcal{A}_1 e^{-\kappa d} - \frac{\kappa}{ik_0\varepsilon}\frac{2H_0}{1 + i\varepsilon_h\kappa/k_h\varepsilon}\,. \tag{3.42}$$

Finally, we return to the second equation of Eqs. (3.34) and in the second order of μ

obtain an equation for the correction $H_1^{(2)}$:

$$\begin{aligned}
&\frac{d^2H_1^{(2)}}{dx^2} - \kappa^2 H_1^{(2)} - \frac{4\pi}{c} i\sigma^{(I)}\dot{\delta}(x+d/2)E_{1z}^{(2)} = F_1\,,\\
&F_1 = -\left(2ik_0\beta_1\frac{\partial\mathcal{A}_1}{\partial z} + \frac{\partial^2\mathcal{A}_1}{\partial y^2}\right)h_1(x) + \frac{4\pi}{c}\dot{\delta}(x+d/2)\cdot\\
&\left(\left[\sigma^{(R)} + \sigma^{\mathrm{NL}}|\mathcal{A}_1|^2\right]\mathcal{A}_1 + i\sigma^{(I)}E_{2z}^{(1)}(d/2)e^{-\kappa d}\right)\,,
\end{aligned} \tag{3.43}$$

where $\dot{\delta}$ is the derivative of the delta function. According to the Fredholm theorem of alternative [185], the solution of Eq. (3.43) is non-divergent provided that the eigenmodes of its homogeneous part are orthogonal to the right-hand-side of the equation, and this condition can be mathematically written as $\int_{-\infty}^{+\infty} F_1(x)h_1^*(x)dx = 0$. Applying this theorem to Eq. (3.43), we obtain the equation for the envelope of the surface plasmon polariton in the form

$$2ik_0\beta_1\left(\frac{\partial\mathcal{A}_1}{\partial z} + (\gamma+\gamma_r)\mathcal{A}_1 + i\Delta_r\mathcal{A}_1\right) + \frac{\partial^2\mathcal{A}_1}{\partial y^2} + g|\mathcal{A}_1|^2\mathcal{A}_1 = QH_0e^{i\Delta z}\,, \tag{3.44}$$

where linear detuning Δ, linear damping due to losses in graphene γ, damping due to radiation into the high index medium γ_r, radiative detuning Δ_r, nonlinear detuning coefficient g, coupling coefficient Q are derived as

$$\begin{aligned}
g &= \frac{4\pi}{c}\sigma^{\mathrm{NL}}\frac{ik_0\varepsilon}{q}\,,\quad \gamma = \frac{2\pi}{c\beta_1}\sigma^{(R)}\frac{\varepsilon}{q}\,,\\
Q &= \frac{4\pi}{c}i\sigma^{(I)}\frac{\kappa}{q}\frac{2e^{-\kappa d}}{1+i\frac{\varepsilon_h\kappa}{k_h\varepsilon}}\,,\quad \Delta = k_0(\beta_2-\beta_1)\,,\\
R &\equiv \gamma_r + i\Delta_r = \frac{2\pi}{c\beta_1}i\sigma^{(I)}\frac{\varepsilon}{q}\frac{\varepsilon k_h - i\varepsilon_h\kappa}{\varepsilon k_h + i\varepsilon_h\kappa}e^{-2\kappa d}\,,\\
q &\equiv \int_{-\infty}^{+\infty} h_1(x)h_1^*(x)dx = k_0^2\frac{\varepsilon^2}{\kappa^3}\,.
\end{aligned} \tag{3.45}$$

The right-hand side of Eq. (3.44) contains an external force, which in our further simulations is homogeneous due to plane wave excitation. To simplify our further analysis, we introduce new variables

$$\begin{aligned}
\xi &= (\gamma_r+\gamma)z\,,\quad \eta = \sqrt{2k_0\beta_1(\gamma_r+\gamma)}y\,,\quad \Theta = \frac{\Delta_r+\Delta}{\gamma_r+\gamma}\,,\\
u &= \frac{P_1}{|\mathcal{A}_1|^2}\sqrt{\frac{2k_0\beta_1(\gamma_r+\gamma)}{g}}\mathcal{A}_1e^{-i\Delta z}\,,\\
P_1 &= \int_{-\infty}^{+\infty}\frac{c}{8\pi}\left[\mathbf{E}_1\mathbf{H}_1^*\right]_z dx = \frac{c}{8\pi k_0}\frac{\beta_1\epsilon}{(\beta_1^2-\epsilon)^{3/2}}|\mathcal{A}_1|^2 + O(\mu^2)\,,\\
iu_I &= Q\sqrt{\frac{g}{(2k_0\beta_1(\gamma_r+\gamma))^3}}H_0
\end{aligned} \tag{3.46}$$

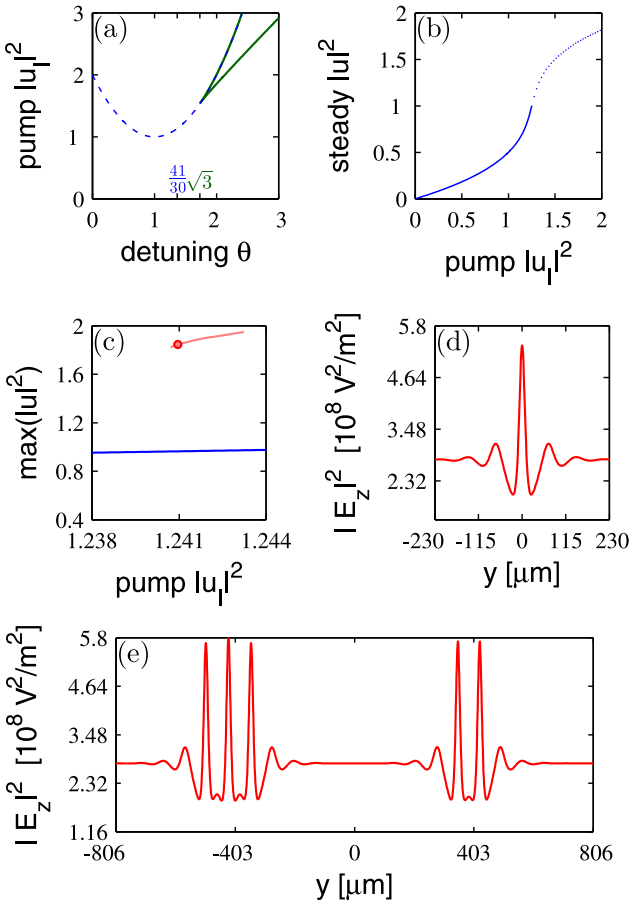

Figure 3.12: (a) The plane of parameters of pump intensity and detuning. Two green curves show the boundary of the bistable region: inside the curves there are three equilibrium states, on the lines there are two equilibria, and one equilibrium exists outside this region. The homogeneous excitation becomes modulationally unstable above the dashed line, which is defined by $|u|^2 = 1$. (b) Intensity of the excited plasmon as a function of pump intensity for $\Theta = 1.5$. The dotted curve indicates modulationally unstable part of the dependence. (c) Single peak soliton properties: upper and lower curves show peak soliton intensity and steady background, respectively, $\Theta = 1.5$. (d) Transverse profile of a soliton calculated for the parameters corresponding to the dot in the Fig. 2.3 (c). (e) Transverse profile of plasmon-solitons containing two and three peaks.

and obtain the dimensionless form of Eq. (3.44)

$$\frac{\partial u}{\partial \xi} = u_I - (1 + i\Theta - i|u|^2)u + i\frac{\partial^2 u}{\partial \eta^2}\,. \tag{3.47}$$

This is the Lugiato-Lefever equation [206], studied in a number of previous works. In particular, bifurcation analysis is available in Ref. [173] and references therein.

Discussion

Here, we only briefly focus on some of the features of equation [206], which are important for the effects related to our plasmon-soliton excitation. For the steady state homogeneous solutions of Eq. (3.47), we obtain a cubic equation. This equation has only one solution when $\Theta < \sqrt{3}$, and three solutions otherwise, indicating the presence of bistability, see

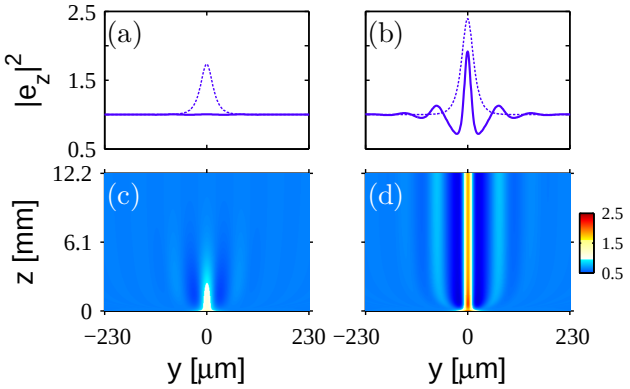

Figure 3.13: Evolution of the spatial profile of the localized plasmon excited at $z = 0$. Initial profiles [dashed lines in (a,b)] are of the same widths but of different amplitudes. (a,c) Diffraction and damping of the initial excitation and (b,d) soliton formation. Shown is the intensity normalized to the homogeneous steady state background. In panels (a) and (b) dashed and solid lines correspond to the initial and final intensity distributions, respectively.

Fig. 3.12(a). The latter domain of parameters comprises several bifurcations that, in particular, may result in *breathing solitons* and even *chaos* [207, 208]. If $\Theta < \sqrt{3}$, the only bifurcation that occurs leads to the Turing patterns [206]. At the critical value of detuning $\Theta = 41/30$, the character of this bifurcation changes from supercritical to subcritical. In subcritical regime, the stationary solutions have the form of localized dissipative structures (usually called *cavity solitons*) and their bound states sitting on the background of a homogeneous steady state solution [209]. Considering the case when the latter is a single-valued function of the pump, in Figs 3.12(c,d) we show the dependence of the soliton amplitude on the pump intensity and also the soliton profile. This soliton has a single main intensity peak falling away into oscillating tails. Such one-peak solutions exist in a certain range of pump powers. The soliton is calculated for the following parameters $\varepsilon = 1$, $\varepsilon_h = 11.56$, the Fermi energy $\mathcal{E}_F = 0.2$ eV, $\hbar\omega = 0.25\mathcal{E}_F$ ($\lambda = 2\pi/k_0 \approx 25$ μm), $\beta_1 = 3.03$, the relaxation time $\tau_{\text{intra}} = 1$ ps, the number of graphene layers $N = 6$, linear detuning $\beta_2 - \beta_1 = 0.09$, and $d = 3$ μm. For this structure and considered wave intensities, the smallness parameter $\mu \sim 0.1$ and our approximate approach is well justified. To put the spatial scales in some context, the ratios of the plasmon wavelength to soliton width, to free space wavelength and to the Fermi wavelength are 0.08, 0.33 and 400, respectively.

We would like to note that if the relaxation time is decreased to 0.1ps, what is observed in most of the available graphene samples, then in order to balance the increased dissipative losses it is necessary to increase the electric field amplitude in the incident wave as well as radiative losses, roughly, by a factor of 10. This will lead to the decrease of the soliton width by $\sqrt{10}$. However, though the formation of dissipative structures is expected even in this case, the developed asymptotic description is not strictly applicable.

The Lugiato-Lefever equation (3.47) is characterised by a snaking bifurcation diagram for cavity solitons [173,209], and that is why the patterned multi-peak solutions can coexist on a stable uniform pedestal. These solutions are frequently regarded as controllable bits for all-optical memory applications [173]. Noticeably, the plethora of possible steady states can be interpreted as the parts of subcritical Turing patterns with a number of elements defined by initial conditions. Such multi-peak structures with finite even or odd numbers of peaks [see two and three-peak steady solutions in Fig. 3.12(e)] are sometimes called soliton molecules or soliton clusters, emphasizing their spatial localization. Importantly,

because of the subcritical nature, a bright soliton can not be switched on by arbitrarily small perturbations of the background field (intensity) and hence low-energetic excitations will decay, as illustrated in Figs 3.13(a,c), while Figs 3.13(b,d) display the dynamic formation of a soliton from a narrow perturbation of a higher amplitude.

Summary

We have derived novel nonlinear equations describing the excitation of dissipative TM-polarized plasmon solitons in graphene. We have employed the multilayer graphene structure in order to increase the wavelength of the plasmon-polaritons to be excited in the Otto configuration for the attenuated total internal reflection. We have obtained the Lugiato-Lefever type nonlinear equation and predicted the existence of single- and multi-peak dissipative solitons in such graphene structures.

3.4 Electromagnetic Tamm states in truncated graphene metamaterials

An interface separating two different layered media or photonic crystals can support electromagnetic surface waves, and these waves are often called "electromagnetic Tamm states" in analogy to the electronic Tamm states predicted to exist at an interface of crystalline solid state materials [210]. The electromagnetic Tamm states have been studied in different structures, including the waves localized at an interface separating homogeneous and periodic dielectric media [211], an interface between two photonic crystals [212], and an interface between a photonic crystal and a left-handed metamaterial [213].

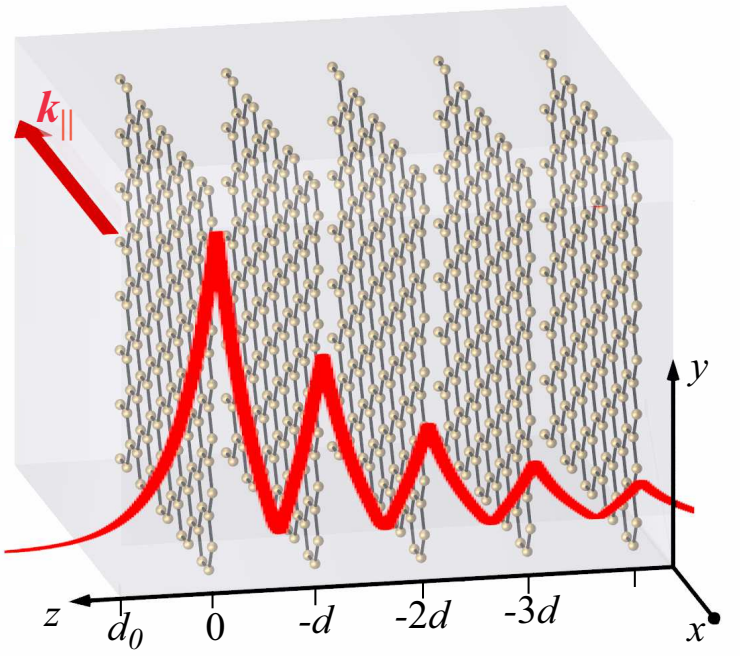

Figure 3.14: Geometry of the problem: a truncated multilayer structure composed of graphene sheets separated by dielectric layers with permittivity ε and thickness d. A thin dielectric layer of the thickness d_0 is a cap layer. The external dielectric has permittivity ε'. The red curve shows an example of a profile of the surface mode (shown for the tangential electric field component).

Conventional electromagnetic Tamm states, which can exist at an interface separating two photonic crystals or a photonic crystal and a homogeneous dielectric, are known to possess a parabolic dispersion. In contrast, the surface modes existing at an interface between two metal-dielectric periodic structures [214] are characterized by the dispersion resembling that of surface plasmon polaritons. It was shown that these modes can have the negative group velocity as well as subwavelength localization.

In this Section we study the properties of the electromagnetic Tamm states localized at the surface of a multilayer graphene structure, or a *terminated graphene metamaterial*. As was shown [196,197,215–217], the graphene metamaterials exhibit many properties of conventional metal-dielectric multilayer structures, but at lower frequencies. These properties include the existence of the near-field Bloch waves [218] as well as a hyperbolic dispersion. Graphene multilayer structures have two significant differences which can potentially be useful for future optoelectronic devices. First, the period of the graphene multilayer structures can be as small as several nanometers [219], that is about an order of magnitude smaller than that of metal-dielectric structures. Second, due to smaller carrier densities in graphene as compared to metals, the plasma frequency of graphene and all plasmonic features, such as the plasmonic Bloch waves, appear in far-infrared to THz frequency ranges. This frequency range is extremely important for biomedical and security applications [220].

Model and impedance conditions for surface waves

We consider a truncated multilayer graphene structure and study the electromagnetic waves localized near its surface, as shown schematically in Fig. 3.19. We assume that the first dielectric layer of this multilayer structure has the thickness d_0, which in a general case may differ from the period of the structure d. As we show below, this allows us to achieve tunability of the dispersion properties of the Tamm modes by varying the parameter d_0. While the graphene metamaterials support both TM and TE polarized surface plasmons, here we consider only the TM polarized modes, because the coupling of the weakly localized TE plasmons does not produce the near-field Bloch waves [196].

The dispersion equation for surface waves is derived from the matching surface impedances at the interface of the multilayer structure and the uniform medium. The impedance is defined as a ratio of the tangential components of the electric and magnetic fields, $\tilde{Z} = E_\parallel / H_\parallel$. As follows from Maxwell's equations, the impedance of the uniform dielectric medium Z' is given by

$$Z' = -i \left(\frac{q'}{k_0 \varepsilon'} \right), \tag{3.48}$$

where $q' = \left(k_\parallel^2 - \varepsilon' k_0^2 \right)^{1/2}$, $k_\parallel$ is the propagation constant, $k_0 = \omega / c$ is the wavenumber in a free space. For a periodic structure, the surface impedance can be found by means of the transfer-matrix method and by applying the Bloch theorem

$$\begin{pmatrix} E_\parallel(d) \\ H_\parallel(d) \end{pmatrix} = \exp(iKd) \begin{pmatrix} E_\parallel(0) \\ H_\parallel(0) \end{pmatrix} = \hat{T} \begin{pmatrix} E_\parallel(0) \\ H_\parallel(0) \end{pmatrix}, \tag{3.49}$$

where K is the Bloch wavenumber. The dispersion relation for the Bloch wavenumber can be written as

$$\cos Kd = \cosh qd + 2\pi i \left(\frac{q}{k_0 \varepsilon} \frac{\sigma}{c} \right) \sinh qd \,. \tag{3.50}$$

The transfer matrix $\hat{T}$ relates the tangential components of the electric and magnetic fields at $z = 0, d, 2d...$, and it has the elements given by the expressions

$$\begin{aligned}
T_{11} &= \cosh qd + \frac{2\pi i\sigma}{c}\frac{q}{k_0\varepsilon}\left[\sinh qd + \sinh q(d-2d_0)\right], \\
T_{12} &= \frac{-iq}{k_0\varepsilon}\left(\sinh qd + \frac{2\pi i\sigma}{c}\frac{q}{k_0\varepsilon}[\cosh qd - \cosh q(d-2d_0)]\right), \\
T_{21} &= \frac{ik_0\varepsilon}{q}\left(\sinh qd + \frac{2\pi i\sigma}{c}\frac{q}{k_0\varepsilon}[\cosh qd + \cosh q(d-2d_0)]\right), \\
T_{22} &= \cosh qd + \frac{2\pi i\sigma}{c}\frac{q}{k_0\varepsilon}\left[\sinh qd - \sinh q(d-2d_0)\right],
\end{aligned}$$

where $q = \left(k_\parallel^2 - \varepsilon k_0^2\right)^{1/2} \equiv -ik_z$ is the transverse wavenumber in dielectric layers, and σ is the frequency-dependent graphene conductivity which was derived in a number of papers by using different assumptions [70, 186, 187]. In our calculations, neglecting losses and assuming $\hbar\omega < 1.67\mathcal{E}_F$ ($\mathrm{Im}\,\sigma > 0$),for doped graphene $k_BT \ll \mathcal{E}_F$, we again use the result of Ref. [70] simplified to the form (3.19). As a result, the impedance Z for the graphene metamaterial can be expressed through the matrix elements, and at the surface of the periodic structure (at $z = 0$) can be written as

$$Z = \frac{T_{12}}{e^{iKd} - T_{11}} = \frac{e^{iKd} - T_{22}}{T_{21}}. \tag{3.51}$$

Once both the impedances of the homogeneous dielectric and periodic structure are found, the dispersion relation $Z = Z'$ can be written implicitly, and can be solved numerically in order to find the mode wavenumber $k_{||}$.

Dispersion and field profiles of surface modes

First, we consider the case when a cap dielectric layer is absent, $d_0 = 0$, and the dispersion equation can be written as

$$1 + 4\pi i\frac{\sigma}{c}\frac{q'}{k_0\varepsilon'} = \frac{q'\varepsilon}{q\varepsilon'}\frac{[e^{iKd} - \cosh(qd)]}{\sinh(qd)}. \tag{3.52}$$

In the limit $d \longrightarrow \infty$ or for large wavenumbers, Eq. (3.52) reduces to the dispersion of the p-polarized plasmons at the graphene layer sandwiched between two different dielectric media:

$$\frac{k_0\varepsilon'}{q'} + \frac{k_0\varepsilon}{q} + i\frac{4\pi\sigma}{c} = 0. \tag{3.53}$$

In Fig. 3.15 we show the dispersion curves of the surface waves obtained from Eq. (3.52) with solid lines for two permittivities of the external dielectric - larger and smaller than the permittivity of the dielectric infilling the separations between graphene layers in the periodic structure. The respective asymptotic solutions of Eq. (3.53) are plotted with thin dashed lines. The large-wavenumber asymptote of the shaded area (band) corresponds to the plasmon mode localized at the graphene layer surrounded by dielectric layers with permittivity ε. Noticeably, if $\varepsilon' < \varepsilon$, the localized mode's dispersion is blue-shifted with respect to the band whereas in the opposite case, ($\varepsilon' > \varepsilon$), this branch is red-shifted.

With increasing the period of the structure, coupling between individual surface plasmons at the graphene layers decreases, and the band shrinks gradually to a single curve

corresponding to the dispersion of an individual surface plasmon polariton. This allows the existence of the surface states in the lower frequency region.

When the thickness of the dielectric cap layer with positive dielectric permittivity is finite, the surface wave is localized at the graphene sheet closest to the interface of the structure. As shown in Fig. 3.15, increasing d_0 from zero gradually makes the dispersion curve of the surface wave approach the band of the periodic structure.

Now we consider the situation of a negative frequency-dependent $\varepsilon'(\omega)$ described by the Drude model $\varepsilon'(\omega) = 1 - \omega_p^2/\omega^2$. Such a substrate with plasma frequency ω_p in the THz range can be made of a doped semiconductor. In this case, for all values of d_0 the large-wavenumber asymptote for the localized waves is the dispersion of the surface plasmon at the interface of two media with ε and $\varepsilon'(\omega)$ which has the asymptotic value of $\omega = \omega_p/\sqrt{\varepsilon+1}$. When $qd \ll 1$ but $q, q' \approx k_\parallel \gg 1$, the mode wavevenumber can be approximated by the following expression

$$|k_\parallel d| \approx \frac{2(1+\alpha)[(1+\alpha)^{-1/2} - \varepsilon/|\varepsilon'|]}{1 - 2\alpha(1 - d_0/d)}, \tag{3.54}$$

where $\alpha = 4\pi \mathrm{Im}\sigma/ck_0\varepsilon d$,. In the particular case $d_0 = d$ the dispersion equation is simplified to the form

$$\left(\frac{q\varepsilon'}{q'\varepsilon}\right)\frac{\sinh(qd)}{e^{iKd} - \cosh(qd)} = 1. \tag{3.55}$$

The dispersion of surface waves for two different values of ω_p is presented in Fig. 3.16. Again if $|\varepsilon'(\omega)| < \varepsilon$, the surface mode branch is blue-shifted with respect to the band and red-shifted in the opposite case, $|\varepsilon'(\omega)| > \varepsilon$.

In Fig. 3.16 we observe the negative slope for the blue-shifted surface wave in a certain frequency range. As we show in Fig. 3.17 this corresponds to the negative group velocity, i.e. the wave becomes essentially a backward wave. At the same time, for the lower

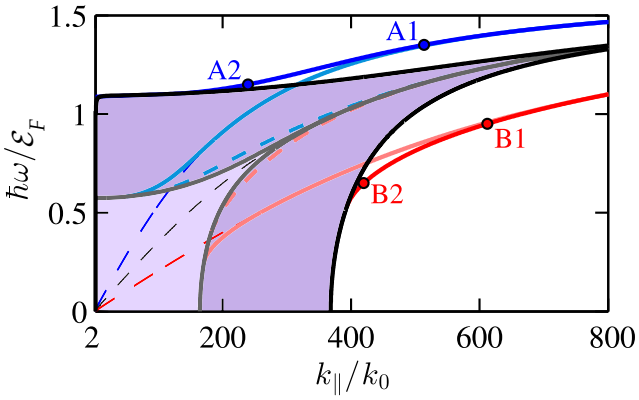

Figure 3.15: Dispersion of surface waves in the case of positive ε', and $\varepsilon = 4$. Bright and light purple areas show the bands of the periodic structures with periods $d = 8$ nm and $d = 40$ nm, respectively. Red and blue lines correspond to the dielectic constant of the cap layer $\varepsilon' = 1$ and $\varepsilon' = 10$, respectively. Thin black dashed line shows the dispersion of the single graphene sheet with dielectric permittivity ε on both sides. Thin red and blue dashed lines show the dispersions of single graphene sheet given by Eq. (3.53). Light thick solid and dashed lines correspond to $d = 40$nm, $d_0 = 0$ (solid) and $d_0 = 0.2d$ (dashed). Bright thick solid lines correspond to $d = 8$nm, $d_0 = 0$. Points A1, A2 and B1, B2 correspond to the parameters for which the mode profiles are presented in Figs. 3.18(a,b) below.

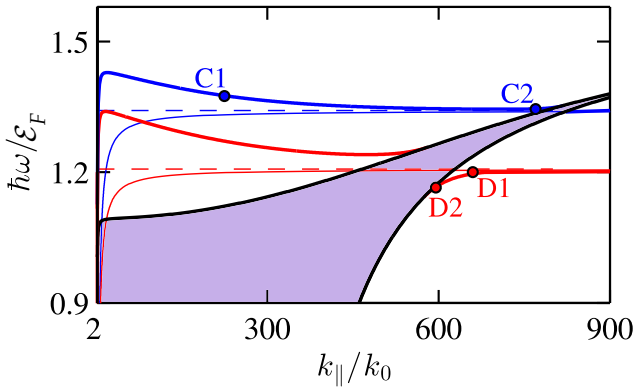

Figure 3.16: Dispersion of the surface waves in the case of negative frequency-dependent $\varepsilon'(\omega)$. Parameters of the periodic structure are $\varepsilon = 4$ and $d = 8$ nm. Shaded area is the band. Red and blue thick lines depict the dispersion of surface waves for $\hbar\omega_p = 2.7\mathcal{E}_F$ and $\hbar\omega_p = 3\mathcal{E}_F$, respectively. The asymptotes $\omega = \omega_p/\sqrt{\varepsilon+1}$ are shown by dashed lines. Thin solid lines are dispersion curves of conventional plasmons supported by the interface of $\varepsilon'(\omega)$ and ε. Points C1, C2 and D1, D2 were taken for the profile calculation in Figs. 3.18(c,d) below.

frequencies, where $|\varepsilon'(\omega)| > \varepsilon$, the group velocity is always positive and the surface wave is forward.

It should be noted that in real structures, where the losses in the graphene layers and semiconductor substrate play a significant role, the stronger localized modes corresponding to larger wavenumbers decay faster due to the stronger localization at the interfaces. Thus, for structures with smaller periods there will be an interplay between stronger localization and at the same time stronger damping.

If we look on the transverse field profile, then two different types of the surface states can be naturally distinguished — those lying in the proximity of the transmission band and those that are far from it. Far from the transmission band (points A1, B1 in Fig. 3.15 and C1, D1 in Fig. 3.16), the character of the propagating waves is similar to that of plasmonic modes [see Figs. 3.18(a,c)] that means their strong localization — the field almost completely vanishes on two periods of the structure. In essence, only the boundary influences the propagating surface wave and the extension of the periodic multilayer graphene

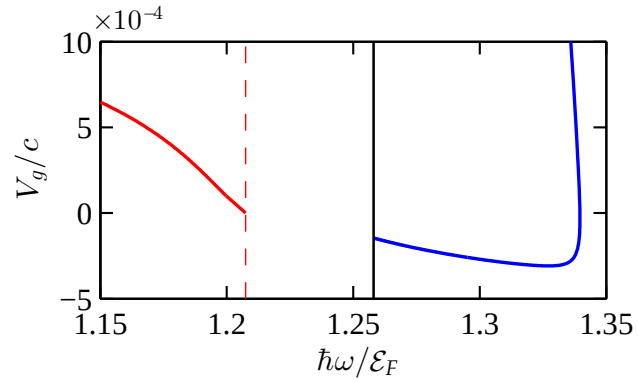

Figure 3.17: Group velocity of the surface waves when the plasma frequency of the adjoined semiconductor is $\hbar\omega_p = 2.7\mathcal{E}_F$. Red dashed and black solid lines mark asymptotic frequency $\omega = \omega_p/\sqrt{\varepsilon+1}$ and the boundary of the band, respectively.

structure has a little impact. By contrast, closer to the transmission bands (points A2, B2 in Fig. 3.15 and C2, D2 in Fig. 3.16), the coupling is stronger, and the field penetrates deeper into in the periodic multilayer graphene structure [see Figs. 3.18(b,d)].

It is also important to mention the effect of losses in graphene on the dispersion properties of the studied surface Tamm states. There are several mechanisms responsible for damping of THz plasmons in graphene [57, 221], and they include electron scattering, interband absorption and coupling to optical phonons. While the latter two mechanisms can be suppressed by choosing the frequencies below the graphene chemical potential and optical phonon frequencies (about 0.2 eV), the finite electron free propagation time will cause damping of the surface states and limit the minimal available localization lengths. While for the case of a single graphene sheet the figure of merit (which is a ratio of the real and imaginary parts of the in-plane wavevector) is a function of the ratio $\mathrm{Re}\sigma/\mathrm{Im}\sigma$ and frequency, in our case it should also depend on the period of the structure and the thickness of the cap layer. We expect that losses will affect stronger the states with larger wavenumbers, while the waves with smaller wavenumbers will qualitatively have the same dispersion properties.

Summary

We have studied the electromagnetic surface waves existing at the surface of a truncated graphene multilayer structure, the graphene metamaterial. We have shown that the disper-

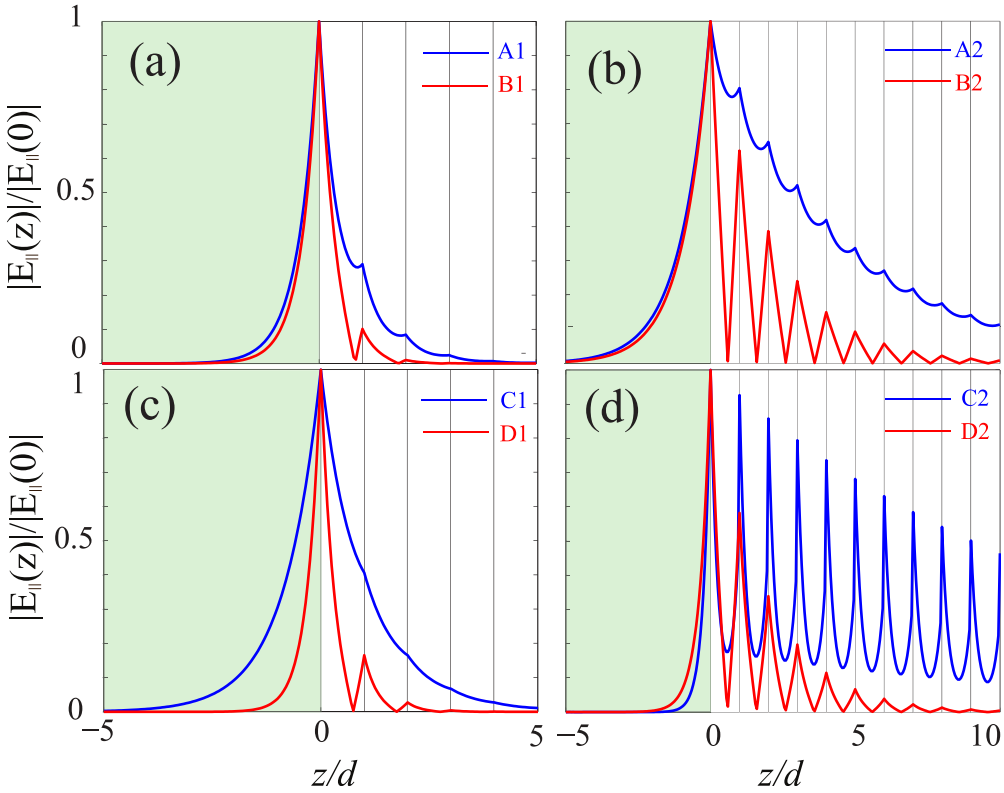

Figure 3.18: Field profiles for the Tamm states corresponding to the points marked in Figs. 3.15 and 3.16. Shown is the normalized tangential component of the electric field. (a),(c) Plasmonic-like surface waves strongly localized in the vicinity of the boundary; (b),(d) Surface waves decaying slowly inside the graphene metamaterial. Branching from the bottom of the transmission band, modes B1, B2, D1, D2 are staggered.

sion properties of these modes can be tuned by varying thickness of the cap dielectric layer, and this type of modes can acquire the negative group velocity.

3.5 Nonlinear modes in graphene metamaterials

Discrete solitons appear as intrinsic localized modes in homogeneous periodic physical systems, such as nonlinear atomic chains [222, 223], Bose-Einstein condensates loaded into optical lattices [224, 225], arrays of nonlinear optical waveguides [226] and semiconductor-dielectric periodic nanostructures [227]. If compared to continuous localized waves, the discrete solitons possess a number of additional properties such as the Peierls-Nabarro barrier [228] and staggering transformation [229]. In plasmonics, discrete solitons were studied in metal-dielectric multilayer structures [181, 230–233], arrays of nanowires [182, 234–236], and arrays of nanoparticles [146–148, 237] described in Chapter 2.

Less than a decade ago, an interesting type of discrete solitons, *surface solitons*, was predicted theoretically [238] and then observed experimentally [239,240]. It is sustained by the boundary between a periodic structure and an uniform medium (although the maximum of soliton can be either exactly at the interface [238] or at some distance from it [241]), i.e. a surface soliton can be considered as a nonlinear analogue of surface Tamm states [242,243].

In this Section we study nonlinear graphene-based multilayer structures and demonstrate that, similar to metal-dielectric metamaterials, they can be described by the discrete nonlinear Schrödinger (NLS) equation and support nonlinear localized modes in the form of discrete solitons, see Fig. 3.19(a). We also analyze such modes near the surfaces and predict the existence of nonlinear surface modes being a nonlinear analogue of surface Tamm states, as shown schematically in Fig. 3.19(b).

Discrete solitons

We consider a periodic multilayer graphene stack, consisting of an infinite number of parallel graphene layers placed parallel to the plane xy and arranged at equal distances d from each other at the planes $z = md$, $m = (-\infty, \infty)$, inside a dielectric medium with relative permittivity ε. For definiteness, the electric field is supposed to be directed along the x axis, i.e. $\mathbf{E} = [E(t), 0, 0]$, and in the calculations below the temporal dependence of $E(t)$ is considered to be of the form $E(t) = E_0 \exp(-i\omega t) + (c.c.)$, where E_0 and ω are the amplitude and the frequency. In this case, the electric $\mathbf{E}$ and magnetic $\mathbf{H}$ fields are governed by Maxwell's equations:

$$\nabla \times \mathbf{E} = \frac{i\omega}{c}\mathbf{H}, \qquad \nabla \cdot \mathbf{E} = \frac{4\pi\rho}{\varepsilon},$$
$$\nabla \times \mathbf{H} = -\frac{i\omega}{c}\varepsilon\mathbf{E} + \frac{4\pi}{c}\mathbf{J}, \qquad \nabla \cdot \mathbf{H} = 0,$$

where c is the speed of light, and $\mathbf{J}$, ρ are full three-dimensional (3D) current and charge densities, respectively, given by

$$\mathbf{J} = \sum_{m=-\infty}^{\infty} \mathbf{J}^{(m)}\delta(z - md), \qquad \rho = \sum_{m=-\infty}^{\infty} \varrho^{(m)}\delta(z - md), \tag{3.56}$$

where $\mathbf{J}^{(m)}$ and $\varrho^{(m)}$ are 2D current and charge densities in the m-th graphene layer. In all above equations the time-dependence $\exp(-i\omega t)$ is implied.

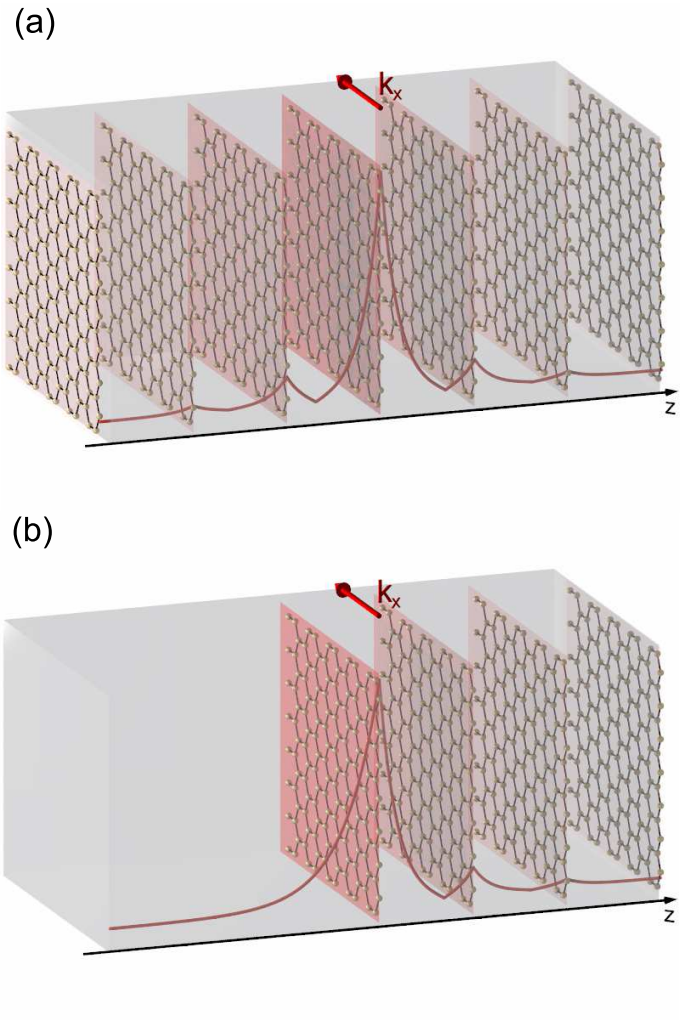

Figure 3.19: Geometry of the problem: a multilayer structure is composed of graphene sheets separated by dielectric layers with permittivity ε and thickness d. Red curves show example profiles of the plasmonic solitons: (a) a discrete soliton in an infinite structure, and (b) surface soliton in a truncated metamaterial. Shown is the absolute value of the tangential electric field component.

The electric and magnetic fields can be expressed through scalar φ and vector $\mathbf{A}$ potentials as

$$\mathbf{E} = -\nabla\varphi + \frac{i\omega}{c}\mathbf{A}, \qquad \mathbf{H} = \nabla \times \mathbf{A}. \tag{3.57}$$

These relations, jointly with the Lorentz gauge

$$\nabla \cdot \mathbf{A} - (i\omega\varepsilon/c)\varphi = 0, \tag{3.58}$$

result in inhomogeneous Helmholtz equations for both scalar and vector potentials

$$\Delta\varphi + \frac{\omega^2\varepsilon}{c^2}\varphi = -\frac{4\pi\rho}{\varepsilon}, \tag{3.59}$$

$$\Delta\mathbf{A} + \frac{\omega^2\varepsilon}{c^2}\mathbf{A} = -\frac{4\pi}{c}\mathbf{J}. \tag{3.60}$$

We assume the electromagnetic field uniform along the y direction, $\partial/\partial y \equiv 0$, and propagating in the x direction, $\mathbf{A}$, $\mathbf{J}$, ρ, $\varphi \sim \exp(ik_x x)$. Under these assumptions, Eq. (3.60) can

be solved by using a standard Green function formalism. Accordingly, a general solution of Eq. (3.60) has the form

$$A_x(z) = -\mu_0 \int_{-\infty}^{\infty} dz' G\left(z - z'\right) J_x, \tag{3.61}$$

where

$$G(z) = -\frac{2\pi \exp\left(-p\,|z|\right)}{cp}, \quad p = \sqrt{k_x^2 - \frac{\omega^2 \varepsilon}{c^2}}$$

is the one-dimensional (1D) Green function. The latter is a solution of the equation

$$\left(\frac{d^2}{dz^2} - p^2\right) G(z) = \frac{4\pi}{c}\delta(z)$$

with the boundary conditions $G(\pm\infty) = 0$, denoting the evanescent character of waves (when $k_x^2 > (\omega/c)^2 \varepsilon$ and $\mathrm{Re}(p) > 0$), or absence of waves coming from $z = \pm\infty$ for traveling waves, when $k_x^2 < (\omega/c)^2 \varepsilon$ and $\mathrm{Im}(p) < 0$. Substituting Eq. (3.56) into Eq. (3.61) and using the properties of Delta-functions, we obtain:

$$A_x(z) = \frac{2\pi}{cp} \sum_{m=-\infty}^{\infty} j_x^{(m)} \exp(-p\,|z - md|).$$

Due to the 2D nature of currents in graphene layers $A_z \equiv 0$, while the vector potential components A_x and A_y describe p- and s-polarized waves, correspondingly. Further we will concentrate on the p-polarized waves only. Thus, using the Lorentz gauge (3.58), we can express the x-component of the electric field through A_x as

$$E_x(z) = \frac{cp^2}{i\omega\varepsilon} A_x(z). \tag{3.62}$$

After substituting this relation into the expression for the induced nonlinear current density at ω, $j_x = i[\nu^{(1)} - \nu^{(3)}|E_0|^2]E_0 \exp(-i\omega t)$, where $\nu^{(1)} \equiv -i\sigma(\omega)$ and $\nu^{(3)} \equiv i\sigma^{\mathrm{NL}}(\omega)$ (see Appendix A for details), A_x can be represented in the form

$$A_x(z) = \frac{2\pi p}{\omega\varepsilon} \sum_{m=-\infty}^{\infty} \left[\nu^{(1)} - \nu^{(3)} \frac{c^2 p^4}{\omega^2 \varepsilon^2} |A_x(md)|^2\right] A_x(md) \exp(-p\,|z - md|). \tag{3.63}$$

Alternatively, Eq. (3.63) can be rewritten in the form of the stationary discrete nonlinear Schrödinger equation

$$\begin{aligned} &A_x([n+1]\,d) + A_x([n-1]\,d) - 2A_x(nd)\cosh(pd) = \\ &-\frac{4\pi p}{\omega\varepsilon}\left[\nu^{(1)} - \nu^{(3)} \frac{c^2 p^4}{\omega^2 \varepsilon^2} |A_x(nd)|^2\right] A_x(nd) \sinh(pd) \end{aligned} \tag{3.64}$$

for $n \in (-\infty, \infty)$.

The linear counterpart (when $\nu^{(3)} = 0$) of the discrete nonlinear Schrödinger equation (3.64) defines the linear spectrum. Domains of allowed frequencies (where in the linear case the wave propagation is possible) are parametrized by the real Bloch wavevector q [such that $A_x(nd) = A_x(0)\exp(iqnd)$]. As a result, the equation

$$\cos(qd) = \cosh(pd) - \frac{2\pi p}{\omega\varepsilon}\nu^{(1)} \sinh(pd) \tag{3.65}$$

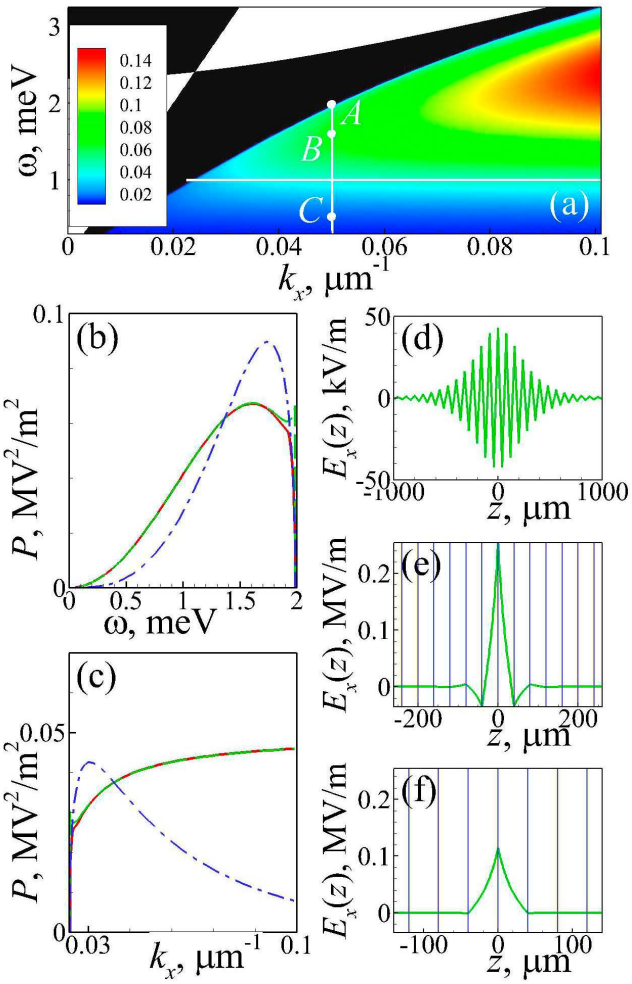

Figure 3.20: (a)–(c) Dependence of soliton norm P (in MV^2/m^2) upon frequency ω and wavevector k_x [panel (a)], or upon frequency ω for fixed value $k_x = 0.05\,\mu\text{m}^{-1}$[panel (b)], or upon frequency k_x for fixed value $\omega = 1\,\text{meV}$ [panel (c)]. Dependencies in panels (b) and (c) are taken along the vertical and horizontal lines in panel (a), respectively. Dependencies in panel (a) as well as those in panels (b) and (c) [depicted by solid lines] are calculated by numerical solution of Eq. (3.64), while continuum (dash-and-dot lines) and anti-continuum (dashed lines) limit approximations in panels (b) and (c) are calculated according to Eqs. (3.68) and (3.5); (d)–(f) Soliton spatial profiles for $k_x = 0.05\,\mu\text{m}^{-1}$ and $\omega = 1.98\,\text{meV}$ [panel (d)], $\omega = 1.6\,\text{meV}$ [panel (e)], or $\omega = 0.52\,\text{meV}$ [panel (f)]. The parameters of panels (d), (e) and (f) correspond to points A, B and C in panel (a), respectively. Other parameters are $E_F = 0.157\,\text{eV}$, $d = 40\,\mu\text{m}$, $\varepsilon = 3.9$.

determines the propagating bands of the spectrum $\omega = \Omega_l(k_x, q)$ ($l \geq 1$ is the number of band), which are depicted in Figs. 3.20(a) and 3.21(a) in black (see, e.g., Ref. [244]).

Although generally the nonlinear Eq. (3.64) possesses an infinite number of solutions [229], here we concentrate on the properties of the fundamental bright solitons, bifurcating from the edge of the allowed band of the spectrum. To describe the solitons properties, we introduce a soliton norm as

$$P = \sum_{m=-\infty}^{\infty} |E_x(md)|^2 = \frac{c^2 p^4}{\omega^2 \varepsilon^2} \sum_{m=-\infty}^{\infty} |A_x(md)|^2 .$$

The fundamental mode of discrete soliton is depicted in Fig. 3.20. Due to effectively defo-

cusing nonlinearity [245] (positive cubic term) in Eq. (3.64), bright solitons [see Fig. 3.20(a)] bifurcate from the low-frequency boundary of the first band $\Omega_1(k_x, q)$ (which corresponds to the phase shift $qd = \pi$ between oscillations in adjacent graphene layers) and exist in the semi-infinite gap $\omega \leq \Omega_1(k_x, \pi/d)$. Since in this region $k_x > \omega\varepsilon^{1/2}/c$, this type of solitons is characterized by the evanescent waves in the dielectric between the graphene layers, and these solitons will be further referred to as *plasmonic solitons*. For fixed k_x [Fig. 3.20(b)] the soliton norm P, being zero at the band edge $\omega = \Omega_1(k_x, \pi/d)$, initially grows up to values $\sim 10^{11}\,\mathrm{V}^2/\mathrm{m}^2$, but after that decreases and attains zero at zero frequency. At the same time, the frequency defines the degree of soliton localization, as follows from the comparison of Figs. 3.20(d)–3.20(f). Thus, in the vicinity of the band edge $\Omega_1(k_x, q)$ the soliton is delocalized – its electric field is distributed over a large number of graphene layers [Fig. 3.20(d)]. When frequency is gradually detuned from the band edge, the soliton becomes more localized – its electric field is either distributed over a few graphene layers [Fig. 3.20(e)], or effectively concentrated in the vicinity of one graphene layer, as shown in Fig. 3.20(f). It should be underlined that the soliton inherits the properties of a Bloch wave at the band edge from which it bifurcates: signs of the electric field tangential components at adjacent graphene layers are opposite (staggered soliton). For fixed frequency ω [Fig. 3.20(c)] the soliton norm increases monotonically with increasing k_x.

Equation (3.64) possesses two approximate types of solutions. The first type, so-called *continuum limit*, is valid for low amplitude solutions. To obtain this solution, we use the ansatz $A_x(nd) = \epsilon(-1)^n \psi(\zeta)$ with ϵ being a small parameter, and $\zeta = \epsilon n$. As a result, function $\psi(\zeta)$ satisfies the nonlinear Schrodinger equation

$$\frac{d^2\psi}{dx^2} + \nu^{(3)} \frac{4\pi c^2 p^5}{\omega^3 \varepsilon^3} \sinh(pd)\, \psi^3(x) = \frac{2\cosh(\beta) - 2}{\epsilon^2} \psi(x), \tag{3.66}$$

which is parameterized by parameter β such that

$$\cosh(\beta) = \frac{2\pi p}{\omega\varepsilon} \nu^{(1)} \sinh(pd) - \cosh(pd). \tag{3.67}$$

The parameter β can be formally considered as the imaginary part of the Bloch wavevector $q = (\pi + i\beta)/d$ (note, inside the gap the Bloch wavevector is complex that in the linear case corresponds to the evanescent wave). Using the exact solution of Eq. (3.66), we now approximate the solution of Eq. (3.64) in the continuum limit

$$A_x(nd) = \sqrt{\frac{\omega^3\varepsilon^3}{2\pi c^2 p^5 \nu^{(3)} \sinh(pd)}} \frac{(-1)^n \sqrt{2\cosh(\beta) - 2}}{\cosh\left(\sqrt{2\cosh(\beta) - 2}\, n\right)}.$$

Consequently, the soliton norm in the continuum limit can be expressed as

$$P = \frac{\omega\varepsilon\,[2\cosh(\beta) - 2]}{2\pi p \nu^{(3)} \sinh(pd)} \sum_{n=-\infty}^{\infty} \frac{1}{\cosh^2\left(\sqrt{2\cosh(\beta) - 2}\, n\right)} \approx \frac{2\,\omega\varepsilon\sqrt{2\cosh(\beta) - 2}}{\pi p \nu^{(3)} \sinh(pd)}. \tag{3.68}$$

In the last equation the summation has been replaced by the integration. As seen from Fig. 3.20, the continuum approximation (depicted by blue dash-and-dot line) is valid in the narrow domain in the vicinity of band edge $\Omega_1(k_x, \pi/d)$ [more specifically, in domains 1.95 meV$\lesssim \omega \lesssim$1.987 meV in Fig. 3.20(b) and $0.0236\,\mu\mathrm{m}^{-1} \lesssim k_x \lesssim 0.0245\,\mu\mathrm{m}^{-1}$ in Fig. 3.20(c)].

The other type of approximate solutions, so-called *anti-continuum limit*, is valid far from the band edge $\Omega_1(k_x, \pi/d)$ (deeply in the gap). Hence, introducing scaled dimensionless

variables

$$a_n = \left(\nu^{(3)} \frac{2\pi c^2 p^5}{\omega^3 \varepsilon^3} \frac{\sinh(pd)}{2\cosh(\beta)} \right)^{1/2} A_x(nd),$$

and taking into account Eq.(3.67), we obtain

$$\frac{a_{n+1} + a_{n-1}}{2\cosh(\beta)} + a_n - a_n^3 = 0.$$

As a result, when $\beta \to \infty$, a_n become independent and acquire one of the three values: $a_n = -1$, $a_n = 0$, or $a_n = +1$. In this limit, the fundamental mode [see, e.g., Fig. 3.20(e)] corresponds to the case, where $a_n = \delta_{n,0}$. This case allows for the approximate analytical continuation valid for large values of β:

$$a_0 = 1 - \frac{1}{4\cosh^2(\beta)},$$
$$a_1 = a_{-1} = -\frac{1}{2\cosh(\beta)} - \frac{1}{8\cosh^3(\beta)},$$
$$a_2 = a_{-2} = \frac{1}{4\cosh^2(\beta)}.$$

As a result, the soliton norm can be represented in the form

$$P = \frac{\omega\varepsilon}{2\pi p \nu^{(3)}} \frac{\cosh(\beta)}{\sinh(pd)} \left[a_0^2 + 2a_1^2 + 2a_2^2 \right] = \frac{\omega\varepsilon}{4\pi p \nu^{(3)}} \frac{1}{\sinh(pd)} \left[2\cosh(\beta) + \frac{7}{8\cosh^3(\beta)} \right].$$

As seen from Fig. 3.20, anti-continuum limit approximation (depicted by green dashed line) well describes the solution in the domains $0 \lesssim \omega \lesssim 1.95$ meV in Fig. 3.20(b) and $k_x \gtrsim 0.0245\,\mu\mathrm{m}^{-1}$ in Fig. 3.20(c).

Solitons can also exist in the upper (finite) gaps of the spectrum. Notice that in those gaps $k_x < \omega\varepsilon^{1/2}/c$, and solitons are characterized by propagating waves in the dielectric between graphene layers (this type of solitons will be further referred to as *photonic solitons*). An example of photonic solitons is shown in Fig. 3.21. Photonic solitons are characterized by considerably larger soliton norms P if compared to the plasmonic ones [soliton norm is of order of $500\,\mathrm{MV}^2/\mathrm{m}^2$ in Fig. 3.21(a) and $0.1\,\mathrm{MV}^2/\mathrm{m}^2$ in Fig. 3.20(a)]. Photonic solitons bifurcate from the upper edge of the gap – the soliton norm, being zero at the high-frequency boundary of the gap $\Omega_3(k_x, \pi/d)$, is increased, when the frequency is decreased [see Fig. 3.21(b)]. The decrease of the frequency also leads to the growth of the soliton amplitude [compare Figs. 3.21(c,d,e)]. At the same time, photonic solitons are considerably wider than plasmonic ones, and at large amplitudes they become two-hump [Figs. 3.21(d) and 3.21(e)]. This happens due to the fact that, by contrast to plasmonic solitons, for photonic solitons local maxima and minima of the electromagnetic field are generally not located at graphene layers.

Discrete surface solitons

Finally, we consider a semi-infinite array of graphene layers, arranged at equal distances d from each other at planes $z = md$, $m = [0, \infty)$, as shown in Fig. 3.19(b). In other words, graphene layers are embedded inside a semi-infinite dielectric medium at $z \geq 0$, while at $z < 0$ there is just a homogeneous dielectric. The 3D current and charge density for this

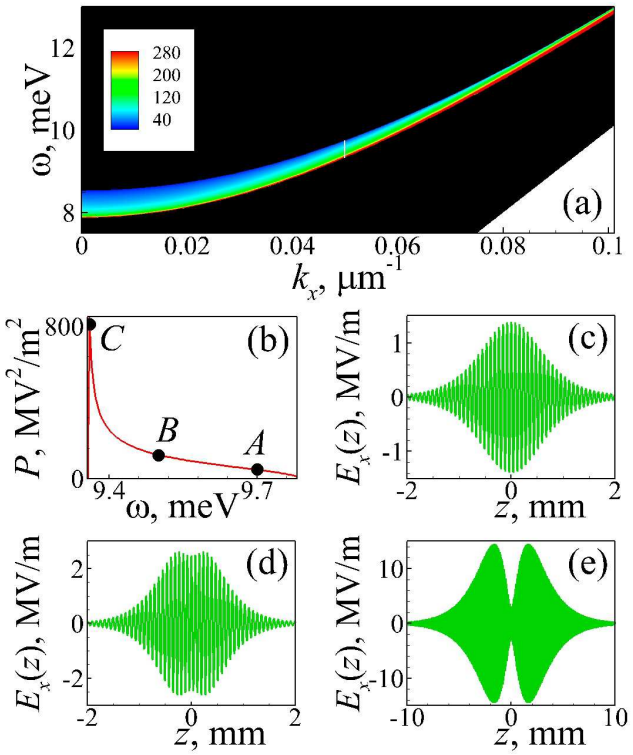

Figure 3.21: Dependence of soliton norm P (in MV^2/m^2) upon frequency ω (in the second gap) and wavevector k_x [panel (a)], or upon frequency ω for fixed value $k_x = 0.05\,\mu\text{m}^{-1}$[panel (b)]. Dependence in panel (b) is taken along the vertical lines in panel (a); (c)–(e) Soliton spatial profiles for $k_x = 0.05\,\mu\text{m}^{-1}$ and $\omega = 9.7\,\text{meV}$ [panel (c)], $\omega = 9.5\,\text{meV}$ [panel (d)], or $\omega = 9.36\,\text{meV}$ [panel (e)]. The parameters of panels (c), (d) and (e) correspond to points A, B and C in panel (b), respectively. Other parameters are the same as those in Fig. 3.20.

semi-infinite array can be written as

$$\mathbf{J} = \sum_{m=0}^{\infty} \mathbf{J}^{(m)} \delta(z - md), \qquad \rho = \sum_{m=0}^{\infty} \varrho^{(m)} \delta(z - md), \tag{3.69}$$

and the solution of the wave equation (3.60) has [in full analogy with Eq. (3.63)] the form

$$A_x(z) = \frac{2\pi p}{\omega\varepsilon} \sum_{m=0}^{\infty} \left[\nu^{(1)} - \nu^{(3)} \frac{c^2 p^4}{\omega^2 \varepsilon^2} |A_x(md)|^2 \right] A_x(md) \exp(-p\,|z - md|), \tag{3.70}$$

or

$$\begin{aligned} A_x([n+1]\,d) + A_x([n-1]\,d) - 2A_x(nd)\cosh(pd) = \\ -\frac{4\pi p}{\omega\varepsilon} \left[\nu^{(1)} - \nu^{(3)} \frac{c^2 p^4}{\omega^2 \varepsilon^2} |A_x(nd)|^2 \right] A_x(nd) \sinh(pd), \qquad \text{for } n > 0; \\ A_x(d) - A_x(0)\exp(pd) = -\frac{4\pi p}{\omega\varepsilon} \left[\nu^{(1)} - \nu^{(3)} \frac{c^2 p^4}{\omega^2 \varepsilon^2} |A_x(0)|^2 \right] A_x(0) \sinh(pd). \end{aligned}$$

Properties of plasmonic surface solitons are summarized in Fig. 3.22. The principal difference between the cases of surface and bulk solitons is the nonexistence of the low-amplitude surface soliton in the vicinity of the band edge $\Omega_1(k_x, \pi/d)$ [compare, e.g., Figs. 3.22 (a) and 3.20 (b), as well as Figs. 3.22(b) and 3.20(c)]. More specifically, there exists

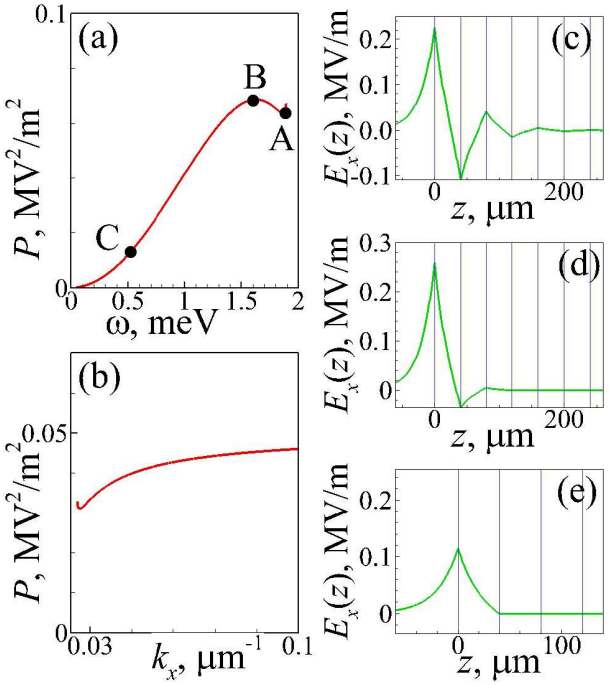

Figure 3.22: Dependence of surface soliton norm P (in $\mathrm{MV}^2/\mathrm{m}^2$) upon frequency ω for fixed value $k_x = 0.05\,\mu\mathrm{m}^{-1}$[panel (a)], or upon frequency k_x for fixed value $\omega = 1\,\mathrm{meV}$ [panel (b)]; (c)–(e) Soliton spatial profiles for $k_x = 0.05\,\mu\mathrm{m}^{-1}$ and $\omega = 1.89\,\mathrm{meV}$ [panel (c)], $\omega = 1.6\,\mathrm{meV}$ [panel (d)], or $\omega = 0.52\,\mathrm{meV}$ [panel (e)]. The parameters of panels (c), (d) and (e) correspond to points A, B and C in panel (a), respectively.

an end-point of the spectrum, at which the fundamental mode bifurcates with the other type of the surface soliton mode, for details see, e.g., Ref. [246]. In the vicinity of the end-point of the spectrum soliton norm P achieves a local minimum. At the same time, from the comparison of Figs. 3.22(c-e) it follows that, similar to the case of bulk solitons, lower frequencies correspond to more localized solitons (when the power is mostly concentrated at the graphene layer, truncating the photonic crystal).

It is also worth noting that the principal difference between linear and nonlinear cases is the possibility to have the nonlinear surface state (namely, surface soliton) in the uniform structure (semi-infinite array of *equally* doped graphene layers, placed at *equal* distances from each other, and embedded into the *uniform* dielectric medium), while in the linear case the existence of surface state is possible only in the nonuniform structure – it is necessary to have either the defect of the periodicity at the surface of photonic crystal [243], the defect of graphene doping at surface, or to truncate the photonic crystal with the dielectric, characterized by the dielectric constant, different from that of the medium inside the photonic crystal.

Summary

We have analyzed nonlinear graphene-based multilayer metamaterials and demonstrated that they can support spatially localized nonlinear modes in the form of discrete plasmon solitons. We have described the properties of this novel class of discrete solitons, including the dependence of their parameters on graphene conductivity. We have also predicted the existence of nonlinear surface modes in the form of discrete surface solitons.

Chapter 4

Frequency conversion with graphene-based structures

This Chapter focuses on *frequency conversion effects* in different settings with graphene that may serve as basic building blocks for graphene-incorporated nonlinear nanodevices. First, we elaborate a peculiar analytical model of a *resonant surface nonlinearity* for the second harmonic generation (SHG) by a graphene-wrapped dielectric spherical nanoparticle. Second, we derive comprehensive models of nonlinear *plasmon-to-plasmon conversion* in graphene-based plasmonic waveguides, taking advantage of the possibility to phase-match the nonlinearly interacting guiding modes by tailoring the modal dispersion. Finally, we propose a complex concept of *nonlinear graphene metasurfaces* employing the controllable interaction between a graphene layer and a planar metamaterial. By performing the first-principles numerical simulations, we prove that such hybrid plasmonic metasurfaces, exhibiting the cascaded Fano resonances, benefit from a high tunability and the subwavelength nature of the graphene plasmons and may be exceptionally promising for tunable absorption and nonlinear harmonic generation.

4.1 Second-harmonic generation by a graphene nanoparticle

Interestingly, graphene is not only employed for planar geometries, and there are also attempts to create graphene-wrapped objects [247–249]. In this regard, recent theoretical studies suggest that by wrapping spherical nanoparticles in graphene it becomes possible, for instance, to achieve tunable cloaking effect [21, 22, 250].

In this Section, we study a nonlinear response of a graphene-wrapped dielectric spherical nanoparticle. We consider a nanoparticle with an outer graphene layer and analyze the second-harmonic generation induced by the nonlinear conductivity of graphene. First, we develop the theoretical model which allows to obtain analytical expressions for the multipole decomposition of the second-harmonic scattered field. We then study second-harmonic radiation patterns in such a structure and explore the possibilities to control the radiation direction by inhomogeneous fields.

Since a graphene layer is many orders of magnitude thinner than the wavelength of electromagnetic waves that we consider, graphene can be treated as a conductive surface described by the Dirac δ-function [205], whose frequency-dependent surface conductivity is given by Eq. (3.12).

We note that, as was discussed in Chapter 3, for a randomly stacked multilayer graphene film consisting of N layers, at low frequencies the equivalent surface conduc-

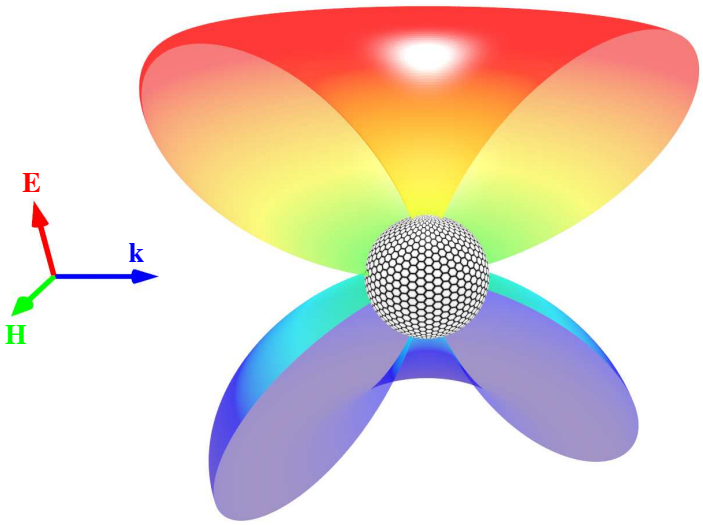

Figure 4.1: Schematic view of the graphene-wrapped nanoparticle illuminated by a plane wave. Surface plot shows predominantly quadrupole *second harmonic* radiation pattern formed in the far field when the fundamental frequency is close to the one-photon dipolar resonance.

tivity is N times larger than that of a monolayer graphene [132, 160, 201–204]. This allows us to engineer the conductivity of graphene-based structures. Importantly, the increase of the effective conductivity with a number of layers leads to a substantial reduction of the wavenumber of the p-polarised plasmons supported by multilayer graphene structures. This provides a mechanism for efficient control of both the plasmon localization and dispersion which is important for real nanophotonic applications [132, 160]. In what follows we develop the theoretical approach which is applicable to both mono- and multi-layer graphene structures.

Model

First, we consider the Rayleigh scattering of a linearly polarized plane monochromatic electromagnetic wave [$\mathbf{E} = E_0\mathbf{z}_0 \exp -(i\omega_0 t - ik_0\sqrt{\varepsilon_h}y)$] on a graphene sphere of radius $a << \lambda_0 = 2\pi/k_0\sqrt{\varepsilon_h}$, $k_0 = \omega_0/c$, see schematics in Fig. 4.1.

The incident wave excites the fundamental frequency harmonics whose electric field is governed by the equation:

$$-\nabla\times\nabla\times\mathbf{E}_\omega + \frac{\omega^2}{c^2}\varepsilon(\mathbf{r})\mathbf{E}_\omega = -\frac{4\pi i\omega}{c^2}(\mathbf{j}^{\mathrm{L}}_\omega + \mathbf{j}^{\mathbb{NL}}_\omega)\delta(r-a)\,, \tag{4.1}$$

where $\mathbf{j}^{\mathrm{L}}_\omega = \sigma(\omega)\mathbf{E}_\tau$ and $\mathbf{j}^{\mathbb{NL}}_\omega$ are the surface densities of the linear and nonlinear currents at the frequency ω, respectively, subscript τ refers to the field component tangential to the surface. Here, we introduced the dielectric permittivity function:

$$\varepsilon(\mathbf{r}) = \begin{cases} \varepsilon_p, & |\mathbf{r}| < a \\ \varepsilon_h, & |\mathbf{r}| > a\,, \end{cases} \tag{4.2}$$

which describes the dielectric permittivity distribution in space. This permittivity describes a dielectric particle located in a homogeneous host medium. In what follows, we assume that the particle is placed in vacuum, i.e. $\varepsilon_h = 1$.

The approach we employ is based on the multipole expansion of the electromagnetic fields [251,252]. For describing nanoparticles this method is mainly associated with the Mie scattering theory and it gives basic understanding of harmonic generation from nanoparticles as it was discussed theoretically e.g. by Dadap et al. [31, 253] for small spheres. In particular, previous studies show that the SHG response of a nanoparticle irradiated by a linearly polarized plane wave is dominated by an electric quadrupole and electric dipole originating from the finite size effect and from retardation effect. Remarkably, the magnetic dipole despite being of the same order as an electric quadrupole is not excited because of symmetry constraints. This will be also relevant in the problem that we consider in this Section. The strength of the excited leading multipoles and their interference determine far-field radiation characteristics, such as a radiation pattern and radiation efficiency.

In what follows we present a self-consistent derivation underlining the important specifics of graphene as a nonlinear material that, in some sense, may be regarded as a very peculiar model of the surface nonlinearity associated with Dirac particles. We would also like to note that though we solve a model problem in the simplest spherical geometry we believe that our findings can be useful in designing more complex shape graphene-based nanoantennas.

Linear scattering

As follows from (4.1), in an approximation that is linear in E_ω, outside and inside the sphere

$$\nabla \cdot \mathbf{D}_\omega = 0\,, \tag{4.3}$$

where $\mathbf{D}_\omega = \varepsilon(\mathbf{r})\mathbf{E}_\omega$ is the electric displacement vector. In the case when the radius a of the particle is small, i.e. $ka << 1$ and $k\sqrt{\varepsilon_p}a << 1$ ($k = \omega/c$) are fulfilled, the solution can be found using a perturbation method with the small parameter $\mathcal{M}(\omega) = ka \equiv a\omega/c << 1$, assuming $\varepsilon_p \sim 1$. The first term in this expansion corresponds to the quasi-static approximation [1,251].

We represent the total field in the structure $\mathbf{E}_{\omega_0}$ as a superposition of the field of the incident wave $\mathbf{z}_0 E_0 e^{ik_0 y}$ and the scattered field $\boldsymbol{\mathcal{E}}_{\omega_0}$:

$$\mathbf{E}_{\omega_0} = \mathbf{z}_0 E_0 e^{ik_0 y} + \boldsymbol{\mathcal{E}}_{\omega_0}\,. \tag{4.4}$$

Next, we represent the scattered field as an asymptotic series with the small parameter $\mathcal{M}_0 = \mathcal{M}(\omega_0)$ in the region $k_0 r \ll 1$ in the form

$$\mathbf{E}_{\omega_0} = E_0\mathbf{z}_0 + \boldsymbol{\mathcal{E}}^{(0)}_{\omega_0} + \left(\boldsymbol{\mathcal{E}}^{(1)}_{\omega_0} + ik_0 y E_0 \mathbf{z}_0\right) + \dots\,, \tag{4.5}$$

where the fields in the brackets are of the order of $\mathcal{M}_0$.

In the zeroth and first orders of smallness in $\mathcal{M}_0$ the scattered fields $\boldsymbol{\mathcal{E}}^{(0)}_{\omega_0}$ and $\boldsymbol{\mathcal{E}}^{(1)}_{\omega_0}$ are potential:

$$\boldsymbol{\mathcal{E}}^{(0,1)}_{\omega_0} = -\nabla\Phi^{(0,1)}_{\omega_0}\,, \tag{4.6}$$

From Eq. (4.3) it follows that the potential functions $\Phi^{(0)}_{\omega_0}$ and $\Phi^{(1)}_{\omega_0}$ both outside and inside the sphere satisfy the Laplace's equation

$$\nabla^2\Phi^{(0,1)}_{\omega_0} = 0 \quad (r < a\,,\, r > a)\,. \tag{4.7}$$

The tangential electric field components, in general, can experience a discontinuity at the

surface of the nanoparticle. This discontinuity is proportional to the the surface gradient of the normal component of the current density. In our case of small energies near the K-point where transitions occur between the $\pi - \pi^*$ bonds, the normal component of the current is negligible. Therefore, the tangential component of the electric field is continuous at the boundary $r = a$, i.e. $\mathbf{E}^{(0)}_{\omega_0} = E_0\mathbf{z}_0 - \nabla\Phi^{(0)}_{\omega_0}$ and $\mathbf{E}^{(1)}_{\omega_0} = ik_0yE_0\mathbf{z}_0 - \nabla\Phi^{(1)}_{\omega_0}$ are continuous, whereas the normal components of the vectors $\mathbf{D}^{(0)}_{\omega_0} = \varepsilon(\mathbf{r})\left(-\nabla\Phi^{(0)}_{\omega_0} + E_0\mathbf{z}_0\right)$ and $\mathbf{D}^{(1)}_{\omega_0} = \varepsilon(\mathbf{r})\left(-\nabla\Phi^{(1)}_{\omega_0} + ik_0yE_0\mathbf{z}_0\right)$ undergo jumps at the surface charges $\rho^{(0,1)}_{\omega_0} = \nabla_s \cdot \mathbf{j}^{\mathrm{L}(0,1)}_{\omega_0}/i\omega_0$, where the operator $\nabla_s\cdot$ stands for the surface divergence. The potentials $\Phi^{(0)}_{\omega_0}$ and $\Phi^{(1)}_{\omega_0}$, which satisfy such boundary conditions and decay away from the particle, are given by

$$\Phi^{(0)}_{\omega_0} = a^3E_0\cos\theta\,\frac{\varepsilon_p - 1 - 2\Theta_1}{\varepsilon_p + 2 - 2\Theta_1}\begin{cases}\dfrac{r}{a^3}, & |\mathbf{r}| < a\\ \dfrac{1}{r^2}, & |\mathbf{r}| > a\end{cases}, \tag{4.8}$$

$$\Phi^{(1)}_{\omega_0} = a^5E_0\sin2\theta\,\sin\varphi\frac{ik_0\left(\varepsilon_p - 1 - 3\Theta_1\right)}{4\left(\varepsilon_p + \dfrac{3}{2} - 3\Theta_1\right)}\begin{cases}\dfrac{r^2}{a^5}, |\mathbf{r}| < a\\ \dfrac{1}{r^3}, |\mathbf{r}| > a\end{cases}, \tag{4.9}$$

where $\Theta_1 = \dfrac{4\pi\sigma_1}{i\omega_0 a}$, $\sigma_1 \equiv \sigma(\omega_0)$, θ is the polar (zenith) angle measured from the z-axis and ϕ is the azimuthal angle measured from the x-axis in a spherical coordinate system with its origin in the center of a nanoparticle.

As seen from (4.8), the scattered field $\boldsymbol{\mathcal{E}}_{\omega_0}$ in the zeroth and first orders of the perturbation theory with respect to the parameter $\mathcal{M}_0$ for $r > a$ is the superposition of the field of a point dipole having the dipole moment

$$\boldsymbol{\mathcal{P}}^{(0)}_{\omega_0} = \mathbf{z}_0E_0a^3\frac{\varepsilon_p - 1 - 2\Theta_1}{\varepsilon_p + 2 - 2\Theta_1}, \tag{4.10}$$

and the field of a quadrupole with the quadrupole moment tensor

$$\hat{Q}^{(1)}_{\omega_0} = Q^{(1)}_{\omega_0}\begin{pmatrix}0 & 0 & 0\\ 0 & 0 & 1\\ 0 & 1 & 0\end{pmatrix} \tag{4.11}$$

with two nonzero components

$$Q_{yz} = Q_{zy} = Q^{(1)}_{\omega_0} = E_0ik_0a^5\frac{\varepsilon_p - 1 - 3\Theta_1}{2\varepsilon_p + 3 - 6\Theta_1}. \tag{4.12}$$

Nonlinear scattering and second-harmonic generation

Because of the graphene nonlinearity, the field $\mathbf{E}_{\omega_0}$ excites higher harmonics, and here we consider only the second harmonic $\mathbf{E}_{2\omega_0}$ generation. To describe nonlinear properties of graphene, we employ the quasi-classical description based on the solution of the Boltzmann equation, applicable at low frequencies, $\hbar\omega \leq \mathcal{E}_F$ [87–90]. (See Appendix A.)

In the case of a plane graphene, in the collisionless limit, the electron distribution func-

tion $f(\mathbf{r},\mathbf{p},t)$ satisfies the kinetic equation written as

$$\frac{\partial f}{\partial t}+\mathbf{v}_\mathbf{p}\frac{\partial f}{\partial \mathbf{r}}+e\left(\mathbf{E}+\frac{1}{c}[\mathbf{v}_\mathbf{p}\times\mathbf{B}]\right)\frac{\partial f}{\partial \mathbf{p}}=0\,,$$

where for Dirac's massless quasi-particles $\mathbf{v}_\mathbf{p}=\dfrac{\partial\mathcal{E}}{\partial\mathbf{p}}=v_F\dfrac{\mathbf{p}}{|\mathbf{p}|}$, the energy $\mathcal{E}=v_Fp$, $v_F\approx c/300$ is the Fermi velocity, and $e=-|e|$ is the charge. Following the perturbation approach [88,91], we solve this equation using iterations. The electric current density at 2ω is given through the second order correction to the Fermi-Dirac distribution function $\mathbf{j}_{2\omega}=4e\sum\limits_{\mathbf{p}}\mathbf{v}_\mathbf{p}f_{2\omega}(\mathbf{p})$.

We look for the distribution function in the form

$$f=f_0(\mathcal{E})+f_\omega e^{-i\omega t}+\text{c.c.}+f_{2\omega}e^{-2i\omega t}+\text{c.c.}+\ldots\,, \tag{4.13}$$

where $f_0(\mathcal{E})$ is the Fermi-Dirac distribution, f_ω and $f_{2\omega}$ are the first and the second order corrections, respectively, whereas the tangential electric field

$$\mathbf{E}_\tau=\mathbf{E}_\omega e^{-i\omega t}+\mathbf{E}_{2\omega}e^{-2i\omega t}\ldots\,. \tag{4.14}$$

Finally, under the assumption $v_F/\omega\ll l_E$, where l_E is a characteristic spatial scale of the field inhomogeneity, we obtain the general expression for the current at the second harmonic

$$\mathbf{j}_{2\omega}=\frac{2e^3i}{\omega^3(2\pi\hbar)^2}\iint d^2\mathbf{p}\,\mathbf{v}_\mathbf{p}\left[\left(\mathbf{E}_\omega\frac{\partial}{\partial\mathbf{p}}\right)\left(\mathbf{v}_\mathbf{p}\frac{\partial}{\partial\mathbf{r}}\right)\times\left(\mathbf{E}_\omega\frac{\partial f_0}{\partial\mathbf{p}}\right)+\frac{1}{2}\left(\mathbf{v}_\mathbf{p}\frac{\partial}{\partial\mathbf{r}}\right)\left(\mathbf{E}_\omega\frac{\partial}{\partial\mathbf{p}}\right)\left(\mathbf{E}_\omega\frac{\partial f_0}{\partial\mathbf{p}}\right)\right]. \tag{4.15}$$

We note in the case of flat graphene and TM-polarized incident wave with the tangential electric field component of the form $\mathbf{E}_\omega=E\mathbf{x}_0e^{iqx}$ (and $v_F/\omega\ll 1/q$) Eq. (4.15) is reduced to

$$\mathbf{j}_{2\omega}=-\mathbf{x}_0\frac{3}{8}\frac{e^3v_F^2}{\pi\hbar^2\omega^3}qE^2\,, \tag{4.16}$$

which is in agreement with the earlier results presented in Ref. [91].

We consider particles which are large enough on the scale of electron motion in graphene (i.e. $v_F/\omega\ll a$ and $v_F\tau_{\text{intra}}\ll a$), then at each point of the surface of the particle, the current can be considered locally flat. As a result, for description of the second harmonic current we can use Eq. (4.15), where $\mathbf{v}_\mathbf{p}$ and $\mathbf{p}$ are vectors tangential to the surface. Then, we find the resulting formula for the second harmonic currents induced on the spherical object in the zeroth order of the small parameter $\mathcal{M}_0$, and it corresponds to the dipole field distribution

$$\mathbf{j}^{(0)}_{2\omega_0}=\boldsymbol{\theta}_0 i\frac{3}{16}\frac{e^3}{\pi\hbar^2\omega_0^3}\frac{v_F^2}{a}E_d^2\sin 2\theta\,. \tag{4.17}$$

In the first order of small parameter $\mathcal{M}_0$ we find

$$\begin{aligned}
&\mathbf{j}^{(1)}_{2\omega_0}=\mathbf{j}^{(1)}_{2\omega_{0\text{I}}}+\mathbf{j}^{(1)}_{2\omega_{0\text{II}}}\,,\\
&\mathbf{j}^{(1)}_{2\omega_{0\text{I}}}=i\frac{e^3}{\pi\hbar^2\omega_0^3}\frac{v_F^2}{a}E_dE_q\left[\boldsymbol{\theta}_0\sin\phi\left(\frac{13}{16}\cos\theta-\frac{9}{16}\cos 3\theta\right)+\boldsymbol{\varphi}_0\frac{1}{4}\cos 2\theta\cos\phi\right]\,,\\
&\mathbf{j}^{(1)}_{2\omega_{0\text{II}}}=i\frac{e^3v_F^2}{\pi\hbar^2\omega_0^3}E_d\left(\frac{-ik_0E_0}{8}\right)\left[\boldsymbol{\theta}_0\sin\phi\cos\theta+\boldsymbol{\varphi}_0\frac{1}{2}\left(3-\cos 2\theta\right)\cos\phi\right]\,,
\end{aligned} \tag{4.18}$$

where the amplitude coefficients

$$E_d = E_0 \left(1 + \frac{2\Theta_1 + 1 - \varepsilon_p}{\varepsilon_p + 2 - 2\Theta_1}\right) = E_0 \frac{3}{\varepsilon_p + 2 - 2\Theta_1}\,, \tag{4.19a}$$

$$E_q = E_0 \frac{2.5ik_0a}{2\varepsilon_p + 3 - 6\Theta_1}\,. \tag{4.19b}$$

For multilayer graphene wrappings, the obtained nonlinear currents should be multiplied by a number of layers.

Similar to how it is done for the fundamental frequency wave, here we represent the field of the second harmonics $\mathbf{E}_{2\omega_0}$ inside and in the vicinity of a nanoparticle as an asymptotic series in the parameter $\mathcal{M}(2\omega_0) = 2\mathcal{M}_0$:

$$\mathbf{E}_{2\omega_0} = \boldsymbol{\mathcal{E}}^{(0)}_{2\omega_0} + \boldsymbol{\mathcal{E}}^{(1)}_{2\omega_0} + \dots\,, \tag{4.20}$$

where the first two terms are

$$\boldsymbol{\mathcal{E}}^{(0,1)}_{2\omega_0} = -\nabla\Phi^{(0,1)}_{2\omega_0}\,, \tag{4.21}$$

and the potential functions $\Phi^{(0,1)}_{2\omega_0}$ are the solutions of the Laplace's equation:

$$\nabla^2\Phi^{(0,1)}_{2\omega_0} = 0 \quad (r < a\,,\, r > a)\,. \tag{4.22}$$

At the boundary $r = a$, the tangential components of electric fields are continuous while the normal components of the electric displacement vectors $\varepsilon(\mathbf{r})\left(-\nabla\Phi^{(0,1)}_{2\omega_0}\right)$ experience discontinuities due to the surface charge density $\rho^{(0,1)}_{2\omega_0} = \nabla_s \cdot \left(\mathbf{j}^{(0,1)}_{2\omega_0} + \sigma_2 \boldsymbol{\mathcal{E}}^{(0,1)}_{2\omega_{0\tau}}\right)/i2\omega_0$, where $\sigma_2 \equiv \sigma(2\omega_0)$. To find field distribution, we need to satisfy these boundary conditions and we expand $\Phi^{(0,1)}_{2\omega_0}(\mathbf{r})$ in spherical harmonics. $\nabla_s \cdot \mathbf{j}^{(0)}_{2\omega_0}$ is proportional to $(1 + 3\cos 2\theta)$ and, thus, the respective potential relative to a symmetric locally excited quadrupole is

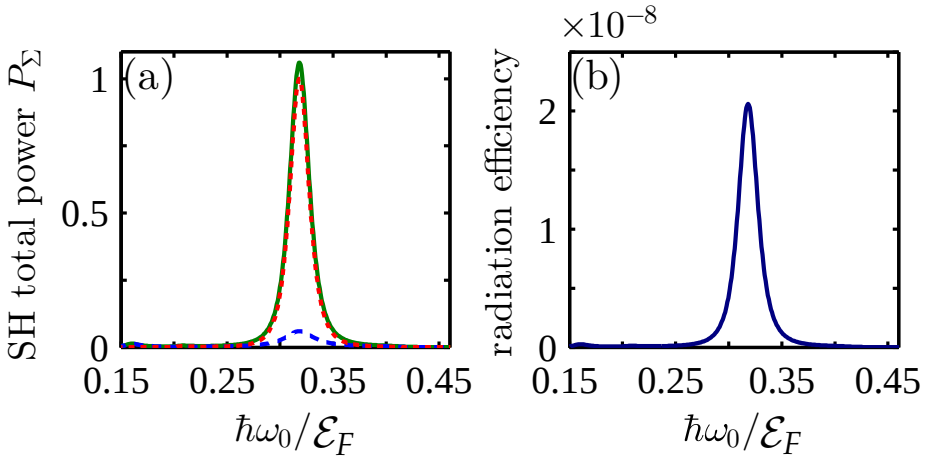

Figure 4.2: (a) Radiated power and (b) second harmonic conversion efficiency as functions of frequency calculated for a nanoparticle of radius $a = 106$ nm, $\varepsilon_p = 2.1$, $N = 1$, $\mathcal{E}_F = 0.25$ eV, $\tau_{\text{intra}} = 0.08$ ps, and incident intensity 10^8 W/cm^2. In (a) green solid line shows the total radiated power, blue dashed and red dotted lines refer to the dipole and quadrupole contributions, respectively. Powers are normalized to the quadrupole maximum value.

expressed as follows

$$\Phi^{(0)}_{2\omega_0} = \frac{(1+3\cos 2\theta)}{4} Q^{(0)}_{2\omega_0} \begin{cases} \dfrac{1}{r^3}, & r > a \\ \dfrac{r^2}{a^5}, & r < a \end{cases}, \tag{4.23}$$

where the quadrupole moment component

$$Q^{(0)}_{2\omega_0} = \frac{3}{2} \frac{e^3 v_F^2}{\hbar^2 \omega_0^4 (3 + 2\varepsilon_p - 3\Theta_2)} a^2 E_d^2 \,, \tag{4.24}$$

where $\Theta_2 = 4\pi\sigma_2 / i\omega_0 a$.

We would like to note that similar analysis can be performed for metal nanoparticles using a free-electron hydrodynamic model. Generally, the potential functions $\Phi^{(0)}_{2\omega_0}$ and $\Phi^{(1)}_{2\omega_0} \sim \cos\tilde{\theta} \equiv \sin\theta \sin\phi$ for $r > a$ would coincide with the potentials of the quadrupole, which is symmetric with respect to the z axis and has a diagonal tensor of the quadrupole moment,

$$\hat{Q}^{(0)}_{2\omega_0} = Q^{(0)}_{2\omega_0} \begin{pmatrix} -1 & 0 & 0 \\ 0 & -1 & 0 \\ 0 & 0 & 2 \end{pmatrix} \tag{4.25}$$

and of the dipole with the dipole moment

$$\boldsymbol{\mathcal{P}}^{(1)}_{2\omega_0} = \mathcal{P}^{(1)}_{2\omega_0} \mathbf{y}_0 \,, \tag{4.26}$$

which is directed along the wave vector of the incident wave. The radiation intensities (powers) of the quadrupole $\hat{Q}_{2\omega_0}$ and the dipole $\boldsymbol{\mathcal{P}}_{2\omega_0}$ moments given by [251]

$$P^{(\mathrm{quad})}_{\Sigma} = \frac{c(2k_0)^6}{60} |Q^{(0)}_{2\omega_0}|^2 \,, \tag{4.27a}$$

$$P^{(\mathrm{dip})}_{\Sigma} = \frac{c(2k_0)^4}{3} |\mathcal{P}^{(1)}_{2\omega_0}|^2 \,. \tag{4.27b}$$

have the same order of smallness. The radiation pattern of the quadrupole is symmetric with respect to the z axis, along which the electric field in the incident wave is oriented and has maxima at $\theta = \pi/4, 3\pi/4$. The dipole radiation is symmetric with respect to the wave vector of the incident wave, parallel to the y axis, and is maximum in the $y = 0$ plane.

In our case of a graphene sphere, the dipole moment associated with the current $\mathbf{j}^{(1)}_{2\omega_0}$ is given by the expression

$$\mathcal{P}^{(1)}_{2\omega_0} = \frac{3}{4} \frac{ie^3 v_F^2}{\hbar^2 \omega_0^4 (3/2 + \varepsilon_p - 3\Theta_1)} \frac{5/4 + \varepsilon_p - 3\Theta_1}{2 + \varepsilon_p - \Theta_2} k_0 a^2 E_d E_0 \,. \tag{4.28}$$

As follows from Eqs. (4.19a), (4.24), (4.28), the resonant enhancement in the SH scattering occurs near the frequencies of localized plasmons. The total radiated SH power possesses a pronounced peak at the frequency of the one-photon dipolar resonance where the radiation pattern appears to be predominantly quadrupolar, as shown in Fig. 4.2 (a).

We note here that the scattering object containing graphene benefits from its tunability. In our problem, there is a large number of parameters that can be adjusted for controlling the effect. In particular, one can choose the operating frequency ω_0, the chemical potential of graphene $\mathcal{E}_F$, the particle radius a, the number of graphene layers in the wrapping N, the

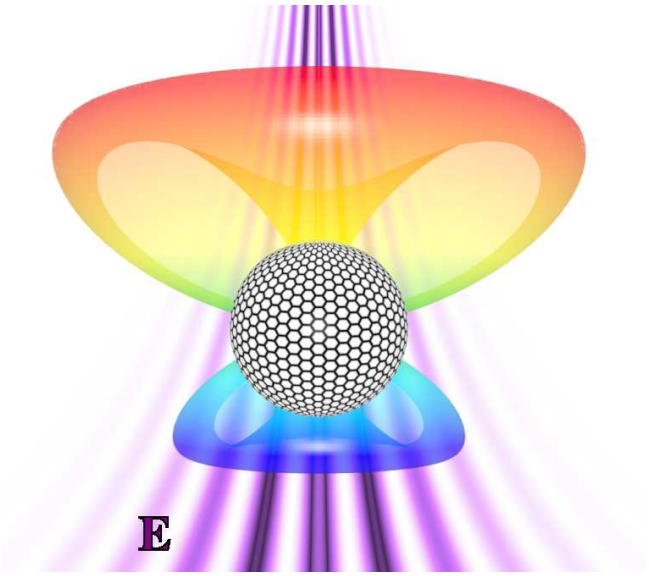

Figure 4.3: Schematic view of a graphene-wrapped nanoparticle placed into axially symmetric slightly inhomogeneous external field. The SH radiation is predominantly directed into the upper half-space.

dielectric permittivity of the particle ε_p and the relaxation time τ_{intra}, which is responsible for the broadening of the resonant peaks.

SH signal from a single nanoparticle is rather weak. To quantify the conversion efficiency, we introduce the SHG efficiency for a single particle η defined as the ratio of the total SH radiated power to the energy flux of the fundamental wave through the physical area of the particle $s = \pi a^2$, $\eta = P_\Sigma / \left[(c/8\pi)|E_0|^2 \pi a^2\right]$. Dependence of the efficiency on frequency clearly shows resonance (see Fig. 4.2 (b)), and in the maximum it reaches the value of $\sim 2 \times 10^{-8}$.

Control of radiation patterns by inhomogeneous external fields

Now we consider the case when a graphene-wrapped nanoparticle is placed in a weakly inhomogeneous quasistatic external field, which is axially symmetric with respect to z-axis (see schematics in Fig. 4.3). Such field distribution can be realized in two counter-propagating Bessel beams forming a standing wave. Similar field profiles can be realised if we place our nanoparticle near a larger particle, e.g. an elongated nanoparticle or near a tip of an atomic force microscope, positioned in the maximum of the standing wave created by two counter-propagating plane waves.

Using the Taylor series expansion around the center of the particle, we introduce the electric potential of the external field in the form which satisfies the Laplace's equation

$$\Phi_{\omega_0}^{(\text{ext})} = -E_0 r \cos\theta - \frac{1}{8}\frac{\partial E_0}{\partial z} r^2 (1 + 3\cos 2\theta) + \dots , \tag{4.29}$$

where $\dfrac{\partial E_0}{\partial z} \equiv \gamma$ is a tunable parameter characterizing variation of the field along z axis. Next, we follow the procedure described above, expand the fields and apply the boundary conditions.

In the previous sections we considered the linear dipole described by the first term in Eq. (4.29) and associated quadrupole at the double frequency. The resonant enhancement

in this case due to surface plasmon resonances is expected near the frequencies where $\varepsilon_p = -2 + 8\pi \operatorname{Im}\sigma(\omega_0)/\omega_0 a$ and $\varepsilon_p = -3/2 + 6\pi \operatorname{Im}\sigma(2\omega_0)/\omega_0 a$, i.e. where the real parts of the corresponding denominators vanish. However, as we show in Fig. 4.4, the one-photon dipolar plasmon resonance is much more pronounced than the two-photon quadrupolar.

The field inhomogeneity given by the second term in Eq. (4.29) determines a linear potential

$$\Phi^{(1)}_{\omega_0} = \frac{(1+3\cos 2\theta)}{4} Q^{(1)}_{\omega_0} \begin{cases} \dfrac{1}{r^3}, & r > a \\ \dfrac{r^2}{a^5}, & r < a \end{cases}, \tag{4.30}$$

that can be attributed to a symmetric quadrupole

$$\hat{Q}^{(1)}_{\omega_0} = Q^{(1)}_{\omega_0} \begin{pmatrix} -1 & 0 & 0 \\ 0 & -1 & 0 \\ 0 & 0 & 2 \end{pmatrix} \tag{4.31}$$

with the amplitude

$$Q^{(1)}_{\omega_0} = \frac{\varepsilon_p - 1 - 3\Theta_1}{2\varepsilon_p + 3 - 6\Theta_1} \gamma a^5 . \tag{4.32}$$

Now we calculate the induced second harmonic current

$$\mathbf{j}^{(1)}_{2\omega_0} = -i \frac{e^3}{\pi\hbar^2\omega_0^3} \frac{v_F^2}{a} E_d E_q^{(\mathrm{ext})} \boldsymbol{\theta}_0 \frac{1}{32} \left(3\sin 3\theta - \sin\theta\right) , \tag{4.33}$$

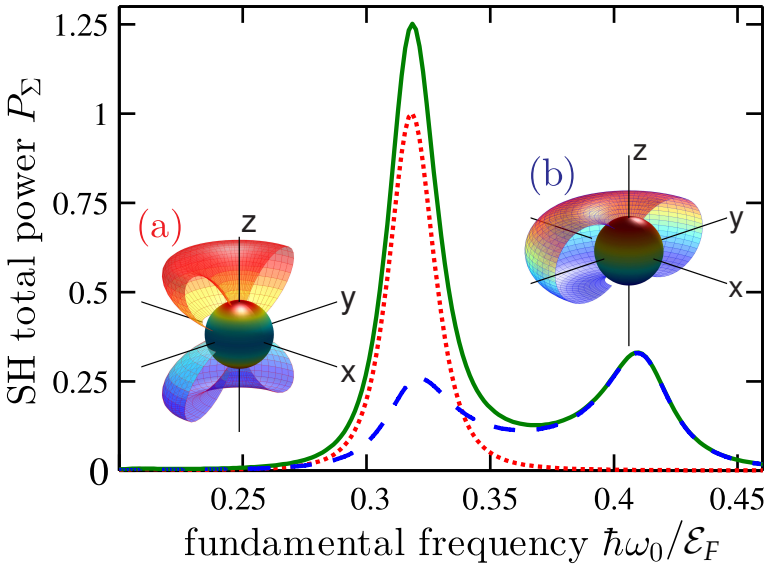

Figure 4.4: Spectra of the radiated powers of the SH quadrupole (red dotted curve), SH dipole (blue dashed curve), and total SH emission (green solid curve), calculated for a nanoparticle of radius $a = 106$ nm, $\varepsilon_p = 2.1$, $N = 1$, $\mathcal{E}_F = 0.25$ eV, $\tau_{\mathrm{intra}} = 0.08$ ps, $\bar{\gamma} = 0.5$. Powers are normalized to the pure quadrupole maximum value. Insets show far-field radiation patterns and surface charge distributions of the pure (a) SH quadrupole ($\bar{\gamma} = 0$), and (b) SH dipole, which is excited predominantly near the higher-frequency resonance.

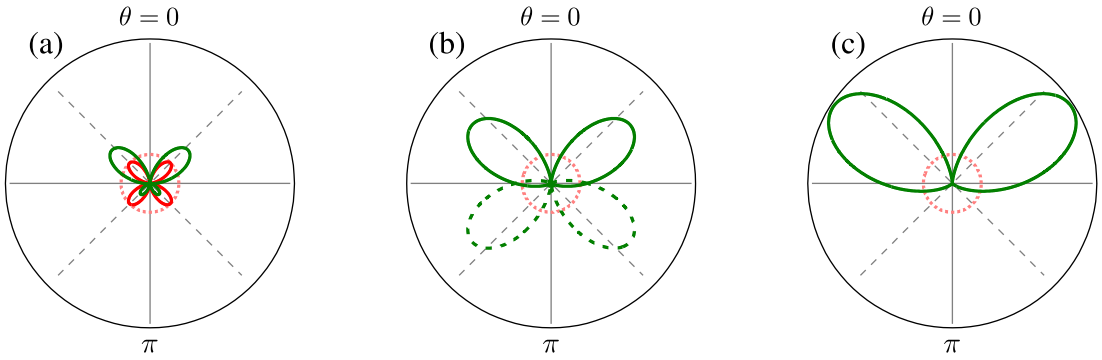

Figure 4.5: SH radiation patterns shown as polar θ-diagrams (green solid lines) calculated at $\hbar\omega_0 = 0.318\mathcal{E}_F$ for the parameters of Fig. 4.4, ($k_0 a \approx 0.06$) and different values of $\bar{\gamma}$: (a) $\bar{\gamma} = 0.5$, (b) $\bar{\gamma} = 1.25$, and the reverse at $\bar{\gamma} = -1.25$ (dashed green line), (c) $\bar{\gamma} = 1.75$. The inner circle in all the plots corresponds to the same maximum intensity of the pure SH quadrupole. For reference, a four-lobbed pattern of a radiating SH quadrupole source ($\bar{\gamma} = 0$) is also depicted in panel (a).

where the quadrupole amplitude coefficient is

$$E_q^{(\mathrm{ext})} = -\frac{15}{4}\frac{\gamma a}{2\varepsilon_p + 3 - 6\Theta_1}\,, \tag{4.34}$$

and taking the surface divergence $\nabla_s \cdot \mathbf{j}^{(1)}_{2\omega_0} \sim \left[-3.2\cos\theta + 9.6\left(5\cos^3\theta - 3\cos\theta\right)\right]$ containing the leading term proportional to $\cos\theta$ we obtain the respective potential

$$\Phi^{(1)}_{2\omega_0} = \mathcal{P}^{(1)}_{2\omega_0}\cos\theta \begin{cases} \dfrac{r}{a^3}, & |\mathbf{r}| < a \\ \dfrac{1}{r^2}, & |\mathbf{r}| > a \end{cases}, \tag{4.35}$$

that corresponds to a dipole oriented along z axis

$$\boldsymbol{\mathcal{P}}^{(1)}_{2\omega_0} = \mathcal{P}^{(1)}_{2\omega_0}\mathbf{z}_0\,, \tag{4.36}$$

with a dipole moment

$$\mathcal{P}^{(1)}_{2\omega_0} = \frac{3.2}{16}\frac{e^3 v_F^2}{\hbar^2\omega_0^4(\varepsilon_p + 2 - \Theta_2)} a E_d E_q^{(\mathrm{ext})}\,. \tag{4.37}$$

Remarkably, this SH dipole is aligned *along the direction* of the electric field of fundamental frequency, similar to the dipole induced by linear scattering, and it is in a sharp contrast with the conventional nonlinear dipole arising from the retardation.

The function of the dipolar radiated power plotted in Fig. 4.4 exhibits two peaks close to the frequencies estimated from $\varepsilon_p = -2 + 8\pi\,\mathrm{Im}\,\sigma(\omega_0)/\omega_0 a$ and $\varepsilon_p = -3/2 + 12\pi\,\mathrm{Im}\,\sigma(\omega_0)/\omega_0 a$, dominating the two-photon dipole resonance at the lower frequency around $\varepsilon_p = -2 + 4\pi\,\mathrm{Im}\,\sigma(2\omega_0)/\omega_0 a$.

The radiation pattern at $2\omega_0$ being determined now by both dipolar and quadrupolar contributions can be varied. We illustrate this aspect with examples of the radiation pattern transformations in the far field at frequency $\hbar\omega_0 = 0.318\mathcal{E}_F$ close to the peak SHG enhancement. The angular distributions of the SH radiation are shown in Fig. 4.5 as polar plots for different values of a dimensionless parameter $\bar{\gamma} = \bar{\gamma}E_0/a$. This diagrams show that the

SH radiation predominantly occurs in the direction of the stronger field at fundamental frequency. Note, near the points where E_0 vanishes, for example, near the nodes of the standing Bessel wave, the value of $\bar{\gamma}$ can be arbitrarily large, although the total radiation power is obviously decreased. Importantly, the radiation pattern remains axially symmetric with respect to the z-axis but due to the phase relations at some value of $\bar{\gamma}$ two lower lobes almost disappear and the SH source effectively emits into the upper half-space as shown in Fig. 4.5 (b). This is in a sharp contrast to the conventional multipolar interaction for small spherical nanoparticles, placed in the field of the plane monochromatic wave, where the resonant enhancement close to the distinctive localized plasmon resonances is never accompanied by strongly asymmetric radiation patterns since the dipole and quadrupole fields are out of phase and, hence, do not interfere (see e.g. Ref. [253]). We note that the directivity can be changed to the opposite by changing the sign of $\bar{\gamma}$ (for example, moving the particle along the standing wave). Subsequent increase of the $\bar{\gamma}$ leads to the gradual transformation of the radiation pattern into dipole-like (see an intermediate step in Fig. 4.5 (c)).

Summary

We have studied the second-harmonic generation by a nanoparticle wrapped into graphene. We have derived the analytical model and analyzed efficiency and radiation directionality of the second-harmonic radiation. We have demonstrated the possibility to control the radiation pattern with an inhomogeneous external field that breaks a balance between the dipole and quadrupole radiation contributions. For the typical parameters, we have predicted that the second harmonic is predominantly radiated in the half-space with stronger external electric field.

4.2 Second-harmonic generation in subwavelength graphene waveguides

Double-layer graphene waveguides are known to support symmetric and antisymmetric plasmonic guiding modes classified with respect to the in-plane electric field profile [131, 200, 202], so we may expect the coupling between different modes when the nonlinear response becomes important. Here, we suggest and study analytically a novel approach for the second-harmonic generation in double-layer graphene waveguides taking advantage of the possibility to modulate spatially the conductivity of one of the graphene layers by doping or electrostatic gating [76, 254, 255] thus assisting the coupling of freely propagating light to plasmons in graphene [161, 163, 256, 257]. Phase matching between parametrically interacting waves is a crucial requirement for the efficient second-order nonlinear effects [29], and in our geometry the phase matching can be achieved by tailoring the modal dispersion of the graphene waveguide enabling plasmon-to-plasmon frequency conversion. More specifically, we demonstrate below that the phase matching becomes possible between an antisymmetric fundamental frequency (FF) mode and a symmetric second-harmonic (SH) mode in a double-layer graphene waveguide.

We employ a theoretical analysis based on the perturbation theory and describe the second-order nonlinear process with graphene plasmons in terms of slowly varying modes of a waveguide structure, the approximation frequently used in nonlinear optics [38]. For definiteness, we consider a planar geometry shown schematically in Fig. 4.6, where a graphene double-layer waveguide is placed into homogeneous surrounding medium with

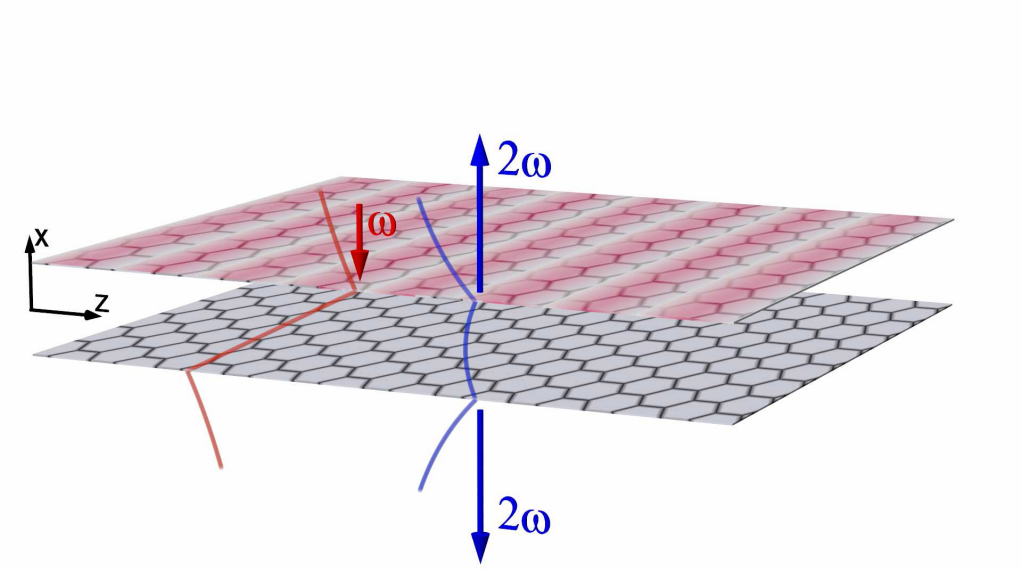

Figure 4.6: Geometry of the problem. A free-standing waveguide created by two graphene layers is illuminated by an external wave being coupled to the phase-matched guided modes of the graphene waveguide. Red curve corresponds to an antisymmetric mode at the fundamental frequency, and a blue curve – to a second-harmonic symmetric mode (shown with the tangential electric field component). Conductivity of the upper layer is periodically modulated.

the dielectric permittivity ε being illuminated by light from the upper half-space $x > d/2$. As a matter of fact, in our analysis we distinguish two parts of the problem and examine them sequentially,

- *Linear scattering.* Radiation at the fundamental frequency normally incident onto the structure is scattered by the periodic conductivity grating, and then excites resonantly an antisymmetric mode of the graphene waveguide;
- *Nonlinear plasmon-to-plasmon conversion.* Due to the second-order nonlocal nonlinearity of graphene [87, 88, 91], the induced current of the antisymmetric mode serves as a source for the phase-matched symmetric mode at the double frequency which eventually radiates into free space.

Similar to the assumptions employed earlier [129, 131, 132], namely low dissipation, weak nonlinearity, and small phase mismatch, here we solve Maxwell's equations following the procedure of the asymptotic expansion, and demonstrate that the second-order nonlinear processes can be achieved with conductivity modulation to allow external pumping to couple to the guided modes of the structure generating output radiation at the doubled frequency.

Linear scattering

We start our derivation by studying the linear resonant excitation of antisymmetric plasmons, and write the corresponding system of Maxwell's equations in the form

$$\begin{aligned} \nabla \times \mathbf{E} &= -\frac{1}{c}\frac{\partial \mathbf{H}}{\partial t}\,, \\ \nabla \times \mathbf{H} &= \frac{\varepsilon}{c}\frac{\partial \mathbf{E}}{\partial t} + \frac{4\pi}{c}\left[j^{(1)}\delta\left(x - \frac{d}{2}\right) + j^{(2)}\delta\left(x + \frac{d}{2}\right)\right]\mathbf{z}_0\,, \end{aligned} \tag{4.38}$$

where $j^{(1,2)}$ are the surface current densities induced in the graphene layers placed at $x = \pm d/2$, as indicated by Dirac's delta functions δ. Assuming the field to be p-polarized with the magnetic component $\mathbf{H} = H(x,z,t)\mathbf{y}_0$, from Eq. (4.38) we find

$$\frac{\varepsilon}{c^2}\frac{\partial^2 H}{\partial t^2} - \Delta H = -\frac{4\pi}{c}\frac{\partial}{\partial x}\left[j^{(1)}\delta\left(x-\frac{d}{2}\right) + j^{(2)}\delta\left(x+\frac{d}{2}\right)\right], \tag{4.39}$$

where, if we assume the harmonic field dependencies $\sim \exp(-i\omega t)$, the currents are given by

$$j^{(1,2)}(\omega,z) = \sigma^{(1,2)}(\omega,z)E_z(x=\pm d/2,z,\omega)\,. \tag{4.40}$$

Here $\sigma^{(2)}(\omega,z) = \sigma(\omega)$, $\sigma^{(1)}(\omega,z) = \sigma(\omega)[1+f(z)]$ are surface conductivities, $\sigma(\omega) \equiv \sigma^{(R)}(\omega) + i\sigma^{(I)}(\omega)$ is the linear frequency-dependent surface conductivity of graphene, while $f(z) = f(z+a) = f_1\cos\left(\frac{2\pi}{a}z\right) + f_2\cos\left(\frac{4\pi}{a}z\right)$ is assumed to be a periodic function of z, i.e. conductivity of one of the graphene layers is spatially modulated.

Assuming the dissipative losses and modulation amplitudes $f_{1,2}$ to be small, we formally introduce the smallness parameter μ

$$\mu = \max\left\{\left|\frac{\sigma^{(R)}}{\sigma^{(I)}}\right|, f_{1,2}\right\}, \tag{4.41}$$

and adopt the following asymptotic ansatz for the magnetic field

$$\begin{aligned} H(x,z,t) = e^{-i\omega t}\Big\{&\mu\tilde{H}_0(x,\mu z) + \left[\mathcal{A}_1(\mu z)h(\omega,x) + \mu\tilde{H}_1(x,\mu z)\right]e^{ik_{\mathrm{sp}}(\omega)z} \\ &+ \left[\mathcal{A}_2(\mu z)h(\omega,x) + \mu\tilde{H}_2(x,\mu z)\right]e^{-ik_{\mathrm{sp}}(\omega)z}\Big\}, \end{aligned} \tag{4.42}$$

where $h(x)$ is the transverse profile of the linear plasmonic mode of the guiding structure, $\mathcal{A}_{1,2}$ are slowly varying mode amplitudes, where the subscripts "1" and "2" refer to the forward and backward propagation along the z direction, respectively. Also $\tilde{H}_{1,2}$ are small corrections to the eigenmode profile, and the term $\bar{H}_0$ does not contain a fast dependence on z.

In the zero-order approximation in μ, for the function $h(x)$ Eq. (4.39) takes the form,

$$\frac{d^2h}{dx^2} - (k_{\mathrm{sp}}^2 - k_0^2\varepsilon)h(x) = \frac{4\pi}{c}i\sigma^{(I)}(\omega)\frac{\partial}{\partial x}\left\{\left[\delta\left(x-\frac{d}{2}\right) + \delta\left(x+\frac{d}{2}\right)\right]e_z(x)\right\}, \tag{4.43}$$

where $e_z(x) = \dfrac{i}{k_0\varepsilon}\dfrac{dh}{dx}$. This equation yields the dispersion relation

$$\left[1 - \frac{2\pi\sigma^{(I)}\kappa^{(\mathrm{s,a})}}{\omega\varepsilon}(1 \pm e^{-\kappa^{(\mathrm{s,a})}d})\right] = 0\,, \tag{4.44}$$

where $\kappa^{(\mathrm{s,a})} = \sqrt{k_{\mathrm{sp}}^{(\mathrm{s,a})2} - k_0^2\varepsilon}$, $k_0 = \omega/c$, and the modal transverse profiles are

$$h^{(\mathrm{s,a})}(\omega,x) = \frac{-ik_0\varepsilon}{\kappa^{(\mathrm{s,a})2}}\frac{de_z^{(\mathrm{s,a})}}{dx}\,, \tag{4.45}$$

where the continuous tangential components of the electric field are expressed as

$$e_z^{(\mathrm{s})}(\omega,x)=\begin{cases} e^{-\kappa^{(\mathrm{s})}(x-d/2)}, & x>d/2\,,\\ \dfrac{\cosh(\kappa^{(\mathrm{s})}x)}{\cosh(\kappa^{(\mathrm{s})}d/2)}, & |x|<d/2\,,\\ e^{\kappa^{(\mathrm{s})}(x+d/2)}, & x<-d/2 \end{cases} \tag{4.46}$$

and

$$e_z^{(\mathrm{a})}(\omega,x)=\begin{cases} e^{-\kappa^{(\mathrm{a})}(x-d/2)}, & x>d/2\,,\\ \dfrac{\sinh(\kappa^{(\mathrm{a})}x)}{\sinh(\kappa^{(\mathrm{a})}d/2)}, & |x|<d/2\,,\\ -e^{\kappa^{(\mathrm{a})}(x+d/2)}, & x<-d/2 \end{cases} \tag{4.47}$$

for both symmetric and antisymmetric eigenmodes guided by a double-layer waveguide [160,200], as indicated by the superscripts.

We now assume that the period of the conductivity grating is chosen to almost compensate the momentum mismatch with the antisymmetric plasmon, $|k_{\mathrm{sp}}^{(\mathrm{a})}(\omega)-2\pi/a|\equiv|\Delta k|\ll 2\pi/a$ so that $|\Delta k/k_{\mathrm{sp}}^{(\mathrm{a})}(\omega)|\lesssim\mu$. Substituting the expression of the total field (B.6) into Eq. (4.39) and keeping only resonant terms, in the first order in μ for the field perturbations $\tilde{H}_{1,2}$, we obtain

$$\begin{aligned}
&\frac{d^2\tilde{H}_{1,2}}{dx^2}-(k_{\mathrm{sp}}^{(\mathrm{a})2}(\omega)-k_0^2\varepsilon)\tilde{H}_{1,2}-\frac{4\pi}{c}i\sigma^{(I)}(\omega)\frac{\partial}{\partial x}\left\{\left[\delta\left(x-\frac{d}{2}\right)+\delta\left(x+\frac{d}{2}\right)\right]\tilde{E}_{1,2z}\right\}=F_{1,2}\,,\\
&F_{1,2}(x,z)=\mp 2ik_{\mathrm{sp}}^{(\mathrm{a})}(\omega)\frac{\partial\mathcal{A}_{1,2}}{\partial z}h^{(\mathrm{a})}(\omega,x)+\frac{4\pi}{c}\sigma^{(R)}(\omega)\mathcal{A}_{1,2}\frac{\partial}{\partial x}\left\{\left[\delta\left(x-\frac{d}{2}\right)+\delta\left(x+\frac{d}{2}\right)\right]\right.\\
&\left.\times\, e_z^{(\mathrm{a})}(\omega,x)\right\}+\frac{4\pi}{c}i\sigma^{(I)}(\omega)\frac{\partial}{\partial x}\left\{\delta\left(x-\frac{d}{2}\right)\left[\frac{f_1}{2}\bar{E}_{0z}e^{\mp i\Delta kz}+\frac{f_2}{2}\mathcal{A}_{2,1}\,e^{\mp 2i\Delta kz}e_z^{(\mathrm{a})}(\omega,x)\right]\right\},
\end{aligned} \tag{4.48}$$

whereas $\bar{H}_0$ satisfies the equation,

$$\begin{aligned}
\frac{d^2\bar{H}_0}{dx^2}+k_0^2\varepsilon\bar{H}_0=\frac{4\pi}{c}i\sigma^{(I)}(\omega)\frac{\partial}{\partial x}\left\{\left[\delta\left(x+\frac{d}{2}\right)+\delta\left(x-\frac{d}{2}\right)\right]\right.\\
\left.\times\, E_{0z}(\omega,x)+\frac{f_1}{2}\left(\mathcal{A}_1e^{i\Delta kz}+\mathcal{A}_2e^{-i\Delta kz}\right)\delta\left(x-\frac{d}{2}\right)\right\}.
\end{aligned} \tag{4.49}$$

Equation (B.4) includes reflection of a plane wave incident from the semi-space $x>d/2$, written as $H_0\exp[-ik_0\sqrt{\varepsilon}(x-d/2)]$, where we assume $H_0\sim\mu$, $E_0=H_0/\sqrt{\varepsilon}$, $E_{0z}(\omega,x)$ is the tangential electric field distribution at $f_{1,2}=0$. Taking into account the boundary conditions at the graphene interface, we find the amplitude of the electric field at $x=d/2$ as follows

$$\bar{E}_{0z}(\omega,x=d/2)=E_0(1+r)-\frac{2\pi}{c\sqrt{\varepsilon}}i\sigma^{(I)}(\omega)\frac{f_1}{2}\left(\mathcal{A}_1e^{i\Delta kz}+\mathcal{A}_2e^{-i\Delta kz}\right). \tag{4.50}$$

where $r=-\dfrac{4\pi}{c\sqrt{\varepsilon}}i\sigma^{(I)}(\omega)\left(1+\dfrac{4\pi}{c\sqrt{\varepsilon}}i\sigma^{(I)}(\omega)\right)^{-1}$ stands for the reflection coefficient from two closely spaced graphene layers, $k_0\sqrt{\varepsilon}d\ll 1$, at $f_1=0$.We assume that at operating frequencies the graphene conductivity is predominantly Drude like, $\omega\gg\tau_{\mathrm{intra}}^{-1}$, where $\tau_{\mathrm{intra}}^{-1}$ is the relaxation rate, and $\dfrac{4\pi}{c\sqrt{\varepsilon}}\sigma^{(I)}(\omega)\ll 1$, leading to the expression $r\approx-\dfrac{4\pi}{c\sqrt{\varepsilon}}i\sigma^{(I)}(\omega)$.

Substituting the expression (4.50) into Eq. (4.48), in order for the corrections $\tilde{H}_{1,2}$ to be nondiverging, in accord with the Fredholm alternative [185], we have to satisfy the orthogonality condition for the right-hand side of Eq. (4.48) with the solution of its homogeneous part, or equivalently, with the plasmonic mode itself. This overintegrating is mathematically written as

$$\int_{-\infty}^{+\infty} F_{1,2}(x,z)h^{(\mathrm{a})^*}(\omega,x)dx = 0, \tag{4.51}$$

and it leads to the nonlinear equations for the slowly varying amplitudes $\mathcal{A}_{1,2}$

$$\pm 2ik_{\mathrm{sp}}^{(\mathrm{a})}(\omega)\left(\frac{\partial \mathcal{A}_{1,2}}{\partial z} \pm (\gamma^{(\mathrm{a})}+\gamma_r^{(\mathrm{a})})\mathcal{A}_{1,2}\right) = (-2ik_{\mathrm{sp}}^{(\mathrm{a})}(\omega)\gamma_r^{(\mathrm{a})}+Q_2^{(\mathrm{a})})\mathcal{A}_{2,1}e^{\mp 2i\Delta kz} + Q_1^{(\mathrm{a})}E_0(1+r)e^{\mp i\Delta kz}, \tag{4.52}$$

where linear damping due to losses in graphene $\gamma^{(\mathrm{a})}$, grating-induced damping due to radiation $\gamma_r^{(\mathrm{a})}$, and coupling coefficients $Q_{1,2}^{(\mathrm{a})}$ are derived, respectively, in the form

$$\gamma^{(\mathrm{a})} = \frac{4\pi}{c}\sigma^{(R)}(\omega)\frac{k_0\varepsilon}{k_{\mathrm{sp}}^{(\mathrm{a})}(\omega)q^{(\mathrm{a})}}, \qquad \gamma_r^{(\mathrm{a})} = \left(\frac{\pi\sigma^{(I)}(\omega)f_1}{c}\right)^2\frac{k_0\varepsilon^{1/2}}{k_{\mathrm{sp}}^{(\mathrm{a})}(\omega)q^{(\mathrm{a})}},$$
$$Q_{1,2}^{(\mathrm{a})} = \frac{2\pi}{c}\sigma^{(I)}(\omega)f_{1,2}\frac{k_0\varepsilon}{q^{(\mathrm{a})}}, \tag{4.53}$$

where in all the expressions we employ the following definition,

$$q^{(\mathrm{a})} = k_0^2\frac{\varepsilon^2}{\kappa^{(\mathrm{a})3}}\left[1+\frac{\sinh(\kappa^{(\mathrm{a})}d)+\kappa^{(\mathrm{a})}d}{2\sinh^2(\kappa^{(\mathrm{a})}d/2)}\right]. \tag{4.54}$$

When we assume a simple homogeneous case, $\dfrac{\partial}{\partial z} = 0$, and also the exact momentum matching, $\Delta k = 0$, from Eq. (4.52) we obtain the slowly varying amplitudes,

$$\mathcal{A}_1 = \mathcal{A}_2 \equiv \mathcal{A} = \frac{Q_1^{(\mathrm{a})}E_0(1+r)}{2ik_{\mathrm{sp}}^{(\mathrm{a})}(\omega)[\gamma^{(\mathrm{a})}(\omega)+2\gamma_r^{(\mathrm{a})}]-Q_2^{(\mathrm{a})}} \tag{4.55}$$

and substitute them into Eq. (4.50). Thus, the excitation of the antisymmetric mode results in changing the reflection coefficient compared to the case without a conductivity grating, $r_{\mathcal{A}} \approx r(1+f_1\mathcal{A}/2E_0)$.

Nonlinear plasmon-to-plasmon conversion

First we notice that, for the case of TM-polarized waves with the tangential electric field of the form $\mathbf{E}_{\tau\omega} = \mathbf{z}_0 E e^{iqz}$ (the monochromatic time dependence $\sim \exp(-i\omega t)$ is omitted), the induced second-harmonic current in graphene depends on the in-plane momentum q manifesting its nonlocal nature. It is expressed as [23,91] (see Appendix A)

$$\mathbf{j}_{2\omega} = -\mathbf{z}_0\frac{3}{8}\frac{e^3v_F^2}{\pi\hbar^2\omega^3}qE^2e^{i2qz}, \tag{4.56}$$

where $v_F \approx c/300$ is the Fermi velocity. This result is derived in the semiclassical limit from the Boltzmann kinetic equation written for Dirac electrons with a linear energy dispersion

under the approximations $\hbar\omega \leq \mathcal{E}_F$, $k_B T \ll \mathcal{E}_F$ and $qv_F/\omega \ll 1$, where $\mathcal{E}_F$ is the Fermi energy, k_B is the Boltzmann constant, T is the temperature. Thereby, a nonlinear source associated with the antisymmetric mode will generate a synchronous symmetric mode. Importantly, in general, when discussing the parametric interaction that involves the modes of different symmetries, the phase matching is not a sufficient condition, and the overlaps of the modes with the respective nonlinear sources should be examined. Since a quadratic nonlinear source localized at the graphene layers is symmetric, the conversion between the FF antisymmetric mode and SH symmetric mode becomes possible.

Similar to the analysis of the fundamental frequency field, we employ here the perturbational method and derive the equations for the envelopes of the second-harmonic fields $\mathcal{B}_{1,2}$,

$$\pm 2ik_{\rm sp}^{(\rm s)}(2\omega)\left(\frac{\partial \mathcal{B}_{1,2}}{\partial z} \pm (\gamma^{(\rm s)} + \gamma_r^{(\rm s)})\mathcal{B}_{1,2}\right) = -2ik_{\rm sp}^{(\rm s)}(2\omega)\gamma_r^{(\rm s)}\mathcal{B}_{2,1}e^{\mp 2i(\widetilde{\Delta k}+2\Delta k)z} + g\mathcal{A}_{1,2}^2 e^{\mp i\widetilde{\Delta k}z}, \tag{4.57}$$

where $\widetilde{\Delta k} = k_{\rm sp}^{(\rm s)}(2\omega) - 2k_{\rm sp}^{(\rm a)}(\omega)$ is a small detuning, and other parameters are

$$\begin{aligned} q^{(\rm s)} &= 4k_0^2\frac{\varepsilon^2}{\kappa^{(\rm s)3}}\left[1 + \frac{\sinh(\kappa^{(\rm s)}d) - \kappa^{(\rm s)}d}{2\cosh^2(\kappa^{(\rm s)}d/2)}\right], \\ \gamma^{(\rm s)} &= \frac{8\pi}{c}\sigma^{(R)}(2\omega)\frac{k_0\varepsilon}{k_{\rm sp}^{(\rm s)}(2\omega)q^{(\rm s)}}, \\ \gamma_r^{(\rm s)} &= \left(\frac{\pi\sigma^{(I)}(2\omega)f_2}{c}\right)^2\frac{2k_0\varepsilon^{1/2}}{k_{\rm sp}^{(\rm s)}(2\omega)q^{(\rm s)}}, \\ g &= -i\frac{16\pi}{c}\sigma_2(\omega)\frac{k_0\varepsilon}{q^{(\rm s)}}, \end{aligned} \tag{4.58}$$

with $\sigma_2(\omega)$ denoting the quadratic conductivity of graphene defined as

$$\sigma_2(\omega) = -\frac{3}{8}\frac{e^3 v_F^2}{\pi\hbar^2\omega^3}k_{\rm sp}^{(\rm a)}(\omega).$$

Within the undepleted pump approximation, when the amplitude at fundamental frequency is not affected by nonlinearity, for the exact phase matching, $\widetilde{\Delta k} = \Delta k = 0$, and homogeneous case discussed above, we have

$$\mathcal{B}_1 = \mathcal{B}_2 \equiv \mathcal{B} = \frac{g\mathcal{A}^2}{2ik_{\rm sp}^{(\rm s)}(2\omega)(\gamma^{(\rm s)} + 2\gamma_r^{(\rm s)})}. \tag{4.59}$$

Since the radiation associated with SH field is emitted equally to both directions, the normalized conversion efficiency can be introduced as a ratio of the doubled SH energy flux density in the upper half-space to the energy flux of the incident fundamental wave. Equivalently, this definition takes the following form

$$\eta = \frac{2|\bar{E}_{0z}(2\omega, x = d/2)|^2}{|E_0|^2}, \tag{4.60}$$

where $\bar{E}_{0z}(2\omega, x = d/2) = -\dfrac{2\pi}{c\sqrt{\varepsilon}}i\sigma^{(I)}(2\omega)f_2\mathcal{B}$.

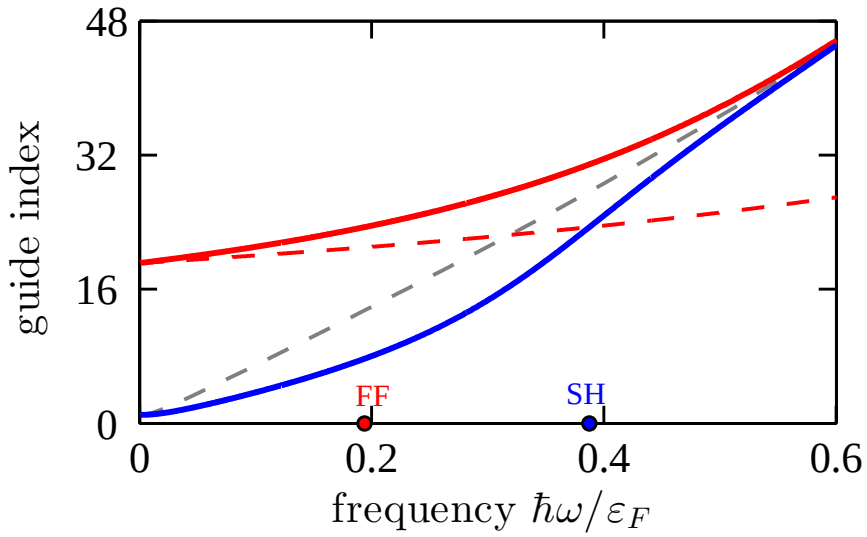

Figure 4.7: Plasmonic guide index vs. frequency at the fixed separation between the graphene layers, $d = 62$ nm, calculated for the doping level of $\mathcal{E}_F = 0.6$ eV, $N = 1$, $\varepsilon = 1$. Blue and red solid curves correspond to the symmetric and antisymmetric modes, respectively. Dashed gray and red lines show dispersion of an isolated graphene sheet and half-frequency antisymmetric mode, for reference. Color dots in the horizontal axis mark the fundamental and second-harmonic frequencies.

Discussions

In the framework of the nonlinear amplitude equations, we can now analyze the parametric effects and estimate the frequency conversion efficiency. To make a period of the conductivity modulation realistic, in our calculations we employ highly doped or multilayer graphene that effectively increases the equivalent surface conductivity leading to a reduction of the wavenumber of the p-polarized plasmons supported by multilayer graphene structures [132, 160]. (See Chapter 3.) We take $\sigma(\omega) = N\sigma_1(\omega)$ for a randomly stacked multilayer graphene film consisting of N layers, with each layer characterized by a surface conductivity $\sigma_1(\omega)$ given by Eq. (3.12), assuming for doped graphene $\hbar\omega < 1.67\mathcal{E}_F$ and $k_BT \ll \mathcal{E}_F$. For multilayer graphene sheets with negligible inter-layer hopping, the nonlinear current in Eq. (4.56) should be also multiplied by a number of layers.

To reveal a possibility of plasmonic frequency conversion in the graphene waveguide, in Fig. 4.7 we plot the frequency-dependence of the plasmonic guide indices for the symmetric and antisymmetric modes. We observe that the first harmonic antisymmetric and second-harmonic symmetric modes of the waveguide can be matched at $\hbar\omega = 0.12$ eV ($\lambda = 2\pi/k_0 \approx 10.6$ μm, corresponding to one of the radiation lines of high power CO_2 lasers), $k_{\mathrm{sp}}^{(\mathrm{a})} \approx 23.4k_0$.

Figure 4.8 shows the dependence of the fundamental frequency on the separation between the layers. Note while discussing the dispersion relations and the possibility of phase-matching conditions we take $\sigma = i\sigma^{(I)}$ and do not take losses into account, however these losses are included into our considerations by means of the perturbative approach. Calculated for $f_1 = f_2 = 0.1$, $a \approx 456$ nm, $\tau_{\mathrm{intra}} = 0.3$ ps, the incident wave intensity, S, of 1 MW/cm^2 and the other parameters of Fig. 4.7, efficiency is $\eta \sim 2.6 \times 10^{-7}$. Overall, for this structure the smallness parameter is found to be $\mu \sim 0.1$, so that our asymptotic approach is well justified. We notice that, within our model, the results remain valid for a broad range of parameters, since the chemical potential of graphene $\mathcal{E}_F$, the number of layers N,

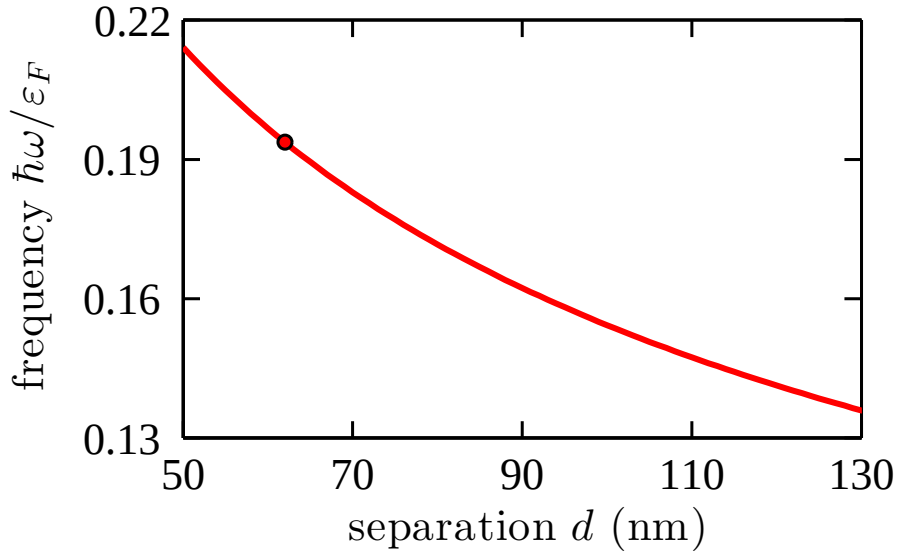

Figure 4.8: Operational fundamental frequency as a function of the separation between the layers for the exact phase-matching at $\mathcal{E}_F = 0.6$ eV, $N = 1$, $\varepsilon = 1$. The point corresponds to the parameters used in Fig. 4.7.

and the spatial separation between the graphene sheets d, can be adjusted for controlling the effect. For comparison, the set of parameters, $N = 5$, $\mathcal{E}_F = 0.3$ eV, $\tau_{\text{intra}} = 0.3$ ps, $\varepsilon = 1$, $d = 123$ nm, $f_1 = f_2 = 0.1$, $a \approx 1$ μm, $S = 1$ MW/cm^2, provides the estimate of $\eta \sim 8.7 \times 10^{-7}$ at the same operational fundamental frequency, $\hbar\omega = 0.12$ eV.

Last but not least, we have considered a simplified model allowing an analytical treatment and transparent interpretation aiming to concentrate on the underlying physical mechanisms of the predicted effect. In particular, we have assumed that the dielectric permittivity is spatially uniform. In a realistic situation, the dielectric slab between the graphene layers can differ from the cladding dielectrics. Besides, the conductivities of both graphene layers can be varied spatially with the modulation profiles containing many spatial harmonics. Such more complicated geometries would lead to a modification of the dispersion relations for the surface modes participating in the nonlinear interaction, with subsequent revisions of the phase-matching conditions. However, the derived nonlinear equations Eqs. (4.52) and (4.57) would preserve their general structure, and only their coefficients would be modified to accord with the additional factors. Further developments of the model for describing other realistic geometries would lead to lengthy mathematics, however, they will not bring any new physics, entirely outlined in this Section.

Summary

By employing the approximation of slowly-varying field amplitudes, we have derived nonlinear equations for describing the second-harmonic generation from a double-layer graphene structure with modulated conductivity. We have revealed that the quadratic phase matching between the plasmonic modes of different symmetries becomes possible in a planar waveguide geometry with conductivity modulation playing a role of an effective grating that couples the external pumping radiation to the waveguiding modes with the subsequent parametric conversion into radiation at the double frequency.

4.3 Cascaded third-harmonic generation in hybrid graphene-semiconductor waveguides

Parametric wavelength conversion in general and harmonic generation in particular are among the most intensively studied phenomena in optics and photonics [29]. It was demonstrated that important advantages can be obtained by cascading several parametric processes [258, 259]. For instance, since a wide range of materials provide stronger quadratic nonlinear response compared to cubic nonlinear response, the efficiency of the third-harmonic generation (THG) can be strongly enhanced by utilizing a cascaded process consisting of second-harmonic generation (SHG) and sum-frequency generation (SFG), which mixes fundamental wave (FW) and second harmonic (SH) to generate the third harmonic (TH). The conversion efficiency in this regime is the highest when the phase-matching (PM) conditions for both SHG and SFG are satisfied.

Being an atomically thin tunable plasmonic material [52, 55], doped graphene can be incorporated into various components in nanoscale and microscale optics, and it demonstrates strong optical nonlinearity. It is therefore of significant interest to establish a theoretical framework and explore the viability of cascaded nonlinear optical processes in graphene-enhanced wavelength conversion devices.

In this Section, we develop a theoretical model for cascaded third-harmonic generation in graphene-based plasmonic waveguides. We show that engineering modal dispersion allows us to simultaneously satisfy SHG and SFG phase matching for efficient cascaded THG, and offers a 5 times increase of TH output compared to direct non-cascaded THG. We consider a planar waveguiding system consisting of a graphene sheet placed over a doped semiconductor sandwiched between two dielectric layers; see Fig. 4.9. The dielectric permittivity of a doped semiconductor is described by the Drude model with the plasma

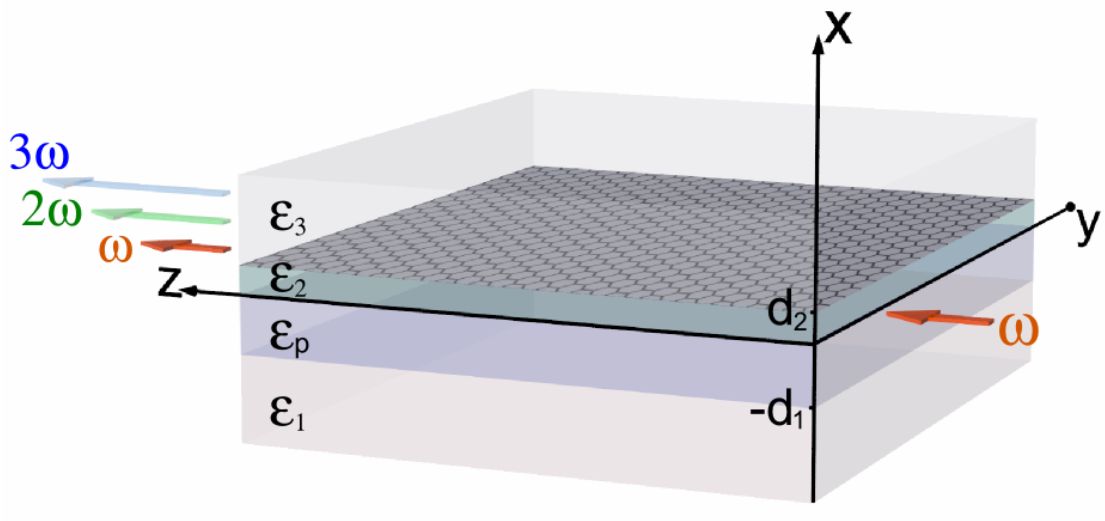

Figure 4.9: Geometry of a planar hybrid graphene-semiconductor waveguide. A waveguide consists of a monolayer graphene sheet placed at the height d_2 above the doped semiconductor with permittivity ε_p and thickness d_1 sandwiched between two dielectric layers with permittivities ε_1 and ε_2. The third dielectric layer with permittivity ε_3 is placed on top of a graphene layer. The optical pump at the frequency ω (red arrow) is generating the second harmonic at the frequency 2ω (green arrow) and the third harmonic at the frequency 3ω (blue arrow).

frequency comparable to the Fermi energy in graphene. This geometry allows the coexistence of three plasmonic modes [260], which as we show below can be phase-matched, strongly increasing effective nonlinear optical interaction. In our model we assume that the nonlinear interaction of propagating plasmons is achieved due to the nonlinear response in graphene. Here we focus only on nonlinear processes in the waveguide; the way of linear in-coupling and out-coupling of light to and from such hybrid-graphene waveguides was discussed in Section 4.2.

Coupled mode equations

Neglecting losses, the dispersion relation and *p*-polarized eigenmodes of a hybrid graphene-semiconductor waveguide were analyzed in Ref. [260]. Similar to the approach outlined in Section 4.2 and Ref. [125], to describe the plasmon conversion due to the graphene nonlinearity, we derive equations for the modal envelopes. The frequency conversion can be modeled by coupled equations for the amplitudes of FW, SH and TH plasmonic modes, $\mathcal{A}_1$, $\mathcal{A}_2$ and $\mathcal{A}_3$, respectively. In this geometry surface currents induced in graphene are slow waves with the wavenumbers exceeding those in free space, and thus do not couple to the radiative modes. Assuming that the conversion efficiency is small, we utilize the following magnetic field ansatz

$$\begin{aligned} H_y(x,z,t) =& e^{-i\omega t}\mathcal{A}_1(\mu z)h_1(\omega,x)e^{ik^1_{\mathrm{sp}}(\omega)z} + e^{-i2\omega t}\mathcal{A}_2(\mu z)h_2(2\omega,x)e^{ik^2_{\mathrm{sp}}(2\omega)z} \\ &+ e^{-i3\omega t}\mathcal{A}_3(\mu z)h_3(3\omega,x)e^{ik^3_{\mathrm{sp}}(3\omega)z}\,, \end{aligned} \tag{4.61}$$

where $h_{1,2,3}(x)$ are the transverse profiles of the modes. Disregarding the influence of the generated modes on the pump, the coupled-mode equations can be written in the form

$$\frac{d\mathcal{A}_1}{dz} + \gamma_1\mathcal{A}_1 = 0\,, \tag{4.62a}$$

$$\frac{d\mathcal{A}_2}{dz} + \gamma_2\mathcal{A}_2 = g_2\mathcal{A}_1^2 e^{-i[k^2_{\mathrm{sp}}(2\omega)-2k^1_{\mathrm{sp}}(\omega)]z}\,, \tag{4.62b}$$

$$\frac{d\mathcal{A}_3}{dz} + \gamma_3\mathcal{A}_3 = \bar{g}_2\mathcal{A}_1\mathcal{A}_2 e^{-i[k^3_{\mathrm{sp}}(3\omega)-k^2_{\mathrm{sp}}(2\omega)-k^1_{\mathrm{sp}}(\omega)]z} + g_3\mathcal{A}_1^3 e^{-i[k^3_{\mathrm{sp}}(3\omega)-3k^1_{\mathrm{sp}}(\omega)]z}\,, \tag{4.62c}$$

where the term proportional to $\bar{g}_2$ is responsible for the so-called *cascaded* contribution to the THG [258, 259](see Appendix A for details on the derivation of the expressions for the nonlinear conductivities at FW, SH and TH in graphene). Assuming that the FW plasmon is launched at $z = 0$, we study the plasmon frequency conversion modeled by Eqs.(4.62). The conversion from the TH to the SH can be neglected, because, as will be shown below, the TH efficiency in this kind of graphene-semiconductor waveguides remains much smaller than the SH efficiency, $\mathcal{A}_3(z) \ll \mathcal{A}_2(z)$.

For moderate losses, the loss coefficients $\gamma_{1,2,3}$ in Eqs.(4.62) can be obtained perturbatively from the dispersion equation, introducing dissipative corrections, namely the linear frequency-dependent surface conductivity of graphene

$$\sigma(\omega) \equiv \sigma^{(R)}(\omega) + i\sigma^{(I)}(\omega), \tag{4.63}$$

and the dielectric permittivity of the semiconductor

$$\varepsilon_p(\omega) = 1 - \frac{\omega_p^2}{\omega(\omega + i\nu)} = 1 - \frac{\omega_p^2}{\omega^2} + \frac{i\nu\omega_p^2}{\omega^3}, \tag{4.64}$$

where ν is a damping coefficient. The coefficients g_2, $\bar{g}_2$, g_3 in nonlinear sources can be derived from the equations for the energy flows in the corresponding modes as follows

$$\frac{dP_z^2}{dz} = -\frac{1}{2}\,\mathrm{Re}\int_{-\infty}^{+\infty} \mathbf{j}_{2\omega}^{*}\mathbf{E}_{2\omega}dx\,, \tag{4.65a}$$

$$\frac{dP_z^3}{dz} = -\frac{1}{2}\,\mathrm{Re}\int_{-\infty}^{+\infty} \mathbf{j}_{3\omega}^{*}\mathbf{E}_{3\omega}dx\,, \tag{4.65b}$$

where $P_z^{2,3} = G_{2,3}|\mathcal{A}_{2,3}|^2$; $G_{2,3}$ are defined as

$$G_{2,3} = \mathrm{Re}\,\frac{c}{8\pi}\int_{-\infty}^{+\infty}\left[\mathbf{e}_{2,3}\times\mathbf{h}_{2,3}^{*}\right]_z dx = \mathrm{Re}\,\frac{c}{8\pi}\int_{-\infty}^{+\infty} e_x^{2,3}(x)h_y^{2,3*}(x)dx\,. \tag{4.66}$$

Here $e_x^{2,3}(x)$ and $h_y^{2,3}(x)$ are the transverse profiles of the SH and TH modes normalized in such a way that at the graphene layer $e_z(d_2) = 1$. The field components of the p-polarized surface wave are connected as

$$e_z(x) = \frac{1}{-ik_0\varepsilon(x)}\frac{dh_y}{dx} = \frac{1}{-ik_{\mathrm{sp}}}\frac{de_x}{dx}. \tag{4.67}$$

Finally, we can write the nonlinear coefficients as follows:

$$g_2 = -\frac{\sigma_2}{4G_2},\quad \bar{g}_2 = -\frac{\frac{2}{3}\sigma_2}{4G_3},\quad g_3 = -\frac{\sigma_3}{4G_3}\,. \tag{4.68}$$

These coefficients determine the strength of the nonlinear interactions between FW, SH and TH plasmons. Phase matching, another important parameter that defines the conversion between these harmonics, is discussed in the next section.

Phase matching and wavelength conversion

We now show that three guided modes corresponding to FW, SH and TH can be phase-matched, so that at some ω, dependent on the geometrical parameters (separations between the layers, dielectric permittivity distribution and doping levels), they have almost equal effective indexes $\beta^1(\omega) \approx \beta^2(2\omega) \approx \beta^3(3\omega)$ (or, equivalently, $k_{\mathrm{sp}}^1(\omega) = k_{\mathrm{sp}}^2(2\omega)/2 = k_{\mathrm{sp}}^3(3\omega)/3$). To calculate the dispersion and the mode profiles, we use the transfer matrix method [199].

To demonstrate the predicted behavior, we employ the following set of realistic waveguide parameters. The permittivities of the dielectric layers shown in Fig. 4.9 are chosen as $\varepsilon_1 = 8$, $\varepsilon_2 = 2$, and $\varepsilon_3 = 1$. For simplicity, we do not take into account the dispersion in the dielectric layers. Adding the dielectric dispersion will require adjusting the thicknesses of the dielectric layers to compensate for it. We choose the thickness of a semiconductor layer as $d_1 = 25$ nm, and the thickness of the dielectric layer between the semiconductor and graphene as $d_2 = 20$ nm. Then, for the Fermi energy $\mathcal{E}_F = 0.5$ eV, plasma frequency $\hbar\omega_p = 0.95\mathcal{E}_F$, relaxation parameter $\tau_{\mathrm{intra}} = 0.3$ ps and the damping coefficient $\nu = 0.001\omega_p$, we obtain simultaneous phase-matching for FW, SH and TH, as depicted in Fig. 4.10(a), at the respective fundamental wavelength in free space of 11.7 μm. In Fig. 4.10(b) we show the corresponding overlap between the FW, SH and the TH modes. Strong graphene nonlinearity allows efficient nonlinear interaction even between the modes with moderate field confinement, which can be further improved by optimizing the waveguide parameters.

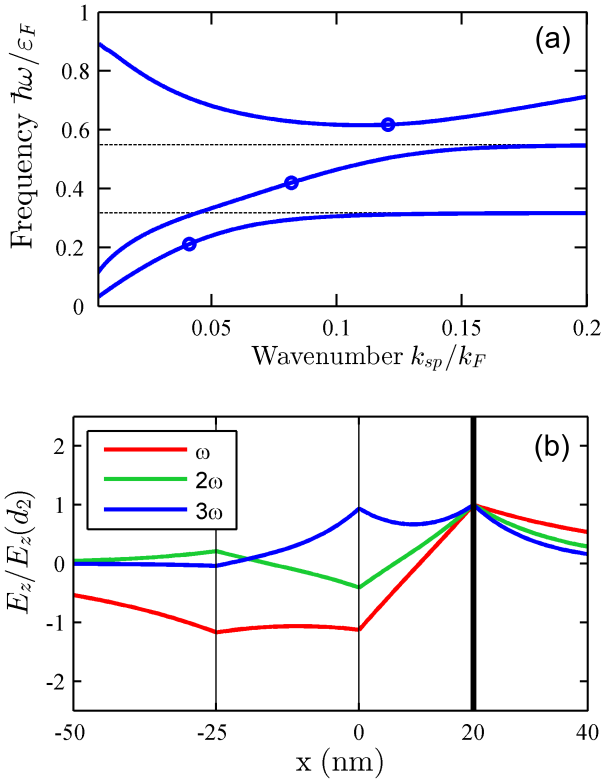

Figure 4.10: (a) Dispersion of three supported plasmon modes in a hybrid graphene-semiconductor waveguide (solid blue lines), corresponding asymptotes (dashed black lines), and points of phase-matching for FW, SH and TH (blue circles); (b) FW, SH and TH mode profiles shown for the continuous in-plane electric field component. Bold black line corresponds to the graphene layer, thin black lines mark the interfaces between the semiconductor and dielectric layers.

Remarkably, for different dielectric and semiconductor parameters, the TH mode can be phase-matched in the backward direction, although here we focus on the case when all three modes are phase-matched in the forward direction.

In Fig. 4.11 we demonstrate the evolution of the interacting FW, SH and TH plasmons. We take a realistic pump intensity of 1 MW/cm^2 on a graphene layer [176–179]. The resulting SHG and THG conversion efficiencies and optimal conversion lengths are comparable to the previous works [105, 109, 125, 261]. Particularly, choosing y dimension of 1 cm and the pump Poynting flux per unit length 1 W/cm, the outcome energy flows $P_z^{2,3}$ reach 2×10^{-3} and 3×10^{-5} W/cm, respectively, at the distance of about 2 μm. We note that the direct contribution to THG governed by the term proportional to g_3 in Eq.(4.62c) is an order of magnitude smaller than the cascaded one. To show this explicitly, as a dashed line in Fig. 4.11, we plot the TH intensity evolution calculated by formally setting $\bar{g}_2 = 0$. The difference is remarkable because the plasmon wavevector can notably exceed that in free space, leading to the efficent SHG process stimulating a cascaded conversion to the third harmonic plasmon.

The efficient cascaded THG regime in graphene-based waveguides requires a number of conditions outlined in this Section, such as moderate plasmon wave numbers and moderate losses. Then high field confinement and phase matching of the nonlinearly interacting modes can be engineered by choosing the appropriate thicknesses and materials of the waveguide layers. Although the example presented above discusses only one set of param-

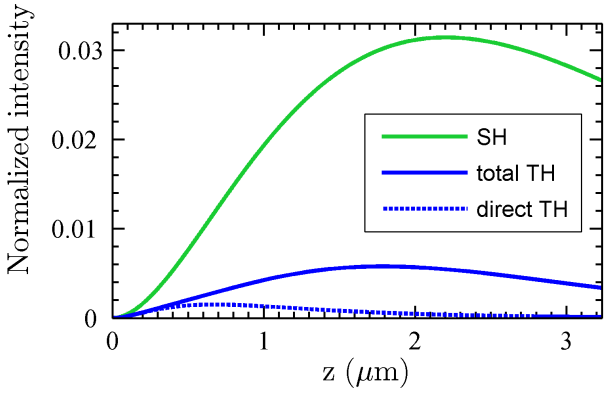

Figure 4.11: Spatial evolution along the propagation direction of the normalized SH intensity $|\mathcal{A}_2(z)|^2/|\mathcal{A}_1(0)|^2$ (solid green line), total TH intensity including direct THG and cascaded THG $|\mathcal{A}_3(z)|^2/|\mathcal{A}_1(0)|^2$ (solid blue line), and the direct TH intensity $|\mathcal{A}_3(z)|^2/|\mathcal{A}_1(0)|^2$ in the absence of the cascading effect assuming $\bar{g}_2 = 0$ (dashed blue line).

eters, by varying graphene doping and adjusting the other characteristics, similar results for the predicted cascaded effect in harmonics generation can be achieved throughout the mid-IR wavelength range.

Summary

We have established the theoretical framework for the direct and the cascaded THG in graphene-semiconductor waveguides, including a detailed derivation of all coefficients in the coupled-mode equations based on the waveguide parameters. We have shown that these waveguides can support simultaneous phase matching of FW, SH and TH plasmon modes, and that the cascaded THG can be several times stronger than the direct THG.

4.4 Tunable nonlinear graphene metasurfaces

One of the important directions in the physics of *metasurfaces*, thin-layer patterned structures strongly interacting with light and possessing advanced functionalities, is the use of graphene as a component of metadevices. The approach to place graphene into close proximity with metallic and dielectric photonic structures has been already employed to design highly tunable infrared and THz metasurfaces enabling both amplitude and phase modulation [80, 262–267]. Besides, doped graphene, exhibiting a plasmonic response, can be patterned to form tunable planar plasmonic metasurfaces operating at infrared and THz frequencies [61, 164, 268].

In this Section we discuss a novel type of Fano-resonant hybrid metasurfaces composed of a graphene layer and a planar metamaterial where two types of subradiant modes of different origin, asymmetric plasmonic modes of metallic metamolecules and graphene plasmons, are strongly coupled. We show that such metasurfaces support *cascaded Fano resonances* [269, 270] originating from the interference of subradiant plasmonic modes in graphene and localized modes of metamolecules. We demonstrate that such hybrid graphene metasurfaces provide strong tunability and dramatic field enhancement giving rise to enhanced nonlinear response.

Model and parameters

We consider a metasurface composed of a square lattice of metallic split-ring-resonators (SRRs) placed on top of a graphene layer, as shown in Figs. 4.12(a,b). The electromagnetic response is calculated by using the finite-element method solver COMSOL Multiphysics with a graphene layer modelled as a surface current. At low frequencies $\hbar\omega < 2\mathcal{E}_F$, graphene is described by the frequency-dependent surface conductivity [70], defined by Eq. (3.12), where we take $\tau_{\text{intra}} = 0.15$ ps. At frequencies $\hbar\omega < \mathcal{E}_F$, the Drude-like conductivity (3.13) originating in intra-band transitions dominates and graphene supports highly confined extremely short-wavelength p-polarized plasmons, whose dispersion can be tuned by changing the Fermi level of graphene $\mathcal{E}_F$. Considering the normal incidence of a y-polarized plane wave, we calculate numerically both transmission and reflection spectra for different values of the chemical potential.

Without a graphene layer, the metasurface becomes a conventional two-dimensional metamaterial of double SRRs, supporting symmetric (superradiant) and asymmetric (subradiant) modes that correspond to the in-phase and out-of-phase current distribution along two arms of the metamolecule [see Fig. 4.13(a)]. When the symmetry of the metamolecules is reduced, the interference between these two modes results in a characteristic Fano-like asymmetric lineshape in far-field spectra, the transition illustrated by black dotted and dashed lines in Fig. 4.13(c) [35, 271–273]. By introducing a graphene layer, we can excite graphene plasmons whose wavelength can be tuned to match one of the characteristic scales of the metasurface. Note, however, that even without plasmonic modes of graphene tuned to the spectral range of interest, the surface conductivity of graphene modifies electromagnetic interactions on the metasurface leading to the overall blue shift of the resonances [80].

Due to the subwavelength nature of graphene plasmons, it is natural to match their wavelength to the smallest scale associated with the gaps of the split-ring resonators, which effectively become a cavity for plasmons [264]. Here we are interested in graphene plasmons forming a subradiant mode, and such mode can be designed from two plasmons localized within the SRR gaps and interacting with each other through SRR arms. This interaction gives rise to a new asymmetric subradiant mode with the plasmons within two gaps being out of phase [see Fig. 4.13(b)]. Owing to their matching symmetries, this additional subradiant mode can efficiently couple to the asymmetric mode of SRRs when their frequencies are tuned [see Fig. 4.13(c)], resulting in a cascaded double Fano resonance in the far-field spectra [274–276]. Moreover, since the wavelength of graphene plasmons can be altered by changing the Fermi level, this enables dynamically controllable interaction between the two subradiant modes making one of them less pronounced. Direct numerical calculations of the far-field spectra shown in Fig. 4.14(a) confirm that the hybrid metasurface supports one superradiant (broad peak) and two subradiant resonances associated with the Fano resonances, one of them being highly tunable. Profiles of two subradiant asymmetric modes are shown in Fig. 4.13(b) for the case of their strong hybridization. Changing the frequency of the incident plane wave allows to see clearly the features of two resonances in near-field.

Analytical approach

The basic principle of the formation of the cascaded Fano resonances can be illustrated by applying the coupled-mode theory [271]. In this approach, each mode of the metasurface is described by a complex amplitude (S, A, and P), corresponding to the bright symmetric

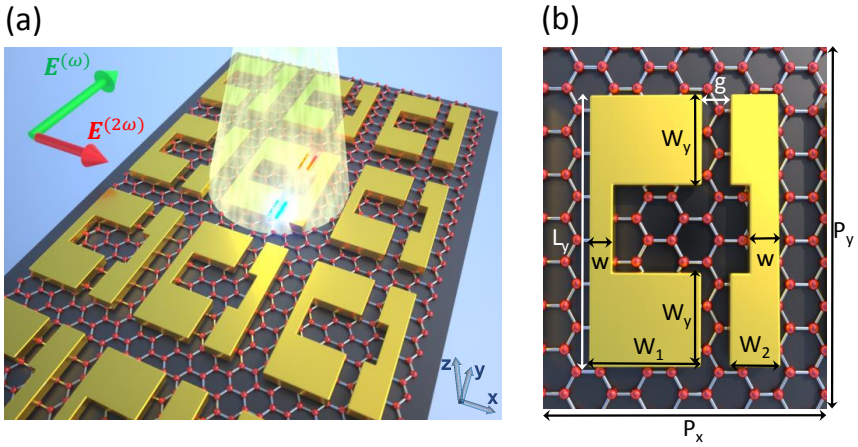

Figure 4.12: (a) Artistic view of the light interaction with a hybrid metasurface created by a lattice of asymmetric gold SRRs placed on top of a graphene layer. (b) Top view and size definitions of a unit cell of the hybrid metasurface.

and dark asymmetric modes of SRR, and a dark asymmetric graphene plasmonic mode, respectively. All modes are normalized in such a way that $|S|^2$, $|A|^2$, $|P|^2$ are the energy densities. The amplitudes of the incident E^+ and reflected E^- waves are also normalized such that $|E^{(+,-)}|^2$ represent the incoming and outgoing power fluxes. Then, the system dynamics is described by a set of coupled equations

$$\begin{cases} \dot{S} = (-i\omega_S - \gamma_S)S + ig_1 A + i\varkappa_S E^+_{\text{in}}\,, \\ \dot{A} = (-i\omega_A - \gamma_A)A + ig_1 S + ig_2 P\,, \\ \dot{P} = (-i\omega_P - \gamma_P)P + ig_2 A\,, \end{cases} \tag{4.69}$$

where ω_m and γ_m are bare frequencies and decay rates of the modes, $g_{1,2}$ characterize the interaction strengths, and $\varkappa_S$ determines coupling of the symmetric mode to an incident plane wave. In general, the total decay rate is composed of two parts $\gamma_{S,A,P} = \gamma^{\text{ohm}}_{S,A,P} + \gamma^{\text{rad}}_{S,A,P}$, Ohmic (resistive) and radiative loss, respectively. It is assumed that only the symmetric mode is driven by the time-harmonic incident field, while the asymmetric modes can be excited only indirectly through coupling. Additional constraints should be imposed on the coefficients to satisfy the energy conservation and time-reversal: $\gamma^{\text{rad}}_{A,P} = 0$, $|\varkappa_S| = \sqrt{\gamma^{\text{rad}}_S}$; $E^+_{\text{in}} = E^+_1$, where the numeric subscript (1 or 2) refers to the media surrounding the metasurface. For simplicity, the structure is assumed to be top-bottom symmetric, which neglects the substrate effect that justified by small optical contrast (the reflection coefficient without resonances $r = 0$) so that $E^-_{1(2)} = E^+_{2(1)} + i\varkappa_S S$. Complex reflection can then be found from expression $r = E^-_1/E^+_1 = (i\varkappa_S S)/E^+_1$ and assumes the form of a "nested" Fano resonance:

$$r = \frac{i\varkappa_S^2}{[(\omega_S - i\gamma_S) - \omega] - \dfrac{g_1^2}{[(\omega_A - i\gamma_A) - \omega] - \dfrac{g_2^2}{[(\omega_P - i\gamma_P) - \omega]}}},$$

which clearly reflects cascaded coupling of the plasmonic asymmetric mode to the radiative continuum via the asymmetric and symmetric modes of SRRs. The transmission coefficient

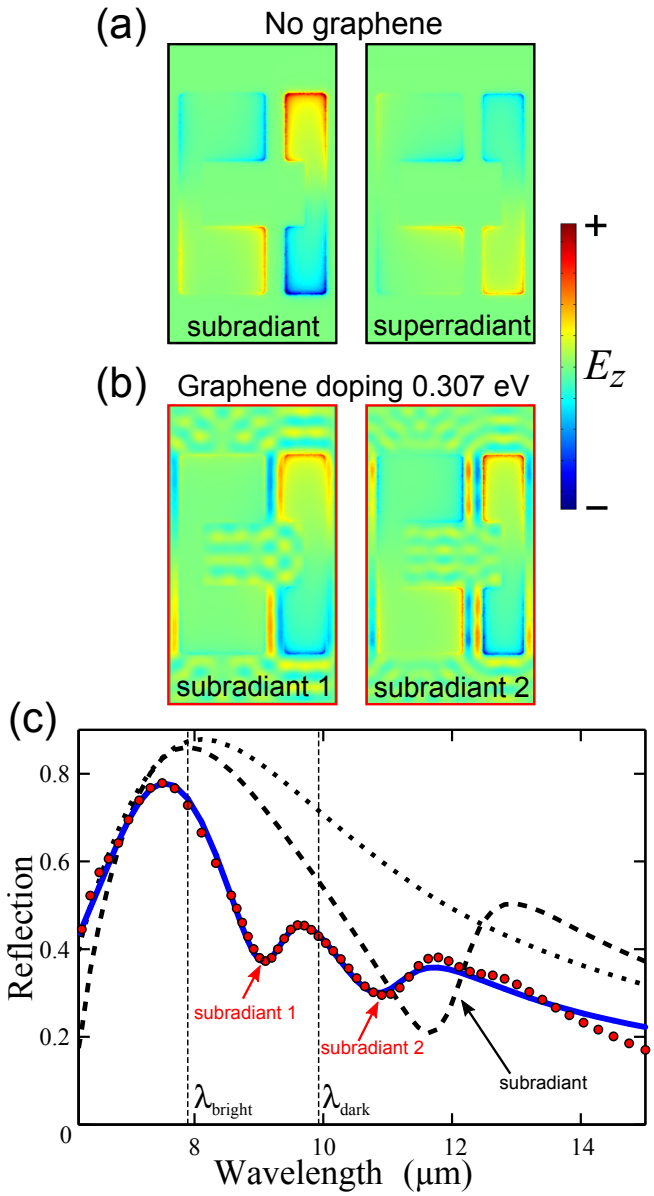

Figure 4.13: (a,b) Near-field images of the resonances shown by the E_z field component without and with a graphene layer, respectively. (c) Numerically calculated reflection spectrum at $\mathcal{E}_F = 0.307$ eV (red circles) along with the fitting obtained by the coupled-mode theory (blue solid curve). For the cases of symmetric and asymmetric split-rings, the spectra without graphene are shown by black dotted and dashed lines, respectively. Structure parameters are: the substrate permittivity $\varepsilon_2 = 1.35^2$, $P_x = 2.5$ μm and $P_y = 4.5$ μm, the parameters of the gold SRR are $L_y = 3$ μm, $g = 310$ nm, w$= 0.3$ μm, $W_y = 1$ μm, $W_1 = 1.28$ μm, $W_2 = 0.6$ μm, and gold thickness is $h = 40$ nm.

can then be found from the equation $t = E_2^- / E_1^+ = 1 + r$.

A change in the graphene chemical potential leads to variation of the spectral position of the plasmonic resonance ω_P. Due to strong near-field coupling of two subradiant modes their interaction reveals anticrossing of associated Fano resonances, shown in Fig. 4.14(a). The analytical model nicely reproduces this behavior. In Fig. 4.14(a) transmission calculated with the use of COMSOL Multiphysics is superimposed with the dispersion curves found from the coupled-mode theory, with parameters recovered from the fitting. The spectral positions of the noninteracting modes are shown by dashed lines. Here the graphene

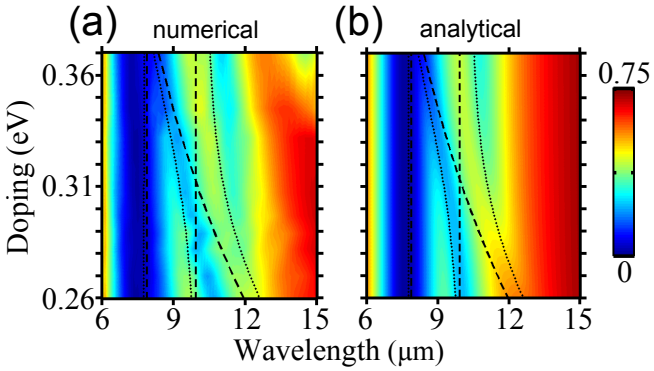

Figure 4.14: (a) Numerically calculated transmission spectra of the metasurface compared to (b) analytical results. Black dotted curves in panels (a,b) illustrate the anticrossing between the dark modes.

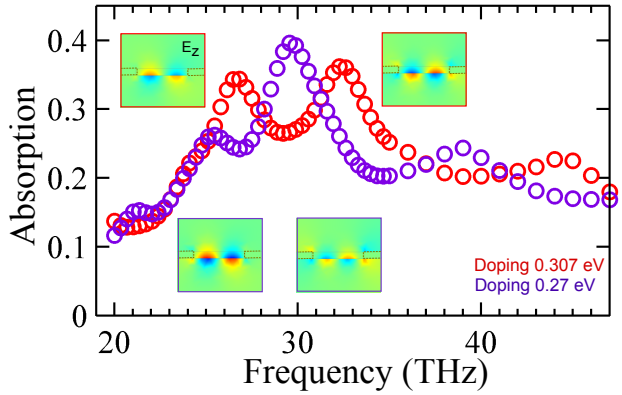

Figure 4.15: Numerically calculated absorption by the metasurface for graphene doping $\mathcal{E}_F = 0.27$ eV (purple circles) and $\mathcal{E}_F = 0.307$ eV (red circles). The insets show the field distributions in the SRR gap in the vicinity of two main absorption peaks associated with the excitation of Fano resonances.

plasmon branch is obtained from the standing-wave condition $2\pi/k_{sp} \approx g$, where k_{sp} satisfies the dispersion of the p-polarized plasmons on the graphene layer on top of dielectric substrate ε_2: $\frac{1}{\sqrt{k_{sp}^2 - k_0^2}} + \frac{\varepsilon_2}{\sqrt{k_{sp}^2 - \varepsilon_2 k_0^2}} = -i\frac{4\pi\sigma(\omega)}{\omega}$. Interaction between the resonances leads to their hybridization with dispersion branches of the normal modes shown by dotted lines. Since the resonant frequency of graphene plasmons depends strongly on doping, the plasmonic mode intersects the subradiant SRR mode. Their interaction results in the characteristic avoided crossing behaviour with the frequency splitting between two modes. The results of the numerical and analytical calculations are plotted alongside in Fig. 4.14(a) and Fig. 4.14(b), respectively, where one can see that the tunable anti-crossing behavior described by these approaches agrees perfectly well.

It is interesting to mention that, in a sharp contrast to conventional tunable plasmonic resonances in graphene, the subradiant nature of the graphene resonance considered here allows not only tuning its spectral position, but also coupling to a radiative continuum. Indeed, as demonstrated in Fig. 4.14, the intensity of the asymmetric plasmonic mode fades away as one moves away from the SRR asymmetric mode, evidencing the reduction of the radiative coupling caused by the suppression of the cascaded interaction between the modes. Therefore, the proposed metasurface offers an unprecedented control over

its scattering characteristics, including spectral position, radiative coupling strength, and phase, unattainable in conventional designs of Fano-resonant metasurfaces. The ability to control radiative coupling can be of special interest for applications where the tunable near-field enhancement is a key requirement. To demonstrate the possibility of a control over strength of light-matter interaction, below we consider two examples: tunable absorption enhancement and nonlinear second-harmonic generation.

Tunable absorption

Frequency-dependent absorption is plotted in Fig. 4.15 for two levels of graphene doping, with the insets showing the field distribution in the gap in the vicinity of two absorption peaks stemming from excitation of subradiant modes. The enhanced absorption due to excitation of hybrid graphene plasmon-quadrupole resonances clearly correlates with near-field enhancement. As expected, for the case of poorly interacting subradiant modes, corresponding to the case of lower Fermi energy ($\mathcal{E}_F = 0.27$ eV, shown by purple circles in Fig. 4.15), the asymmetric plasmonic mode has smaller amplitude and the losses are not as prominent as for the asymmetric SRR resonance. For higher doping level ($\mathcal{E}_F = 0.307$ eV, shown by red circles in Fig. 4.15) the two dark modes are strongly hybridized leading to a higher absorption rate by the tunable subradiant mode. This confirms that the system considered here can be promising for various applications where tunable strong field enhancement is in demand.

Enhanced second-harmonic generation

Extreme surface confinement of electromagnetic fields due to excitation of plasmons is known to result in enhanced nonlinear response [33, 35, 277]. Such enhancement, in particular, was demonstrated for multiple quantum wells and a thin layer of ITO placed in the proximity of resonant plasmonic metasurfaces [278, 279]. Even stronger field confinement in hybrid metasurfaces proposed here can further boost the efficiency of various nonlinear optical effects.

As an example, we employ the local field enhancement associated with the excitation of subradiant plasmonic mode in graphene for nonlinear frequency conversion and study the resonant second-harmonic generation (SHG) caused by a quadratic nonlocal nonlinearity of graphene. The nonlinear surface current induced in graphene by the incident wave of the fundamental frequency (FF) ω, at the double frequency 2ω has the form $j_i(2\omega) = \sigma^{(2)}_{ijkl}(\omega) E^{\omega}_j \nabla_k E^{\omega}_l$, where i, j, k, l are the Cartesian components. It depends on the gradient of FF electric field at the graphene surface, and it can be expressed through the second-order conductivity tensor [126],

$$\sigma^{(2)}_{ijkl}(\omega) = \frac{ie^3 v_F^2}{8\pi\hbar^2\omega^3}(5\delta_{ij}\delta_{kl} - 3\delta_{ik}\delta_{jl} + \delta_{il}\delta_{jk}),$$

which is derived within the quasi-classical approach based on the Boltzmann equation [23, 88, 91, 125], applicable at low frequencies $\hbar\omega \leq \mathcal{E}_F$ corresponding to the plasmonic regime (see Appendix A). In what follows, we neglect nonlinearity in the metal.

The nonlinear response of the metasurface is simulated in COMSOL Multiphysics with the use of two coupled electromagnetic models assuming undepleted pump field. As the first step, we perform simulations at the fundamental (pump) wavelength 10.65 μm (matching one of the radiation lines of CO_2 laser) and stimulating excitation of graphene plasmon resonance in the SRR gap for the doping level $\mathcal{E}_F = 0.31$ eV. Next, the nonlinear current

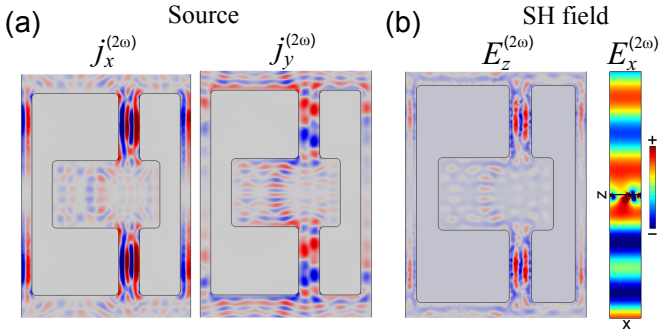

Figure 4.16: (a) Nonlinear source and (b) SH fields generated by the hybrid metasurface; the z-component of the electric field is evaluated 40 nm above the graphene layer (left), and a side-view of the x-component evaluated in the middle of the SRR gap (right).

induced at every point on the graphene surface for the second-harmonic (SH) frequency is calculated. This current is employed as a nonlinear source for the electromagnetic simulation and the SH fields generated by this current are obtained.

As expected, SHG predominantly arises from the gap, where the field of the asymmetric plasmonic mode is localized and strongly enhanced. The calculated nonlinear current generated by this subradiant mode is found to have the dominant x-component driving the entire metasurface at the SH frequency. As confirmed by numerical simulations shown in Fig. 4.16, this results in a non-vanishing nonlinear dipole moment aligned along x axis within the SRR gaps, which leads to the generation of a x-polarized plane wave in the far-field region. It is interesting that the SH wave appears to be cross-polarized with respect to y-polarized incident plane wave at the fundamental frequency, indicating the nonlinear polarization conversion. We find that due to the strong field enhancement associated with two complementary trapping mechanisms of electromagnetic field, namely the plasmonic confinement and a subradiant character of the plasmonic mode, the structure exhibits high efficiency of nonlinear conversion $\sim 10^{-6}$ at the incident wave intensity of 1 MW/cm^2 even without matching to any resonances at the SH frequency [277,280].

Summary

We have proposed a novel type of graphene-based metasurfaces exhibiting cascaded Fano resonances originating from the coupling of standing graphene plasmons and the modes of structured metasurfaces. We have shown that such hybrid metasurfaces allow high tunability of the subradiant modes facilitated by controllable intermodal coupling. Such tunable interaction between subradiant modes, achieved though graphene doping, enables controlling the spectral position and lifetime of the Fano resonances. By utilizing two complementary mechanisms of light confinement originating in the subwavelength localization and subradiant nature of the engineered graphene plasmonic modes, we have shown tunable and enhanced light-matter interaction. In particular, a significant enhancement of light absorption and nonlinear effects have been demonstrated. The proposed concept envisions tunable nonlinear response of either graphene or any nonlinear materials sputtered on top of the metasurfaces supporting cascaded Fano resonances. The demonstrated possibility to enhance and switch the second-harmonic generation by graphene gating can be used in various applications, e.g. for the efficient generation of short pulses of the second-harmonic field.

Chapter 5

Conclusions

The rapidly growing demands of modern technologies in globally important applications, such as telecommunication, data processing and information storage, biomedical diagnostics and security screening, have launched a race for materials with highly tunable and controllable optical response even in subwavelength dimensions. Recent progress in nanotechnologies permits fabricating artificial nanostructures with pre-engineered properties exhibiting specific interaction with light. Employing plasmonic materials facilitates strong light-matter interaction at the nanoscale giving rise to the resonant effects achievable with moderate incoming intensities of light. High electromagnetic field confinement feasible in plasmonic systems may further lead to manifestations of the nonlinear optical response bringing many novel capabilities of all-optical light control. The development of ideas for promising optical nanodevices utilizing various kinds of optical nonlinearities lies within the scope of contemporary nonlinear nanophotonics.

In this thesis, we addressed a number of concrete problems which appear in nonlinear nanophotonics of plasmonic structures and present detailed derivations of the analytical models that give us deep physical insight.

As we demonstrated with our model in Chapter 2, arrays of resonant plasmonic nanoparticles and doped graphene flakes exhibit interesting nonlinear polarization dynamics and generation of plasmonic kinks, Faraday ripples and solitons that can be applied to construct narrow guiding subwavelength elements and to realize the soliton-based routing in assemblies of metal nanoparticles or optoelectronic circuits based on nanostructured graphene.

As a result of our research presented in Chapters 3 and 4, several nonlinear effects with graphene plasmons have been predicted and studied. It was revealed that graphene-based structures can exhibit a range of practically important effects, including the generation of subwavelength spatial plasmon-solitons and discrete nonlinear plasmonic modes in graphene waveguides/metamaterials, and efficient frequency conversion in different graphene-enhanced settings. We have shown that being an easily integrable one-atom-thin strongly nonlinear material with exceptional tunability of properties, graphene can be of significant interest for nanoscale nonlinear optics, especially, in combination with plasmonic effects. All our conclusions originate from a theoretical analysis performed by means of justified approaches and accompanied with numbers taken from the current experimental data. On this basis, there are expectations for an experimental observation of predicted nonlinear phenomena that can be used to design subwavelength nonlinear elements with graphene able to operate in the THz and infrared frequency ranges.

With the active development of techniques to produce high-quality graphene samples, the ideas for photonic applications of graphene are already tested experimentally in the

leading research groups head by D. Basov, F. Koppens, S. Ganichev and H. Altug, to name a few. To better match the experiment, further refinements of the theoretical models developed here may be performed taking account of irregularities in the parameters introducing disorder, and applying more involved methods of condensed matter theory.

Overall, we believe that our findings may pave a way towards the further experimental studies of nonlinear effects in graphene-based and plasmonic nanostructures which could have important implications for nanophotonic devices operating beyond the diffraction limit.

Statement

This thesis is based on 12 published journal papers. In Secs. 2.3, 3.1–3.4, 4.1–4.3, I developed theoretical models, conducted numerical analysis and wrote the first drafts of the papers; Yu. S. Kivshar provided a guidance to the theory; all coauthors discussed the results and contributed to writing the manuscripts. R. E. Noskov and Yu. V. Bludov suggested the ideas and theoretical concepts for the works presented in Secs. 2.1, 2.2 and Sec. 3.5, respectively. The work reported in Sec. 4.4 was done in close collaboration with A. B. Khanikaev.

Appendix A

Nonlinear conductivities of graphene

For the sake of clarity, here we extract a brief summary on the *Kinetic equation method* and nonlinear conductivities for surface plasmons in graphene.

Generally, if we are interested in the response to the harmonic electric field ($\propto e^{-i\omega t}$), a wide range of possible nonlinear effects in different orders can be illustratively captured by the simplistic formula for the nonlinear current induced in graphene

$$\mathbf{j}(\mathbf{r},t) = \underbrace{\hat{\sigma}\mathbf{E}}_{\substack{\text{Ohm's law} \\ \propto e^{-i\omega t}}} + \underbrace{\hat{\sigma}^{(2')}\mathbf{E}\otimes\mathbf{E}^*}_{\text{DC current}} + \underbrace{\hat{\sigma}^{(2)}\mathbf{E}\otimes\mathbf{E}}_{\substack{\text{second harmonic} \\ \propto e^{-2i\omega t}}} + \underbrace{\hat{\sigma}^{(3)}\mathbf{E}\otimes\mathbf{E}\otimes\mathbf{E}}_{\substack{\text{third harmonic} \\ \propto e^{-3i\omega t}}} + \underbrace{\hat{\sigma}^{(\mathrm{NL})}\mathbf{E}\otimes\mathbf{E}^*\otimes\mathbf{E}}_{\substack{\text{self-action} \\ \propto e^{-i\omega t}}} \ldots,$$

which underlines, apart from a linear current, the DC current and SHG in the second order, and the self-action effect and THG in the third order, expressed through the field's multiplications and the respective conductivity operators. This expression constitutes an asymptotic expansion of the current in a series with respect to the electric field, assuming the weak electron response in graphene.

To describe nonlinear properties of doped graphene, we employ the quasi-classical description based on the solution of the Boltzmann equation [23,87–90,92,93,110,125,126,281]. This approach is applicable at low frequencies, $\hbar\omega \leq \mathcal{E}_F$, encompassing the plasmonic regime. In the relaxation time approximation, graphene charge-carriers transport properties are governed by the kinetic equation written for the electron distribution function $f(\mathbf{r},\mathbf{p},t)$:

$$\frac{\partial f}{\partial t} + \mathbf{v}_\mathbf{p}\frac{\partial f}{\partial \mathbf{r}} + e\left(\mathbf{E} + \frac{1}{c}[\mathbf{v}_\mathbf{p}\times\mathbf{B}]\right)\frac{\partial f}{\partial \mathbf{p}} = -\gamma\left[f(\mathbf{p},t) - f_0(\mathbf{p})\right], \tag{A.1}$$

where for Dirac's massless quasi-particles $\mathbf{v}_\mathbf{p} = \dfrac{\partial \mathcal{E}}{\partial \mathbf{p}} = v_F\dfrac{\mathbf{p}}{|\mathbf{p}|}$, the energy $\mathcal{E} = v_F p$, $v_F \approx c/300$ is the Fermi velocity, and $e = -|e|$ is the charge, $f_0(\mathbf{p})$ is the equilibrium Fermi-Dirac distribution function (assuming for the degenerate electrons at zero temperature the step-like Fermi-Dirac distribution function), and $\gamma \equiv \tau_{\text{intra}}^{-1}$ is the inverse relaxation time. Here, the second term is responsible for spatial variations.

In the *homogeneous* case, and if there is no component of magnetic field normal to the graphene surface, i.e. $B_n = 0$, Eq. (A.1) can be solved analytically, and its *exact* solution is given by [87,110,281]

$$f(\mathbf{p},t) = f_0[\mathbf{p} - \mathbf{p}_0(t)]e^{-\gamma t} + \gamma e^{-\gamma t}\int_{-\infty}^{t} dt' e^{\gamma t'} f_0[\mathbf{p} - \mathbf{p}_0(t) + \mathbf{p}_0(t')], \tag{A.2}$$

where $\mathbf{p}_0(t) = e\int_0^t \mathbf{E}(t'')dt''$ is the classical momentum. The induced 2D current in graphene is expressed through the function

$$\mathbf{j} = 4e\sum_{\mathbf{p}} \mathbf{v}_{\mathbf{p}} f_\omega(\mathbf{p}) = -\frac{4e}{(2\pi\hbar)^2}\int d\mathbf{p}\, f(\mathbf{p},t)\,\frac{\partial \mathcal{E}\,(\mathbf{p})}{\partial \mathbf{p}}\,. \tag{A.3}$$

In particular, for the normally incident harmonic radiation with the electric field of the form $\mathbf{E} = \mathbf{E}_0\exp(-i\omega t)$, at $t \gg \gamma^{-1}$, Eq. (A.3) leads to the following expression for the induced current (up to the third order) [87,110,281]

$$\mathbf{j} = \left[\sigma(\omega) + \sigma^{\mathrm{NL}}(\omega)E_0^2\right]\mathbf{E}_0\exp(-i\omega t) + \sigma_3(\omega)E_0^2\mathbf{E}_0 e^{-3i\omega t}\,, \tag{A.4}$$

where, in the limit $\omega/\gamma \gg 1$,

- linear intra-band Drude conductivity in the low-loss case

$$\sigma_{\mathrm{intra}}(\omega) = \frac{ie^2}{\pi\hbar^2}\frac{\mathcal{E}_F}{\omega}\,, \tag{A.5}$$

- Kerr-type self-action nonlinear correction to the graphene conductivity (considered earlier in Refs. [89,90] for the ballistic regime)

$$\sigma^{\mathrm{NL}}(\omega) = -i\frac{9}{8}\frac{e^2}{\pi\hbar^2}\left(\frac{ev_F}{\mathcal{E}_F\omega}\right)^2\frac{\mathcal{E}_F}{\omega}, \tag{A.6}$$

- third-harmonic conductivity σ_3

$$\sigma_3(\omega) = i\frac{1}{8}\frac{e^2}{\pi\hbar^2}\left(\frac{ev_F}{\mathcal{E}_F\omega}\right)^2\frac{\mathcal{E}_F}{\omega}. \tag{A.7}$$

We can use the result (A.6), obtained as seen by free-space light normally incident on a graphene layer, for the effective self-action nonlinear conductivity of surface plasmons propagating along graphene layers, assuming the additional correction due to the in-plane wavevector k_{sp} to be small, which is well-justified if $k_{\mathrm{sp}}/(\omega/c) \ll 300$.

We now methodologically derive expressions for nonlinear conductivities taking into account an in-plane plasmon momentum, which results in a nonzero quadratic conductivity and enables SHG in graphene.

In the collisionless limit, the electron distribution function satisfies the kinetic equation rewritten as

$$\frac{\partial f}{\partial t} + \mathbf{v}_{\mathbf{p}}\frac{\partial f}{\partial \mathbf{r}} + e\left(\mathbf{E} + \frac{1}{c}[\mathbf{v}_{\mathbf{p}}\times\mathbf{B}]\right)\frac{\partial f}{\partial \mathbf{p}} = 0\,. \tag{A.8}$$

Following the *perturbation approach* [23,88,91,133], we solve this equation using iterations. Here we consider the case of *p*-plasmons or TM-polarized incident waves with the tangential electric field component of the form $\mathbf{E}_\omega = E\mathbf{z}_0 e^{iqz}$ (and $qv_F/\omega \ll 1$). To make it consistent with Section 4.3, we assume that a graphene monolayer is placed in the plane yz and the in-plane electric field is directed along the z axis. We note that in this case $B_n = 0$. Because of the graphene nonlinearity, the field $\mathbf{E}_\omega$ excites higher harmonics. We look for the distribution function in the form

$$f = f_0(\mathcal{E}) + f_0^{(2)} + (f_\omega^{(1)} + f_\omega^{(3)})e^{-i(\omega t - qz)} + \text{c.c.} + f_{2\omega}^{(2)}e^{-2i(\omega t-qz)} + \text{c.c.} + f_{3\omega}^{(3)}e^{-3i(\omega t-qz)} + \text{c.c.}\ldots\,, \tag{A.9}$$

where $f_0(\mathcal{E})$ is the Fermi-Dirac distribution (steplike at low temperatures, $k_BT \ll \mathcal{E}_F$), $f_\omega^{(1)}$, $f_{2\omega}^{(2)}$, $f_{3\omega}^{(3)}$ are the first, the second, and third order oscillating corrections (the superscripts are omitted below), respectively, whereas the tangential electric field is as follows:

$$\mathbf{E}_\tau = \mathbf{E}_\omega e^{-i(\omega t - qz)} + \text{c.c.} + \mathbf{E}_{2\omega} e^{-2i(\omega t - qz)} + \text{c.c.} + \mathbf{E}_{3\omega} e^{-3i(\omega t - qz)} + \text{c.c.} + \dots . \tag{A.10}$$

The electric current density at frequency ω is given by the first-order correction to the Fermi-Dirac distribution function,

$$\mathbf{j}_\omega = 4e \sum_{\mathbf{p}} \mathbf{v}_\mathbf{p} f_\omega(\mathbf{p}) = 4e \iint \frac{dp_y dp_z}{(2\pi\hbar)^2} v_{p_z} f_\omega \mathbf{z}_0 \,,$$

where

$$f_\omega = \frac{e\left(\dfrac{\partial f_0}{\partial \mathbf{p}} \mathbf{E}_\omega\right)}{i(\omega - v_{p_z} q)} \approx \frac{1}{i\omega}\left(1 + \frac{v_{p_z} q}{\omega}\right) eE \frac{p_z}{p} \frac{\partial f_0}{\partial p} \,. \tag{A.11}$$

Therefore, the first-order current amplitude can be written as follows:

$$\begin{aligned} j_{\omega_z} &= \iint 4e v_{p_z} \left(\frac{eE}{i\omega} \frac{p_z}{p} \frac{\partial f_0}{\partial p}\right) \frac{dp_y dp_z}{(2\pi\hbar)^2} \\ &= \int_0^\infty \frac{p dp}{(2\pi\hbar)^2} \int_0^{2\pi} d\Theta \left(\frac{4e^2 E}{i\omega} \frac{\partial f_0}{\partial p}\right) v_F \cos^2\Theta = \frac{ie^2}{\pi\hbar^2} \frac{\mathcal{E}_F}{\omega} E \,, \end{aligned} \tag{A.12}$$

where the double integral in Cartesian coordinates $\{p_z, p_y\}$ is converted to an iterated integral in polar coordinates $\{p, \Theta\}$. This is a known result [89]. In the local semiclassical limit, the linear conductivity of graphene can be reduced to the Drude model (A.5), which only takes into account intraband processes. It can also be corrected to include relaxation, $\sigma_{\text{intra}}(\omega) = \dfrac{ie^2}{\pi\hbar^2} \dfrac{\mathcal{E}_F}{\left(\omega + i\tau_{\text{intra}}^{-1}\right)}$.

The second-order correction, expressed as

$$\begin{aligned} f_{2\omega} &= \frac{eE \dfrac{\partial f_\omega}{\partial p_z}}{2i(\omega - v_{p_z} q)} \approx \frac{1}{2i\omega}\left(1 + \frac{v_{p_z} q}{\omega}\right) eE \frac{\partial}{\partial p_z}\left(\frac{1}{i\omega}\left(1 + \frac{v_{p_z} q}{\omega}\right) eE \frac{p_z}{p} \frac{\partial f_0}{\partial p}\right) \approx \\ &- \frac{1}{2\omega^2} e^2 E^2 \frac{\partial}{\partial p_z}\left(\frac{p_z}{p} \frac{\partial f_0}{\partial p}\right) - \frac{1}{2\omega^2} e^2 E^2 \left(\frac{v_{p_z} q}{\omega} \frac{\partial}{\partial p_z}\left(\frac{p_z}{p} \frac{\partial f_0}{\partial p}\right) + \frac{\partial}{\partial p_z}\left[\frac{v_{p_z} q}{\omega} \frac{p_z}{p} \frac{\partial f_0}{\partial p}\right]\right) , \end{aligned} \tag{A.13}$$

gives rise to the electric current density at 2ω, $\mathbf{j}_{2\omega} = 4e \sum\limits_{\mathbf{p}} \mathbf{v}_\mathbf{p} f_{2\omega}(\mathbf{p})$. Integrating the first term in Eq. (A.13) returns zero, while integrating the second term leads to the following formula:

$$\begin{aligned} j_{2\omega_z} = -4e \left(\frac{e^2 E^2}{2\omega^2}\right) \frac{q}{\omega} \int_0^\infty \frac{p dp}{(2\pi\hbar)^2} \int_0^{2\pi} d\Theta v_F \cos\Theta \Bigg[v_F \cos\Theta \\ \times \left(\cos\Theta \frac{\partial}{\partial p} - \frac{\sin\Theta}{p} \frac{\partial}{\partial \Theta}\right)\left(\cos\Theta \frac{\partial f_0}{\partial p}\right) + \left(\cos\Theta \frac{\partial}{\partial p} - \frac{\sin\Theta}{p} \frac{\partial}{\partial \Theta}\right)\left(v_F \cos^2\Theta \frac{\partial f_0}{\partial p}\right)\Bigg] , \end{aligned} \tag{A.14}$$

which can be reduced to

$$j_{2\omega_z} = -\frac{3}{8} \frac{e^3 v_F^2}{\pi\hbar^2 \omega^3} q E^2 \,. \tag{A.15}$$

Thereby, we obtain the nonlinear source

$$\mathbf{j}_{2\omega} = -\mathbf{z}_0 \frac{3}{8} \frac{e^3 v_F^2}{\pi \hbar^2 \omega^3} q E^2 \exp(-i2\omega t + i2qz)\,, \tag{A.16}$$

which is in agreement with the earlier results [23, 91, 125]. Thus, considering frequency conversion with plasmons, the quadratic conductivity of graphene $\sigma_2(\omega)$ can be defined as follows

$$\sigma_2(\omega) = -\frac{3}{8} \frac{e^3 v_F^2}{\pi \hbar^2 \omega^3} q, \tag{A.17}$$

where $q = k_{\rm sp}(\omega)$ is the plasmon wavenumber supported by a waveguide at ω.

Next, the third-order correction is derived as

$$f_{3\omega} = \frac{1}{3i(\omega - v_{p_z} q)} \left(eE_\omega \frac{\partial f_{2\omega}}{\partial p_z} + eE_{2\omega} \frac{\partial f_\omega}{\partial p_z} \right) \equiv f_{3\omega}^{(\rm I)} + f_{3\omega}^{(\rm II)}\,. \tag{A.18}$$

To obtain the contribution to the third harmonic current $\mathbf{j}_{3\omega} = 4e \sum\limits_{\mathbf{p}} \mathbf{v}_{\mathbf{p}} f_{3\omega}(\mathbf{p})$ from the first term,

$$f_{3\omega}^{(\rm I)} = \frac{1}{3i(\omega - v_{p_z} q)} eE_\omega \frac{\partial f_{2\omega}}{\partial p_z}, \tag{A.19}$$

we expand this term as follows

$$\begin{aligned} f_{3\omega}^{(\rm I)} = {} & \frac{1}{3i\omega} \left[1 + \frac{v_{p_z} q}{\omega} + \left(\frac{v_{p_z} q}{\omega} \right)^2 \right] eE_\omega \\ & \times \frac{\partial}{\partial p_z} \left[\frac{1}{2i\omega} \left[1 + \frac{v_{p_z} q}{\omega} + \left(\frac{v_{p_z} q}{\omega} \right)^2 \right] eE_\omega \frac{\partial}{\partial p_z} \left(\frac{1}{i\omega} \left[1 + \frac{v_{p_z} q}{\omega} + \left(\frac{v_{p_z} q}{\omega} \right)^2 \right] eE_\omega \frac{p_z}{p} \frac{\partial f_0}{\partial p} \right) \right]. \end{aligned} \tag{A.20}$$

Here, integrating the expressions proportional to q^1 returns zero. After integrating the terms proportional to q^0 and q^2, the current amplitude can be written as

$$j_{3\omega_z}^{(\rm I)} = \sigma_3(\omega) E_\omega^3 = \left[\sigma_3(\omega, q = 0) + \Delta\sigma_3(\omega, q) \right] E_\omega^3\,, \tag{A.21}$$

where the third-order conductivity, in the homogeneous case [87, 89, 90, 110] given by

$$\sigma_3(\omega, q = 0) = i \frac{1}{8} \frac{e^2}{\pi \hbar^2} \left(\frac{e v_F}{\mathcal{E}_F \omega} \right)^2 \frac{\mathcal{E}_F}{\omega} = i \frac{1}{8} \frac{e^4}{\pi \hbar^2} \frac{v_F^2}{\mathcal{E}_F \omega^3}\,, \tag{A.22}$$

is corrected by an additional term

$$\Delta\sigma_3(\omega, q) = i \frac{5}{16} \frac{e^4}{\pi \hbar^2} \frac{v_F^2}{\mathcal{E}_F \omega^3} \left(\frac{q v_F}{\omega} \right)^2 = \frac{5}{2} \sigma_3(\omega, q = 0) \left(\frac{q v_F}{\omega} \right)^2. \tag{A.23}$$

Further, by analogy with the second-harmonic contribution $f_{2\omega}$, we derive the third-harmonic current corresponding to the second term in Eq. (A.18),

$$f_{3\omega}^{(\rm II)} = \frac{1}{3i(\omega - v_{p_z} q)} eE_{2\omega} \frac{\partial f_\omega}{\partial p_z} = \frac{1}{3i\omega} \left(1 + \frac{v_{p_z} q}{\omega} \right) eE_{2\omega} \frac{\partial}{\partial p_z} \left(\frac{1}{i\omega} \left(1 + \frac{v_{p_z} q}{\omega} \right) eE_\omega \frac{p_z}{p} \frac{\partial f_0}{\partial p} \right), \tag{A.24}$$

and get the z projection of the nonlinear current in the form

$$j_{3\omega_z}^{(\rm II)} = \frac{2}{3} \sigma_2(\omega) E_{2\omega} E_\omega\,, \tag{A.25}$$

which entirely corresponds to the cascaded process in THG studied in Section 4.3.

Appendix B

On the derivation of amplitude equations for graphene plasmons

In this thesis we several times refer to the equations for the envelopes of surface modes supported by graphene layers. Here we sketch the procedure of the derivation of those equations with an example of TM-polarized surface plasmon propagating along the graphene monolayer placed in the plane $x = 0$. Accepting harmonic $\exp(-i\omega t)$ time-dependence, Maxwell's equations for this geometry can be written as follows

$$\nabla \times \mathbf{E} = ik_0\mathbf{H}\,, \tag{B.1a}$$

$$\nabla \times \mathbf{H} = -ik_0\varepsilon(x)\mathbf{E} + \frac{4\pi}{c}\delta(x)\sigma(\omega)\mathbf{E}_\tau\,, \tag{B.1b}$$

where $k_0 = \omega/c$ is the wavenumber in free space, $\sigma(\omega) = i\sigma^{(I)}(\omega) + \sigma^{(R)}(\omega) + \sigma^{\mathrm{NL}}(\omega)|E_\tau|^2 \equiv i\sigma^{(I)} + \tilde{\sigma}$ is the frequency-dependent surface conductivity of graphene, the function $\varepsilon(x)$ describes the dielectric permittivity distribution,

$$\varepsilon(x) = \begin{cases} \varepsilon_2\,, & x < 0, \\ \varepsilon_1\,, & x > 0. \end{cases} \tag{B.2}$$

The Dirac delta-function $\delta(x)$ in Eqs. (B.5) indicates that the graphene layer is placed at $x = 0$, and the subscript τ refers to the field component tangential to the surface.

To develop the consistent perturbation theory, we introduce a small parameter μ, assuming the losses in graphene, nonlinearity and diffraction to be weak,

$$\mu^2 = \max\left\{(k_{\mathrm{sp}}\Lambda)^{-2}, \left|\frac{\sigma^{(R)}}{\sigma^{(I)}}\right|, \left|\frac{\sigma^{\mathrm{NL}}|E_\tau|^2}{\sigma^{(I)}}\right|\right\},$$

where Λ is the wave localization width in the y direction, and k_{sp} is the plasmon wavenumber for propagating solutions with fast $\exp(ik_{\mathrm{sp}}z)$ dependence.

In the zero order in μ, Eqs. (B.5) return the dispersion relation

$$\frac{\varepsilon_1}{\kappa_1} + \frac{\varepsilon_2}{\kappa_2} = \frac{4\pi}{\omega}\sigma^{(I)}(\omega)\,, \tag{B.3}$$

where $\kappa_{1,2} = \left(k_{\mathrm{sp}}^2 - k_0^2\varepsilon_{1,2}\right)^{1/2}$, and transverse profile for the unperturbed plasmon on a

flat graphene,

$$h(x) = -ik_0 \begin{cases} \varepsilon_1 e^{-\kappa_1 x}/\kappa_1, & x > 0\,, \\ -\varepsilon_2 e^{\kappa_2 x}/\kappa_2, & x < 0\,. \end{cases} \tag{B.4}$$

Choosing for definiteness the unit in-plane electric field at the graphene surface $e_z(x=0) = 1$, the fields can be written as follows

$$\begin{cases} \mathbf{E}_0 = (e_x(x)\mathbf{x}_0 + e_z(x)\mathbf{z}_0)e^{ik_{\mathrm{sp}}z}\,, \\ \mathbf{H}_0 = h(x)e^{ik_{\mathrm{sp}}z}\mathbf{y}_0\,. \end{cases} \tag{B.5}$$

For $\mu^2 \ll 1$, the solution of Eqs. (B.5) can be sought in the form

$$\begin{aligned} \mathbf{E} &= \mathsf{A}(\mu^2\mathsf{y}, \mu\mathsf{z})\mathbf{E}_0 + \mu\mathbf{E}_1(\mu^2\mathsf{y}, \mu\mathsf{z}, x) + \mu^2\mathbf{E}_2(\mu^2\mathsf{y}, \mu\mathsf{z}, x) + \ldots \\ &= \mathcal{A}(y,z)\mathbf{E}_0 + \mathbf{E}_1(y,z,x) + \mathbf{E}_2(y,z,x) + \ldots \qquad \text{(B.6a)} \\ \mathbf{H} &= \mathsf{A}(\mu^2\mathsf{y}, \mu\mathsf{z})\mathbf{H}_0 + \mu\mathbf{H}_1(\mu^2\mathsf{y}, \mu\mathsf{z}, x) + \mu^2\mathbf{H}_2(\mu^2\mathsf{y}, \mu\mathsf{z}, x) + \ldots \\ &= \mathcal{A}(y,z)\mathbf{H}_0 + \mathbf{H}_1(y,z,x) + \mathbf{H}_2(y,z,x) + \ldots \qquad \text{(B.6b)} \end{aligned}$$

where $\mathcal{A}(z,y)$ is slowly varying amplitude of the propagating plasmonic mode.

I. First, we consider the y-independent case, i.e. $\Lambda \to \infty$ and $\dfrac{\partial \mathcal{A}}{\partial y} = 0$, and thus, $\mathbf{E}_1 = 0$, $\mathbf{H}_1 = 0$ in the order $O(\mu)$. For the second-order corrections $\mathbf{E}_2$, $\mathbf{H}_2$ we get the following equations

$$\nabla \times \mathbf{E}_2 = ik_0\mathbf{H}_2 - \frac{\partial \mathcal{A}}{\partial z}\left[\mathbf{z}_0 \times \mathbf{E}_0\right]\,, \tag{B.7a}$$

$$\nabla \times \mathbf{H}_2 = -ik_0\varepsilon(x)\mathbf{E}_2 + \frac{4\pi}{c}i\sigma^{(I)}\delta(x)E_{2_z}\mathbf{z}_0 - \frac{\partial \mathcal{A}}{\partial z}\left[\mathbf{z}_0 \times \mathbf{H}_0\right] + \frac{4\pi}{c}\mathcal{A}\tilde{\sigma}\delta(x)E_{2_z}\mathbf{z}_0\,. \tag{B.7b}$$

Substracting Eq. (B.7b) multiplyed by $\mathbf{E}_0^*$ from Eq. (B.7a) multiplyed by $\mathbf{H}_0^*$ gives

$$\begin{aligned} \mathbf{H}_0^*\mathrm{rot}\mathbf{E}_2 - \mathbf{E}_0^*\mathrm{rot}\mathbf{H}_2 =& ik_0\mathbf{H}_0\mathbf{H}_0^* - \frac{\partial \mathcal{A}}{\partial z}[\mathbf{z}_0 \times \mathbf{E}_0]\mathbf{H}_0^* + \frac{\partial \mathcal{A}}{\partial z}[\mathbf{z}_0 \times \mathbf{H}_0]\mathbf{E}_0^* - \frac{4\pi}{c}\tilde{\sigma}\delta(x)|E_{0_z}|^2\mathcal{A} \\ &+ ik_0\varepsilon(x)\mathbf{E}_2\mathbf{E}_0^* - \frac{4\pi}{c}i\sigma^{(I)}\delta(x)E_{2_z}E_{0_z}^*\,. \end{aligned} \tag{B.8}$$

We also take into account the following relations

$$\mathbf{H}_0^*\mathrm{rot}\mathbf{E}_2 - \mathbf{E}_0^*\mathrm{rot}\mathbf{H}_2 = \mathrm{div}\left\{[\mathbf{E}_2 \times \mathbf{H}_0^*] - [\mathbf{H}_2 \times \mathbf{E}_0^*]\right\} + \mathbf{E}_2\mathrm{rot}\mathbf{H}_0^* - \mathbf{H}_0\mathrm{rot}\mathbf{E}_0^* \tag{B.9}$$

and

$$\begin{aligned} \nabla \times \mathbf{E}_0^* &= -ik_0\mathbf{H}_0^*\,, \\ \nabla \times \mathbf{H}_0^* &= ik_0\varepsilon(x)\mathbf{E}_0^* - \frac{4\pi}{c}i\sigma^{(I)}\delta(x)\mathbf{E}_{0_z}^*\mathbf{z}_0\,. \end{aligned} \tag{B.10}$$

Substituting Eqs. (B.10) into Eq. (B.9) and then into the left-hand side of Eq. (B.8), we find

$$\mathrm{div}\left\{[\mathbf{E}_2 \times \mathbf{H}_0^*] + [\mathbf{H}_2 \times \mathbf{E}_0^*]\right\} = -\frac{\partial \mathcal{A}}{\partial z}\left\{[\mathbf{E}_0 \times \mathbf{H}_0^*] + [\mathbf{H}_0 \times \mathbf{E}_0^*]\right\} - \frac{4\pi}{c}\tilde{\sigma}\delta(x)|E_{0_z}|^2\mathcal{A}\,. \tag{B.11}$$

Overintegrating Eq. (B.11) in x from zero to infinity leads to the desired equation for the plasmon amplitude $\mathcal{A}$:

$$\frac{\partial \mathcal{A}}{\partial z} + \frac{\tilde{\sigma}}{4P}\mathcal{A} = 0\,, \tag{B.12}$$

where

$$P = \mathbf{z}_0 \cdot \frac{c}{8\pi} \operatorname{Re} \int_{-\infty}^{+\infty} [\mathbf{E}_0 \times \mathbf{H}_0^*]\, dx = \frac{c}{8\pi} \operatorname{Re} \int_{-\infty}^{+\infty} e_x(x) h^*(x) dx$$

is the z-projection of the energy flow in the mode $\{\mathbf{E}_0, \mathbf{H}_0\}$ per unit y-length.

In the case of y-localized solutions, accounting for the terms proportional to derivative $\dfrac{\partial \mathcal{A}}{\partial y}$ of the first order in μ results in the substitution $\dfrac{\partial}{\partial z} \longrightarrow \dfrac{\partial}{\partial z} + \dfrac{1}{2ik_{\rm sp}} \dfrac{\partial^2}{\partial y^2}$ in Eq. (B.12). The method described is the development and conformation of the theory of excitation for waveguides [134, 135].

II. Another method, based on applying the Fredholm theorem to the correction $\mathbf{H}_2 = H_2 \mathbf{y}_0$, was used by us in the case of the symmetric dielectric environment, $\varepsilon_1 = \varepsilon_2 = \varepsilon$. The field correction $\mathbf{H}_1 = H_1 \mathbf{z}_0$ of the first order in μ is determined from $\nabla \cdot \mathbf{H} = 0$.

Taking the curl of Eq. (B.1b) and substituting expansion (B.6b) there, we obtain the following equation for the correction H_2

$$\frac{d^2 H_2}{dx^2} + \left(k_0^2 \varepsilon - k_{\rm sp}^2\right) H_2 - \frac{4\pi}{c} i\sigma^{(I)} \left(\frac{d}{dx} \delta(x) E_{2_z}\right) = F\,, \tag{B.13}$$

where

$$\begin{aligned} F &= -\left(2ik_{\rm sp} \frac{\partial \mathcal{A}}{\partial z} + \frac{\partial^2 \mathcal{A}}{\partial y^2}\right) h(x) + \mathcal{A} \frac{4\pi}{c} \tilde{\sigma} \frac{d}{dx} \left(\delta(x) e_z\right)\,, \\ e_z &= \frac{\dfrac{dh}{dx}}{ik_0 \varepsilon + \dfrac{4\pi}{c} i\sigma^{(I)} \delta(x)}\,, \qquad E_{2_z} = \frac{\dfrac{\partial H_2}{\partial x} - e_z \dfrac{4\pi}{c} \tilde{\sigma} \delta(x) \mathcal{A}}{ik_0 \varepsilon + i \dfrac{4\pi}{c} \sigma^{(I)} \delta(x)}\,. \end{aligned} \tag{B.14}$$

Operating with the Dirac delta function in our derivation here, we treat it as an ordinary localized continuous function. Integrating by parts, we first obtain the following auxilary relations:

$$\begin{aligned} &\int_{-\infty}^{+\infty} \frac{d^2 H_2}{dx^2} h^*(x) dx = \int_{-\infty}^{+\infty} H_2 \frac{d^2 h^*}{dx^2} dx\,, \\ &\int_{-\infty}^{+\infty} h^* \left(\frac{d}{dx} \delta(x) E_{2_z}\right) dx = -\int_{-\infty}^{+\infty} \frac{dh^*}{dx} \delta(x) E_{2_z} dx = -\int_{-\infty}^{+\infty} \frac{dh^*}{dx} \delta(x) \frac{\dfrac{\partial H_2}{\partial x} - e_z \dfrac{4\pi}{c} \tilde{\sigma} \delta(x) \mathcal{A}}{i\left(k_0 \varepsilon + \dfrac{4\pi}{c} \sigma^{(I)} \delta(x)\right)} dx \\ &= \int_{-\infty}^{+\infty} e_z^* \delta(x) \left(\frac{\partial H_2}{\partial x} - e_z \frac{4\pi}{c} \tilde{\sigma} \delta(x) \mathcal{A}\right) dx = -\int_{-\infty}^{+\infty} \left(H_2 \frac{d}{dx} (e_z^* \delta(x)) + |e_z|^2 \frac{4\pi}{c} \tilde{\sigma} \delta^2(x) \mathcal{A}\right) dx\,, \end{aligned} \tag{B.15}$$

We now multiply Eq. (B.13) by $h^*(x)$ and integrate, assuming $H_2(x)$ is localized in x function. By using Eqs. (B.15) and integrating by parts, we get

$$\begin{aligned} &\int_{-\infty}^{+\infty} H_2 \left(\frac{d^2 h^*}{dx} + (k_0^2 \varepsilon - k_{sp}^2) h^* + \frac{4\pi}{c} i\sigma^{(I)} \frac{d}{dx} (\delta(x) e_z^*)\right) dx + i \int_{-\infty}^{+\infty} \sigma^{(I)} \left(\frac{4\pi}{c}\right)^2 \mathcal{A} |e_z|^2 \delta^2(x) dx \\ &= \left(2ik_{\rm sp} \frac{\partial \mathcal{A}}{\partial z} + \frac{\partial^2 \mathcal{A}}{\partial y^2}\right) \int_{-\infty}^{+\infty} |h(x)|^2 dx + \mathcal{A} \frac{4\pi}{c} \tilde{\sigma} \int_{-\infty}^{+\infty} i \left(k_o \varepsilon + \frac{4\pi}{c} \sigma^{(I)} \delta(x)\right) |e_z|^2 \delta(x) dx\,. \end{aligned} \tag{B.16}$$

The first term in the left-hand side of Eq. (B.16) returns zero, and Eq. (B.16) is transformed to

$$\left(2ik_{\rm sp} \frac{\partial \mathcal{A}}{\partial z} + \frac{\partial^2 \mathcal{A}}{\partial y^2}\right) \int_{-\infty}^{+\infty} |h(x)|^2 dx - \mathcal{A} \frac{4\pi}{c} \tilde{\sigma} ik_0 \varepsilon \int_{-\infty}^{+\infty} |e_z(x)|^2 \delta(x) dx = 0\,. \tag{B.17}$$

Taking into account that $e_z(x = 0) = 1$ and the power density flow in the mode $\{\mathbf{e}, h(x)\mathbf{y}_0\} \exp(ik_{\rm sp}z)$ is given by

$$P = \frac{c}{8\pi} \mathrm{Re} \int_{-\infty}^{+\infty} e_x(x) h^*(x) dx = \frac{c}{8\pi} \frac{k_{\rm sp}}{k_0 \varepsilon} , \int_{-\infty}^{+\infty} |h(x)|^2 dx ,$$

we come to the equation

$$\frac{\partial \mathcal{A}}{\partial z} + \frac{1}{2ik_{\rm sp}} \frac{\partial^2 \mathcal{A}}{\partial y^2} + \frac{\tilde{\sigma}}{4P} \mathcal{A} = 0 , \tag{B.18}$$

which coincides with Eq. (B.12) if setting $\dfrac{\partial \mathcal{A}}{\partial y} = 0$.

III. Finally, we notice that one more approach, where the surface current induced in graphene is introduced into the boundary conditions for fields, was outlined in Ref. [129] for nonlinear surface plasmon waves, both transverse magnetic (TM) and transverse electric (TE), and also used by us in Ref. [130] for describing linear localized channel plasmons guided by curved graphene.

References

[1] L. Novotny and B. Hecht, *Principles of Nano-Optics*. New York: Cambridge University Press, 2007.

[2] V. M. Shalaev and S. Kawata, eds., *Nanophotonics with Surface Plasmons*. Elsevier Science, 2007.

[3] S. Gaponenko, *Principles of Nano-Optics*. New York: Cambridge University Pres, 2010.

[4] D. K. Gramotnev and S. I. Bozhevolnyi, "Plasmonics beyond the diffraction limit," *Nat. Photon.*, vol. 4, pp. 83–91, 2010.

[5] V. M. Menon, L. I. Deych, and A. A. Lisyansky, "Nonlinear optics: Towards polaritonic logic circuits," *Nat. Photon.*, vol. 4, pp. 345–346, jun 2010.

[6] D. A. B. Miller, "Are optical transistors the logical next step?," *Nat. Photon.*, vol. 4, pp. 3–5, jan 2010.

[7] S. Kawata, Y. Inouye, and P. Verma, "Plasmonics for near-field nano-imaging and superlensing," *Nat. Photon.*, vol. 3, pp. 388–394, jul 2009.

[8] N. Liu, M. L. Tang, M. Hentschel, H. Giessen, and A. P. Alivisatos, "Nanoantenna-enhanced gas sensing in a single tailored nanofocus," *Nat. Mater.*, vol. 10, pp. 631–636, may 2011.

[9] D. Rodrigo, O. Limaj, D. Janner, D. Etezadi, F. J. G. de Abajo, V. Pruneri, and H. Altug, "Mid-infrared plasmonic biosensing with graphene," *Science*, vol. 349, pp. 165–168, jul 2015.

[10] M. L. Brongersma and P. G. Kik, eds., *Surface Plasmon Nanophotonics*. Springer Netherlands, 2007.

[11] S. A. Maier, ed., *Plasmonics: Fundamentals and Applications*. Springer-Verlag, 2007.

[12] L. Cao and M. L. Brongersma, "Active plasmonics: Ultrafast developments," *Nat. Photon.*, vol. 3, pp. 12–13, jan 2009.

[13] V. V. Klimov, *Nanoplasmonics*. Moskow: Fismatlit, 2010.

[14] A. A. Maradudin, J. R. Sambles, and W. L. Barnes, *Modern Plasmonics*. Poland: Elsevier B.V., 2014.

[15] M. A. Noginov, G. Zhu, M. Mayy, B. A. Ritzo, N. Noginova, and V. A. Podolskiy, "Stimulated emission of surface plasmon polaritons," *Phys. Rev. Lett.*, vol. 101, p. 226806, nov 2008.

[16] M. I. Stockman, "Nanofocusing of optical energy in tapered plasmonic waveguides," *Phys. Rev. Lett.*, vol. 93, p. 137404, sep 2004.

[17] A. R. Davoyan, I. V. Shadrivov, A. A. Zharov, D. K. Gramotnev, and Y. S. Kivshar, "Nonlinear nanofocusing in tapered plasmonic waveguides," *Phys. Rev. Lett.*, vol. 105, p. 116804, sep 2010.

[18] A. Krasnok, S. Makarov, M. Petrov, R. Savelev, P. Belov, and Y. Kivshar, "Towards all-dielectric metamaterials and nanophotonics," in *Metamaterials X* (V. Kuzmiak, P. Markos, and T. Szoplik, eds.), SPIE-Intl Soc Optical Eng, may 2015.

[19] L. Novotny and N. van Hulst, "Antennas for light," *Nat. Photon.*, vol. 5, pp. 83–90, feb 2011.

[20] A. E. Krasnok, I. S. Maksymov, A. I. Denisyuk, P. A. Belov, A. E. Miroshnichenko, C. R. Simovski, and Y. S. Kivshar, "Optical nanoantennas," *Phys.-Usp.*, vol. 56, pp. 539–564, jun 2013.

[21] P.-Y. Chen and A. Alù, "Atomically thin surface cloak using graphene monolayers," *ACS Nano*, vol. 5, pp. 5855–5863, jul 2011.

[22] P.-Y. Chen, J. Soric, Y. R. Padooru, H. M. Bernety, A. B. Yakovlev, and A. Alù, "Nanostructured graphene metasurface for tunable terahertz cloaking," *New J. Phys.*, vol. 15, p. 123029, dec 2013.

[23] D. A. Smirnova, I. V. Shadrivov, A. E. Miroshnichenko, A. I. Smirnov, and Y. S. Kivshar, "Second-harmonic generation by a graphene nanoparticle," *Phys. Rev. B*, vol. 90, p. 035412, jul 2014.

[24] I. Staude, A. E. Miroshnichenko, M. Decker, N. T. Fofang, S. Liu, E. Gonzales, J. Dominguez, T. S. Luk, D. N. Neshev, I. Brener, and Y. Kivshar, "Tailoring directional scattering through magnetic and electric resonances in subwavelength silicon nanodisks," *ACS Nano*, vol. 7, pp. 7824–7832, sep 2013.

[25] A. E. Krasnok, P. A. Belov, A. E. Miroshnichenko, A. I. Kuznetsov, B. S. Lukyanchuk, and Y. S. Kivshar, "All-dielectric optical nanoantennas," in *Progress in Compact Antennas*, InTech, sep 2014.

[26] A. K. Sarychev and V. M. Shalaev, *Electrodynamics of Metamaterials*. Singapore: World Scientific, 2007.

[27] A. Boltasseva and V. M. Shalaev, "Fabrication of optical negative-index metamaterials: Resent advances and outlook," *Metamaterials*, vol. 2, pp. 1–17, 2008.

[28] W. Cai and V. Shalaev, *Optical Metamaterials*. Springer Science + Business Media, 2010.

[29] R. W. Boyd, *Nonlinear Optics*. USA: Elsevier Science, 2003.

[30] J. E. Sipe and G. I. Stegeman, *Surface Polaritons: Electromagnetic waves at surfaces and interfaces*. Amsterdam: North-Holland, 1982.

[31] J. I. Dadap, J. Shan, K. B. Eisenthal, and T. F. Heinz, "Second-harmonic Rayleigh scattering from a sphere of centrosymmetric material," *Phys. Rev. Lett.*, vol. 83, no. 20, pp. 4045–4048, 1999.

[32] Z. Chen and R. Morandotti, eds., *Nonlinear Photonics and Novel Optical Phenomena*. Springer New York, 2012.

[33] M. Kauranen and A. V. Zayats, "Nonlinear plasmonics," *Nat. Photon.*, vol. 6, pp. 737–748, nov 2012.

[34] I. V. Shadrivov, M. Lapine, and Y. S. Kivshar, eds., *Nonlinear, Tunable and Active Metamaterials*. Springer International Publishing, 2015.

[35] A. E. Minovich, A. E. Miroshnichenko, A. Y. Bykov, T. V. Murzina, D. N. Neshev, and Y. S. Kivshar, "Functional and nonlinear optical metasurfaces," *Laser Photon. Rev.*, vol. 9, pp. 195–213, mar 2015.

[36] M. R. Shcherbakov, D. N. Neshev, B. Hopkins, A. S. Shorokhov, I. Staude, E. V. Melik-Gaykazyan, M. Decker, A. A. Ezhov, A. E. Miroshnichenko, I. Brener, A. A. Fedyanin, and Y. S. Kivshar, "Enhanced third-harmonic generation in silicon nanoparticles driven by magnetic response," *Nano Lett.*, vol. 14, pp. 6488–6492, nov 2014.

[37] M. R. Shcherbakov, A. S. Shorokhov, D. N. Neshev, B. Hopkins, I. Staude, E. V. Melik-Gaykazyan, A. A. Ezhov, A. E. Miroshnichenko, I. Brener, A. A. Fedyanin, and Y. S. Kivshar, "Nonlinear interference and tailorable third-harmonic generation from dielectric oligomers," *ACS Photonics*, vol. 2, pp. 578–582, may 2015.

[38] Y. S. Kivshar and G. A. Agrawal, *Optical Solitons: From Fibers to Photonic Crystals*. San Diego: Academic, 2003.

[39] S. I. Bozhevolnyi, V. S. Volkov, E. Devaux, and T. W. Ebbesen, "Channel plasmon-polariton guiding by subwavelength metal grooves," *Phys. Rev. Lett.*, vol. 95, p. 046802, jul 2005.

[40] S. I. Bozhevolnyi, V. S. Volkov, E. Devaux, J.-Y. Laluet, and T. W. Ebbesen, "Channel plasmon subwavelength waveguide components including interferometers and ring resonators," *Nature*, vol. 440, pp. 508–511, mar 2006.

[41] Y. Fang and M. Sun, "Nanoplasmonic waveguides: towards applications in integrated nanophotonic circuits," *Light Sci. Appl.*, vol. 4, p. e294, jun 2015.

[42] N. L. Rosi and C. A. Mirkin, "Nanostructures in biodiagnostics," *Chem. Rev.*, vol. 105, pp. 1547–1562, apr 2005.

[43] C. Forestiere, A. J. Pasquale, A. Capretti, G. Miano, A. Tamburrino, S. Y. Lee, B. M. Reinhard, and L. D. Negro, "Genetically engineered plasmonic nanoarrays," *Nano Lett.*, vol. 12, pp. 2037–2044, apr 2012.

[44] A. G. Curto, G. Volpe, T. H. Taminiau, M. P. Kreuzer, R. Quidant, and N. F. van Hulst, "Unidirectional emission of a quantum dot coupled to a nanoantenna," *Science*, vol. 329, pp. 930–933, aug 2010.

[45] V. K. Valev, X. Zheng, C. Biris, A. Silhanek, V. Volskiy, B. D. Clercq, O. A. Aktsipetrov, M. Ameloot, N. C. Panoiu, G. A. E. Vandenbosch, and V. V. Moshchalkov, "The origin of second harmonic generation hotspots in chiral optical metamaterials [invited]," *Opt. Mater. Express*, vol. 1, no. 1, p. 36, 2011.

[46] N. I. Zheludev and Y. S. Kivshar, "From metamaterials to metadevices," *Nat. Mater.*, vol. 11, pp. 917–924, oct 2012.

[47] T. Utikal, M. Hentschel, and H. Giessen, "Nonlinear photonics with metallic nanostructures on top of dielectrics and waveguides," *Appl. Phys. B*, vol. 105, p. 51, 2011.

[48] T. Schumacher, K. Kratzer, D. Molnar, M. Hentschel, H. Giessen, and M. Lippitz, "Nanoantenna-enhanced ultrafast nonlinear spectroscopy of a single gold nanoparticle," *Nat. Commun.*, vol. 2, p. 333, may 2011.

[49] P. Ginzburg, A. Krasavin, Y. Sonnefraud, A. Murphy, R. J. Pollard, S. A. Maier, and A. V. Zayats, "Nonlinearly coupled localized plasmon resonances: Resonant second-harmonic generation," *Phys. Rev. B*, vol. 79, p. 155420, 2012.

[50] P. Ginzburg, A. V. Krasavin, and A. V. Zayats, "Cascaded second-order surface plasmon solitons due to intrinsic metal nonlinearity," *New J. of Phys.*, vol. 15, p. 013031, jan 2013.

[51] G. V. Naik, V. M. Shalaev, and A. Boltasseva, "Alternative plasmonic materials: Beyond gold and silver," *Adv. Mater.*, vol. 25, pp. 3264–3294, may 2013.

[52] A. N. Grigorenko, M. Polini, and K. S. Novoselov, "Graphene plasmonics," *Nat. Photon.*, vol. 6, pp. 749–758, nov 2012.

[53] A. K. Geim, "Graphene: Status and prospects," *Science*, vol. 324, pp. 1530–1534, jun 2009.

[54] F. H. L. Koppens, D. E. Chang, and F. J. Garcia de Abajo, "Graphene plasmonics: A platform for strong light-matter interactions," *Nano Lett.*, vol. 11, no. 8, p. 3370, 2011.

[55] Y. E. Lozovik, "Plasmonics and magnetoplasmonics based on graphene and a topological insulator," *Phys.-Usp.*, vol. 55, pp. 1035–1039, oct 2012.

[56] Q. Bao and K. P. Loh, "Graphene photonics, plasmonics, and broadband optoelectronic devices," *ACS Nano*, vol. 6, pp. 3677–3694, may 2012.

[57] M. Jablan, M. Soljacic, and H. Buljan, "Plasmons in graphene: Fundamental properties and potential applications," *Proc. IEEE*, vol. 101, no. 7, pp. 1689–1704, 2013.

[58] X. Luo, T. Qiu, W. Lu, and Z. Ni, "Plasmons in graphene: Recent progress and applications," *Mater. Sci. Eng.*, vol. 74, pp. 351–376, nov 2013.

[59] T. Stauber, "Plasmonics in Dirac systems: from graphene to topological insulators," *J. Phys.: Condens. Matter*, vol. 26, p. 123201, mar 2014.

[60] T. Low and P. Avouris, "Graphene plasmonics for terahertz to mid-infrared applications," *ACS Nano*, vol. 8, pp. 1086–1101, feb 2014.

[61] F. J. G. de Abajo, "Graphene plasmonics: Challenges and opportunities," *ACS Photonics*, vol. 1, pp. 135–152, mar 2014.

[62] N. K. Emani, A. V. Kildishev, V. M. Shalaev, and A. Boltasseva, "Graphene: A dynamic platform for electrical control of plasmonic resonance," *Nanophotonics*, vol. 4, p. 214223, jan 2015.

[63] R. R. Nair, P. Blake, A. N. Grigorenko, K. S. Novoselov, T. J. Booth, T. Stauber, N. M. R. Peres, and A. K. Geim, "Fine structure constant defines visual transparency of graphene," *Science*, vol. 320, pp. 1308–1308, jun 2008.

[64] F. Bonaccorso, Z. Sun, T. Hasan, and A. C. Ferrari, "Graphene photonics and optoelectronics," *Nat. Photon.*, vol. 4, pp. 611–622, aug 2010.

[65] Z. Q. Li, E. A. Henriksen, Z. Jiang, Z. Hao, M. C. Martin, P. Kim, H. L. Stormer, and D. N. Basov, "Dirac charge dynamics in graphene by infrared spectroscopy," *Nat. Phys.*, vol. 4, pp. 532–535, jun 2008.

[66] S. Bae, H. Kim, Y. Lee, X. Xu, J.-S. Park, Y. Zheng, J. Balakrishnan, T. Lei, H. R. Kim, Y. I. Song, Y.-J. Kim, K. S. Kim, B. Özyilmaz, J.-H. Ahn, B. H. Hong, and S. Iijima, "Roll-to-roll production of 30-inch graphene films for transparent electrodes," *Nat. Nanotechnol.*, vol. 5, pp. 574–578, jun 2010.

[67] H.-S. P. Wong and D. Akinwande, *Carbon Nanotube and Graphene Device Physics*. New York: Cambridge University Press, 2011.

[68] M. Katsnelson, *Graphene: Carbon in Two Dimensions*. New York: Cambridge University Press, 2012.

[69] L. E. F. F. Torres, S. Roche, and J.-C. Charlier, *Introduction to Graphene-Based Nanomaterials*. New York: Cambridge University Press, 2014.

[70] L. A. Falkovsky and A. A. Varlamov, "Space-time dispersion of graphene conductivity," *Eur. Phys. J. B*, vol. 56, pp. 281–284, apr 2007.

[71] J. Chen, M. Badioli, P. Alonso-González, S. Thongrattanasiri, F. Huth, J. Osmond, M. Spasenović, A. Centeno, A. Pesquera, P. Godignon, A. Z. Elorza, N. Camara, F. J. G. de Abajo, R. Hillenbrand, and F. H. L. Koppens, "Optical nano-imaging of gate-tunable graphene plasmons," *Nature*, jun 2012.

[72] Z. Fei, A. S. Rodin, G. O. Andreev, W. Bao, A. S. McLeod, M. Wagner, L. M. Zhang, Z. Zhao, M. Thiemens, G. Dominguez, M. M. Fogler, A. H. C. Neto, C. N. Lau, F. Keilmann, and D. N. Basov, "Gate-tuning of graphene plasmons revealed by infrared nano-imaging," *Nature*, vol. 487, pp. 82–85, jun 2012.

[73] P. Alonso-Gonzalez, A. Y. Nikitin, F. Golmar, A. Centeno, A. Pesquera, S. Velez, J. Chen, G. Navickaite, F. Koppens, A. Zurutuza, F. Casanova, L. E. Hueso, and R. Hillenbrand, "Controlling graphene plasmons with resonant metal antennas and spatial conductivity patterns," *Science*, vol. 344, pp. 1369–1373, may 2014.

[74] T. Mueller, F. Xia, and P. Avouris, "Graphene photodetectors for high-speed optical communications," *Nat. Photon.*, vol. 4, pp. 297–301, mar 2010.

[75] M. Liu, X. Yin, E. Ulin-Avila, B. Geng, T. Zentgraf, L. Ju, F. Wang, and X. Zhang, "A graphene-based broadband optical modulator," *Nature*, vol. 474, pp. 64–67, may 2011.

[76] A. Vakil and N. Engheta, "Transformation optics using graphene," *Science*, vol. 332, pp. 1291–1294, jun 2011.

[77] L. Ju, B. Geng, J. Horng, C. Girit, M. Martin, Z. Hao, H. A. Bechtel, X. Liang, A. Zettl, Y. R. Shen, and F. Wang, "Graphene plasmonics for tunable terahertz metamaterials," *Nat. Nanotechnol.*, vol. 6, pp. 630–634, sep 2011.

[78] Z. Fang, S. Thongrattanasiri, A. Schlather, Z. Liu, L. Ma, Y. Wang, P. M. Ajayan, P. Nordlander, N. J. Halas, and F. J. G. de Abajo, "Gated tunability and hybridization of localized plasmons in nanostructured graphene," *ACS Nano*, vol. 7, pp. 2388–2395, mar 2013.

[79] Q. Bao, H. Zhang, B. Wang, Z. Ni, C. H. Y. X. Lim, Y. Wang, D. Y. Tang, and K. P. Loh, "Broadband graphene polarizer," *Nat. Photon.*, vol. 5, pp. 411–415, may 2011.

[80] S. H. Mousavi, I. Kholmanov, K. B. Alici, D. Purtseladze, N. Arju, K. Tatar, D. Y. Fozdar, J. W. Suk, Y. Hao, A. B. Khanikaev, R. S. Ruoff, and G. Shvets, "Inductive tuning of Fano-resonant metasurfaces using plasmonic response of graphene in the mid-infrared," *Nano Lett.*, vol. 13, pp. 1111–1117, mar 2013.

[81] S. A. Mikhailov and K. Ziegler, "New electromagnetic mode in graphene," *Phys. Rev. Lett.*, vol. 99, p. 016803, jul 2007.

[82] Y. V. Bludov, D. A. Smirnova, Y. S. Kivshar, N. M. R. Peres, and M. I. Vasilevskiy, "Nonlinear TE-polarized surface polaritons on graphene," *Phys. Rev. B*, vol. 89, p. 035406, jan 2014.

[83] B. Wunsch, T. Stauber, F. Sols, and F. Guinea, "Dynamical polarization of graphene at finite doping," *New J. Phys.*, vol. 8, pp. 318–318, dec 2006.

[84] A. Vakil and N. Engheta, "Fourier optics on graphene," *Phys. Rev. B*, vol. 85, p. 075434, feb 2012.

[85] M. Liu, X. Yin, and X. Zhang, "Double-layer graphene optical modulator," *Nano Lett.*, vol. 12, pp. 1482–1485, mar 2012.

[86] S. H. Lee, M. Choi, T.-T. Kim, S. Lee, M. Liu, X. Yin, H. K. Choi, S. S. Lee, C.-G. Choi, S.-Y. Choi, X. Zhang, and B. Min, "Switching terahertz waves with gate-controlled active graphene metamaterials," *Nat. Mater.*, vol. 11, pp. 936–941, sep 2012.

[87] M. Glazov and S. Ganichev, "High frequency electric field induced nonlinear effects in graphene," *Phys. Rep.*, vol. 535, pp. 101–138, feb 2014.

[88] M. M. Glazov, "Second harmonic generation in graphene," *JETP Lett.*, vol. 93, pp. 366–371, jun 2011.

[89] S. A. Mikhailov, "Non-linear electromagnetic response of graphene," *Europhys. Lett.*, vol. 79, p. 27002, jun 2007.

[90] S. A. Mikhailov and K. Ziegler, "Nonlinear electromagnetic response of graphene: frequency multiplication and the self-consistent-field effects," *J. Phys.: Condens. Matter*, vol. 20, p. 384204, aug 2008.

[91] S. A. Mikhailov, "Theory of the giant plasmon-enhanced second-harmonic generation in graphene and semiconductor two-dimensional electron systems," *Phys. Rev. B*, vol. 84, p. 045432, jul 2011.

[92] S. Mikhailov, "Frequency mixing effects in graphene," in *Physics and Applications of Graphene - Theory*, InTech, mar 2011.

[93] S. Mikhailov, "Electromagnetic nonlinearities in graphene," in *Carbon Nanotubes and Graphene for Photonic Applications*, pp. 171–221e, Elsevier BV, 2013.

[94] E. G. Mishchenko, "Dynamic conductivity in graphene beyond linear response," *Phys. Rev. Lett.*, vol. 103, p. 246802, dec 2009.

[95] A. R. Wright, X. G. Xu, J. C. Cao, and C. Zhang, "Strong nonlinear optical response of graphene in the terahertz regime," *Appl. Phys. Lett.*, vol. 95, no. 7, p. 072101, 2009.

[96] K. L. Ishikawa, "Nonlinear optical response of graphene in time domain," *Phys. Rev. B*, vol. 82, p. 201402, nov 2010.

[97] Z. Zhang and P. L. Voss, "Full-band quantum-dynamical theory of saturation and four-wave mixing in graphene," *Opt. Lett.*, vol. 36, no. 23, p. 4569, 2011.

[98] Z. Zhang and P. L. Voss, "A quantum-dynamical theory for nonlinear optical interactions in graphene," *arxiv:1106.4838v1*.

[99] X. Yao and A. Belyanin, "Giant optical nonlinearity of graphene in a strong magnetic field," *Phys. Rev. Lett.*, vol. 108, p. 255503, jun 2012.

[100] X. Yao and A. Belyanin, "Nonlinear optics of graphene in a strong magnetic field," *J. Phys.: Condens. Matter*, vol. 25, p. 054203, jan 2013.

[101] H. Dong, C. Conti, A. Marini, and F. Biancalana, "Terahertz relativistic spatial solitons in doped graphene metamaterials," *J. Phys. B: At. Mol. Opt. Phys.*, vol. 46, p. 155401, jul 2013.

[102] M. Ghaffarian, F. Ebrahimi, and S. Feizabadi, "Linear and nonlinear optical properties of graphene nanodisk out of equilibrium," *Physica E: Low-dimensional Systems and Nanostructures*, vol. 53, pp. 240–250, sep 2013.

[103] K. L. Ishikawa, "Electronic response of graphene to an ultrashort intense terahertz radiation pulse," *New J. Phys.*, vol. 15, p. 055021, may 2013.

[104] M. Gullans, D. Chang, F. Koppens, F. de Abajo, and M. Lukin, "Single-photon nonlinear optics with graphene plasmons," *Phys. Rev. Lett.*, vol. 111, p. 247401, dec 2013.

[105] X. Yao, M. Tokman, and A. Belyanin, "Efficient nonlinear generation of THz plasmons in graphene and topological insulators," *Phys. Rev. Lett.*, vol. 112, p. 055501, feb 2014.

[106] J. L. Cheng, N. Vermeulen, and J. E. Sipe, "DC current induced second order optical nonlinearity in graphene," *Opt. Express*, vol. 22, no. 13, p. 15868, 2014.

[107] J. L. Cheng, N. Vermeulen, and J. E. Sipe, "Third order optical nonlinearity of graphene," *New J. Phys.*, vol. 16, p. 053014, may 2014.

[108] I. Al-Naib, J. E. Sipe, and M. M. Dignam, "High harmonic generation in undoped graphene: Interplay of inter- and intraband dynamics," *Phys. Rev. B*, vol. 90, p. 245423, dec 2014.

[109] S. A. Mikhailov, "Quantum theory of third-harmonic generation in graphene," *Phys. Rev. B*, vol. 90, p. 241301, dec 2014.

[110] N. M. R. Peres, Y. V. Bludov, J. E. Santos, A.-P. Jauho, and M. I. Vasilevskiy, "Optical bistability of graphene in the terahertz range," *Phys. Rev. B*, vol. 90, p. 125425, sep 2014.

[111] J. D. Cox and F. J. G. de Abajo, "Electrically tunable nonlinear plasmonics in graphene nanoislands," *Nat. Commun.*, vol. 5, p. 5725, dec 2014.

[112] J. L. Cheng, N. Vermeulen, and J. E. Sipe, "Third-order nonlinearity of graphene: Effects of phenomenological relaxation and finite temperature," *Phys. Rev. B*, vol. 91, p. 235320, jun 2015.

[113] E. Hendry, P. J. Hale, J. Moger, A. K. Savchenko, and S. A. Mikhailov, "Coherent nonlinear optical response of graphene," *Phys. Rev. Lett.*, vol. 105, p. 097401, aug 2010.

[114] J. J. Dean and H. M. van Driel, "Graphene and few-layer graphite probed by second-harmonic generation: Theory and experiment," *Phys. Rev. B*, vol. 82, p. 125411, sep 2010.

[115] H. Yang, X. Feng, Q. Wang, H. Huang, W. Chen, A. T. S. Wee, and W. Ji, "Giant two-photon absorption in bilayer graphene," *Nano Lett.*, vol. 11, pp. 2622–2627, jul 2011.

[116] R. Wu, Y. Zhang, S. Yan, F. Bian, W. Wang, X. Bai, X. Lu, J. Zhao, and E. Wang, "Purely coherent nonlinear optical response in solution dispersions of graphene sheets," *Nano Lett.*, vol. 11, pp. 5159–5164, dec 2011.

[117] H. Zhang, S. Virally, Q. Bao, L. K. Ping, S. Massar, N. Godbout, and P. Kockaert, "Z-scan measurement of the nonlinear refractive index of graphene," *Opt. Lett.*, vol. 37, no. 11, p. 1856, 2012.

[118] T. Gu, N. Petrone, J. F. McMillan, A. van der Zande, M. Yu, G. Q. Lo, D. L. Kwong, J. Hone, and C. W. Wong, "Regenerative oscillation and four-wave mixing in graphene optoelectronics," *Nat. Photon.*, vol. 6, pp. 554–559, jul 2012.

[119] A. Y. Bykov, P. S. Rusakov, E. D. Obraztsova, and T. V. Murzina, "Probing structural inhomogeneity of graphene layers via nonlinear optical scattering," *Opt. Lett.*, vol. 38, no. 22, p. 4589, 2013.

[120] N. Kumar, J. Kumar, C. Gerstenkorn, R. Wang, H.-Y. Chiu, A. L. Smirl, and H. Zhao, "Third harmonic generation in graphene and few-layer graphite films," *Phys. Rev. B*, vol. 87, p. 121406, mar 2013.

[121] S.-Y. Hong, J. I. Dadap, N. Petrone, P.-C. Yeh, J. Hone, and R. M. Osgood, "Optical third-harmonic generation in graphene," *Phys. Rev. X*, vol. 3, p. 021014, jun 2013.

[122] M. J. Paul, Y. C. Chang, Z. J. Thompson, A. Stickel, J. Wardini, H. Choi, E. D. Minot, T. B. Norris, and Y.-S. Lee, "High-field terahertz response of graphene," *New J. Phys.*, vol. 15, p. 085019, aug 2013.

[123] H. Harutyunyan, R. Beams, and L. Novotny, "Controllable optical negative refraction and phase conjugation in graphite thin films," *Nat. Phys.*, vol. 9, pp. 423–425, may 2013.

[124] X.-L. Zhang, Z.-B. Liu, X.-C. Li, Q. Ma, X.-D. Chen, J.-G. Tian, Y.-F. Xu, and Y.-S. Chen, "Transient thermal effect, nonlinear refraction and nonlinear absorption properties of graphene oxide sheets in dispersion," *Opt. Express*, vol. 21, no. 6, p. 7511, 2013.

[125] D. Smirnova and Y. S. Kivshar, "Second-harmonic generation in subwavelength graphene waveguides," *Phys. Rev. B*, vol. 90, p. 165433, oct 2014.

[126] M. T. Manzoni, I. Silveiro, F. J. G. de Abajo, and D. E. Chang, "Second-order quantum nonlinear optical processes in single graphene nanostructures and arrays," *New J. Phys.*, vol. 17, p. 083031, aug 2015.

[127] L. E. Golub and S. A. Tarasenko, "Valley polarization induced second harmonic generation in graphene," *Phys. Rev. B*, vol. 90, p. 201402, nov 2014.

[128] D. A. Smirnova, A. E. Miroshnichenko, Y. S. Kivshar, and A. B. Khanikaev, "Tunable nonlinear graphene metasurfaces," *Phys. Rev. B*, vol. 92, p. 161406, oct 2015.

[129] A. V. Gorbach, "Nonlinear graphene plasmonics: Amplitude equation for surface plasmons," *Phys. Rev. A*, vol. 87, p. 013830, Jan 2013.

[130] D. Smirnova, S. H. Mousavi, Z. Wang, Y. S. Kivshar, and A. B. Khanikaev, "Trapping and guiding surface plasmons in curved graphene landscapes," *arXiv:1508.02729*, 2015.

[131] D. A. Smirnova, A. V. Gorbach, I. V. Iorsh, I. V. Shadrivov, and Y. S. Kivshar, "Nonlinear switching with a graphene coupler," *Phys. Rev. B*, vol. 88, p. 045443, Jul 2013.

[132] D. A. Smirnova, I. V. Shadrivov, A. I. Smirnov, and Y. S. Kivshar, "Dissipative plasmon-solitons in multilayer graphene," *Laser Photon. Rev.*, vol. 8, pp. 291–296, dec 2013.

[133] D. A. Smirnova and A. S. Solntsev, "Cascaded third-harmonic generation in hybrid graphene-semiconductor waveguides," *Phys. Rev. B*, vol. 92, p. 155410, oct 2015.

[134] A. W. Snyder and J. D. Love, eds., *Optical Waveguide Theory*. London: Chapman and Hall, 1983.

[135] A. A. Sukhorukov, A. S. Solntsev, S. S. Kruk, D. N. Neshev, and Y. S. Kivshar, "Nonlinear coupled-mode theory for periodic plasmonic waveguides and metamaterials with loss and gain," *Opt. Lett.*, vol. 39, no. 3, p. 462, 2014.

[136] S. Y. Park and D. Stroud, "Surface-plasmon dispersion relations in chains of metallic nanoparticles: An exact quasistatic calculation," *Phys. Rev. B*, vol. 69, p. 125418, mar 2004.

[137] P. B. Johnson and R. W. Christy, "Optical constants of the noble metals," *Phys. Rev. B*, vol. 6, p. 4370, 1972.

[138] P. Ginzburg, A. Hayat, N. Berkovitch, and M. Orenstein, "Nonlocal ponderomotive nonlinearity in plasmonics," *Opt. Lett.*, vol. 35, p. 1551, 2010.

[139] S. G. Rautian, "Nonlinear saturation spectroscopy of the degenerate electron gas in spherical metallic particles," *JETP*, vol. 85, p. 451, 1997.

[140] V. P. Drachev, A. K. Buin, H. Nakotte, and V. M. Shalaev, "Size dependent $\chi^{(3)}$ for conduction electrons in Ag nanoparticles," *Nano Lett.*, vol. 4, p. 1535, 2004.

[141] A. A. Govyadinov, G. Y. Panasyuk, J. C. Schotland, and V. A. Markel, "Theoretical and numerical investigation of the size-dependent optical effects in metal nanoparticles," *Phys. Rev. B*, vol. 84, p. 155461, 2011.

[142] F. Hache, D. Ricard, C. Flytzanis, and U. Kreibig, "The optical Kerr effect in small metal particles and metal colloids: the case of gold," *Appl. Phys. A: Solids Surf.*, vol. 47, p. 347, 1988.

[143] A. Marini, M. Conforti, G. D. Valle, H. W. Lee, T. X. Tran, W. Chang, M. A. Schmidt, S. Longhi, R. P. St. J, and F. Biancalana, "Ultrafast nonlinear dynamics of surface plasmon polaritons in gold nanowires due to the intrinsic nonlinearity of metals," *New J. Phys.*, vol. 15, p. 013033, 2013.

[144] B. Palpant, "Third-order nonlinear optical response of metal nanoparticles," in *Non-Linear Optical Properties of Matter* (M. G. Papadopoulos, A. J. Sadlej, and J. Leszczynski, eds.), pp. 461–508, Springer, Dordrecht, 2006.

[145] R. E. Noskov, P. A. Belov, and Y. S. Kivshar, "Subwavelength plasmonic kinks in arrays of metallic nanoparticles," *Opt. Express*, vol. 20, no. 3, p. 2733, 2012.

[146] R. E. Noskov, P. A. Belov, and Y. S. Kivshar, "Subwavelength modulational instability and plasmon oscillons in nanoparticle arrays," *Phys. Rev. Lett.*, vol. 108, p. 093901, feb 2012.

[147] R. Noskov, P. Belov, and Y. Kivshar, "Oscillons, solitons, and domain walls in arrays of nonlinear plasmonic nanoparticles," *Sci. Rep.*, vol. 2, p. 873, nov 2012.

[148] R. E. Noskov, D. A. Smirnova, and Y. S. Kivshar, "Subwavelength solitons and Faraday waves in two-dimensional lattices of metal nanoparticles," *Opt. Lett.*, vol. 38, no. 14, p. 2554, 2013.

[149] I. V. Shadrivov, A. A. Zharov, N. A. Zharova, and Y. S. Kivshar, "Nonlinear magnetoinductive waves and domain walls in composite metamaterials," *Phot. Nano. Fund. Appl.*, vol. 4, pp. 69–74, may 2006.

[150] N. N. Rosanov, N. V. Vysotina, A. N. Shatsev, I. V. Shadrivov, D. A. Powell, and Y. S. Kivshar, "Discrete dissipative localized modes in nonlinear magnetic metamaterials," *Opt. Express*, vol. 19, no. 27, p. 26500, 2011.

[151] A. Maluckov, G. Gligorić, L. Hadžievski, B. A. Malomed, and T. Pfau, "Stable periodic density waves in dipolar Bose-Einstein condensates trapped in optical lattices," *Phys. Rev. Lett.*, vol. 108, p. 140402, apr 2012.

[152] H. Wang, L. Shi, B. Lukyanchuk, C. Sheppard, and C. T. Chong, "Creation of a needle of longitudinally polarized light in vacuum using binary optics," *Nat. Photon.*, vol. 2, pp. 501–505, jun 2008.

[153] R. M. Hornreich, M. Luban, and S. Shtrikman, "Critical behavior at the onset of $\vec{k}$-space instability on the λ line," *Phys. Rev. Lett.*, vol. 35, pp. 1678–1681, dec 1975.

[154] M. C. Cross and P. C. Hohenberg, "Pattern formation outside of equilibrium," *Rev. Mod. Phys.*, vol. 65, pp. 851–1112, jul 1993.

[155] M. G. Clerc, A. Petrossian, and S. Residori, "Bouncing localized structures in a liquid-crystal light-valve experiment," *Phys. Rev. E*, vol. 71, p. 015205, jan 2005.

[156] M. G. Clerc, R. G. Elias, and R. G. Rojas, "Continuous description of lattice discreteness effects in front propagation," *Phil. Trans. R. Soc. A*, vol. 369, pp. 412–424, dec 2010.

[157] N. N. Rosanov, *Spatial Hysteresis and Optical Patterns*. Springer Berlin Heidelberg, 2002.

[158] J. Miles, "On Faraday waves," *J. Fluid Mech.*, vol. 248, p. 671, mar 1993.

[159] C. Torres-Torres, N. Peréa-López, J. A. Reyes-Esqueda, L. Rodríguez-Fernández, A. Crespo-Sosa, J. C. Cheang-Wong, and A. Oliver, "Ablation and optical third-order nonlinearities in Ag nanoparticles," *Int. J. Nanomedicine*, vol. 5, p. 925, 2010.

[160] D. A. Smirnova, I. V. Iorsh, I. V. Shadrivov, and Y. S. Kivshar, "Multilayer graphene waveguides," *Jetp Lett.*, vol. 99, pp. 456–460, jun 2014.

[161] Y. V. Bludov, A. Ferreira, N. M. R. Peres, and M. I. Vasilevskiy, "A primer on surface plasmon-polaritons in graphene," *Int. J. Mod. Phys. B*, vol. 27, p. 1341001, apr 2013.

[162] A. Y. Nikitin, F. Guinea, F. J. Garcia-Vidal, and L. Martin-Moreno, "Surface plasmon enhanced absorption and suppressed transmission in periodic arrays of graphene ribbons," *Phys. Rev. B*, vol. 85, p. 081405, feb 2012.

[163] T. M. Slipchenko, M. L. Nesterov, L. Martin-Moreno, and A. Y. Nikitin, "Analytical solution for the diffraction of an electromagnetic wave by a graphene grating," *J. Opt.*, vol. 15, p. 114008, oct 2013.

[164] S. Thongrattanasiri, F. H. L. Koppens, and F. J. G. de Abajo, "Complete optical absorption in periodically patterned graphene," *Phys. Rev. Lett.*, vol. 108, p. 047401, jan 2012.

[165] H. Yan, X. Li, B. Chandra, G. Tulevski, Y. Wu, M. Freitag, W. Zhu, P. Avouris, and F. Xia, "Tunable infrared plasmonic devices using graphene/insulator stacks," *Nat. Nanotechnol.*, vol. 7, pp. 330–334, apr 2012.

[166] S. Thongrattanasiri, A. Manjavacas, and F. J. Garcia de Abajo, "Quantum finite-size effects in graphene plasmons," *ACS Nano*, vol. 6, no. 2, p. 1766, 2012.

[167] J. Christensen, A. Manjavacas, S. Thongrattanasiri, F. H. L. Koppens, and F. J. Garcia de Abajo, "Graphene plasmon waveguiding and hybridization in individual and paired nanoribbons," *ACS Nano*, vol. 6, no. 1, pp. 431–440, 2012.

[168] S. Thongrattanasiri, I. Silveiro, and F. J. G. de Abajo, "Plasmons in electrostatically doped graphene," *Appl. Phys. Lett.*, vol. 100, p. 201105, 2012.

[169] F. J. Garcia de Abajo and A. Howie, "Retarded field calculation of electron energy loss in inhomogeneous dielectrics," *Phys. Rev. B*, vol. 65, p. 115418, Mar 2002.

[170] U. Hohenester and A. Trugler, "MNPBEM – A Matlab toolbox for the simulation of plasmonic nanoparticles," *Comput. Phys. Commun.*, vol. 183, no. 2, pp. 370 – 381, 2012.

[171] L. D. Landau and E. M. Lifshitz, *Electrodynamics of Continuous Media*. New York: Pergamon, 1984.

[172] *Dissipative Solitons: From Optics to Biology and Medicine*. Springer Berlin Heidelberg, 2008.

[173] T. Ackemann, W. Firth, and G.-L. Oppo, "Chapter 6: Fundamentals and applications of spatial dissipative solitons in photonic devices," in *Advances In Atomic, Molecular, and Optical Physics*, pp. 323–421, Elsevier BV, 2009.

[174] U. Peschel, O. Egorov, and F. Lederer, "Discrete cavity solitons," *Opt. Lett.*, vol. 29, no. 16, p. 1909, 2004.

[175] O. A. Egorov, F. Lederer, and Y. S. Kivshar, "How does an inclined holding beam affect discrete modulational instability and solitons in nonlinear cavities?," *Opt. Express*, vol. 15, no. 7, p. 4149, 2007.

[176] B. Krauss, T. Lohmann, D.-H. Chae, M. Haluska, K. von Klitzing, and J. H. Smet, "Laser-induced disassembly of a graphene single crystal into a nanocrystalline network," *Phys. Rev. B*, vol. 79, p. 165428, apr 2009.

[177] M. Currie, J. D. Caldwell, F. J. Bezares, J. Robinson, T. Anderson, H. Chun, and M. Tadjer, "Quantifying pulsed laser induced damage to graphene," *Appl. Phys. Lett.*, vol. 99, no. 21, p. 211909, 2011.

[178] A. Roberts, D. Cormode, C. Reynolds, T. Newhouse-Illige, B. J. LeRoy, and A. S. Sandhu, "Response of graphene to femtosecond high-intensity laser irradiation," *Appl. Phys. Lett.*, vol. 99, no. 5, p. 051912, 2011.

[179] V. Kiisk, T. Kahro, J. Kozlova, L. Matisen, and H. Alles, "Nanosecond laser treatment of graphene," *Appl. Surf. Sci.*, vol. 276, pp. 133–137, jul 2013.

[180] N.-C. Panoiu and R. M. Osgood, "Subwavelength nonlinear plasmonic nanowire," *Nano Lett.*, vol. 4, pp. 2427–2430, dec 2004.

[181] Y. Liu, G. Bartal, D. A. Genov, and X. Zhang, "Subwavelength discrete solitons in nonlinear metamaterials," *Phys. Rev. Lett.*, vol. 99, p. 153901, oct 2007.

[182] F. Ye, D. Mihalache, B. Hu, and N. C. Panoiu, "Subwavelength plasmonic lattice solitons in arrays of metallic nanowires," *Phys. Rev. Lett.*, vol. 104, p. 106802, mar 2010.

[183] M. Jablan, H. Buljan, and M. Soljačić, "Plasmonics in graphene at infrared frequencies," *Phys. Rev. B*, vol. 80, p. 245435, Dec 2009.

[184] M. L. Nesterov, J. Bravo-Abad, A. Y. Nikitin, F. J. García-Vidal, and L. Martin-Moreno, "Graphene supports the propagation of subwavelength optical solitons," *Laser Photon. Rev.*, vol. 7, pp. L7–L11, jan 2013.

[185] G. A. Korn and T. M. Korn, *Mathematical Handbook for Scientists and Engineers*. McGraw-Hill, 1961.

[186] T. Stauber, N. M. R. Peres, and A. K. Geim, "Optical conductivity of graphene in the visible region of the spectrum," *Phys. Rev. B*, vol. 78, p. 085432, aug 2008.

[187] F. T. Vasko and V. Ryzhii, "Voltage and temperature dependencies of conductivity in gated graphene," *Phys. Rev. B*, vol. 76, p. 233404, dec 2007.

[188] T. Otsuji, S. A. B. Tombet, A. Satou, H. Fukidome, M. Suemitsu, E. Sano, V. Popov, M. Ryzhii, and V. Ryzhii, "Graphene-based devices in terahertz science and technology," *J. Phys. D: Appl. Phys.*, vol. 45, p. 303001, jul 2012.

[189] J. Eilbeck, P. Lomdahl, and A. Scott, "The discrete self-trapping equation," *Physica D*, vol. 16, pp. 318–338, jul 1985.

[190] T. Heil, I. Fischer, W. Elsässer, J. Mulet, and C. R. Mirasso, "Chaos synchronization and spontaneous symmetry-breaking in symmetrically delay-coupled semiconductor lasers," *Phys. Rev. Lett.*, vol. 86, pp. 795–798, jan 2001.

[191] P. Kevrekidis, Z. Chen, B. Malomed, D. Frantzeskakis, and M. Weinstein, "Spontaneous symmetry breaking in photonic lattices: Theory and experiment," *Phys. Lett. A*, vol. 340, pp. 275–280, jun 2005.

[192] L. E. Sadler, J. M. Higbie, S. R. Leslie, M. Vengalattore, and D. M. Stamper-Kurn, "Spontaneous symmetry breaking in a quenched ferromagnetic spinor Bose–Einstein condensate," *Nature*, vol. 443, pp. 312–315, sep 2006.

[193] G. Herring, P. G. Kevrekidis, B. A. Malomed, R. Carretero-González, and D. J. Frantzeskakis, "Symmetry breaking in linearly coupled dynamical lattices," *Phys. Rev. E*, vol. 76, dec 2007.

[194] T. Mayteevarunyoo, B. A. Malomed, and G. Dong, "Spontaneous symmetry breaking in a nonlinear double-well structure," *Phys. Rev. A*, vol. 78, p. 053601, nov 2008.

[195] P. Neugebauer, M. Orlita, C. Faugeras, A.-L. Barra, and M. Potemski, "How perfect can graphene be?," *Phys. Rev. Lett.*, vol. 103, p. 136403, sep 2009.

[196] I. V. Iorsh, I. S. Mukhin, I. V. Shadrivov, P. A. Belov, and Y. S. Kivshar, "Hyperbolic metamaterials based on multilayer graphene structures," *Phys. Rev. B*, vol. 87, p. 075416, feb 2013.

[197] M. A. K. Othman, C. Guclu, and F. Capolino, "Graphene-based tunable hyperbolic metamaterials and enhanced near-field absorption," *Opt. Express*, vol. 21, no. 6, p. 7614, 2013.

[198] P. Yeh, *Optical Waves in Layered Media*. New York: Wiley, 1988.

[199] M. Born and E. Wolf, *Principles of Optics: Electromagnetic Theory of Propagation, Interference and Diffraction of Light*. Cambridge: Cambridge University Press, 1999.

[200] P. I. Buslaev, I. V. Iorsh, I. V. Shadrivov, P. A. Belov, and Y. S. Kivshar, "Plasmons in waveguide structures formed by two graphene layers," *JETP Lett.*, vol. 97, pp. 535–539, jul 2013.

[201] A. A. Dubinov, V. Y. Aleshkin, V. Mitin, T. Otsuji, and V. Ryzhii, "Terahertz surface plasmons in optically pumped graphene structures," *J. Phys.: Condens. Matter*, vol. 23, no. 14, p. 145302, 2011.

[202] G. W. Hanson, "Quasi-transverse electromagnetic modes supported by a graphene parallel-plate waveguide," *J. Appl. Phys.*, vol. 104, no. 8, p. 084314, 2008.

[203] M. Nakamura and L. Hirasawa, "Electric transport and magnetic properties in multilayer graphene," *Phys. Rev. B*, vol. 77, p. 045429, Jan 2008.

[204] M. Orlita and M. Potemski, "Dirac electronic states in graphene systems: optical spectroscopy studies," *Semicond. Sci. Technol.*, vol. 25, no. 6, p. 063001, 2010.

[205] L. A. Falkovsky and S. S. Pershoguba, "Optical far-infrared properties of a graphene monolayer and multilayer," *Phys. Rev. B*, vol. 76, p. 153410, Oct 2007.

[206] L. A. Lugiato and R. Lefever, "Spatial dissipative structures in passive optical systems," *Phys. Rev. Lett.*, vol. 58, pp. 2209–2211, May 1987.

[207] D. Turaev, A. G. Vladimirov, and S. Zelik, "Long-range interaction and synchronization of oscillating dissipative solitons," *Phys. Rev. Lett.*, vol. 108, p. 263906, jun 2012.

[208] F. Leo, L. Gelens, P. Emplit, M. Haelterman, and S. Coen, "Dynamics of one-dimensional Kerr cavity solitons," *Opt. Express*, vol. 21, no. 7, p. 9180, 2013.

[209] D. Gomila, A. Scroggie, and W. Firth, "Bifurcation structure of dissipative solitons," *Physica D*, vol. 227, no. 1, pp. 70 – 77, 2007.

[210] I. Tamm, "On the possibility of bound states of electrons on the surface of a crystal," *Zh. Eksp. Teor. Fiz.*, vol. 3, p. 34, 1933.

[211] P. Yeh, A. Yariv, and A. Y. Cho, "Optical surface waves in periodic layered media," *Appl. Phys. Let*, vol. 32, no. 2, p. 104, 1978.

[212] A. P. Vinogradov, A. V. Dorofeenko, A. M. Merzlikin, and A. A. Lisyansky, "Surface states in photonic crystals," *Phys.-Usp.*, vol. 53, pp. 243–256, jun 2010.

[213] A. Namdar, I. V. Shadrivov, and Y. S. Kivshar, "Backward Tamm states in left-handed metamaterials," *Appl. Phys. Lett.*, vol. 89, no. 11, p. 114104, 2006.

[214] I. Iorsh, A. Orlov, P. Belov, and Y. Kivshar, "Interface modes in nanostructured metal-dielectric metamaterials," *Appl. Phys. Lett.*, vol. 99, no. 15, p. 151914, 2011.

[215] C. S. R. Kaipa, A. B. Yakovlev, G. W. Hanson, Y. R. Padooru, F. Medina, and F. Mesa, "Enhanced transmission with a graphene-dielectric microstructure at low-terahertz frequencies," *Phys. Rev. B*, vol. 85, p. 245407, jun 2012.

[216] Y. Fan, Z. Wei, H. Li, H. Chen, and C. M. Soukoulis, "Photonic band gap of a graphene-embedded quarter-wave stack," *Phys. Rev. B*, vol. 88, p. 241403, dec 2013.

[217] K. V. Sreekanth, S. Zeng, J. Shang, K.-T. Yong, and T. Yu, "Excitation of surface electromagnetic waves in a graphene-based Bragg grating," *Sci. Rep.*, vol. 2, p. 737, oct 2012.

[218] A. Dorofeenko, A. Zyablovsky, A. A. Pukhov, A. Lisyansky, and A. P. Vinogradov, "Light propagation in composite materials with gain layers," *Usp. Fiz. Nauk*, vol. 182, no. 11, pp. 1157–1175, 2012.

[219] Y.-J. Li, Q.-Q. Sun, L. Chen, P. Zhou, P.-F. Wang, S.-J. Ding, and D. W. Zhang, "Hexagonal boron nitride intercalated multi-layer graphene: a possible ultimate solution to ultra-scaled interconnect technology," *AIP Advances*, vol. 2, no. 1, p. 012191, 2012.

[220] J. M. Chamberlain, "Where optics meets electronics: recent progress in decreasing the terahertz gap," *Phil. Trans. R. Soc. A*, vol. 362, pp. 199–213, feb 2004.

[221] H. Yan, T. Low, W. Zhu, Y. Wu, M. Freitag, X. Li, F. Guinea, P. Avouris, and F. Xia, "Damping pathways of mid-infrared plasmons in graphene nanostructures," *Nat. Photon.*, vol. 7, pp. 394–399, apr 2013.

[222] A. J. Sievers and S. Takeno, "Intrinsic localized modes in anharmonic crystals," *Phys. Rev. Lett.*, vol. 61, pp. 970–973, aug 1988.

[223] N. Kuroda, Y. Wakabayashi, M. Nishida, N. Wakabayashi, M. Yamashita, and N. Matsushita, "Decay kinetics of long-lived photogenerated kinks in an MX chain compound," *Phys. Rev. Lett.*, vol. 79, pp. 2510–2513, sep 1997.

[224] A. Trombettoni and A. Smerzi, "Discrete solitons and breathers with dilute Bose-Einstein condensates," *Phys. Rev. Lett.*, vol. 86, pp. 2353–2356, mar 2001.

[225] G. L. Alfimov, P. G. Kevrekidis, V. V. Konotop, and M. Salerno, "Wannier functions analysis of the nonlinear Schrödinger equation with a periodic potential," *Phys. Rev. E*, vol. 66, oct 2002.

[226] D. N. Christodoulides and R. I. Joseph, "Discrete self-focusing in nonlinear arrays of coupled waveguides," *Opt. Lett.*, vol. 13, no. 9, p. 794, 1988.

[227] A. V. Gorbach and D. V. Skryabin, "Spatial solitons in periodic nanostructures," *Phys. Rev. A*, vol. 79, p. 053812, may 2009.

[228] Y. S. Kivshar and D. K. Campbell, "Peierls-Nabarro potential barrier for highly localized nonlinear modes," *Phys. Rev. E*, vol. 48, pp. 3077–3081, oct 1993.

[229] G. Alfimov, V. Brazhnyi, and V. Konotop, "On classification of intrinsic localized modes for the discrete nonlinear Schrödinger equation," *Physica D*, vol. 194, pp. 127–150, jul 2004.

[230] A. Marini, A. V. Gorbach, and D. V. Skryabin, "Coupled-mode approach to surface plasmon polaritons in nonlinear periodic structures," *Opt. Lett.*, vol. 35, no. 20, p. 3532, 2010.

[231] Y. Kou, F. Ye, and X. Chen, "Multipole plasmonic lattice solitons," *Phys. Rev. A*, vol. 84, p. 033855, sep 2011.

[232] Y. Kou, F. Ye, and X. Chen, "Surface plasmonic lattice solitons," *Opt. Lett.*, vol. 37, no. 18, p. 3822, 2012.

[233] Y. Kou, F. Ye, and X. Chen, "Multiband vector plasmonic lattice solitons," *Opt. Lett.*, vol. 38, no. 8, p. 1271, 2013.

[234] F. Ye, D. Mihalache, B. Hu, and N. C. Panoiu, "Subwavelength vortical plasmonic lattice solitons," *Opt. Lett.*, vol. 36, no. 7, p. 1179, 2011.

[235] M. G. Silveirinha, "Theory of spatial optical solitons in metallic nanowire materials," *Phys. Rev. B*, vol. 87, p. 235115, jun 2013.

[236] D. E. Fernandes and M. G. Silveirinha, "Bright and dark spatial solitons in metallic nanowire arrays," *Phot. Nano. Fund. Appl.*, vol. 12, pp. 340–349, aug 2014.

[237] D. A. Smirnova, R. E. Noskov, L. A. Smirnov, and Y. S. Kivshar, "Dissipative plasmon solitons in graphene nanodisk arrays," *Phys. Rev. B*, vol. 91, p. 075409, feb 2015.

[238] K. G. Makris, S. Suntsov, D. N. Christodoulides, G. I. Stegeman, and A. Hache, "Discrete surface solitons," *Opt. Lett.*, vol. 30, no. 18, p. 2466, 2005.

[239] S. Suntsov, K. G. Makris, D. N. Christodoulides, G. I. Stegeman, A. Haché, R. Morandotti, H. Yang, G. Salamo, and M. Sorel, "Observation of discrete surface solitons," *Phys. Rev. Lett.*, vol. 96, p. 063901, feb 2006.

[240] C. R. Rosberg, D. N. Neshev, W. Krolikowski, A. Mitchell, R. A. Vicencio, M. I. Molina, and Y. S. Kivshar, "Observation of surface gap solitons in semi-infinite waveguide arrays," *Phys. Rev. Lett.*, vol. 97, p. 083901, aug 2006.

[241] M. I. Molina, R. A. Vicencio, and Y. S. Kivshar, "Discrete solitons and nonlinear surface modes in semi-infinite waveguide arrays," *Opt. Lett.*, vol. 31, no. 11, p. 1693, 2006.

[242] I. E. Tamm, "A possible kind of electron binding on crystal surfaces," *Z. Phys.*, vol. 76, p. 849, 1932.

[243] D. Smirnova, P. Buslaev, I. Iorsh, I. V. Shadrivov, P. A. Belov, and Y. S. Kivshar, "Deeply subwavelength electromagnetic Tamm states in graphene metamaterials," *Phys. Rev. B*, vol. 89, p. 245414, jun 2014.

[244] Y. V. Bludov, N. M. R. Peres, and M. I. Vasilevskiy, "Unusual reflection of electromagnetic radiation from a stack of graphene layers at oblique incidence," *J. Opt.*, vol. 15, p. 114004, oct 2013.

[245] P. G. Kevrekidis, H. Susanto, and Z. Chen, "High-order-mode soliton structures in two-dimensional lattices with defocusing nonlinearity," *Phys. Rev. E*, vol. 74, p. 066606, dec 2006.

[246] Y. V. Bludov and V. V. Konotop, "Surface modes and breathers in finite arrays of nonlinear waveguides," *Phys. Rev. E*, vol. 76, oct 2007.

[247] J. W. Ko, S.-W. Kim, J. Hong, J. Ryu, K. Kang, and C. B. Park, "Synthesis of graphene-wrapped CuO hybrid materials by CO_2 mineralization," *Green Chem.*, vol. 14, no. 9, p. 2391, 2012.

[248] J. S. Lee, K. H. You, and C. B. Park, "Highly photoactive, low bandgap TiO_2 nanoparticles wrapped by graphene," *Adv. Mater.*, vol. 24, pp. 1084–1088, jan 2012.

[249] S. Sheng, L. Zhang, and G. Chen, "Low-cost fabrication of graphene ball electrodes for the amperometric detection of capillary electrophoresis," *Electrochem. Commun.*, vol. 24, pp. 13–16, oct 2012.

[250] M. Farhat, C. Rockstuhl, and H. Bağcı, "A 3d tunable and multi-frequency graphene plasmonic cloak," *Opt. Express*, vol. 21, no. 10, p. 12592, 2013.

[251] J. Jackson, *Classical electrodynamics*. Moskow: Mir, 1965.

[252] C. F. Bohren and D. R. Huffman, *Absorption and Scattering of Light by Small Particles*. New York: Wiley, 1983.

[253] J. I. Dadap, J. Shan, and T. F. Heinz, "Theory of optical second-harmonic generation from a sphere of centrosymmetric material: small-particle limit," *J. Opt .Soc. Am. B*, vol. 21, no. 7, pp. 1328–1347, 2004.

[254] F. Wang, Y. Zhang, C. Tian, C. Girit, A. Zettl, M. Crommie, and Y. R. Shen, "Gate-variable optical transitions in graphene," *Science*, vol. 320, pp. 206–209, apr 2008.

[255] H. Liu, Y. Liu, and D. Zhu, "Chemical doping of graphene," *J. Mater. Chem.*, vol. 21, no. 10, pp. 3335–3345, 2011.

[256] Y. V. Bludov, N. M. R. Peres, and M. I. Vasilevskiy, "Graphene-based polaritonic crystal," *Phys. Rev. B*, vol. 85, p. 245409, jun 2012.

[257] N. M. R. Peres, A. Ferreira, Y. V. Bludov, and M. I. Vasilevskiy, "Light scattering by a medium with a spatially modulated optical conductivity: the case of graphene," *J. Phys.: Condens. Matter*, vol. 24, p. 245303, may 2012.

[258] S. M. Saltiel, A. A. Sukhorukov, and Y. S. Kivshar, *Multistep parametric processes in nonlinear optics*. Elsevier, 2005.

[259] A. S. Solntsev, A. A. Sukhorukov, D. N. Neshev, R. Iliew, R. Geiss, T. Pertsch, and Y. S. Kivshar, "Cascaded third harmonic generation in lithium niobate nanowaveguides," *Appl. Phys. Lett.*, vol. 98, no. 23, p. 231110, 2011.

[260] I.-T. Lin and J.-M. Liu, "Coupled surface plasmon modes of graphene in close proximity to a plasma layer," *Appl. Phys. Lett.*, vol. 103, no. 20, p. 201104, 2013.

[261] S. A. Mikhailov, "Erratum: Quantum theory of third-harmonic generation in graphene [phys. rev. b 90 , 241301(r) (2014)]," *Phys. Rev. B*, vol. 91, p. 039904, jan 2015.

[262] C. Wu, A. B. Khanikaev, R. Adato, N. Arju, A. A. Yanik, H. Altug, and G. Shvets, "Fano-resonant asymmetric metamaterials for ultrasensitive spectroscopy and identification of molecular monolayers," *Nat. Mater.*, vol. 11, pp. 69–75, nov 2011.

[263] Y. Yao, M. A. Kats, P. Genevet, N. Yu, Y. Song, J. Kong, and F. Capasso, "Broad electrical tuning of graphene-loaded plasmonic antennas," *Nano Lett.*, vol. 13, pp. 1257–1264, mar 2013.

[264] Z. Li and N. Yu, "Modulation of mid-infrared light using graphene-metal plasmonic antennas," *Appl. Phys. Lett.*, vol. 102, no. 13, p. 131108, 2013.

[265] N. K. Emani, T.-F. Chung, A. V. Kildishev, V. M. Shalaev, Y. P. Chen, and A. Boltasseva, "Electrical modulation of Fano resonance in plasmonic nanostructures using graphene," *Nano Lett.*, vol. 14, pp. 78–82, jan 2014.

[266] C. Wu, N. Arju, G. Kelp, J. A. Fan, J. Dominguez, E. Gonzales, E. Tutuc, I. Brener, and G. Shvets, "Spectrally selective chiral silicon metasurfaces based on infrared Fano resonances," *Nat. Commun.*, vol. 5, may 2014.

[267] N. Dabidian, I. Kholmanov, A. B. Khanikaev, K. Tatar, S. Trendafilov, S. H. Mousavi, C. Magnuson, R. S. Ruoff, and G. Shvets, "Electrical switching of infrared light using graphene integration with plasmonic Fano resonant metasurfaces," *ACS Photonics*, vol. 2, pp. 216–227, feb 2015.

[268] P. Alonso-Gonzalez, A. Y. Nikitin, F. Golmar, A. Centeno, A. Pesquera, S. Velez, J. Chen, G. Navickaite, F. Koppens, A. Zurutuza, F. Casanova, L. E. Hueso, and R. Hillenbrand, "Controlling graphene plasmons with resonant metal antennas and spatial conductivity patterns," *Science*, vol. 344, pp. 1369–1373, may 2014.

[269] B. Lukyanchuk, N. I. Zheludev, S. A. Maier, N. J. Halas, P. Nordlander, H. Giessen, and C. T. Chong, "The Fano resonance in plasmonic nanostructures and metamaterials," *Nat. Mater.*, vol. 9, pp. 707–715, aug 2010.

[270] A. E. Miroshnichenko, S. Flach, and Y. S. Kivshar, "Fano resonances in nanoscale structures," *Rev. Mod. Phys.*, vol. 82, pp. 2257–2298, aug 2010.

[271] A. B. Khanikaev, C. Wu, and G. Shvets, "Fano-resonant metamaterials and their applications," *Nanophotonics*, vol. 2, p. 247264, jan 2013.

[272] B. Gallinet and O. J. F. Martin, "Influence of electromagnetic interactions on the line shape of plasmonic Fano resonances," *ACS Nano*, vol. 5, pp. 8999–9008, nov 2011.

[273] N. Arju, T. Ma, A. Khanikaev, D. Purtseladze, and G. Shvets, "Optical realization of double-continuum Fano interference and coherent control in plasmonic metasurfaces," *Phys. Rev. Lett.*, vol. 114, p. 237403, jun 2015.

[274] V. A. Fedotov, M. Rose, S. L. Prosvirnin, N. Papasimakis, and N. I. Zheludev, "Sharp trapped-mode resonances in planar metamaterials with a broken structural symmetry," *Phys. Rev. Lett.*, vol. 99, p. 147401, oct 2007.

[275] S. H. Mousavi, A. B. Khanikaev, J. Allen, M. Allen, and G. Shvets, "Gyromagnetically induced transparency of metasurfaces," *Phys. Rev. Lett.*, vol. 112, p. 117402, mar 2014.

[276] A. D. Khan, "Multiple Fano resonances in bimetallic layered nanostructures," *Int. Nano Lett.*, vol. 4, p. 110, jun 2014.

[277] P.-Y. Chen, C. Argyropoulos, G. D'Aguanno, and A. Alù, "Enhanced second-harmonic generation by metasurface nanomixer and nanocavity," *ACS Photonics*, vol. 2, pp. 1000–1006, aug 2015.

[278] Y. Zhu, X. Hu, Y. Fu, H. Yang, and Q. Gong, "Ultralow-power and ultrafast all-optical tunable plasmon-induced transparency in metamaterials at optical communication range," *Sci. Rep.*, vol. 3, p. 2338, aug 2013.

[279] J. Lee, M. Tymchenko, C. Argyropoulos, P.-Y. Chen, F. Lu, F. Demmerle, G. Boehm, M.-C. Amann, A. Alù, and M. A. Belkin, "Giant nonlinear response from plasmonic metasurfaces coupled to intersubband transitions," *Nature*, vol. 511, pp. 65–69, jul 2014.

[280] K. O'Brien, H. Suchowski, J. Rho, A. Salandrino, B. Kante, X. Yin, and X. Zhang, "Predicting nonlinear properties of metamaterials from the linear response," *Nat. Mater.*, vol. 14, pp. 379–383, feb 2015.

[281] Y. V. Bludov, D. A. Smirnova, Y. S. Kivshar, N. M. R. Peres, and M. I. Vasilevskiy, "Discrete solitons in graphene metamaterials," *Phys. Rev. B*, vol. 91, p. 045424, jan 2015.